Max-Planck-Institut für
Extraterrestrische Physik

RESEARCH 2005 – 2006

A Book of Highlights

Observations – Measurements

Theory – Simulations

Experiments – Projects – Detector Developments

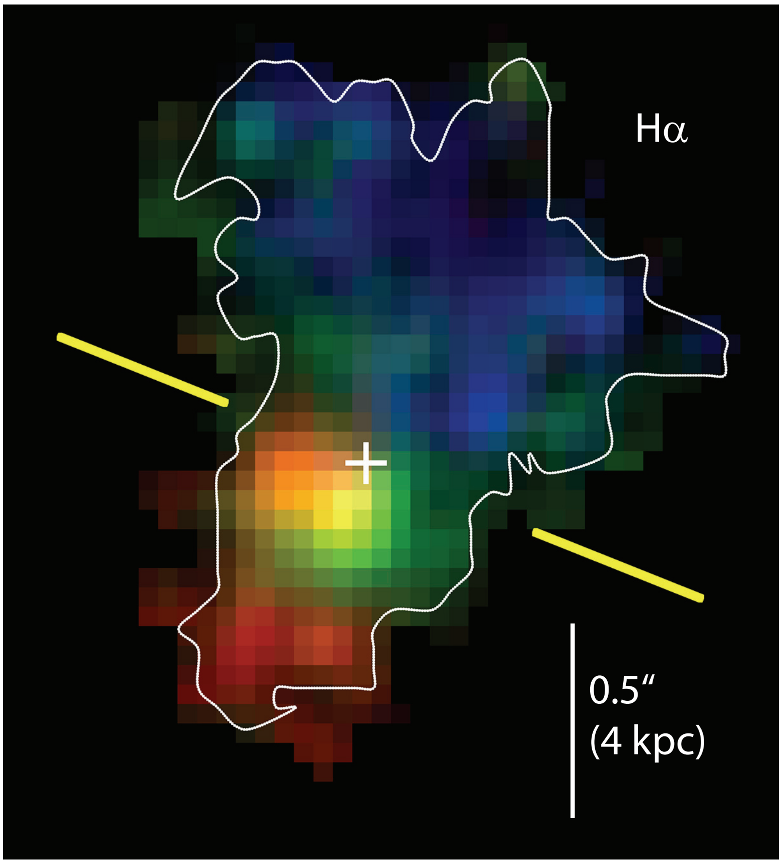

May 2007

Book of MPE Research Highlights

This book of MPE research highlights for the years 2005 and 2006 was produced for the MPE Fachbeirat Meeting of May 7 to 9, 2007. Its goal is to provide a comprehensive overview as well as detailed information on science results, data analysis activities, ongoing experimental projects and detector developments in a fashion that is supplementary to the Annual Reports for these years. The authors of individual posters are clearly identified and are solely responsible for their contents. Each scientist was encouraged to submit one highlight contribution. At an internal MPE science meeting on March 12 to 14, 2007, these contributions were presented to all scientists by talks and posters.

In this book the oral contributions are given at the beginning of the relevant sections. They are marked in the table of contents by **bold** letters, and their abstracts are framed by a red box.

Edited by G. Hasinger, B. Boller, Th. Boller, W. Collmar

Table of Contents

Table of Contents

Table of Contents

Table of Contents

Galaxy Evolution,

Large-Scale Structure and Cosmology

SINS: Spectroscopic Imaging survey of high redshift galaxies in the Near-infrared with SINFONI

Observations and theoretical simulations have established a global framework for galaxy formation and evolution in the young Universe. Galaxies formed as baryonic gas cooled at the center of collapsing dark matter haloes, and subsequently grew through mergers and collisions leading to the hierarchical build-up of galaxy mass. Observational evidence indicates that roughly half of the stellar mass in galaxies was put in place by redshift z~1. However, the details of how galaxies assembled their mass and evolved into the present-day population remain unclear. Our SINS survey of distant luminous galaxies now sheds new light on these questions by exploiting the new opportunities afforded by the integral field spectrometer SINFONI, partly built by the MPE IR/submm group and mounted at ESO's Very Large Telescope.

High resolution imaging spectroscopy of distant galaxies to map key rest-frame optical spectral diagnostics promises new empirical information about the crucial epoch of galaxy evolution at z~1–4. Using the near-infrared integral field spectrometer SINFONI, we are carrying out a large and coherent program aiming at a better understanding of the baryonic processes that drive galaxy formation and evolution. Our samples include representative galaxies of various classes at z~1–4. SINFONI provides spatially-resolved information on their dynamics, stellar populations, metallicities, and ionization state of the gas on typical scales of 4–5 kpc in seeing-limited mode, and 1–2 kpc for adaptive optics-assisted observations. To date, we have observed ~30 galaxies and investigated their nature, dynamics, evolution, star formation properties, metallicities, and feedback; more results are expected as we pursue SINS.

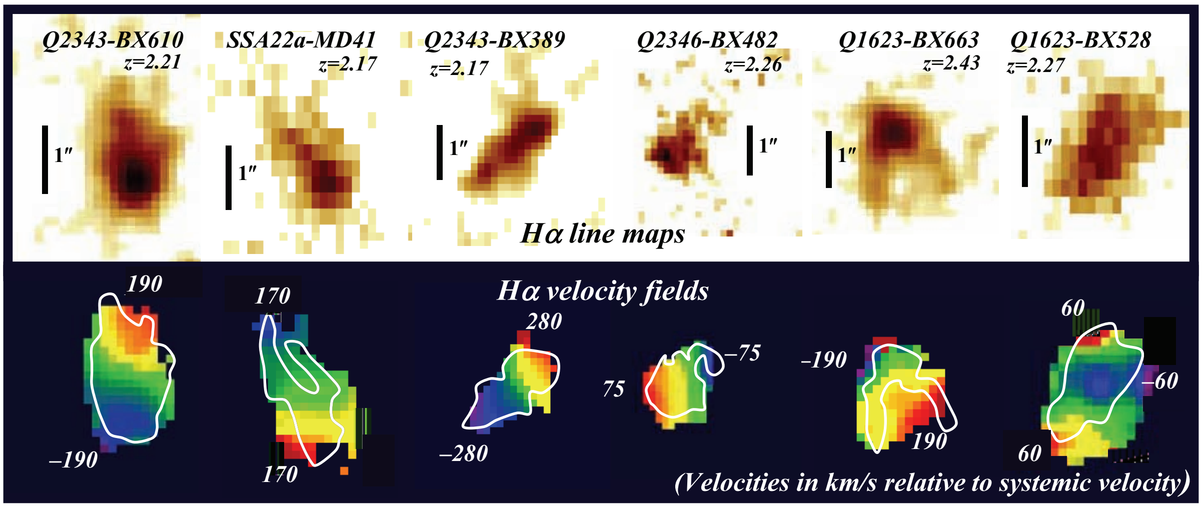

The figure highlights one of the first major outcome of SINS: the discovery of several large massive rotating disk-like systems at z~2, a rather surprising result in view of the higher merger rate at high redshift. For the four leftmost galaxies, the morphology and kinematics from the Hα line emission are in excellent agreement with rotating disks in which star formation takes places in large distinct complexes. In contrast, Q1623-BX528 seems to be a counter-rotating merger while Q1623-BX663 could be a merger remnant or disturbed spiral hosting an AGN. The large disks among our SINS samples have specific angular momenta of ~ 1000 km s^{-1} kpc, similar to those of present-day late-type spirals, and our analysis suggests possibly little net loss of angular momentum of the baryonic matter upon collapse from the parent dark matter halo. These disks appear to be turbulent, gas-rich, and likely unstable to global star formation and fragmentation. The star-forming clumps could later sink towards the gravitational center by dynamical friction to form a central bulge, providing a mechanism whereby some of these young disks may ultimately become early-type galaxies.

SINS publications:

- Förster Schreiber, N.M., et al. 2006, ApJ, 645, 1062
- Genzel, R., et al. 2006, Nature, 442, 786
- Bouché, N., et al. 2007, ApJ, submitted
- Nesvadba, N., et al. 2006, ApJ, 650, 661
- Nesvadba, N., et al. 2006, ApJ, 650, 693
- Nesvadba, N., et al. 2007, ApJ, in press (astro-ph/0611769)
- Tecza, M., et al. 2004, ApJ, 605, L109

N.M. Förster Schreiber, R. Genzel, M. Lehnert, N. Bouché, and the SINS team

First comparison of the kinematic properties of high redshift galaxies and a universal star formation relation

We compare the dynamical and star formation properties of different galaxy samples. The sample is made of rest-frame UV-, optically selected galaxies and submm galaxies. The results provide insights into their nature and evolution: UV- and optically selected galaxies are dynamically similar and follow the same size-velocity relation as local disk galaxies. In contrast, bright submm galaxies are more compact and have higher matter densities. The three samples lie on the same relationship between star formation rate and gas density, evidence for a universal Schmidt-Kennicutt law out to redshift ~ 2.

The first kinematic comparison of different z~2 galaxy samples is obtained from 29 rest-frame UV- and optically bright star-forming galaxies at z ~ 1.5–3.5 from our SINS survey (Forster Schreiber et al. 2006) combined with a sample of submillimeter-selected galaxies (SMGs) at z ~ 2–3 surveyed in CO line emission with the IRAM Plateau de Bure interferometer. Figure 1(left) shows that the z ~ 2 rest-frame UV-/optically bright galaxies are dynamically similar, and therefore probably drawn from the same halo population. Figure 1(right) shows that these galaxies follow a similar circular velocity-size relationship as present-day late-type disk galaxies (Courteau 1997; grey crosses). Figure 1 also shows that bright SMGs span a comparable range in dynamical mass but are very distinct in that they appear more compact and have higher matter densities in addition to being an order of magnitude more luminous. This suggests different evolutionary scenarios: dissipative major mergers may have dominated for SMGs and resulted in early spheroids. Rest-frame UV-/optically bright galaxies may in part have evolved in a less violent fashion involving successive minor mergers or rapid dissipative collapse from the halo, leading to the formation of early disks. These may subsequently also evolve into spheroids.

Figure 2 shows that the star formation rate of the high redshift samples follow a universal "Schmidt-Kennicutt" relation together with the local star-forming galaxies (grey crosses). This relationship implies that the star formation rates scale as the gas density to a power of ~1.7 or equivalently, that the global star formation efficiency increases by about a factor of 4 between the modern Milky Way and powerful low- and high-redshift star-forming galaxies.

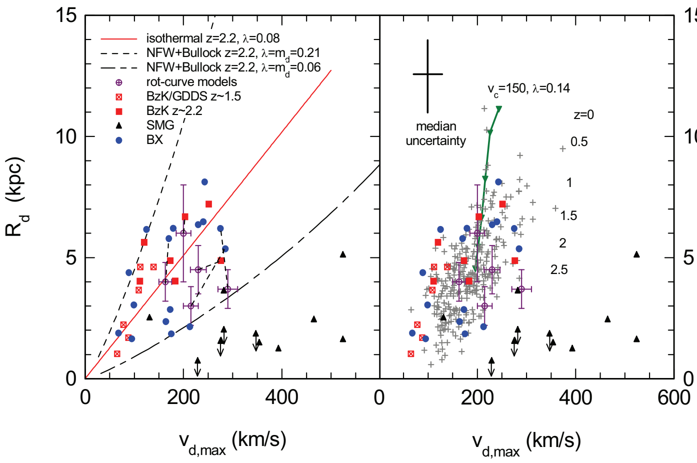

Figure 1: Size-velocity properties of different high-z galaxies and local samples.

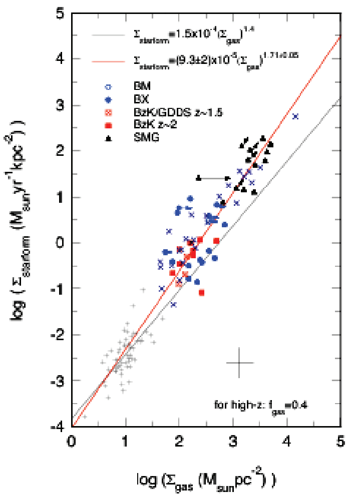

Figure 2: Star formation density vs. gas density

References:
•Forster Schreiber et al. 2006, ApJ, 645, 1062
•Courteau S. 1997, AJ, 114, 2402

N. Bouché, R. Davies, F. Eisenhauer, N.M. Förster Schreiber, R. Genzel, L. Tacconi

Intracluster Stars in Nearby Galaxy Clusters

Galaxy clusters are now known to contain a diffuse population of intracluster stars. The kinematics of these stars is a sensitive probe of galaxy evolution in clusters. We have embarked on measuring the velocities of intracluster planetary nebulae (ICPNe) in nearby galaxy clusters, using Multi-Slit Imaging Spectroscopy (MSIS). Here we report on the velocity distribution in a field in the Coma cluster core at 100 Mpc distance. Combined with galaxy redshift and X-ray data these data suggest that the cluster is currently in the midst of a subcluster merger, where the two subcluster cores around the supergiant galaxies NGC 4874 and NGC 4889 are presently beyond their first and second close passage, during which the elongated distribution of diffuse light has been created.

MSIS combines a mask of parallel slits (Fig.1) with a narrow-band filter, here centered about the redshifted [OIII]5007Å line. Spectra (Fig. 2) are taken for all ICPNe that happen to lie behind the slits. The velocity distribution of 37 ICPNe from three stepped masks in the field (Fig. 3) has a main peak 700 km/s different from the nearby cD galaxy NGC 4874, but coincident with the redshift of the other cD galaxy, NGC 4889. These ICPNe are therefore not bound to NGC 4874, and were probably dissolved from the halo of NGC 4889 during the first pericentre passage of the two galaxies on an orbit like that in Fig. 4.

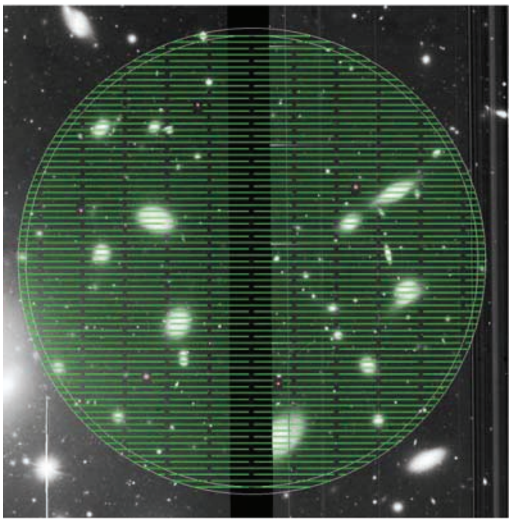

Fig. 1: Multi-slit mask superposed on the Coma cluster core field observed with FOCAS@Subaru. The slits cover ~12% of the field area.

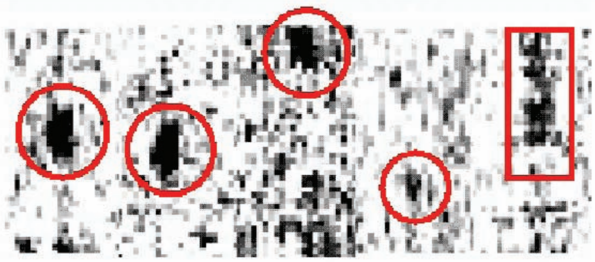

Fig. 2: 2D emission spectra of 4 ICPN and a possible Ly α background galaxy. Line fluxes are (3-17)×10^{-19} ergs $s^{-1}cm^{-2}$.

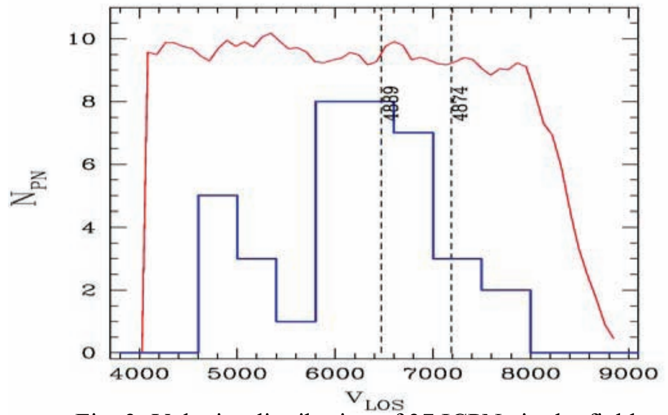

Fig. 3: Velocity distribution of 37 ICPNe in the field.

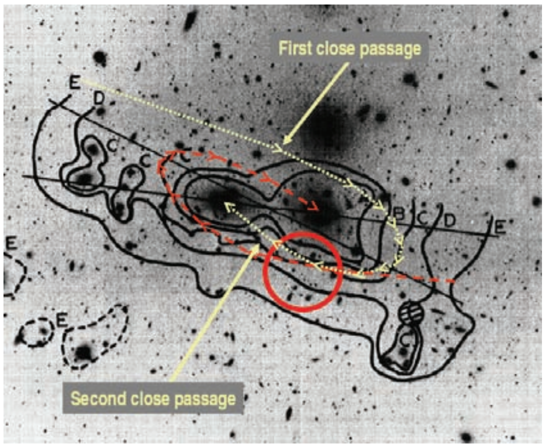

Fig. 4: The observed field (red) superposed on the contours of ICL from Thuan & Kormendy (1977). The inferred orbits of the two cD galaxies are sketched.

References:
Arnaboldi et al., 2007, PASJ, in press
Gerhard et al., 2005, ApJL, 621, L93
Gerhard et al., 2007, A&A, in press
Thuan & Kormendy, 1977, PASP, 89, 466

Ortwin Gerhard, Giulia Ventimiglia, Magda Arnaboldi

The evolution of the EDISCS Fundamental Plane

The EDISCS project is an ESO Large Program to study 20 clusters of galaxies with redshifts 0.4<z<0.9 (White et al. 2005). The clusters are optically selected and therefore span a large range in mass, with velocity dispersions typical of groups to up to 1000 km/s. The large set of high quality spectra, HST photometry and high-resolution FORS imaging allows to determine the Fundamental Plane (FP) parameters (effective radii and surface brightness, central velocity dispersion) of hundreds of early-type galaxies to follow their evolution as a function of redshift AND environment. In particular, for the first time one sees that the zero-point evolution of the FP follows passive evolution independently of cluster velocity dispersion.

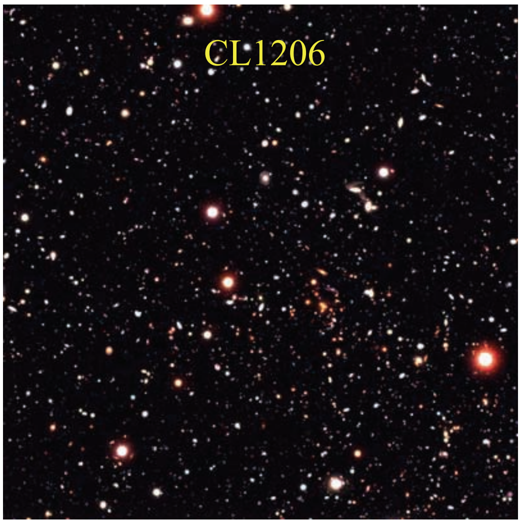

What governs the evolution of galaxies in clusters, is it *Nature* (the formation process) or rather *Nurture* (the environment)? The EDISCS project found that the fraction of star forming galaxies depends both on the cluster σ and Its redshift (Poggianti et al. 2006). Moreover, the color-magnitude relation in high-redshift clusters is depopulated at lower magnitudes (De Lucia et al. 2004, 2007). This points to the existence of two mechanisms of formation of passive, red galaxies in clusters: *primordial* massive Ellipticals (Es) and *quenched Spirals* (possibly today's S0s). The study of the evolution of the FP helps further to constrain the epoch of formation of these galaxies.

The FP of the cluster CL1206 at z~0.8

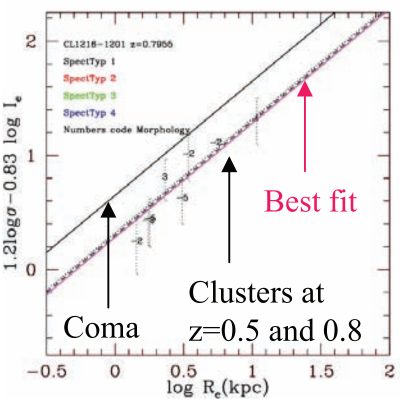

Past studies of the FP of Es in *massive* clusters up to z~1.2 find *passive evolution* of the M/L ratios implied by the zero-point of the plane with high formation redshifts z~2.

The M/L variations as a function of redshift

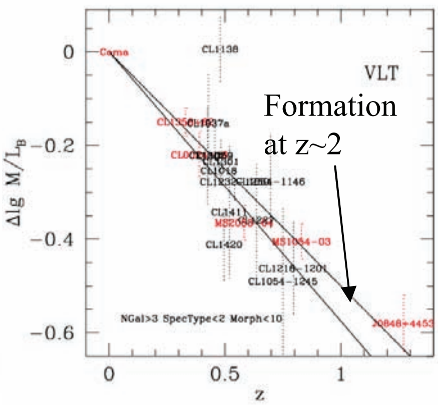

We confirm these finding for the whole range of cluster σ spanned by the EDISCS sample (black labels, red labels from the literature).

The residual variations of M/L as a function of the cluster velocity dispersion

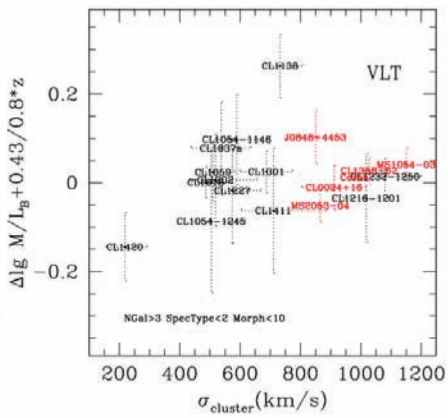

Moreover, no correlation of the residuals is found with cluster σ. Finally, indication for rotation of the FP of z>6 galaxies points to *downsizing,* with small Es forming *after* big ones.

References:
•De Lucia et al. 2004, ApJL, 610, L77
•De Lucia et al. 2007, MNRAS, 374, 809
•Poggianti et al., 2006, ApJ, 642, 188
•White et al. 2005, A&A, 444, 365

R.P. Saglia and the EDISCS collaboration

Stripped Galaxy Halos in Clusters

We assume scaling laws between the truncation radius s and velocity dispersion σ of agalaxy halo and use **strong galaxy-galaxy** lensing to measure the sizes of cluster galaxy dark matter haloes in the rich cluster Abell 1689. The method relies on the parametric strong lensing model presented in Halkola et al.(2006). The strong constraints imposed by the 107 multiple images allow us to measure the ensemble properties for central cluster members. We find that the haloes of the cluster galaxies are strongly truncated when compared to field galaxies.

Introduction: One expects that tidal truncation shrinks the sizes of galaxy haloes in dense clusters compared to galaxies with the same optical properties in the field. Halo sizes are hard to measure using stars and satellites as tracers of their potential. The weak lensing technique, however, has been successfully used in the past to measure galaxy halo sizes in the field and in clusters. We for the first time measure galaxy halos in the strong regime.

Method: We use the multiple lensed images of background galaxies in the field of the galaxy cluster A1689 to measure the sizes of the DM haloes of galaxies in this cluster. The positions of multiple images are sensitive to the total mass in the cluster center and to the small scale perturbations induced by the dark matter associated with galaxies. In fact, one can not obtain satisfying lensing models at all, if dark matter associated with galaxies is not taken into account.

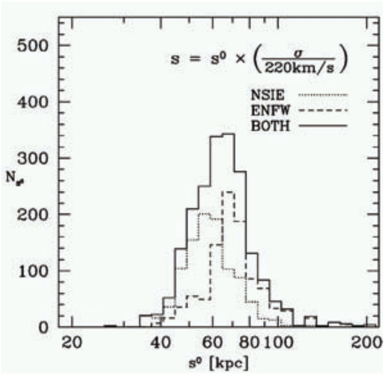

Fig.1: We use Monte-Carlo simulations to analyze the truncation of galaxy haloes. The velocity dispersions of galaxies in the simulated clusters are compatible with the measured ones within the estimated errors of the Fundamental Plane. For the smooth DM profile of the cluster we have used two descriptions, non-singular isothermal ellipsoids (NSIE, dotted line) and elliptical Navarro, Frenk and White profiles (ENFW, dashed line). When the data from the two profiles are combined, we obtain the solid line. S_0 and its error are derived from the distribution of the best fits s0 for all the simulated clusters shown in this figure. The s0 are strongly confined between 40 and 100 kpc. Both, smaller and larger haloes are excluded.

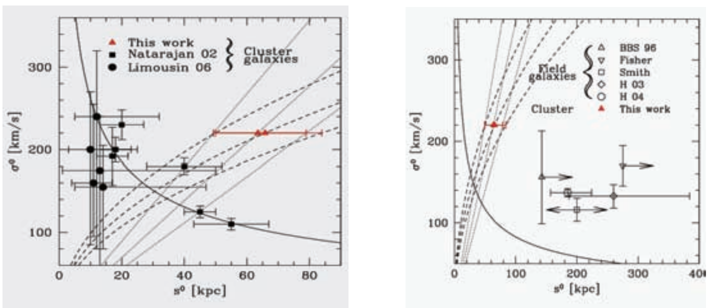

Fig 2, left: A comparison of our results with 3 other studies of galaxy halo truncation in clusters. The dotted lines show the scaling of the best fit values and errors for alpha=1, the dashed lines for alpha=2 where alpha is the power in the scaling law $s \propto \sigma^{\alpha}$ The solid curve shows $s-\sigma$ pairs for a galaxy halo with $5x10^{11}$ solar masses.
right: Measurements for truncations radii of field galaxies (curves are the same as on left panel). Our results are in fair agreement with previous work in clusters, using weak lensing (Natarajan et al. 1998, 2002, Limousin et al. 2007). These weak lensing meaurements, however seem to find a stronger truncation then we.

Results: For scaling laws expected in dense cluster environments (tidal truncation, Merrit 1983) we obtain $s = 64 \mp 15 kpc \bullet (\sigma/220 km/s)$,
For scaling laws as found for field galaxies (constant M/L) we find $s = 66 \mp 18 kpc \bullet (\sigma/220 km/s)^2$
If galaxies had the same size in the clusters
as in the field, we would have expected (see Hoekstra et al) $s \approx (700 \mp 100) kpc \bullet (\sigma/220 km/s)^2$

References: Halkola et al. 2006 & 2007
Bender et al. 1994, Tyson et al. 1984, Brainerd et al. 1996, dell'Antonio & Tyson 1996, Hudson et al. 1998, Fischer et al. 2000, Smith et al. 2001, Wilson et al. 2001, McKay et al. 2001, Hoekstra et al. 2003 & 2004

Aleksi Halkola, Stella Seitz & Maurilio Pannella

A representative galaxy cluster survey

We present preliminary results from the combination of data from 56 galaxy clusters observed as part of two XMM Large Programmes. Both samples were defined in X-ray luminosity alone, and are uniquely representative and complementary.

Observations of the galaxy cluster population offer the potential to deliver cosmological contraints rivalling those from other methods such as supernovae or weak shear. To achieve the required precision, however, we need (i) a better understanding of how observed cluster properties relate to the mass, which is the fundamental link between theory and observation, and (ii) a better understanding of the structural, scaling and statistical properties of the cluster population. The complementary *local* ($z < 0.2$; Boehringer et al, 2007) and *distant* ($0.4 < z < 0.6$; Arnaud et al, 2007) XMM Large Programmes, selected by X-ray luminosity alone, offer an opportunity for the in-depth study of a small sample of clusters with the same selection criteria as would be available from a much larger X-ray survey.

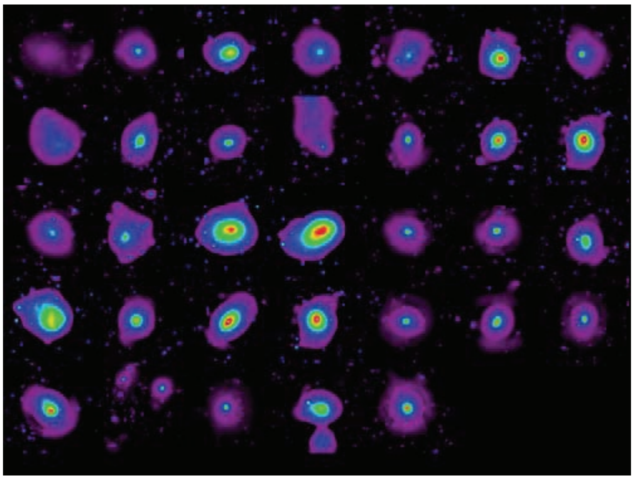

Nearby LP, 33 clusters, z<0.2, arranged by L_X. Note the large variety of morphologies present in the sample.

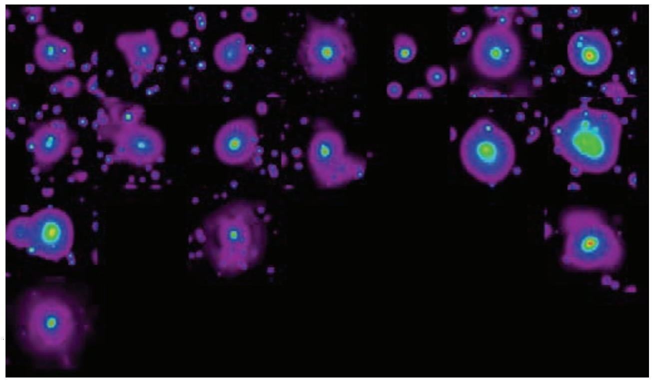

Distant LP, 23 clusters, 0.4<z<0.6, arranged by L_X (not all objects have yet been observed). The distant clusters are less luminous and have more disturbed morphologies.

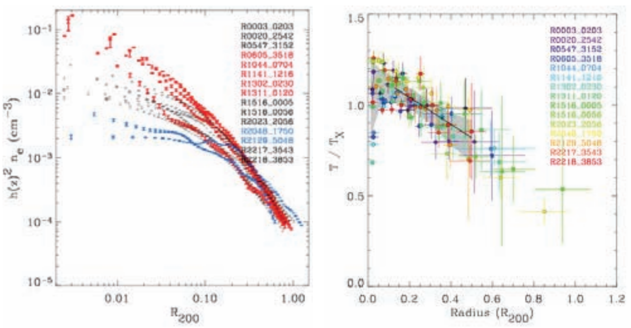

Scaled density (left) and temperature (right) profiles for 15 of the local sample. Despite the morphological variety, angle-averaged properties show impressive similarity.

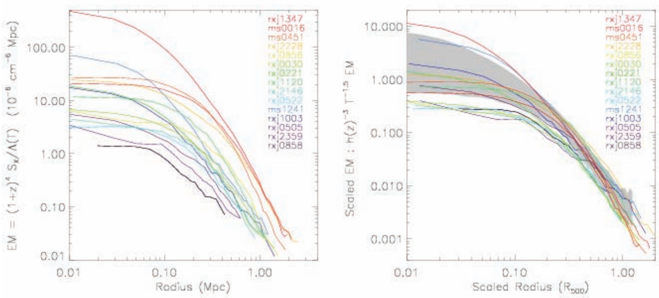

Line of sight emission measure profiles for 15 distant LP data sets. The right panel shows the corresponding scaled EM profiles, using standard scaling with z. The grey region corresponds to the spread defined by the local sample.

Deeper investigation of both samples is on-going. Scaling relations are of particular interest (e.g., L_X-T, M-T, L_X-M) as these will be useful for the large statistical samples available from eROSITA.

References:
• Böhringer, H., Schuecker, P., Pratt, G.W., et al., 2007, A&A, in press
• Arnaud, M., Pointecouteau, E., Pratt, G.W., et al., 2007, in prep.

G.W. Pratt, J.H. Croston, H. Böhringer, M. Arnaud et al.

The XMM-Newton Distant Cluster Project

The XMM-Newton Distant Cluster Project (XDCP) is a serendipitous survey for X-ray luminous clusters of galaxies at redshifts beyond 1. We have analyzed more than 500 archival XMM fields and identified some 250 high-redshift cluster candidates. The survey is about 20 times as wide as the COSMOS survey and has an average depth which is in between the COSMOS and the eROSITA Deep surveys, thus allowing the detection of very rare objects out to the highest redshifts. The final sample is expected to contain about 40 z>1 clusters and will serve as an important tool to characterize distant galaxy clusters and establish their use as cosmological probes for upcoming major cluster surveys.
First spectroscopic redshift confirmations between 0.95<z<1.45 have demonstrated that our selection and follow-up strategy is very efficient. The ongoing follow-up imaging program of the full survey is 50% completed, and further spectroscopy for more than a dozen z>1 cluster candidates is scheduled at different 8m-class telescopes. We are currently compiling a first study sample of 15-20 photometrically confirmed z>1 clusters to address a number of urgent questions of cluster and galaxy evolution scenarios at unprecedented cluster redshifts.

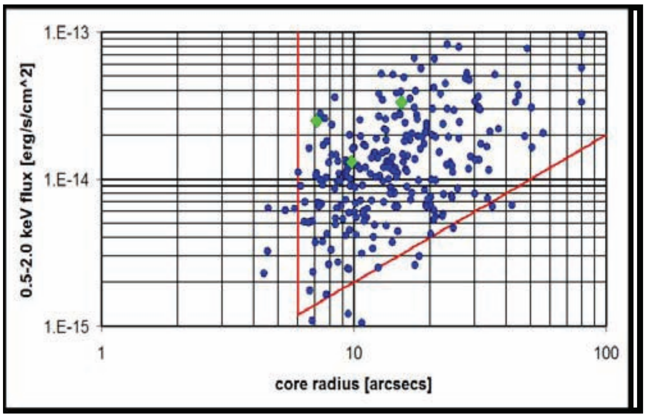

Fig. 1 top: Flux vs. estimated core radius diagram for the 250 X-ray selected distant cluster candidates (blue circles). The red lines indicate the basic accessible parameter range for extended source detection, bounded by the XMM resolution limit (vertical) and the background limit (diagonal). The green diamonds represent the most prominent confirmed distant clusters to date at z=1.39, 1.45, 1.24 (left to right).

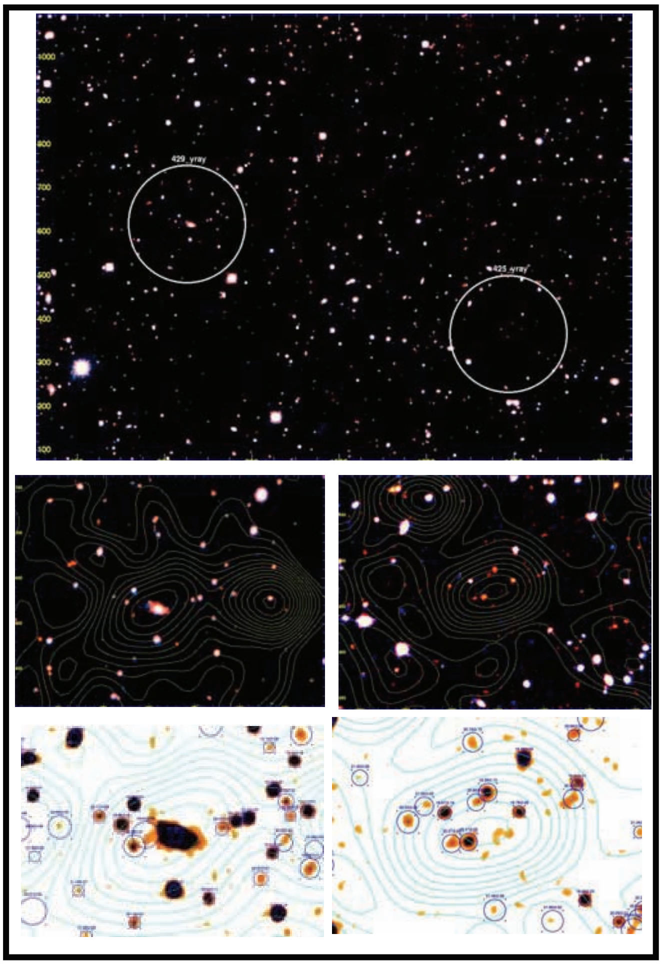

Fig. 2 right: Recent NIR follow-up imaging results of two distant cluster candidates using a newly established z-H color-search method. From top to bottom: (i) 8x8 arcmin z+H image, (ii) 2x2 arcmin zoom on the candidates with X-ray contours, and (iii) smoothed core region (1x1 arcmin) with indicated H (Vega) magnitudes. The candidate on the left has an estimated redshift of z~1, the one on the right is consistent with z≥1.5.

References:
• Böhringer et al., ESO Messenger, 2005, 120, 33
• Mullis et al., 2005, ApJL, 623, L85
• Rosati et al., 2004, AJ, 127, 230
• Stanford et al., 2006, ApJL, L13

R. Fassbender, H.Böhringer, J. Santos, et al.

Galaxy clustering, dark matter and dark energy

The large scale distribution of matter in the universe comprises a wealth of information about cosmological parameter, most important of which are the matter and energy content of the universe. The two-point correlation function is a very good means to measure not only these, but also study the evolution of galaxies. We have used COMBO-17 data (Wolf et al. 2004) to estimate the value of σ_8 and the effective mass of the dark matter haloes different types of galaxies live in, and complementary we investigated the dependence of the colour-dependent luminosity function (LF) on the local density contrast. We will use Pan-STARRS and KIDS data to infer the equation of state parameter *w* using the *acoustic peak* in the correlation function.

COMBO-17: Three (disjoined) fields measuring 30'x31' each, were observed in 17 filters, which allows for reliable classification and redshift determination ($\sigma_z/(1+z) \sim 0.015$) for 15307 galaxies with $z<1$, $R<23.65$, and m_B-5log h<-18. Following Bell et al. 2004 we can split the sample in red and blue galaxies and investigate their correlation function, or, complementary, their local overdensities.

The projected correlation function and the Halo Occupation Distribution (HOD) at <z>=0.6

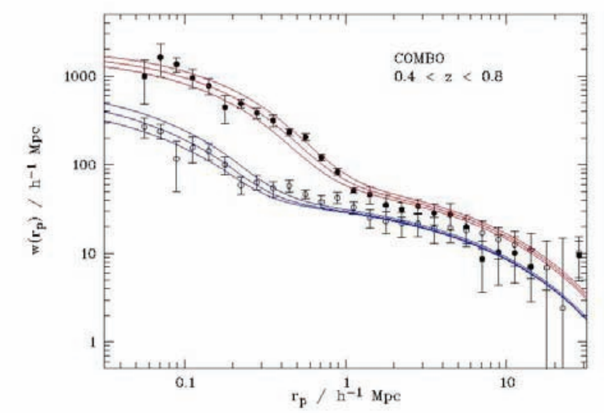

The correlation function (shown here for red sequence and blue cloud galaxies in COMBO-17) can be calculated analytically – input is the dark matter clustering, the mass function of the DM haloes, the conditional LF and a prescription of how the galaxies populate the haloes – the simplest HOD: $N \sim M^{\alpha}$ From a fit to the data we find $\alpha \sim 0.5$ for red and $\alpha \sim 0.2$ for blue galaxies $M_{eff} = 10^{13.2} h^{-1} M_o$ (red) and $M_{eff} = 10^{12.5} h^{-1} M_o$ (blue) $\sigma_8 = 1.02$ (consistent with linear theory)

The dependence of the colour-dependent Luminosity function on environment

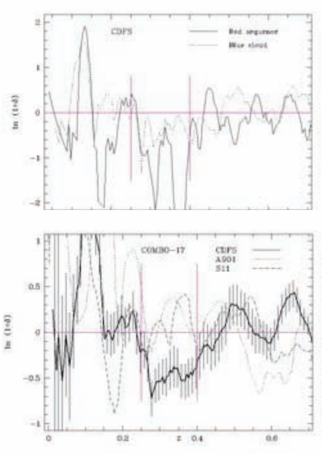

In the Chandra Deep Field South (CDFS) there is a region ($0.25<z<0.4$), where the field is underdense compared to the other two. When we calculate the overdensities ($\delta=\rho/\rho_0-1$) again for red and blue galaxies, we see that the 'hole' is deeper for the red ones. We calculate the LF in this redshift range, split into fields and colours, and find that the deficit there is mainly due to a lack of faint red galaxies.

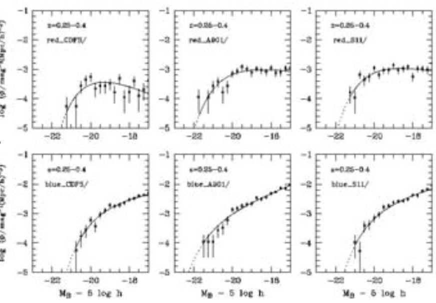

FUTURE:

Pan-STARRS: The PS1 telescope will observe the entire sky visible from Hawaii in five bands over 3.5 years, yielding redshifts for many millions of galaxies up to z=1.2.The unprecedented number and area will allow for a measurement of the imprint of the **baryonic acoustic oscillations** in the large-scale distribution of the galaxies , which can be used as a standard ruler to measure the equation of state parameter *w* of the **dark energy** to a precision of 5%.

References:
•Wolf, C. et al. 2004, A&A 421, 913
•Bell, E. et al. 2004, ApJ 608, 752

S. Phleps, J.A. Peacock, C. Wolf, K. Meisenheimer, E. van Kampen

Galaxy Cluster Structure and Cosmology

Galaxy clusters are one of the most important cosmological probes for testing cosmological models and astrophysical laboratories to trace cosmic evolution. Past surveys lead to robust estimates of Ω_m. Furture surveys in search of Dark Energy (DE) properties require a much deeper understanding of cluster structure. Therefore we are conducting a set of systematic studies of cluster structure and scaling relations with representative X-ray and optical galaxy cluster samples with one of the main goals to understand the mass–observable relations, but also the statistics of cluster structure and evolution.

Our ROSAT based cluster samples at redshifts up to z < 0.15 lead to robust estimates of the matter density in the Universe, Ω_m (Fig. 1), providing important complementary information to other crucial tests, even with a worst assumption cluster mass calibration of less than 30% accuracy. Future studies to constrain the nature of DE require accuracies of a few percent.

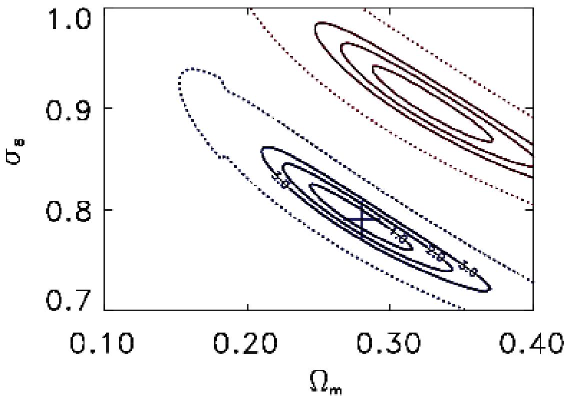

Fig. 1: Cosmological model constraints from the REFLEX Survey X-ray luminosity function (blue: 1,2,3 σ-contours) and result assuming 60% lower masses (red cont.) illustrating the robustness of the Ω_m result.

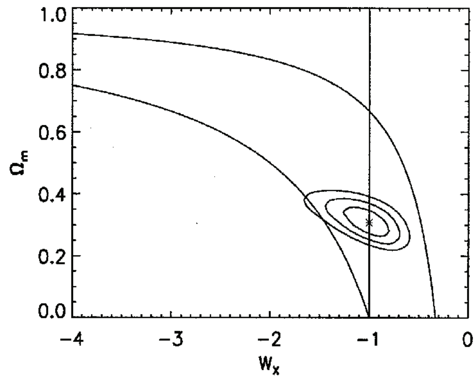

Fig. 2: Constraints for Ω_m and the equation of state parameter of DE, w, combing the REFLEX observations with results on distant supernovae – illustrating the power of combing complementary probes.

To improve our understanding of cluster properties we conduct several surveys of cluster samples in the optical, and X-rays and find for example a well defined correlation between cluster mass and total galaxy light (Fig. 3) and more self-similarity in the galaxy cluster temperature, pressure and entropy distribution in X-ray studies than implied by the X-ray images (Fig. 4), and we compare to simulations (see also posters by G. Prat and Y.-Y. Zhang).

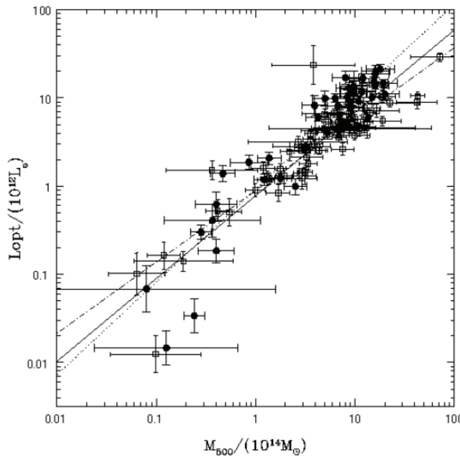

Fig. 3: Correlation of the total optical galaxy light and cluster mass determined for ROSAT detected clusters with SDSS photometric and spectroscipc data.

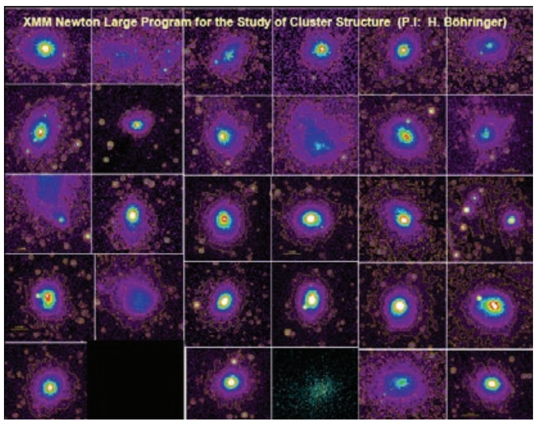

Fig. 4: Gallery of 0.5 – 2 keV images of the galaxy clusters of the XMM Large Program for the systematic study cluster structure for a representative sample of cluster systems with X-ray temperatures from 2 – 12 keV.

H. Böhringer, G. Pratt, P. Popesso, A. Finoguenov, Y. Zhang, R. Fassbender, et al.

Probing non-Gaussianity in the WMAP data

Weighted scaling indices of the co-added foreground-cleaned three-year Wilkinson Microwave Anisotropy Probe (WMAP) data are calculated. The results are compared with 1000 Monte Carlo simulations based on Gaussian fluctuations with a best fit ΛCDM power spectrum and WMAP-like beam and noise properties. Statistical quantities based on the scaling indices are determined. We find for most of the test statistics significant deviations from the Gaussian hypothesis. Thus, our results provide further evidence for both the presence of non-Gaussianities and asymmetries in the WMAP three-year data. More detailed band-and year-wise analyses are needed to elucidate the origin of the detected anomalies.

The Gaussianity of the primordial density fluctuations and statistical isotropy are among the fundamental pillars of the ΛCDM concordance cosmological model, which relies on a minimal inflationary scenario. On the other hand, many alternative scenarios have been studied, which give rise to non-Gaussianity, e.g. non-standard inflation or topological defects models. Gaussianity is tested by measuring suitable statistics of the temperature fluctuations of the CMB and comparing the results with theoretical predictions in terms of significances S or confidence levels (CL). As a novel test statistic we estimate the local scaling properties of the co-added foreground cleaned three-year WMAP data using weighted scaling indices α. We adapted and applied the scaling index method (SIM) - for the first time - to the case of spherical symmetric spatial data as they are typical in full sky CMB observations. For this, we represent the map of temperature fluctuations as a three-dimensional point distribution, where the three coordinates are given by the two angle variables of the pixels on the sphere and radial variations, to which the temperature fluctuations are transformed.

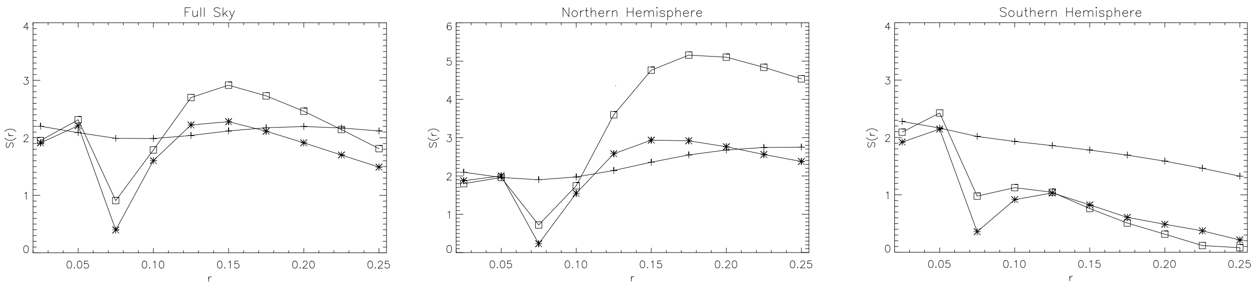

Fig. 1: Significances of the (combined) moments of the α-distribution of the WMAP three year data as a function of the scaling range r. + denotes the mean, ? the standard deviation and □ a χ^2 combination of the mean and standard deviation. While the southern hemisphere is quite consistent with Gaussianity, we find highly significant signatures of non-Gaussianity ($S > 5\sigma$, CL > 99.9 %) in the northern hemisphere at larger scales.

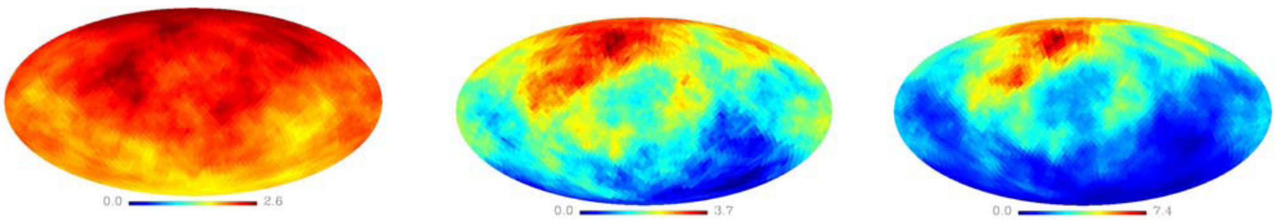

Fig. 2: Significances of the rotated upper hemisphere for the SIM based statistics for one scaling range r. From left to right: mean, standard deviation and χ^2-combination of mean and standard deviation. For the rotated hemispheres the significance rises up to $S = 7.4\sigma$. The asymmetries also become obvious.

References:
• C. Raeth, P. Schuecker, A. J. Banday, MNRAS, submitted, (astro-ph/0702163)

Christoph Räth, Peter Schuecker and Anthony Banday

Swift-BAT measurements of the Cosmic X-ray background and Earth atmosphere spectra

We use Earth occultation data at different magnetic latitudes to independently derive with *Swift*/BAT the spectra of the Cosmic X-ray background (CXB) and Earth albedo emission. We develop an Earth emission model based on COMPTEL and EGRET observations of the Earth albedo which allows us to disentangle the two components without prior knowledge of their spectral shapes. We find that the BAT CXB spectrum is in good agreement with the HEAO-1 measurement. The BAT albedo spectrum is the most accurate measurement of the Earth emission in hard X-rays.

***Understanding the BAT background*:** The BAT background is highly complex and structured; it exhibits variability depending on both orbital position and pointing direction. In order to discriminate the various background components, we correlated the BAT array rate with several orbital parameters. The plots below show: the sharp increase in rate due to SAA passages (left panel) and correlation of rate with cut-off rigidity.

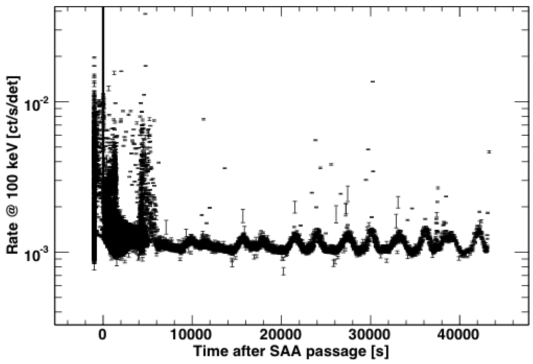

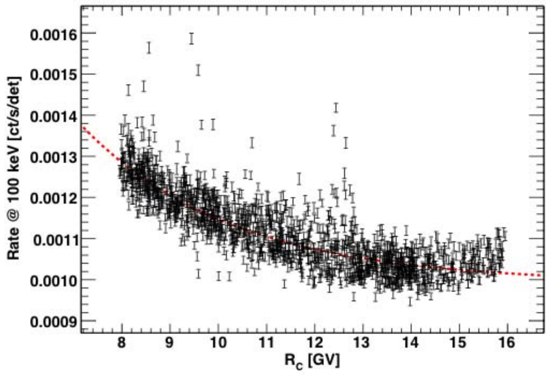

***The Earth model*:** The Earth atmosphere is a powerful source of X- and gamma-rays due to cosmic ray (CR) bombardment of its atmosphere. Analyses of the Earth albedo in gamma-rays (Schönfelder et al. 1977 and Petry et al. 2005) show that a large fraction of the emission comes from the limb. The albedo emission is also expected to correlate with rigidity like the parent CR flux does. All these effects are noticeable in BAT and are used to characterize the Earth model. In three occasions, the Earth drifted in the BAT field of view modulating the CXB signal. The rate modulation, produced by the occultation, could be used to derive the CXB and Earth albedo spectra at the same time. The two graphs below summarize our results. The BAT CXB spectrum is in good agreement with all previous CXB measurement. The goodness of the analysis is confirmed by the Earth albedo spectrum (left panel). The BAT albedo spectrum declines above 40 keV as a power-law with photon index of 1.7 and not 1.4 as commonly believed.

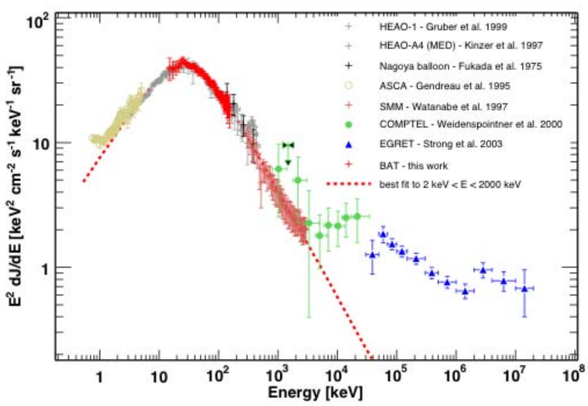

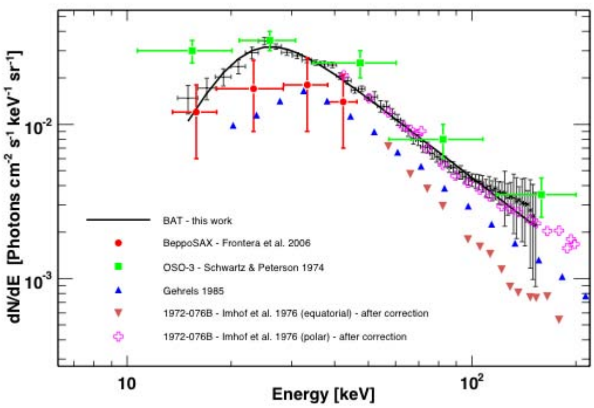

M. Ajello, D. R. Willis, J. Greiner, G. Kanbach, R. Diehl, A. W. Strong

USM: Computational Astrophysics Group

Our group specializes in numerical simulations of various astrophysical problems on all scales. In the context of galaxy formation we study the growth of individual galaxies from cosmological initial conditions. We follow the evolution of interacting galaxy clusters in order to probe Cold Dark Matter theory. Simulations of galaxy interactions are performed to probe the importance of merger events. Another hot topic is the dynamical formation of molecular clouds from turbulent colliding flows. Radiation-induced star formation is an important aspect of stellar feedback. Simulations of evolving protoplanetary disks help to build a consistent theory of low-mass star formation. On the small-scale end planet formation and dust-gas interactions are investigated.

Galaxy Formation

[10^{27} - 10^{24} m]

Evolution of the stellar component of a galaxy simulated from cosmological initial conditions, shown at z=4,1&0

Galaxy Clusters

[10^{24} - 10^{23} m]

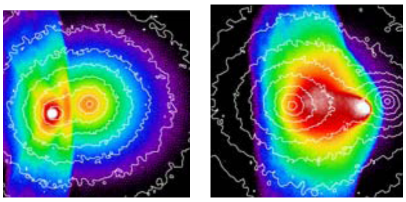

The Bullet Cluster is formed during cluster collision. Images represent X-Ray surface brightness maps (Chandra) overlayed with isodensity contours.

Galaxy Interactions

[10^{23} - 10^{19} m]

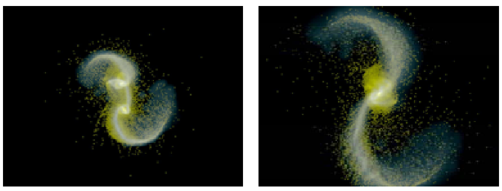

Merger simulations are performed in order to study the properties of the remnant galaxy in relation to their progenitors.

Molecular Cloud Formation

[10^{18} - 10^{15} m]

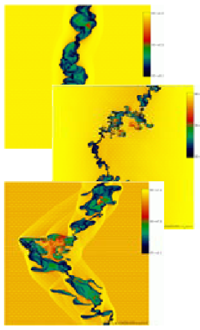

Observations show that molecular clouds are highly filamentary and turbulent. Is it possible to reproduce their structure in colliding interstellar gas flows?

Radiation-Induced Star Formation

[10^{16} - 10^{9} m]

Our group investigates the effect of ionizing radiation of massive OB-stars on the ambient interstellar medium. In particular we examine whether the UV-radiation can lead to pillar-like structures, as observed e.g. in Orion.

Formation of Protoplanetary Disks

[10^{16} - 10^{9} m]

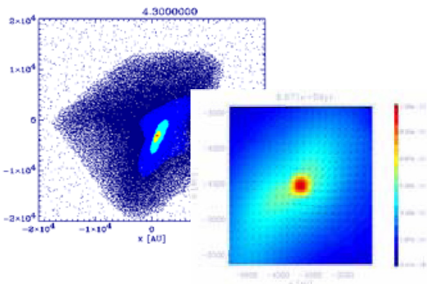

Formation of a protostellar disk from the collapse of an intitially turbulent Bonnor-Ebert sphere.

Planet Formation

[10^{-13} - 10^{6} m]

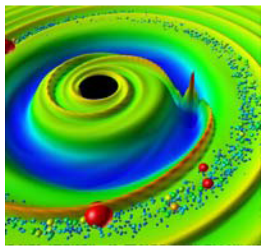

Rocks orbiting in a narrow ring within a protoplanetary disk, and gas density in the disk midplane. A Jupiter mass planet has assembled at the density peak inside the gap.

A.Burkert - VISIT: http:://www.usm.uni-muenchen.de/CAST/

SINS: Far-away galaxy under the microscope

The SINS survey, a large program of near-infrared imaging spectroscopy with SINFONI at ESO's Very Large Telescope, is providing new and unique constraints on the formation and early evolution of luminous high redshift galaxies. One of the most exciting results is the discovery of large massive rotating disk galaxies at redshifts $z \sim 2$, which must have formed on rapid timescales. Adaptive optics-assisted SINFONI observations provided an exceptionally detailed view into one such system, on scales as small as ~ 1 kpc.

The most spectacular data set obtained so far as part of our SINS survey is that of the massive star-forming galaxy BzK-15504 at redshift $z = 2.38$, when the Universe was 20% of its current age. The lucky proximity of a suitable star near the source enabled us to carry out adaptive optics-assisted SINFONI observations of the Hα recombination line emission. This resulted in an angular resolution of 0.15 arcsecond, or a mere 1.2 kpc at the distance of the galaxy, giving the most detailed view to date of the ionized gas morphology and kinematics for a $z \sim 2$ galaxy.

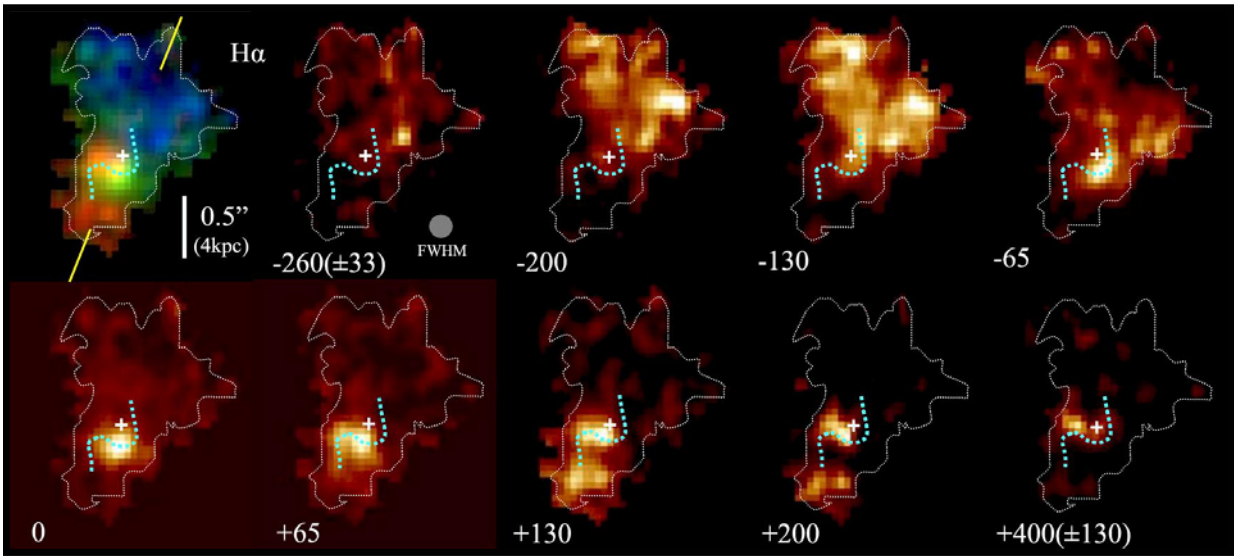

The figure shows, in the top left panel, the integrated Hα line emission of BzK-15504 colour-coded to indicate blue- to redshifted emission relative to the systemic velocity. The other panels show the Hα emission for different velocity intervals (the central velocity in km s^{-1} is labeled). These images reveal a large galaxy ≈16 kpc in diameter, and several very luminous complexes tracing sites of active star formation. The gas kinematics indicate that the system is rotating, with a maximum speed of 230 km s^{-1} implying a dynamical mass of 1.1×10^{11} $M_{\odot}$. The high surface density of gas (~ 350 $M_{\odot}pc^{-2}$), the high rate of star formation (~ 150 $M_{\odot}yr^{-1}$), and the moderately young stellar ages (~ 500 Myr) suggest rapid assembly, fragmentation, and conversion to stars of an initially very gas-rich protodisk, on a timescale of a few hundred Myr only. This massive rotating early disk further appears to be channelling gas towards a growing central stellar bulge hosting an accreting massive black hole. There are no obvious signs for a major merger, a surprising finding given the high star formation rate and rapid mass assembly. This may suggest that BzK-15504 assembled its mass via smoother gas infall from the halo or through a rapid series of minor mergers. These results confirm our findings for several other z~2 star-forming galaxies observed as part of SINS but at lower resolution. Most importantly, they provide key insights and quantitative constraints in exquisite detail into the star formation properties and the physical processes involved in galaxy formation and evolution.

References:

• Genzel, R., et al. 2006, Nature, 442, 786

R. Genzel, L. Tacconi, N.M. Förster Schreiber, F. Eisenhauer, N. Bouché, M. Lehnert

Red disc-like galaxies at intermediate/high z

Bulge-less, disc galaxies can exhibit red near-infrared (IR) colours (observed frame) like J-K>2.3. Not all of them are at redshifts z>2 as expected. Those at z~1 are likely neither old, passively evolving nor normal, dusty, star-forming discs, but either starbursts/ultra-luminous IR galaxies (ULIRGS) or the early, quiescent phases after the starburst/ULIRG activity ceased.

Disc-like galaxies with J-K>2.3 (Vega magnitude system) are expected to be either starbursts or passively evolving systems at z>2 (Franx et al. 2003), but also normal, dusty star-forming discs at z>1.4 (Pierini et al. 2005). Red discs do exist at z>2 (Labbe' et al. 2003; Stockton et al. 2004) but also down to z~0.6 (Conselice et al. 2006; Pierini et al. inpreparation), as shown in Fig. 1.

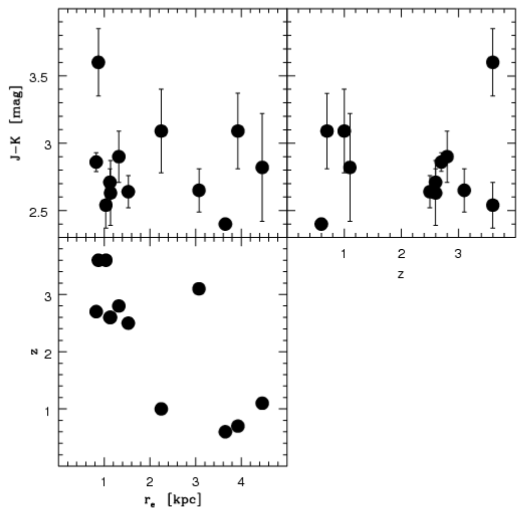

Figure 1: true red discs

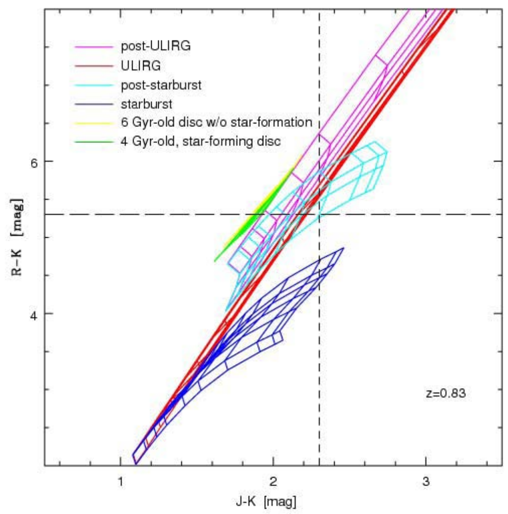

Figure 2: models

At these lower redshifts, red, bulge-less, disc galaxies are likely not forming stars as in normal, dusty spirals, if they do (cf. Pierini et al. 2005). Old, passively evolving stellar populations in a dust-free environment do not produce such red, near-IR colours either (cf. Pierini et al. 2004a). In Fig. 2, we demonstrate that this is also not the case for a disc at z~0.8 that is still dusty (as described in Pierini et al. 2004b) at a look-back time of 7 Gyr, i.e. 2 Gyr after its star-formation activity ceased. Conversely, a system where star-formation activity and dust attenuation behave as in starbursts or ULIRGS can exhibit such red, near-IR colours if it has been forming stars for >1 Gyr and/or is very dusty. Interestingly, this holds for the early, post-starburst/ULIRG phases, when the system does not form stars anymore but it is still very dusty up to 1 Gyr after its star-formation activity ended. These results, based on Monte Carlo calculations of radiative transfer and stellar population synthesis models, are discussed in Pierini et al. (in preparation).

References:
- Conselice, C.J., et al., 2006, astro-ph/0607242
- Franx, M., et al., 2003, ApJ, 587, L79
- Labbe', I., et al., 2003, ApJ, 591, L95
- Pierini, D., Maraston, C., Bender, R., Witt, A.N., 2004a, MNRAS, 347, 1
- Pierini, D., Gordon, K.D., Witt, A.N., Madsen, G.J., 2004b, ApJ, 617, 1022
- Pierini, D., Maraston, C., Gordon, K.D., Witt, A.N., 2005, MNRAS, 363, 131
- Stockton, A., Canalizo, G., Maihara, T., 2004, ApJ, 605, 37

D. Pierini, M. Pannella, M. Salvato, K.D. Gordon, C. Maraston, A.N. Witt

Bulges and Disks over the last 8 Giga years

We study the evolution of the stellar mass density for the separate families of bulge-dominated and disk-dominated galaxies over the redshift range 0.25 < z < 1.15. We find that the morphological mix evolves monotonically with time: the higher the redshift, the more disk systems dominate the total mass content. The contribution from early and late type galaxies to the mass budget at z ~ 1 is nearly equal.

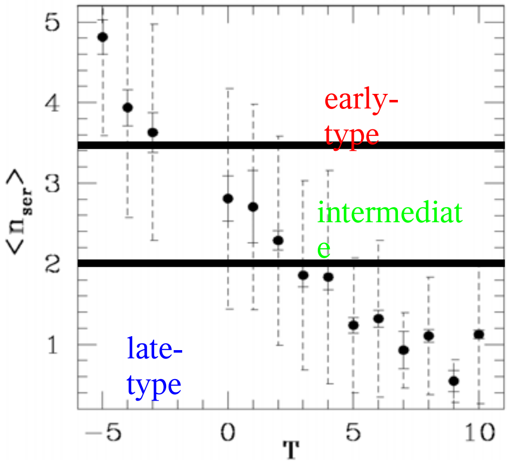

Making use of GIM2D and GALFIT, we fit PSF convolved Sersic profiles to the two-dimensional surface brightness of each object, in the i-band HST/ACS images. Visual morphology is also performed, according to the de Vaucouleurs classification scheme, and turns out to be well correlated with the automatic classification. We split our sample, according to the Sersic index, in early-type (n > 3.5, ~ T < -3), intermediate (2 < n < 3.5, ~ -3 < T < 2) and late-type (n < 2, ~ T > 2). Our broad morphological classification is not significantly affected by morphological k-correction out to z~1.15.

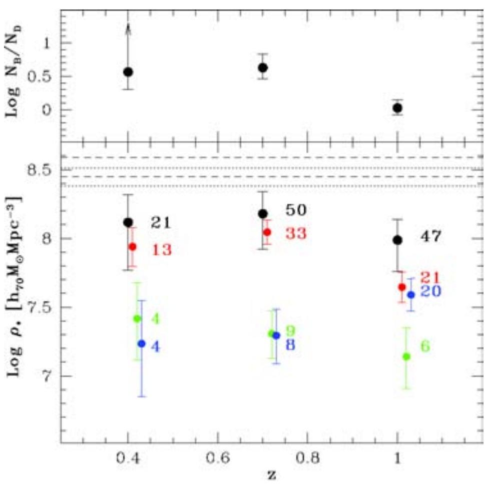

At z~1 massive objects (lower panel) host almost half of the stellar mass contained in similarly massive objects at z=0. The contribution to the total mass budget from early and late type galaxies is almost equal at z~1, but strongly evolves with redshift: **there is a mass pouring from disk systems to bulge-dominated objects.** The evolution (upper panel) of the ratio of bulges to disks number densities is shown. We find that this ratio significantly increases with time.

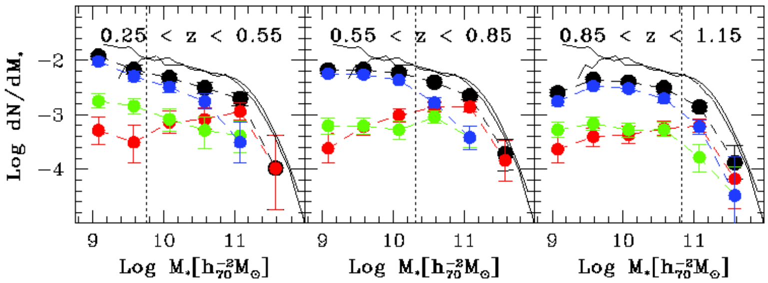

The mass function split by morphological types (early, intermediate and late) in three redshift bins. Black symbols show total values. The dotted line indicates the mass completeness limit in each redshift bin. Solid black lines show local mass function determinations. The relative contribution of disks to the high-mass end of the mass function increases with redshift. This suggests that: **1) the morphological mix at the high-mass end evolves with redshift; 2) the mass at which the disks become dominant over bulges increases with redshift.**

References:
- Bell et al. 2003, ApJS, 149, 289
- Brinchmann & Ellis 2000, ApJ, 536, L77
- Cole et al. 2001, MNRAS, 326, 255
- Drory et al. 2005, ApJ, 619, L131
- Pannella et al. 2006, ApJ, 639, L1
- Peng et al. 2002, AJ, 124, 266
- Simard et al. 1999, ApJ, 519, 563

M. Pannella, U. Hopp, R.P. Saglia, R. Bender, N. Drory, M. Salvato & A. Gabasch

Galaxy morphology and evolution from SWAN Adaptive Optics survey

In this poster we present the results from adaptive optics (AO) assisted imaging in the Ks band of an area of 19 arcmin^2 for SWAN (Survey of a Wide Area with NACO). We have derived high resolution near-IR morphology of ~500 galaxies up to Ks~23 in the first 25 SWAN fields around bright guide star. The extracted morphological properties and number counts of the galaxies are compared with the predictions of different galaxy formation and evolution models separately, for late-type and early-type galaxies for the first time in the near-IR.

AO systems allow ground based telescope to operate at the diffraction limit in the near-IR, making possible to obtain **high angular resolution** (~0.07"@VLT, *better than NICMOS on HST*) and low background per pixel. AO is therefore required to resolve from the ground high-z galaxies (effective radii = 0.1"÷0.3"). In addition, at these wavelengths we gain direct sensitivity to the galaxy stellar mass rather than to the ongoing/recent star formation, smaller K-correction effects, minor influence of dust extinction.

SWAN is a "discrete field" survey, as 42 field centered around bright AO guide stars were selected in different part of the sky. 25 of these were imaged with NACO@VLT, providing a total area of 19 arcmin^2, and obtaining on-axis Strehl ratio ~20%-45%.

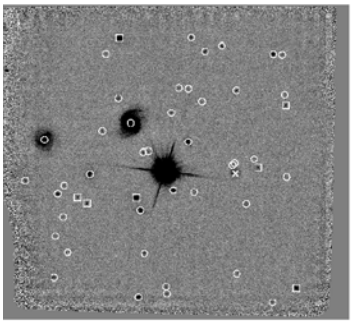

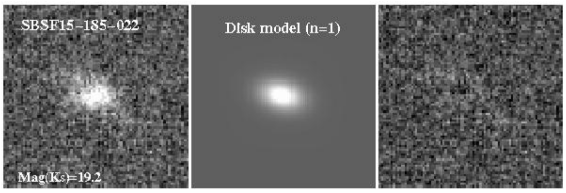

Original **Model** **Residuals**

Thanks to the unique resolution provided by AO, we have derived the **high resolution near-IR morphology** of ~500 galaxies up to Ks~23, carefully taking into account the survey selection effects and using an accurate treatment of the anisoplanatic AO Point Spread Function (Cresci et al. 2005).

We have compared the number counts (*lower*) and size distributions (*upper panel*) of the SWAN galaxies with the predictions of two different galaxy evolution models, the Pure Luminosity Evolution (PLE) model by Totani et al. 2001, and the semi-analytical hierarchical model by Nagashima et al. 2005. We found that that a ***Pure Luminosity Evolution model is found to better reproduce the observed properties in our K-selected sample up to K=22***, without evidence of relevant number evolution, even when *separating between early and late-type galaxies* thanks to the AO morphology (Cresci et al. 2006).

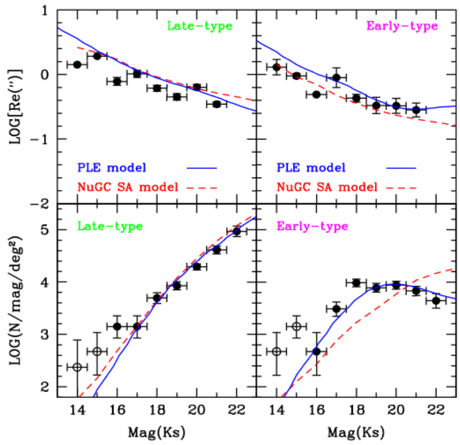

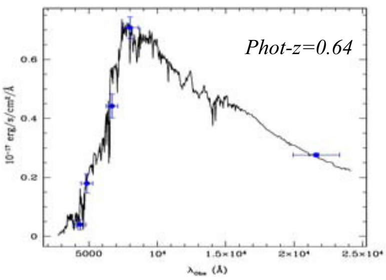

The obtained optical follow-up of the SWAN fields coupled with forthcoming IRAC photometry will provide deeper insight in the properties of the galaxies through SED fitting, e.g. phot-z (*see figure*), mass, SF history…

These results demonstrate the ***unique power of AO observations*** to derive high resolution details of faint galaxies' morphology in the near-IR and drive studies of galaxy evolution.

In addition, SWAN galaxies represent an **unique sample** of galaxies with already known high-resolution near-IR morphology for which it is possible to obtain spectral and morphological information at the diffraction limit, as they are suitable for AO follow-up, e.g. with SINFONI integral field spectrograph (see the SINS posters).

References:

• Cresci, G., Davies, R. I., Baker, A. J., & Lehnert, M. D. 2005, A&A, 438, 757
• Cresci, G., Davies, R. I., Baker, A.J., Mannucci, F., Lehnert, M. D., Totani, T., Minowa, Y. 2006, A&A, 458, 385

G. Cresci, R. Davies et al.

The Dynamical Evolution of Local ULIRGs & QSOs

We have completed a VLT Large Program to trace the dynamical evolution of gas-rich mergers. We obtained VLT ISAAC NIR slit spectroscopy of 54 local Ultraluminous Infrared Galaxies (ULIRGs) and 12 Palomar-Green QSOs.

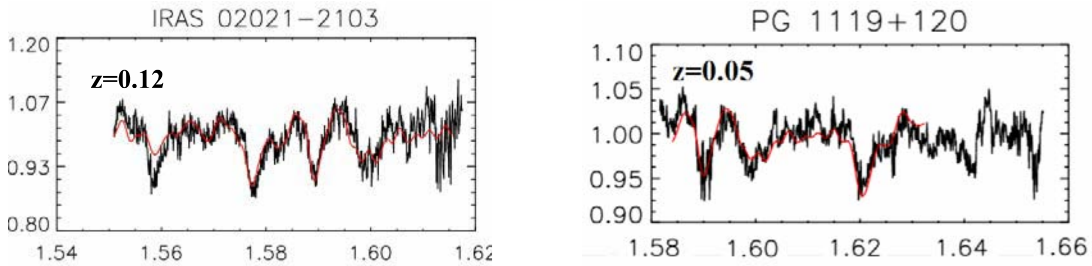

Figure 1: Sample H-band spectra of a ULIRG (left) and a QSO (right) from this study. The selected stellar template for each source after being convolved with the Gaussian that represents the LOS broadening function of the source is overplotted as a solid red line. All spectra are shifted to the rest frame.

The prodigious infrared emission in ULIRGs originates from intense star formation that occurs when large amounts gas are driven to the center of the merging system. About half of our sample sources have two distinct nuclei, and the rest are in later merging stages. From the velocity dispersions of the double nuclei sources we find that ULIRGs are mostly triggered by mergers of roughly equal-mass galaxies. For the late (single) ULIRGs the mean velocity dispersion is 150 km/s. The kinematic, structural, and photometric properties of ULIRGs and their location on the Fundamental Plane indicate that they are dispersion-dominated systems and that they mainly will evolve into 10^{10}-10^{11} $M_\odot$ elliptical galaxies with estimated black hole masses of ~10^7-10^8 $M_\odot$. To investigate whether ULIRGs have an evolutionary link to local QSOs we have made similar observations for 12 local Palomar-Green (PG) QSOs. The mean velocity dispersion of the PG QSOs in our sample is 186 km/s, which implies bulge and BH masses of 10^{11} $M_\odot$ and $5x10^{7-8}$ $M_\odot$ respectively. On the fundamental plane PG QSOs are located between the regions occupied by moderate-mass and giant Es. PG QSOs are likely formed in an analogous manner to ULIRGs. However, other local QSOs with black holes of $5x10^8$-10^9 $M_\odot$ residing in massive spheroids have a different formation mechanism probably linked to a series of merging events.

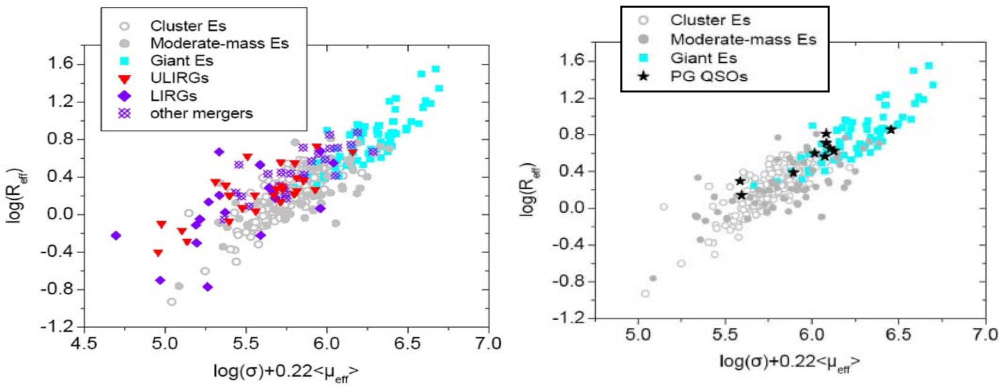

Figure 2: The K-band fundamental plane of early-type galaxies, showing the relationship amongst velocity dispersion, effective radius, and effective surface brightness for dispersion dominated systems. The left panel shows the comparison of elliptical galaxies with ULIRGs and other mergers and the right shows the comparison for the PG QSOs. Giant boxy (cyan squares) and moderate mass disky ellipticals (gray circles) are from Bender et al. (1992) and Faber et al. (1997). Cluster) Es (open circles) are from Pahre (1999). ULIRGs are red triangles and other mergers are plotted in purple. The QSOs of this study are plotted as stars. Most ULIRGs and other mergers lie on the location occupied by moderate mass ellipticals, while PG QSOs are intermediate between moderate mass and giant ellipticals.

References:

• Dasyra, K., Tacconi, L.J., Davies, R., et al. 2006a, ApJ, 638, 745
• Dasyra, K., Tacconi, L.J., Davies, R., et al. 2006b, ApJ, 651, 835
• Dasyra, K., Tacconi, L.J., Davies, R., et al. 2007, ApJ, in press

K. Dasyra, L. Tacconi, R. Genzel, R. Davies, D. Lutz, E. Sturm

Flaming giant galaxies along filaments in A2744

We investigate the relation between substructure and properties of the galaxy population in a 30'x30' region centered on the merging cluster A2744 at z~0.3. Multi-object spectroscopy at medium resolution and BVR photometry are used to detect substructure and large-scale features through dynamical analysis and statistics of the galaxy population and distribution in the cluster.

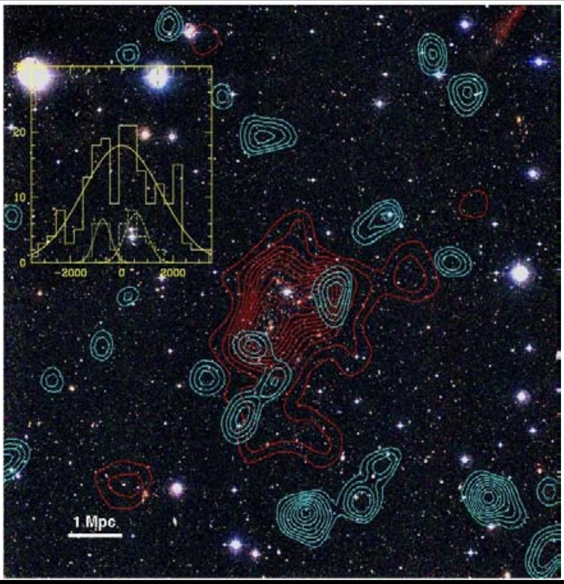

We identify two large-scale filaments associated with A2744, detected from dynamics as distinct secondary peaks in the velocity distribution of the cluster galaxies. In the galaxy distribution they appear as significant overdensities reaching out from the main body of the cluster. In the density map overlaid to the RGB image of the cluster region, filamentary structures are seen in the red galaxy distribution, extending to the S and NW from the core out to the cluster virial radius of 2.5 Mpc. The clumpy distribution of blue galaxies suggests a direct continuation of these large-scale filaments far beyond the virial radius. We calculate a statistical significance of 5σ and 9σ over the background for the NW and S filaments respectively. The upper left inset shows the bimodal velocity distribution of the cluster (σ_v=1509 km/s). The given scale refers to the cluster redshift z=0.3068.

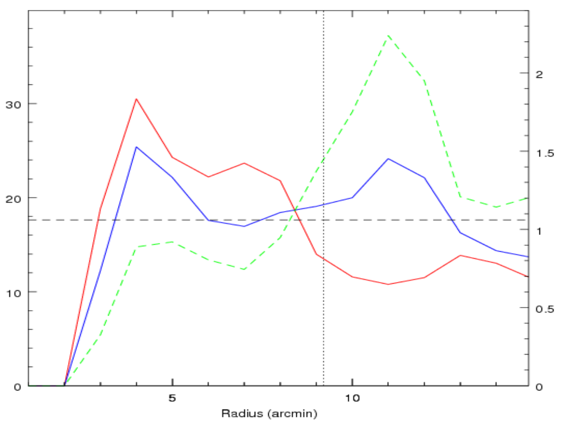

Along the filaments we find an increase in the blue-to-red galaxy number ratio (green line) with cluster-centric distance, which peaks to twice the mean value in the field (horizontal line) beyond the cluster virial radius (vertical line). This reveals an intrinsic increase of the star formation rate towards the outskirts of the cluster. We interprete this behavior as a consequence of the transition from the low-density field to the high-density cluster environment.

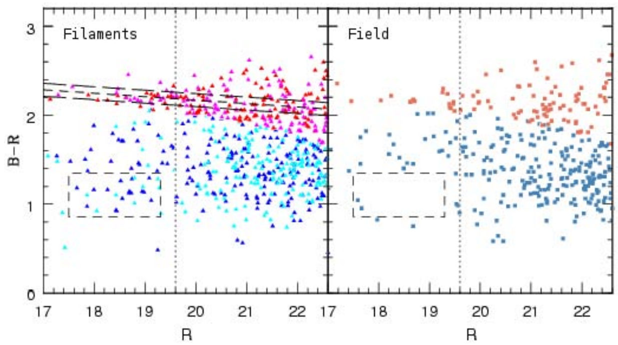

The filaments host a population of giant blue galaxies not found in the field. These galaxies are bright (more luminous than R* for the main cluster), large (about 20 kpc in size) and very blue (0.8<B-R<1.3), suggesting an even higher star formation rate than in the filaments overall. This can be interpreted as a manifestation of galaxy-galaxy harassment: short-time, high-speed interactions with nearby galaxies rearrange the light profile and boost the star formation in the central regions of these massive systems. These galaxies could be the progenitors of the S0 galaxies found in galaxy cluster cores. The locus of the giant blue galaxies is shown as the dashed box in the color-magnitude diagram of the filaments and the field. The red sequence of the main cluster is plotted for comparison.

References:
- Böhringer et al. 2006, The Messenger, 123, 49
- Braglia, Pierini, Böhringer 2007, submitted to A&A

Filiberto Braglia – Daniele Pierini – Hans Böhringer

Galaxy clusters in deep XMM fields

Deep XMM-Newton fields are an invaluable source ot understand the properties of high-redshift groups and clusters of galaxies. I discuss the current progress achieved in two fields, CDFS and COSMOS.

Importance of XMM surveys is in their combination with data at other wavelengths. In Fig.1 we illustrate the multitude of the approaches to cluster search in the COSMOS field by a comparison of weak lensing, galaxy overdensities and X-ray approaches (Massey et al. 2007).

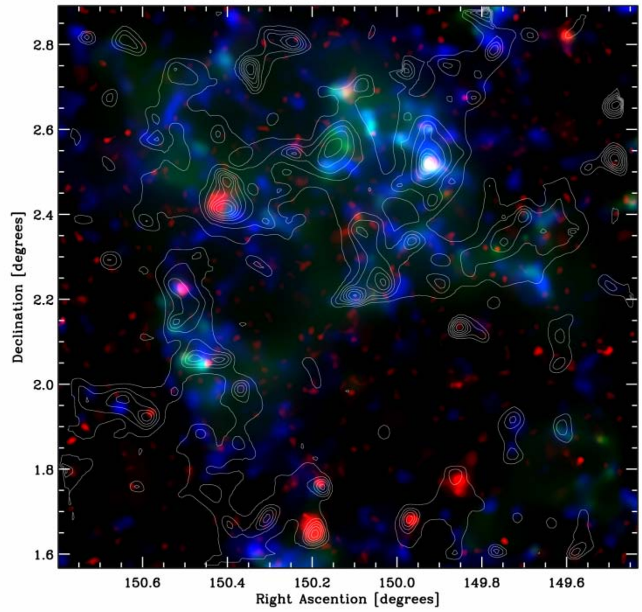

Fig.1 Comparison of baryonic and non-baryonic large-scale structure.The total projected mass from weak lensign, dominated by dark matter, is shown as contours with independent baryonic traces such as stellar mass (blue), galaxy number density (green) and X-ray emission (red)

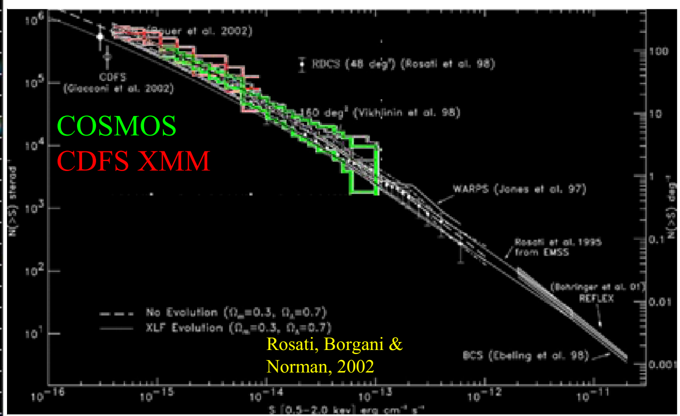

Fig.2 Cumulative cluster number counts (log(N>S)-log(S) for cluster surveys. Our results on XMM surveys of CDFS and COSMOS (Finoguenov et al. 2007 and in prep.) are shown with histograms. The solid line which fits our data is teh no evolution prediction from Rosati et al. 2002.

As illustrated in Fig.2, the cluster research area, covered by deep XMM surveys has not been covered previously. The depths reached by XMM-Newton return up to 150 groups and clusters of galaxies per square degree, a number which can only be achieved in the studies of redshift-selected galaxy concentrations (Scoville et al. 2007).

References:
• Massey, R., …, Finoguenov, A., et al., Nature, 2007, 445, 286
• Finoguenov, A., et al. 2007, ApJ, COSMOS Special Issue in press, astro-ph/0612360
• Scoville, N.,…, Finoguenov, A.,et al. 2007, ApJ, COSMOS Special Issue, in press, astro-ph/0612384
• Rosati, P.,Borgani, S., Norman, C., 2002, ARA&A, 40, 539

Alexis Finoguenov

Searching for Cool Core Clusters at high-z

We present a novel technique to simulate high redshift (z) galaxy clusters, using two cluster samples drawn from the CHANDRA archive: a nearby sample with z=[0.15-0.30], containing both cool core (CC) and non CC clusters and a distant sample (mostly from the Rosat Distant Cluster Survey) with redshifts in the range 0.7-1.4. Assuming no intrinsic evolution, we cloned the starting sample to high-z, in a model independent and parameter free way and investigated the cool core fraction in the distant cluster population, measuring surface brightness concentration (*C*). Our analysis indicates that there is a significant fraction of high-z clusters with moderate CC, similar to those in nearby clusters.

Introduction

Most relaxed galaxy clusters are expected to exhibit at their centres a significant drop in the intra cluster medium (ICM) gas temperature due to radiative cooling. Observationally we expect to see a surface brightness peak in the central region of the cluster (typically of the order of 70kpc), along with some other features such as iron line emission. The so called cooling flow problem resides in the fact that, the gas is not cooling at a rate implied from the radiative losses to low temperature and some form of heating is required. The fraction of Cooling Core Clusters in the local Universe is observed to be in the range 50 to 70% (Peres 98) and recent studies on the evolution of cool cores found no signs of evolution in the redshift range z~0.3 to now (Bauer 04, Vikhlinin). However, how frequent CC are in the distant cluster population is still an open issue.

Method

Following a method to simulate Hubble Deep Fields for testing galaxy evolution (Bouwens 99), we use low-z Chandra clusters z=[0.15-0.3], and clone them to redshifts matching the high-z sample. This technique is based on a flux rescaling (luminosity distance and K-correction), as well as a spatial rescaling (angular distance), using high resolution X-ray images and assuming single temperature clusters. We quantify the strength of the CC using a simple concentration index*C,*which correlates well with classification in the literature. By cloning the low-z sample at high-z (0.7-1.4) we verify the *C*distribution is not biased at increasing redshift. Comparing the*C*index of the nearby and distant samples we find a significant fraction of moderate CC in the z>0.7 cluster population.

Results

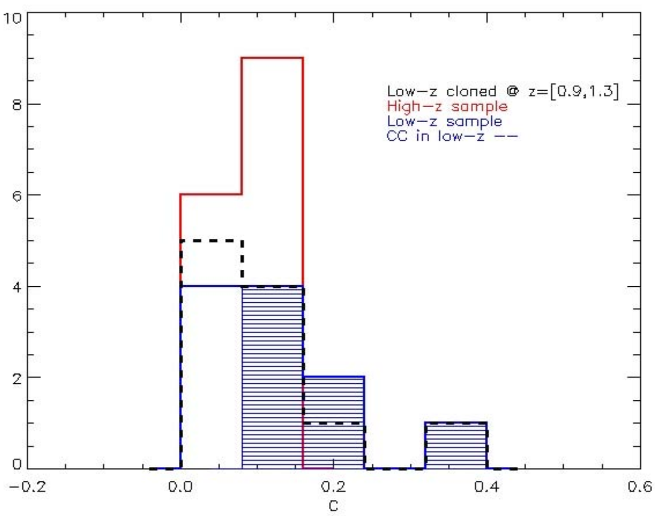

The distribution of the surface brightness (SB) concentration *C,* defined as the ratio *SB(peak) / SB(average)* was sampled with the nearby clusters (in blue, clusters classified as cool cores are in blue hatched). The clones (black) follow well the parent *C* distribution. The high-z sample (red) spans both the non CC and moderate (*C*<0.15) CC regime.

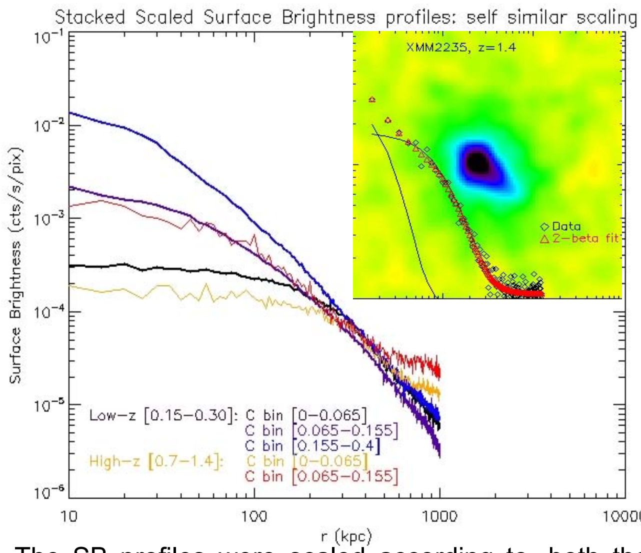

The SB profiles were scaled according to, both the empirical and self similar theory, and stacked in 3 *C* bins: the low-z sample spans the 3 regimes of non CC, moderate and strong CC, whereas the high-z sample covers 2 categories: non CC and moderate CC. On the top-right inset we see the highest redshift cluster in the sample, XMM2235 (z=1.4) and its double-β model fit: this is a moderate CC.

J. Santos, P. Rosati, P. Tozzi, H. Boehringer

Tracing the Fe enrichment of the ICM

Context: We present a Chandra analysis of the X-ray spectra of 56 clusters of galaxies at z > 0.3, in the temperature range 3<kT<15 keV.
Aim: Our analysis is aimed at measuring the Fe abundance (Z_{Fe}) in the ICM out to the highest redshift probed to date.
Methods: We made use of combined spectral analysis performed over five redshift bins at 0.3< z<1.3 to estimate the average emission weighted iron abundance. We applied non-parametric statistics to assess correlations between temperature, metallicity, and redshift.
Results: We find that the emission-weighted Fe abundance measured within (0.15-0.3) R_{vir} in clusters below 5 keV is, on average, a factor of 2 higher than in hotter clusters, following $Z(T) \sim 0.88\ T^{-0.47}\ Z_{sol}$, which confirms the trend seen in local samples. We also find a constant average Fe abundance $Z_{Fe} \sim 0.25\ Z_{sol}$ as a function of redshift, but only for clusters at z>0.5. The emission-weighted Fe abundance is significantly higher ($Z_{Fe} \sim 0.4\ Z_{sol}$) in the redshift range z~0.3-0.5, approaching the value measured locally in the inner 0.15 R_{vir} radii for a mix of cool-core and non cool-core clusters in the redshift range 0.1<z<0.3. The decrease in Z_{Fe} with redshift can be parametrized by a power law of the form $(1+z)^{-1.25}$.
Conclusions: The observed evolution implies that the average Fe content of the ICM at the present epoch is a factor of 2 larger than at z~1.2. We confirm that the ICM is already significantly enriched ($Z_{Fe} \sim 0.25\ Z_{sol}$) at a look-back time of 9 Gyr. Our data provide significant constraints on the time scales and physical processes that drive the chemical enrichment of the ICM.

High-z Chandra sample.
Cut-outs are 8'x6' sorted by increasing z.

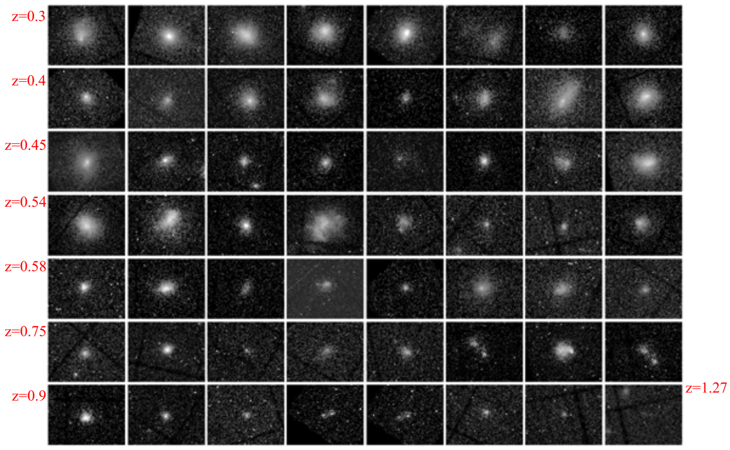

Spectra are extracted from the **radius of maximum S/N** and fitted with a **single-temperature** model

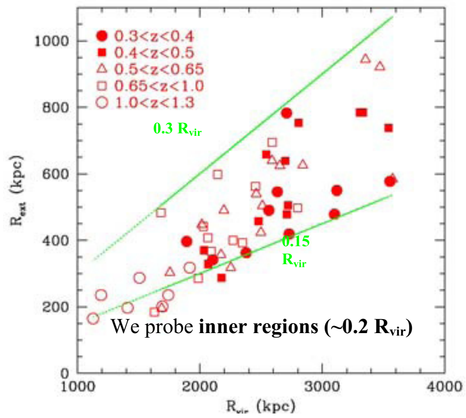

Z_{Fe}-T relation at high-z, at low-z and within the ICM itself.

Is it a universal property of the ICM?

We still miss an explanation.

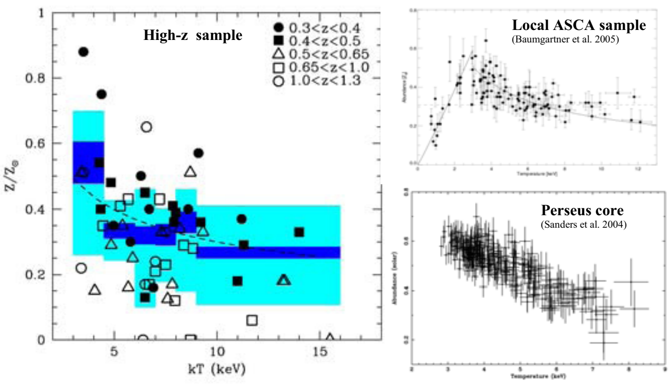

Left: Scatter plot of best-fit Z_{Fe} values versus T for our sample. The dashed line represents the best-fit **Z_{Fe}-T relation** modeled with a power law. Shaded areas show the weighted mean (blue) and average Z_{Fe} with rms dispersion (cyan) in 6 temperature bins. *Top right:* Z_{fe}-T relation for a local sample observed by ASCA. *Bottom right:* Z_{fe}-T relation for the core of the Perseus cluster where different data points refer to different spatial bins.

Iron abundance as a function of redshift

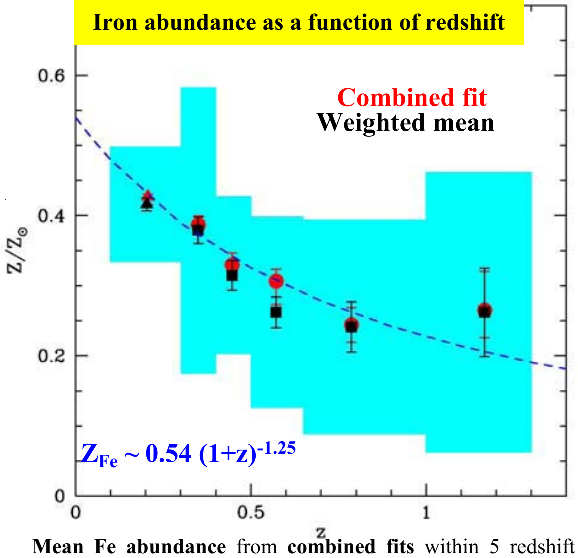

Mean Fe abundance from **combined fits** within 5 redshift bins (red circles) compared with the **weighted average** of single-source measurements in the same bins (black squares). The triangles at z~0.2 are based on the low-z sample (9 clusters at 0.1<z<0.3). Error bars refer to the 1 sigma confidence level. Shaded areas show the rms dispersion. The dashed line indicates the best fit over the 6 redshift bins for a simple power law.

References:
Balestra I., Tozzi P., Ettori S., Rosati P., Borgani S., Mainieri V., Norman C., Viola M. 2007, A&A, 462, 429
Baumgartner W. H., Lowenstein M., Horner D. J., and Mushotzky 2005, ApJ, 620, 680
Sanders J., Fabian A. C., Allen S.W., and Schmidt R.W. 2004, MNRAS, 349, 952

Balestra I., Tozzi P., Ettori S., Rosati P., Borgani S., Mainieri V., Norman C., Viola M.

Cluster Scaling Relations and Mass Calibration

The pilot LoCuSS sample is a flux-limited, morphology-unbiased sample of 12 X-ray luminous galaxy clusters at redshift around 0.2, observed by XMM-Newton to investigate X-ray scaling relations and to calibrate X-ray versus lensing masses (Zhang et al. 2007), in which 9 clusters were also observed by HST to perform the strong lensing analysis (Smith et al. 2005) and 10 clusters by CFHk12 to perform the weak lensing analysis (Bardeau et al. 2006).

Figs. 1-2: The normalization of the X-ray scaling relations agrees to better than 10% for the cool core clusters (triangles) and non-cool core clusters. No evolution of the X-ray scaling relations was observed comparing this sample to the nearby and more distant samples. With the current observations, the cluster temperature (excluding the cool core) and luminosity (corrected for the cool core) can be used as reliable mass indicators with the mass scatter within 20%.

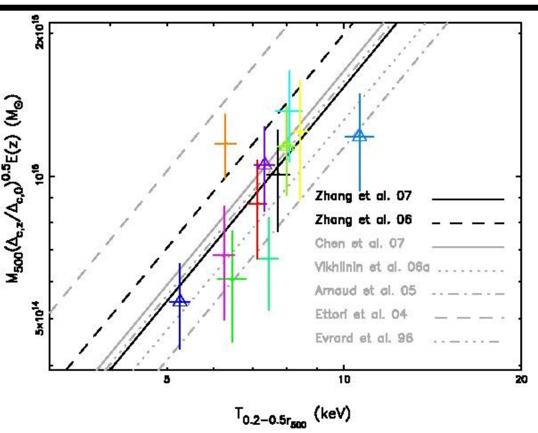

Fig. 1 *Mass-temperature relation*

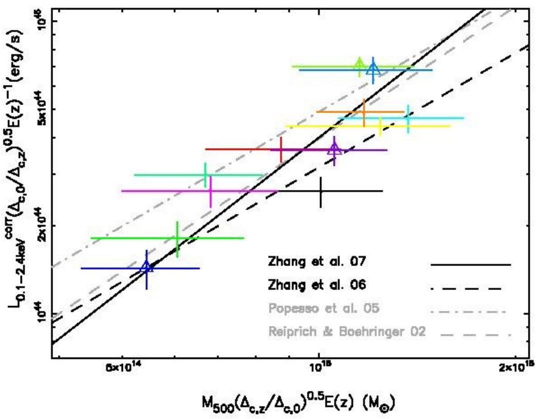

Fig. 2 *Luminosity-mass relation*

Fig. 3: On average, the weak lensing masses agree with the X-ray masses (1.12+/-0.66) and the strong lensing masses are higher than the X-ray masses (1.53+/-1.07). Statistically the strong lensing masses (6/9) agree better than the weak lensing masses (4/10) with the X-ray masses. Fig. 4: The scatter of the luminosity mass relation is larger using weak (strong) lensing masses at r_{200} (r_{2500}) than using X-ray masses at r_{500} and the reasons are discussed in Zhang et al. (2007).

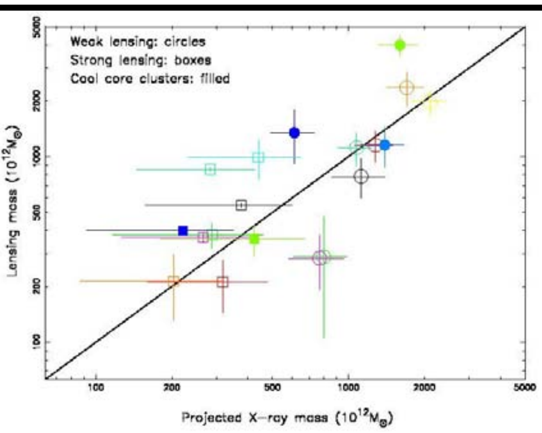

Fig. 3 ***Lensing X-ray mass comparison***

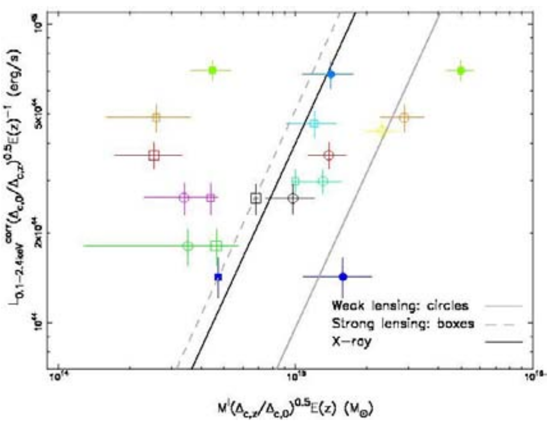

Fig. 4 ***X-ray luminosity vs. lensing mass***

References:

- Bardeau, S., Soucail, G., Kneib, J.-P., 2006, in preparation
- Smith, G. P., Kneib, J.-P., Smail, I., et al. 2005, MNRAS, 359, 417
- Zhang, Y.-Y., Finoguenov, A., Boehringer, H., et al. 2007, A&A, in press, astro-ph/0702739

Y.-Y. Zhang, A. Finoguenov, H. Boehringer, J.-P. Kneib, G. P. Smith, G. Soucail, O. Czoske

Galaxies, Galactic Nuclei and Massive Black Holes

High Resolution Millimeter Imaging of Submillimeter Galaxies

In collaboration with researchers from the IRAM community, the US and the UK and as part of a CO survey of submillimeter galaxies, we have now detected CO in 16 sources, and mapped sub-arcsecond resolution IRAM PdBI interferometry of 8 of these objects, where we detect continuum at 1mm and/or CO lines at 3 and 1 mm.The millimeter line and continuum emission is compact with FWHM sizes ≤0.5” (4 kpc). **In two cases we have have been able to spatially and kinematically resolve the source into two distinct components that are very likely in the process of a major merging event.**The implications are far-reaching: these submillimeter galaxies resemble scaled-up, more gas rich versions of local Universe, ultraluminous galaxies. Their central densities and potential well depths are much greater than in other z~2-3 galaxy samples (see poster by Bouché et al). The SMG properties fulfill the criteria of ‘maximal’ starbursts, where most of the available initial gas reservoir of 10^{10}-10^{11} $M_\odot$ is converted to stars on a few dynamical timescales, ~a few 10^8 years.

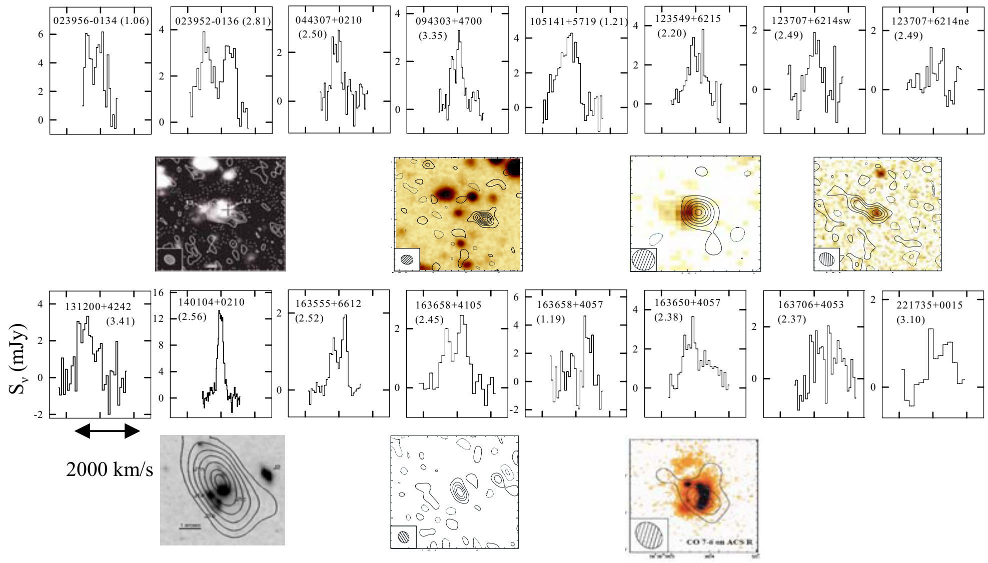

Figure 1: Top rows: Integrated CO (mostly CO 3-2) spectra of submillimeter galaxies observed with the IRAM PdBI (Genzel et al. 2003; Downes et al. 2003; Greve et al. 2005 and Tacconi et al. 2006). Bottom rows are the integrated CO contours superposed on optical images of the sources for the cases where we have obtained high resolution maps. The FWHM resolution is shown in the bottom left of each panel.

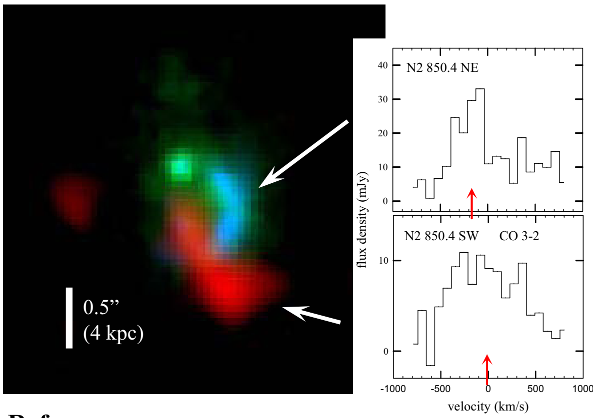

Figure 2: SMMJ163650+4057 (N2 850.4, z=2.39): Integrated CO 7-6 emission (in red) superposed on HST ACS (blue) and NICMOS (green) images of the source, showing a double CO structure and a star-forming ring. The CO map has a FWHM resolution of 0.45". The right panels show the CO(3-2) spectra toward the two sources, with the red arrows indicating the centroids of the line profiles.

References:

- Tacconi, L.J. et al. 2006, ApJ., 640, 228
- Greve, T. et al. 2005, MNRAS, 359, 1165

Collaboration with: F. Bertoldi, A. Blain, S. Chapman, P. Cox, T. Greve, R. Ivison, R. Neri, A. Omont, I. Smail

L.J. Tacconi, R. Genzel

Who am I? The roles of dusty star formation and morphology in intermediate redshift, massive galaxies

In the local Universe, the galaxy population is characterized by a transition from blue, star forming galaxies below stellar masses of ~3x$10^{10}M_\odot$ to a passive population of early-type galaxies which dominates above this mass. Conversely at high redshift (z≥1), many massive galaxies are seen in a strongly star forming mode, associated with massive dust obscuration and infrared and submillimetre re-emission. In our CNOC2 sample (z_{mean}~ 0.4), we combine Spitzer measurements of obscured star formation with optical indicators such as [OII] and colour, and morphological information, to reveal the perhaps surprisingly important role of dusty star formation in the highest mass galaxies at intermediate redshifts.

Within our sample of CNOC2 galaxies, optical indicators of star formation such as (U-R) colour and EW[OII] (left panel) correlate strongly with stellar mass: more massive galaxies (in particular those more massive than the local so-called *transition mass*(~3x1010Mʘ, Kauffmann et al., 2003) are redder, and weaker in EW[OII], than less massive galaxies. This means that emission from young stars is either heavily extincted, or these galaxies are truly dominated by old stars. Galaxy morphology (see key) moves from late to early type as one moves to higher mass and weaker [OII] emission.

Left: EW[OII] distribution of galaxies in our sample, and dependence on stellar mass.
Right: 6.2μm PAH+stellar emission (IRAC band 4, observed frame 8μm) normalized by 3.6μ stellar emission (IRAC band 1).
Both: 10^{th}, 25^{th}, 50^{th}, 75^{th} & 90^{th} percentiles shown (lines) as are HST morphologies (see key).

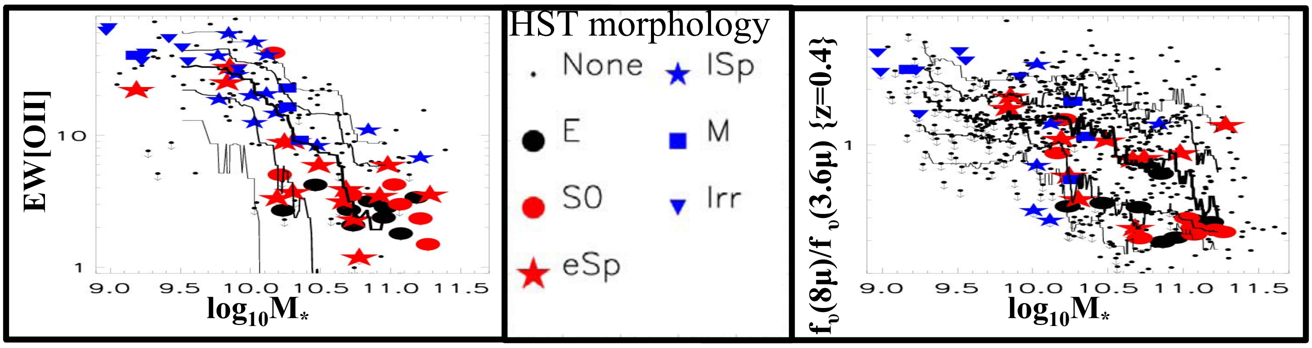

Extincted light from young stars will be re-emitted at Infrared wavelengths. Some of this light will be re-emitted from PAH molecules in the mid-infrared. The IRAC camera on Spitzer captures the strong 6.2 μm PAH emission feature in band 4 (8μm) for intermediate redshift galaxies up to z=0.48. Selecting galaxies at 0.3<z<0.48, we normalize the strong band 4 emission by the stellar continuum at 3.6μm, a good proxy for stellar mass at this redshift. This also serves to remove the contribution from the tail of the stellar continuum at 6.2μm. K-corrected using templates to a z=0.4 bandpass, a non-PAH emitting galaxies lies at $f_\upsilon(8\mu)/f_\upsilon(3.6\mu)$ ~0.3. Anything with stronger PAH emission will have larger values of this flux-ratio.Our results contrast strongly with what is found at optical wavelengths: Right up to stellar masses of ~ 3x$10^{11}M_\odot$ we still find galaxies with PAH to stellar continuum ratios as high as the most star-forming low mass galaxies!! Indeed, considering selection effects (selection against low mass passive galaxies), there is little evidence for any trend of infra-red activity with stellar mass at all. Conversely, the trend with galaxy morphology standsout: late-type galaxies emit significantly more PAH emission per unit mass than their bulgier counterparts, regardless of their mass. This result implies a surprisingly well balanced opposition of star-forming and extinction trends with stellar mass, and implies morphological transformation and highly extincted phases of star-formation may be even more relavent than expected to the truncation of star formation and the resultant formation of passive galaxies.

References: Kauffmann et al., 2003, MNRAS, 341, 54

David Wilman & Daniele Pierini (MPE), Michael Balogh & Sean Mcgee (Waterloo), John Mulchaey & Gus Oemler (Carnegie Observatories), Richard Bower (Durham)

Mid-IR Spectroscopy of SMGs: Luminous Starbursts at High Redshift

MAX-PLANCK-GESELLSCHAFT

MPE

We present rest frame mid-IR spectroscopy of a sample of 13 submm galaxies, obtained using the Infrared Spectrograph (IRS) on board the *Spitzer Space Telescope*. The sample includes exclusively bright objects from blank fields and cluster lens assisted surveys that have accurate interferometric positions. We find that the majority of spectra are well fitted by a starburst template or by the superposition of PAH emission features and a weak mid-IR continuum, the latter a tracer of Active Galactic Nuclei (including Compton-thick ones). We obtain mid-IR spectroscopic redshifts for all nine sources detected with IRS. For three of them the redshifts were previously unknown. The median value of the redshift distribution is z~2.8 if we assume that the four IRS non-detections are at high redshift. The median for the IRS detections alone is z~2.7. Placing the IRS non-detections at similar redshift would require rest frame mid-IR obscuration larger than is seen in local ULIRGs. The rest frame mid-IR spectra and mid- to far-infrared spectral energy distributions are consistent with those of local ULIRGs, but scaled-up further in luminosity. The mid-IR spectra support the scenario that submm galaxies are sites of extreme star formation, rather than X-ray-obscured AGN, and represent a critical phase in the formation of massive galaxies.

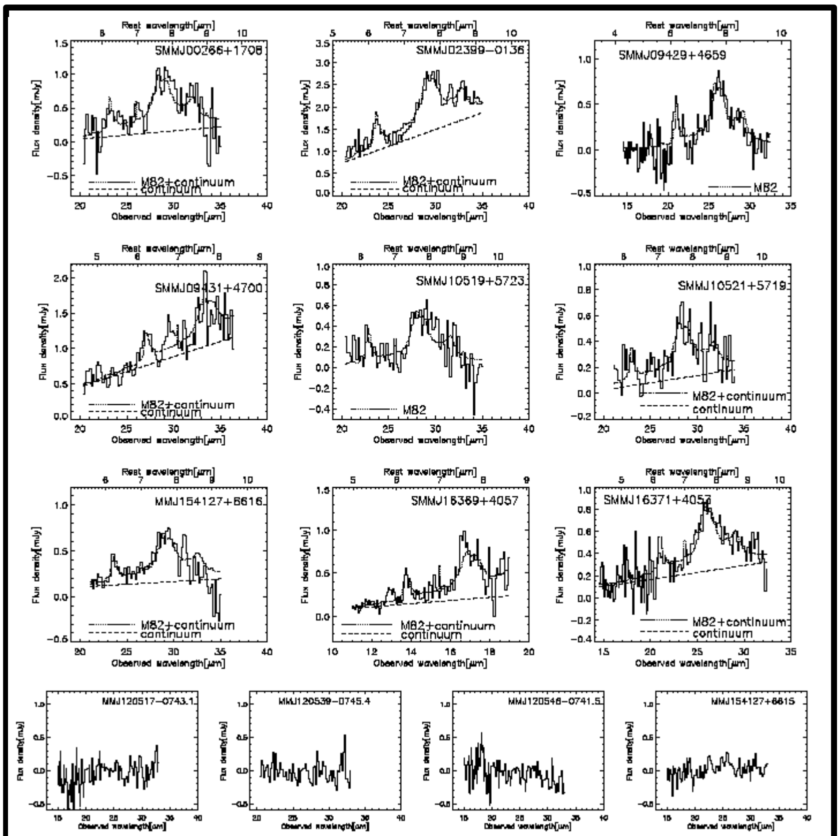

(dotted line) of our sample. The last four spectra show IRS non-detections.

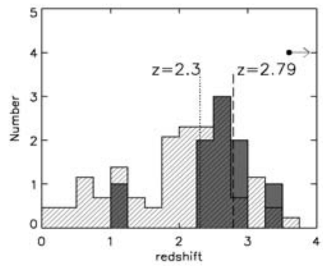

Redshift distribution of our SMGs sample (grey histogram) and for the sample of Chapman et al. (2005, ApJ, 622, 772) (shaded histogram) scaled for the maximum value.

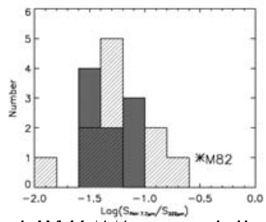

Ratio of PAH 7.7mm peak flux density and rest frame 222mm continuum flux density for our SMGs sample (grey histogram) and for eleven local ULIRGs (shaded histogram).

More informations in: Lutz et al. 2005, ApJ, 625L, 83, Valiante et al. 2007, ApJ in press (astro-ph/0701816)

E. Valiante, D. Lutz, E. Sturm, R. Genzel, L.J. Tacconi

Dark matter and stellar orbits in ellipticals

We have analysed long-slit kinematics of 14 flattened Coma early-types ($-18.8 > M_B > -22.6$) by Schwarzschild's orbit superposition technique. Systematically varying the (spatially constant) stellar mass-to-light ratio and dark halo parameters (NFW and logarithmic potentials were probed) we find that dark matter is required in each object (90% confidence). Central dark matter densities of ellipticals are about 5-100 times higher than in comparable spirals. Similar dynamical models were applied to a comparison sample of collisionless binary disk mergers (from Naab & Burkert 2003). Models of mergers and of ellipticals are mainly flattened by anisotropy, but modelling collisionless mergers predicts a scatter in anisotropies that is larger than seen in models of real galaxies.

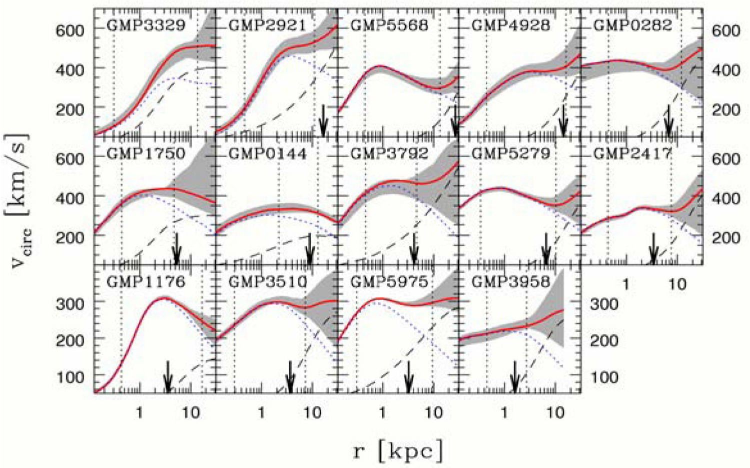

- studied ellipticals have approximately flat circular velocity curves over the observationally sampled region (solid lines: circular velocity of luminous+dark mass; shaded: 68 percent confidence region; dotted/dashed: luminous and dark matter separately; vertical dotted: boundaries of kinematic data)
- 10-50 percent of mass inside r_{eff} is dark matter (r_{eff} indicated by the arrows)
- logarithmic halos fit often marginally better than NFW halos (<68% confidence)
- dark and luminous mass equalise slightly beyond r_{eff} (dotted and dashed curves cross)

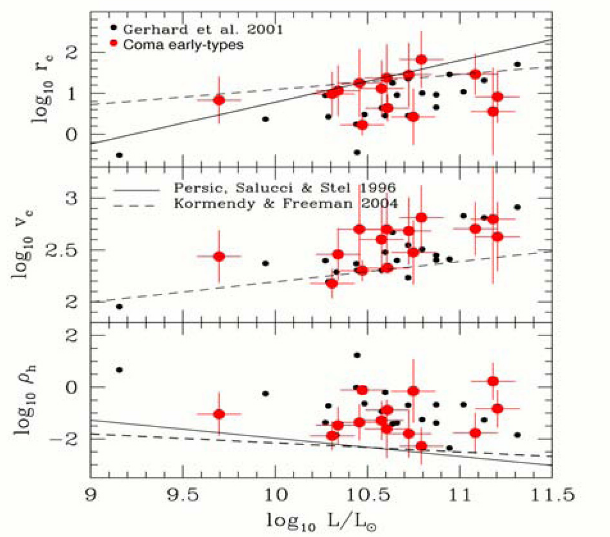

- ellipticals (black: round, non-rotating; red: Coma) and spirals (solid/dashed) follow similar scaling laws, but ellipticals have larger outer velocities v_c, smaller core-radii r_c and higher central dark matter densities ρ_h
- enhanced central dark matter densities imply either a formation redshift Δz_{form}=1-2 earlier than spirals or that some fraction of dark matter is baryonic

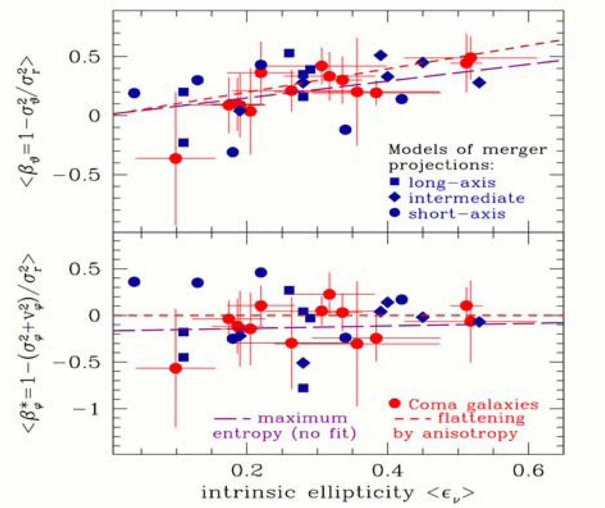

- models of ellipticals and of merger remnants are mostly flattened by anisotropy (red lines), which maximises the orbital entropy (magenta lines)
- triaxiality in mergers causes scatter in anisotropies of our axisymmetric models (Thomas et al. 2007)
- the small scatter in anisotropies of Coma ellipticals therefore points at approximate axial symmetry, possibly driven by gas dynamics during formation

References:

- J. Thomas, R.P. Saglia, R. Bender, D. Thomas, K. Gebhardt, J. Magorrian, et al., 2004, MNRAS, 353,391
- J. Thomas, R.P. Saglia, R. Bender, D. Thomas, K. Gebhardt, J. Magorrian, et al., 2005, MNRAS 360, 1355
- J. Thomas, R. Jesseit, T. Naab, R.P. Saglia, A. Burkert, R. Bender, 2007, submitted to MNRAS

J. Thomas, R. P. Saglia, R. Bender, et al.

Variations in the spectral slope of Sgr A* during a near-infrared flare

We have observed a bright flare of Sgr A* in the near-infrared with the adaptive optics assisted integral-field spectrometer SINFONI. Within the uncertainties, the observed spectrum is featureless and can be described by a power law. Our data suggest that the spectral index is correlated with the instantaneous flux and that both quantities experience significant changes within less than 1 hour. We argue that the near-infrared flares from Sgr A* are due to synchrotron emission of transiently heated electrons, the emission being affected by orbital dynamics and synchrotron cooling, both acting on timescales of 20 minutes.

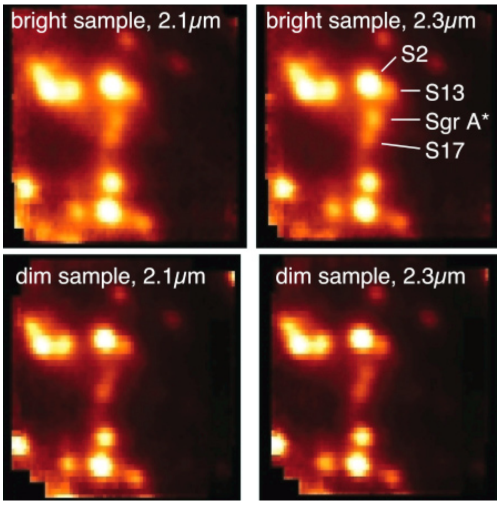

Top: The Galactic center as seen with SINFONI. All images are scaled in the same way and use an identical color map. Sgr A* is brighter in the longer wavelength maps, indicating that it is redder than the field stars. Furthermore, the effect is more pronounced in the dim sample, meaning that Sgr A* is redder therein than in the bright sample.

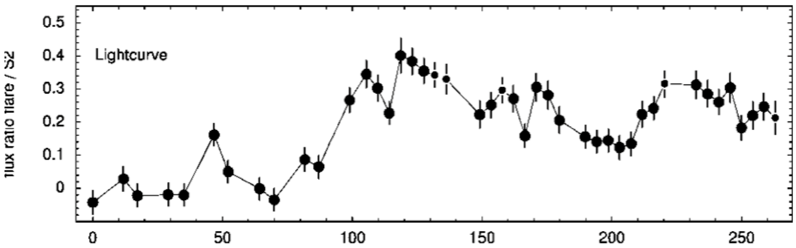

Top: Light curve of the flare. Time is counted from 02:40 UT, brightness is measured as flux ratio flare/S2 (smaller points are exposures affected by bad seeing).

- **The changes of the NIR color of Sgr A* indicate that the flares are due to a Transiently heated population of electrons which emit synchrotron radiation.**
- **Together with X-ray data our observations favor a small emission region, with radii Smaller than 1/3 of the Schwarzschild radius ("hot blob").**
- **For a hot blob model the variations in the light curve are caused by orbital dynamics (Dopplerboosting) as well as by intrinsic changes of the emitting electron population (synchrotron cooling).**

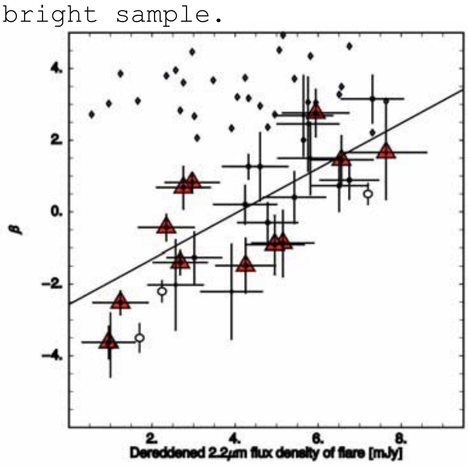

Left: Correlation between the flare flux and the spectral index β. Points with error bars represent the flare, and blue dots are S17. Filled circles mark points with error $\Delta\beta < 1$, and red triangles mark the data with good seeing (FWHM < 75 mas). The lines are fits to the filled circles. Open circles indicate earlier data.

S. Gillessen, F. Eisenhauer, E. Quataert, R. Genzel, T. Paumard, S. Trippe,

Properties of massive stars in the Galactic Center

The properties of the young massive stars in the Galactic Center are derived using near-IR spectroscopy and atmosphere models. We propose a plausible scenario for their evolution. We show that their ionising flux accounts for all the observed nebular properties of the ionised gas. We do not find any failure of stellar evolution in the GC any more.

The presence of more than 100 young massive stars in the central parsec of the Milky Way is a puzzle referred to as the „paradox of youth“: how could star formation take place in such a hostile environment? To uncover this mystery, the knowledge of the properties of the stars is crucial.

We used the instrument SINFONI to obtain near-IR spectra of all the population of young stars. Fig. 1 shows such data for different types of stars. The presence of various lines from different ionisation states and elements allows an accurate spectral classification. Roughly 40 stars are evolved massive objects (Wolf-Rayet, Ofpe/WN9 stars). The other stars are mainly late type O supergiants.

We have used the atmosphere code CMFGEN to derive their stellar and wind properties (T_{eff}, Luminosity, mass loss rate, abundances). Fig.2 shows the best fit model for the WN5/6 star IRS16SE2. We have established a direct evolutionary link between Ofpe/WN9, WN8, WN/C and WC9 stars, all of them corresponding to different phases of evolution of stars with initial masses in the range 25-60 $M_{\odot}$. In addition, we have shown that the population of massive stars produces enough photons to ionise the surrounding gas, solving a long standing problem for the Galactic Center. This result clearly indicates that stellar evolution is normal in this region, and that a starburst model perfectly accounts for the oberved stellar population.

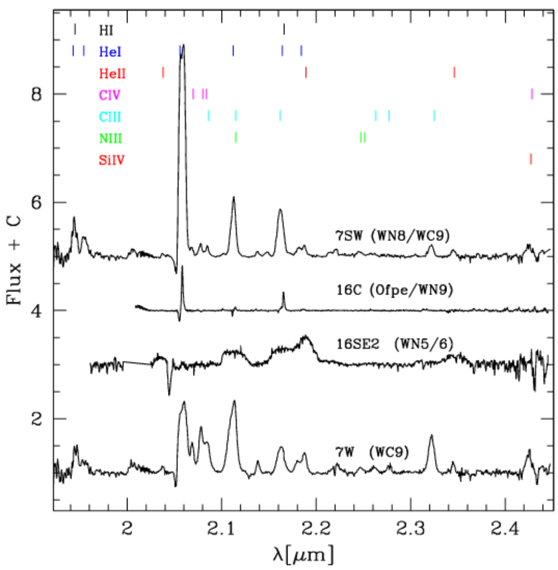

Fig. 1: SINFONI spectra of various types of massive stars in the Galactic Center. The numerous lines identified allow an accurate spectral classification

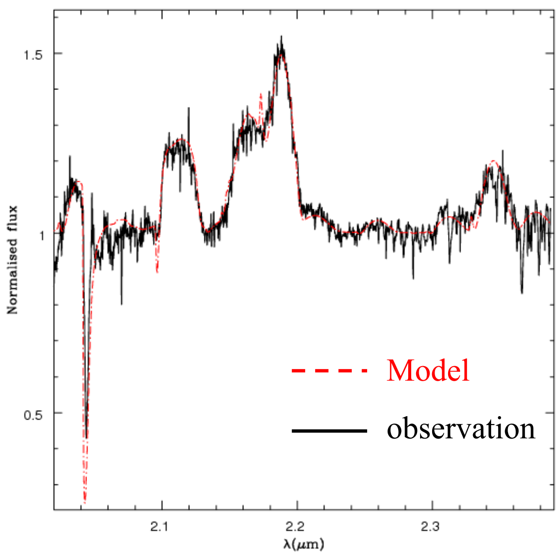

Fig. 2: Best fit model (red dashed line) of the observed K band spectrum (black solid line) of the WN5/6 star IRS16SE2.

Reference:
• Martins, F, Genzel, R., Hillier, D.J., 2007, A&A, submitted

F. Martins, R. Genzel, D.J. Hillier, F. Eisenhauer, T. Paumard, S. Gillessen, T. Ott, S. Trippe

The Gaseous Atmosphere of M87

We use a deep XMM-Newton observation of M87 to produce detailed temperature, pressure and entropy maps, that are needed to further understand the physics of cooling cores. The most prominent features observed are the E and SW X-ray arms that coincide with powerful radio lobes, a weak shock at a radius of 3‘, an overall ellipticity in the pressure map and a NW/SE asymmetry in the entropy map which we associate with the motion of the galaxy towards the NW.

We analyze a 109.3 ksobservation of M87 with XMM-Newton performed on Jan 10th, 2005. We adaptively binned our combined counts image to a signal-to-noise-ratio of 100, extracted spectra from the resulting ~1500 bins and fitted them with a one-temperature mekal model. Using the temperature and normalization from spectral fitting, we computed corresponding pseudo-pressure and entropy maps, which we divided by a radially symmetric smooth model to reveal small scale deviations.

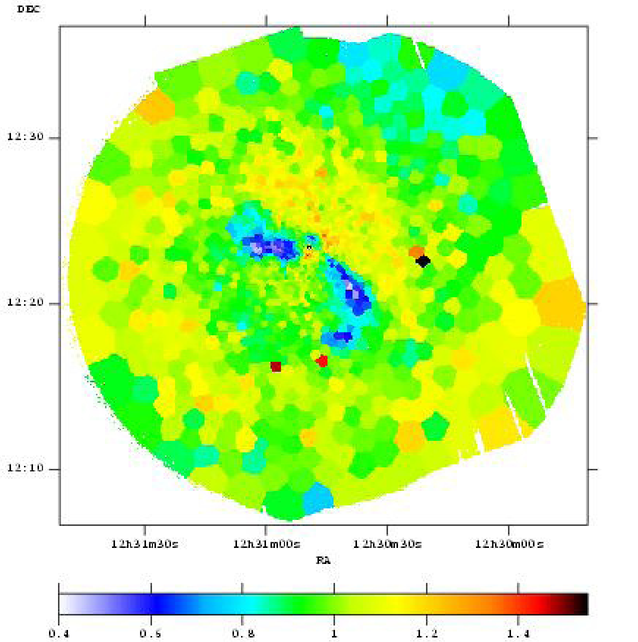

Fig. 1: Entropy map

Both the temperature and entropy maps show similar substructure details:

•The E and SW-arms characterized by low temperature and entropy both curve clockwise following the large-scale radio lobes.

•An edge to the SE at ~8'. Both T and S decrease inside the edge.

•A feature seen in the entropy but not easily visible in the temperature map is a NW/SE asymmetry: within 8' the entropy is higher NW of the core and lower to the SE. The NW limit of the high-entropy region coincides very well with the margin of the large NW radio bubble.

•Systematically lower temperature, entropy, and higher abundances within 8’ to the SE suggest a motion of M87 to the NW, leaving behind a cold, metal-rich trail.

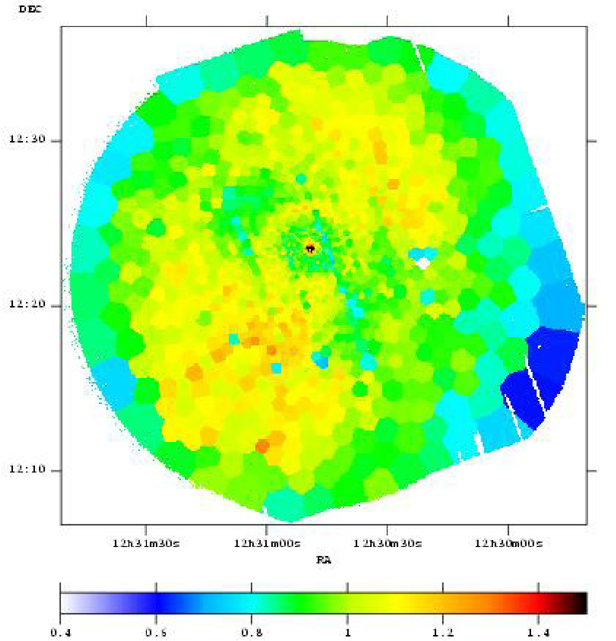

Fig. 2: Pressure map

Features in the pressure/model ratio map:

•A relative pressure increase to the NW and SE, which can be explained by an overall ellipticity of between 0.1-0.13 of the dark matter profile.

•A pressure decrease towards the E and SW arms suggesting that the radio lobes rise parallel to the short axis of the elliptical DM profile following the buoyancy force. Subtracting an elliptical model from the data we still find a decrease in these regions, which indicates the possible presence of nonthermal pressure.

•A ring of enhanced pressure with a radius of ~3', corresponding to the weak shock postulated from Chandra results.

Reference:

• Simionescu, A. et al., A&A in press, astro-ph/0610874

A. Simionescu, H. Böhringer, A. Finoguenov, M. Brüggen

The supermassive black hole in NGC4486a

The near-infrared integral field spectrograph SINFONI at the ESO VLT opens a new window for the study of central supermassive black holes. With a near-IR spatial resolution similar to HST optical and the ability to penetrate dust it provides the possibility to explore the low-mass end of the M_{BH}-σ relation (σ<120km/s). With SINFONI we observed the central region of the low-luminosity elliptical galaxy NGC4486a at a spatial resolution of ~0.1" in the K band. We determined a black hole mass of $M_{BH}=1.25^{+0.75}_{-0.79}\times10^7 M_\odot$ (90% C.L.) using a Schwarzschild orbit superposition method including the full 2-dimensional spatial information. This mass agrees with the predictions of the M_{BH}-σ relation, strengthening its validity at the lower σ end.

NGC4486a is located in the Virgo cluster at a distance of 16 Mpc. It contains an almost edge-on nuclear disk of stars and dust. The SINFONI data on NGC4486a was reduced with the software package SPRED and the stellar kinematics was measured with a maximum penalised likelihood method using the region around the CO absorption bandheads.

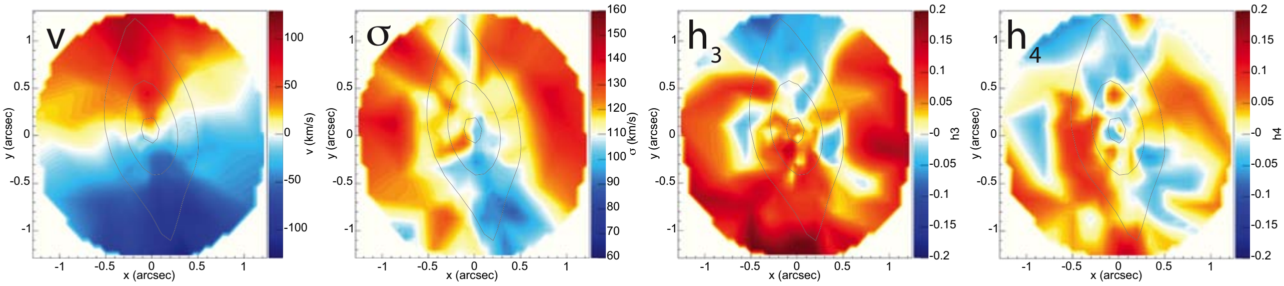

Fig. 1: Stellar kinematic fields (v, σ, h_3, h_4) of NGC4486a.

The mass of the central black hole was determined using the code of Thomas et al. 2004, which is based on the Schwarzschild orbit superposition technique. The best-fitting model gives $M_{BH}=1.25^{+0.75}_{-0.79}\times10^7 M_\odot$ (90% C.L.), which was found by a χ^2-analysis of all models calculated with systematically varied black hole mass M_{BH} and z band mass-to-light ratios ϒ for disk and bulge. Models without black hole are excluded at 4.5σ level. The derived black hole mass strengthens the validity of the M_{BH}-σ relation at low σ, where up to now only three black hole masses were measured with stellar dynamics.

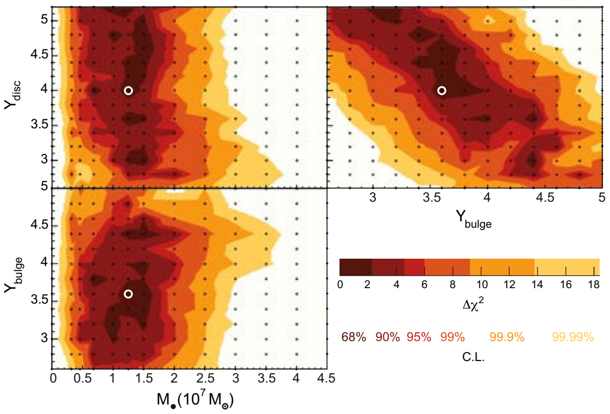

Fig. 2: $\Delta\chi^2$ as a function of two of the three varied parameters M_{BH}, Υ_b and Υ_d, minimised over the third parameter. The black points are the models we calculated and the coloured regions are the unsmoothed confidence intervals for two degrees of freedom.

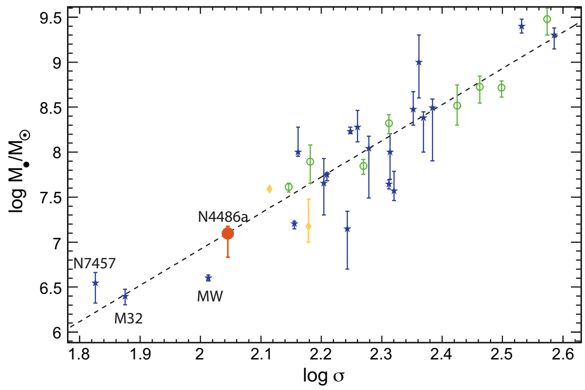

Fig. 3: M_{BH}-σ relation with the black hole mass of NGC4486a overplotted in red.

References:
- N. Nowak et al., 2007, submitted to MNRAS
- J. Thomas et al., 2004, MNRAS, 353, 391

N. Nowak, R. Saglia, J. Thomas, R. Bender and R. Davies

Viewing the Molecular Torus in AGN

SINFONI observations of nine AGN indicates the presence of obscuring tori based on the spatial scales, column densities, and implied vertical heights of their molecular hydrogen gas disks.

A survey of nine nearby AGN at spatial resolutions down to 0”.085 shows that the distribution and kinematics of the nuclear molecular hydrogen is consistent with a torus of gas surrounding the AGN such as those invoked in obscuring torus models. Evidence supporting this includes fits to the flux distributions, which indicate the molecular gas is in a disk-like structure with size scales of 10-60 pc, consistent with model predictions of 10-100 pc. In addition, the gas column density at these same radii, estimated to be at least 10^{23} cm^{-2}, is high enough to provide the needed obscuration of the AGN. Furthermore, the bulk of the molecular hydrogen in these galaxies shows ordered rotation, but with relatively high velocity dispersions of 70-130 km s^{-1}. On scales less than 50 pc the velocity dispersion is greater than, or comparable to, the rotational velocity (i.e. $V_{rot}/\sigma \leq 1$), implying that the gas is geometrically thick with respect to the radial scales. This vertical structure is also a key part of obscuring torus models and is likely due to turbulence in the gas caused by heating from the AGN and/or nuclear star formation. Moreover, the molecular gas is similar in both distribution and kinematics to the nuclear stellar disks (Davies et al. 2007) suggesting that the torus encircling the AGN is composed of a mixture of molecular gas and stars.

H_2 1-0 S(1) Flux Distribution

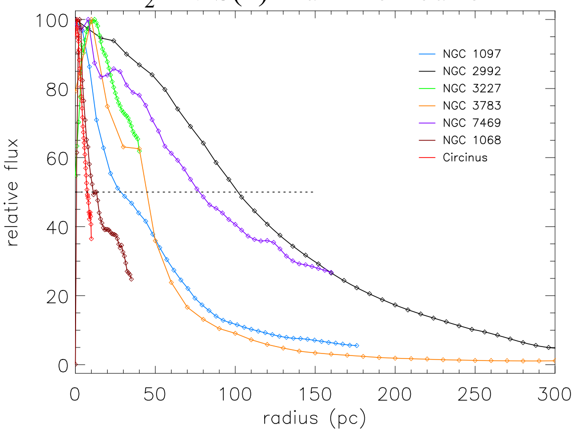

Radial averages of the H_2 flux distribution in each of the AGN, as indicated in the legend. The flux is normalized to the peak of the distribution. The horizontal dashed line indicates the half-width-half-maximum of the flux distribution.

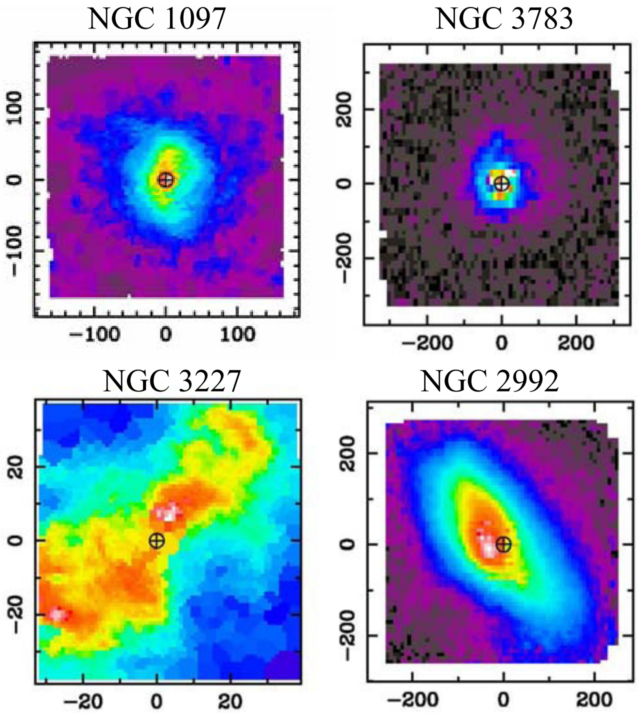

H_2 1-0 S(1) flux distribution in four galaxies from the sample of nine. The symbol plotted on each map indicates the location of the AGN. All axes are in units of parsecs.

Reference: Davies, R. I., Mueller Sanchez, F., Genzel, R., Tacconi, L., Hicks, E. K. S., Friedrich, S., Sternberg, A., 2007, ApJ submitted

E. Hicks, R. Davies, F. Mueller Sánchez, R. Genzel, L. Tacconi, S. Friedrich, A. Sternberg

Gravitatonally redshifted soft X-ray lines

XMM-Newton observations of Mrk 110 have revealed for the first time a broad (13 eV) and redshifted (z = 0.03) soft X-ray emission lines associated with the O VII triplet. The line can be fitted either with a simple Gaussian- or a relativistic disc line. With the present data statistic we can not disentangle between pure GR effects and bulk infall motions. Previous claims on the detection of GR effects on soft X-ray lines from the accretion disc appear unphysical due to the sharpness of red wing (3 eV) and the huge EW values of about 170 eV.

Claims and potential problems with the line interpretation in the past

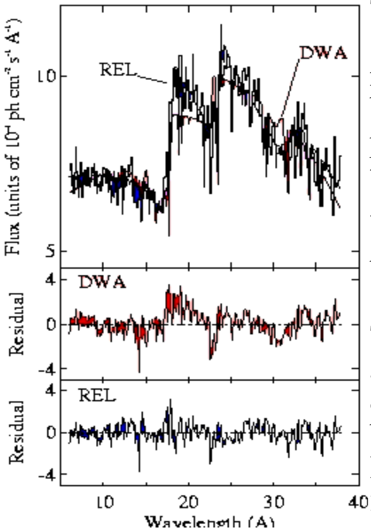

The left Fig. shows the RGS spectrum of Mrk 766 (Mason et al., ApJ 582, 95, 2003). The data are fitted with a dusty warm absorber and a relativistic line model. They argue that the line interpretation gives the best fit to the data. The main problem with the line interpretation in the past is the huge EW of the lines (e.g. 169 eV for OV II, in contrast to theoretical predictions of about 10 eV (e.g. Matt et al. MNRAS 262,179, 1993) and the sharpness of the 707 eV drop of oxygen (Fabian et al. in ´X-rays from AGN`, RSPTA.360.2035, 2002). The bulk of the O lines are produced by highly ionized gas, suffer Compton scattering, since they are produced over a significant Thomson depth. Therefore, they are broadened considerably more than 10 eV. Doppler and gravitational redshifts broaden this further. Consequently, it is difficult to see how the sharp drop at 707 eV can be produced by the blue wing of a relativistic line. **In summary, relativistic soft X-ray lines are expected to be broad and redshifted with respect to the narrow unresolved elements**.

The first detection of a broad and redshifted soft X-ray line

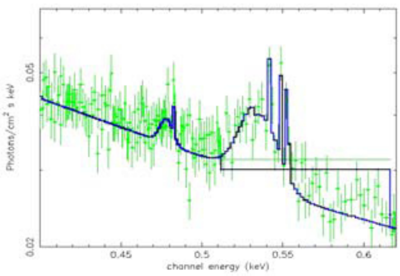

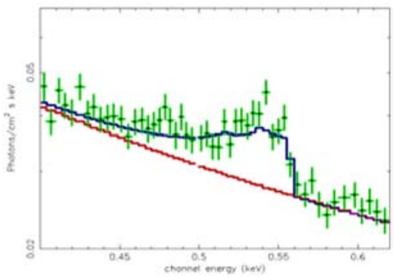

In addition to the narrow unresolved, and neither red-nor blueshifted line of the Oxygen triplet a broad and redshifted line associated with the narrow lines has been detected. The significance of the broad O VII line is above the 3 σ limit. This is the first detection of a broad and redshifted (z = 0.03) soft X-ray line. The line can be either fitted with a simple Gaussian line (left Figure) or with a relativistic disc line (right Figure). All parameters are constrained. With the present data we can not decide whether simple bulk infall motions or GR effects provide the correct physical model.

Expectations due to GR effects

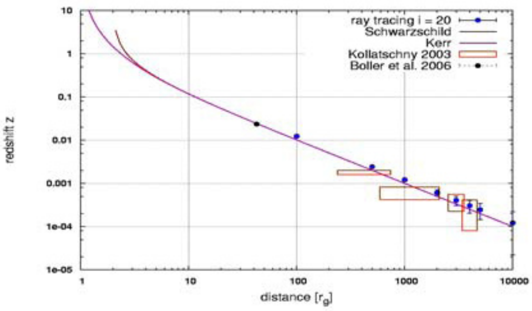

Longer observations are required to disentangle between different physical models to explain the observed redshift and broadness of the O VII line. GR effects might be a possible explanation and there are arguments which might account for this scenario. Assuming that future observation confirm the GR scenario, GR effects on soft X-ray lines would open a new window to study the temperature- and density structure of the BLR more precisely.

Thomas Boller

Radio-loud Narrow-line Seyfert 1 galaxies

A key unsolved problem in the study of Active Galactic Nuclei (AGN) is the question, which mechanism is responsible for the fact that ~15% of all quasars are radio-loud, while the majority is radio-quiet. Studying radio-properties of new subtypes of AGN may shed new light on this issue. We have selected the class of Narrow-line Seyfert 1 (NLS1) galaxies to study this and related topics. Even though studied in detail in the optical and X-ray band, almost nothing was known about the radio-properties of NLS1 galaxies before our study.

We have searched for radio-emission from NLS1 galaxies based on various existing radio surveys (primarily, the FIRST and NVSS surveys at 1.4 GHz), have determined radio-loudness (the radio index R is defined as the flux ratio f_{radio}/f_x), have identified radio-loud sources (Fig. 1), and have performed follow-up studies of these in the optical, X-ray and IR regime – see Komossa et al. (2006a,b) for details.

Our results can be summarized as follows:

- The fraction of radio-loud(RL) NLS1s (7%) is smaller than the fraction of radio-loud broad-line AGN. Very radio-loud NLS1s (with R >100) are extremely rare.
- In the radio regime, most RL NLS1s are compact, of steep spectrum, and not variable.
- The optical and X-ray properties of the radio-louds (emission-lines, spectral shapes, luminosities, accretion rates, etc.) are similar to radio-quiet NLS1s in general (Fig. 3); even though some radio-louds show spectacular X-ray flaring behavior, and extremely blueshifted [OIII] emission-line components.
- Black hole (BH) masses of the RL NLS1s are at the high-mass end of NLS1s, and in a previously rarely populated regime of the M_{BH}-R diagram (Fig. 2).
- We do not find strong positive evidence for beaming in most sources (with 2-3 exceptions), and no evidence for strong orientation effects in NLS1s.
- Accretion mode, spin, and perhaps (BBHs in) the host galaxies might be factors to explain the fact that radioloudness among NLS1 galaxies is relatively rare.

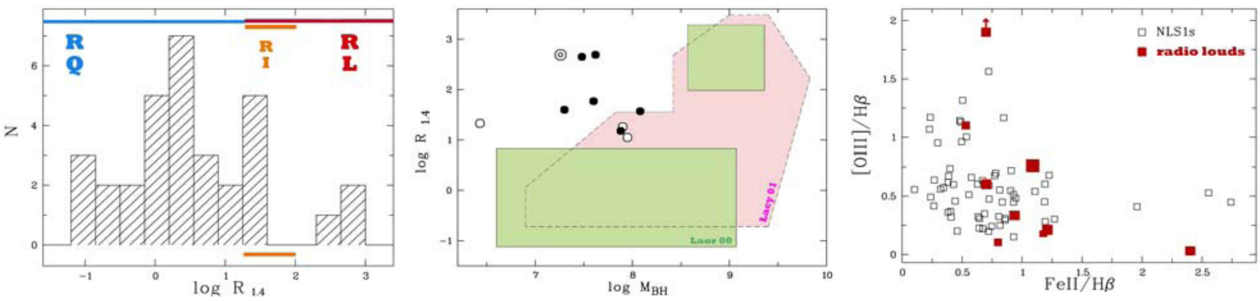

Fig. 1,2 & 3, from left to right: (1) distribution of radio indices, (2) black hole masses M_{BH} of radio-loud NLS1s with good-quality optical spectra, (3) distribution of radio-louds in the FeII-[OIII] diagram (red squares; square size codes radio-loudness), compared to a large sample of radio-quiet NLS1s.

References:

- Komossa, S., et al. 2006a, AJ 132, 531
- Komossa, S., et al., 2006b, ApJ 639, 710

S. Komossa, W. Voges, S. Mathur, D. Xu, et al.

The AGN content of the COSMOS

We present the multiwavelength properties (optical to IRAC) of pointlike X-ray sources selected from the complete XMM-COSMOS X-ray catalog (Hasinger et al. 2007), as a first step to understand the nature and the physical properties of obscured and unobscured AGN

Method:
We collected all the available multifrequencies data for our sources, namely: optical photometry (from multiband Subaru data, Capak et al. 2007), IR photometry (from K-band and IRAC observations, Capak et al. 2007, Sanders et al. 2007), morphological information (from ACS imaging, Leauthaud et al. 2007) and spectroscopic information (from the IMACS and zCOSMOS campaigns, Trump et al. 2007, Lilly et al. 2007).
Results:
We found that for 80% of the counterparts there is a very good agreement between the spectroscopic classication, the morphological parameters as derived from ACS data, and the optical infrared colors: the large majority of spectroscopically identified broad BL AGN have a point-like morphology on ACS data, blue (red) optical (IRAC) colors in color-color diagrams, and an X-ray to optical flux ratio typical of optically selected quasars. Conversely, sources classied as NL AGN or normal galaxies are, on average, associated with extended optical sources, have significantly redder (bluer) R-K (IRAC) colors and span a larger range of X-ray to optical flux ratios.
Here we present two examples from our multicolor analysis.

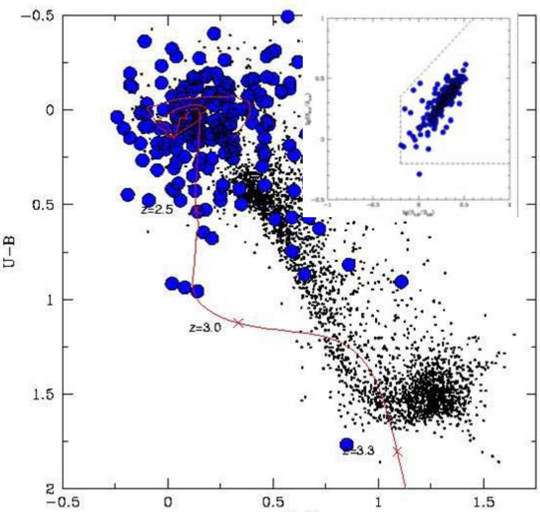

U-B vs. B-V diagram for all field objects (small black points) classified as point-like in the ACS catalog. The locus occupied by stars is very well defined in this diagram (two densely populated regions in the blue and red parts of the sequence). Most of the points with U-B<0.3 are expected to be AGN at z≤2.3. Overplotted as blue symbols are the X-ray sources, spectroscopically confirmed BL AGN. The expected track of quasars from redshift 0 to 3.5 in this color-color diagram is also reported. It is quite reassuring that the majority of the X-ray selected BL AGN occupy the classical QSO locus and would have been selected as outliers from the stellar locus in this color-color plot. The small inset show the BL AGN sample in an IRAC color-color diagram: our type 1 objects lie in the region where most of the AGN selected on the basis of a steep, red power-law SED are distributed (dashed lines).

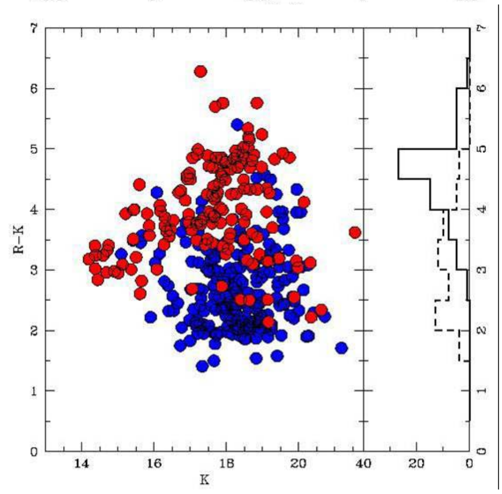

R-K vs. K-band magnitude for BL AGN (blue symbols) and sources Spectroscopically identified ad as NOT BL AGN. A significant difference of R-K distribution for the two classes is present: while the widths of the two distributions are similar (σ~0.8), "red" objects are preferentially associated with NOT BL AGN, while "blue" objects are preferentially associated with BL AGN. We have then investigated the distribution of R-K colors as a function of the X-ray hardness ratio (HR). The hardest sources (HR>-0.3, solid histogram in the right part of the plot) are mostly associated with red and very red objects (R-K>4), indicating an excellent consistency between optical obscuration of the nucleus as inferred from optical to NIR colors, and the presence of X-ray obscuration as inferred from the HR. Conversely, sources detected only in the soft band (HR=-1, dashed histogram) have preferentially blue R-K colors. typical of those of optically selected, unobscured quasars.

References:
• FIGURES and RESULTS updated from: Brusa M. et al., 2007, ApJS special issue, in press (September 2007 issue)
• All the other papers can be found in the COSMOS ApJS special issue

Marcella Brusa and the XMM-COSMOS team

Self-Gravitating Warped Disks Around Supermassive Black Holes

Many galaxies, including our own, contain disks of gas and probably stars surrounding their central supermassive black hole (SMBH) [1,2]. These disks might be relevant for the classification of galactic nuclei in case they obscure the central activity [3], and/or for the paradox of young stars in the vicinity of a SMBH [2]. We search for steadily precessing warped equilibrium configurations for such disks, considering the influence of the black hole and the self-gravity as the only acting forces. We investigate whether these equilibria are stable by perturbation theory and time integration. We show that stable, highly warped disk configurations exist for disk masses between 10^{-3}-$10^{-1}M_{bh}$, and determine how they scale with the disk parameters and the mass of the black hole.

The Model & Equilibria: We adopt a model developed for polar ring galaxies as in [4]. The disk is treated as a collection of concentric circular rings, which are under the influence of the central SMBH and their mutual gravitational attraction. Equilibrium is obtained by setting the torque around line of nodes(LONs) to zero for each of the rings, in which case the disk precesses as a rigid body.

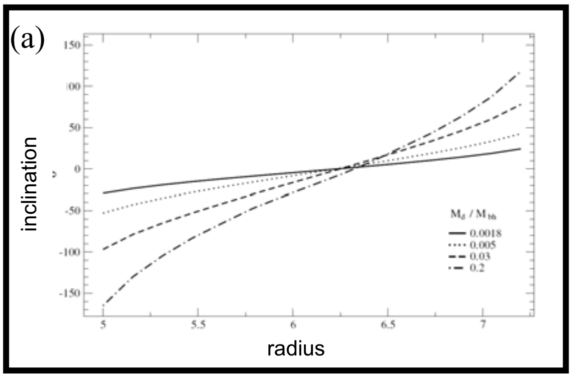

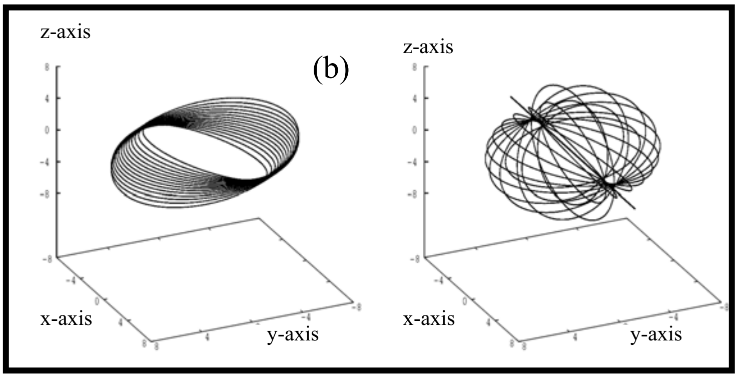

(a) Disk inclination as a function of radius for different disk-to-black hole mass ratios. The degree of warping increases with increasing mass ratio. (b) 3D views of the disks with M_{disk}= 0.0018 M_{bh} (left), and M_{disk}=0.2 M_{bh} (right). As the mass ratio increases, the central region becomes obscured from most lines-of-sight.

Stability of Equilibrium: Figure (a) above shows the disk configurations for the minimum and maximum stable mass, as obtained from perturbation analysis. Figures below show examples of time integration results.

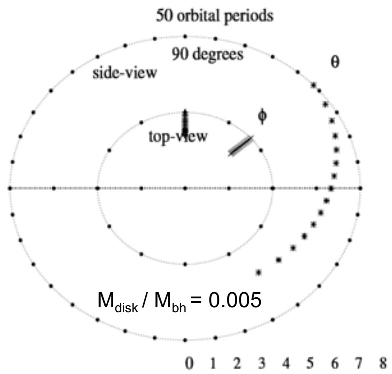

Time evolution of warped disks: (+)'s show the initial configurations, (x)'s after 50 orbital periods. Symbols between the outermost and the innermost circles depict the disk inclination versus radius as shown on the horizontal scale, while the inner region shows azimuthal angle versus radius/2. All rings share the same LONs after 50 orbital periods, hence these disks are stable.

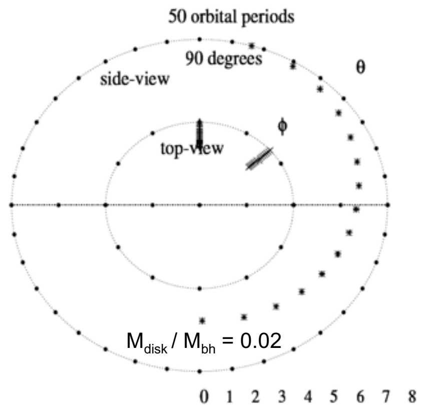

References:

[1] Herrnstein et.al., ApJ, **629**,719 (2005)
[2] Genzel et.al., ApJ, **594**, 812 (2003)
[3] Nayakshin, S., MNRAS, **359**, 545 (2005)
[4] Arnaboldi, M., Sparke, L., AJ, **107**, 958 (1994)

A. Ulubay-Siddiki, O. Gerhard & M. Arnaboldi

A deep XMM-Newton survey of M31

A deep survey of the large local-group spiral galaxy M31 is a milestone project for X-ray astronomy, as it allows a detailed X-ray inventory of an archetypal low-star-formation-rate galaxy like our own. Following our interesting results from an analysis of archival XMM-Newton observations, we were granted a deep homogeneous XMM-Newton survey of M31 as a large program which - at a limiting point source luminosity of 10^{35} erg/s - will include all active X-ray binaries and cover the entire galaxy. A first quick-look analysis showed that some of the pointings were affected by high background and have been reapproved in XMM-Newton AO-6. A first image and detection results are presented.

For our analyses we use five energy bands (0.2-0.5, 0.5-1, 1-2, 2-4.5, 4.5-12 keV), defining four hardness ratios from adjacent energy bands, and all EPIC instruments to create images and do source detection. In the 15 additional pointings of the survey about 1000 new sources are found. With the sources in the archival and the re-observations in AO-6, we will detect about 2000 X-ray sources in the FOV of M31, that will be classified by their X-ray hardness ratios and by correlations with data from other wavelength bands. Optical follow up observations are proposed.

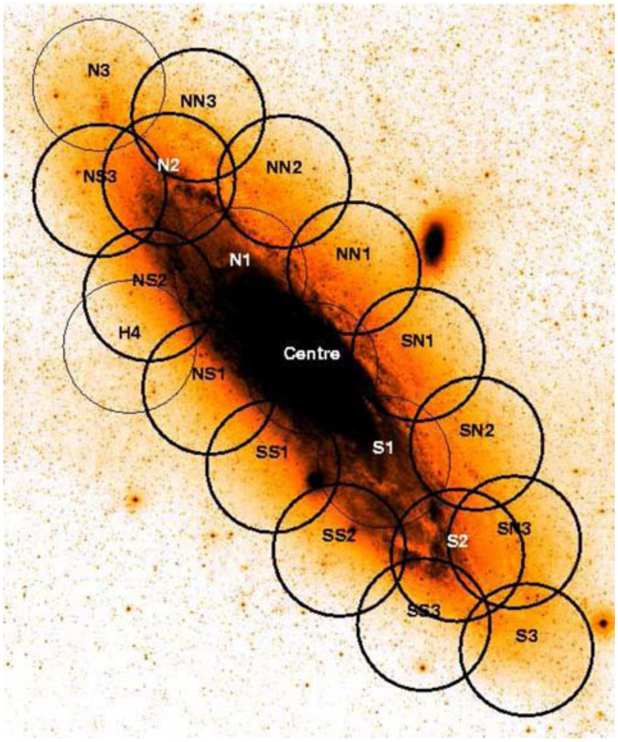

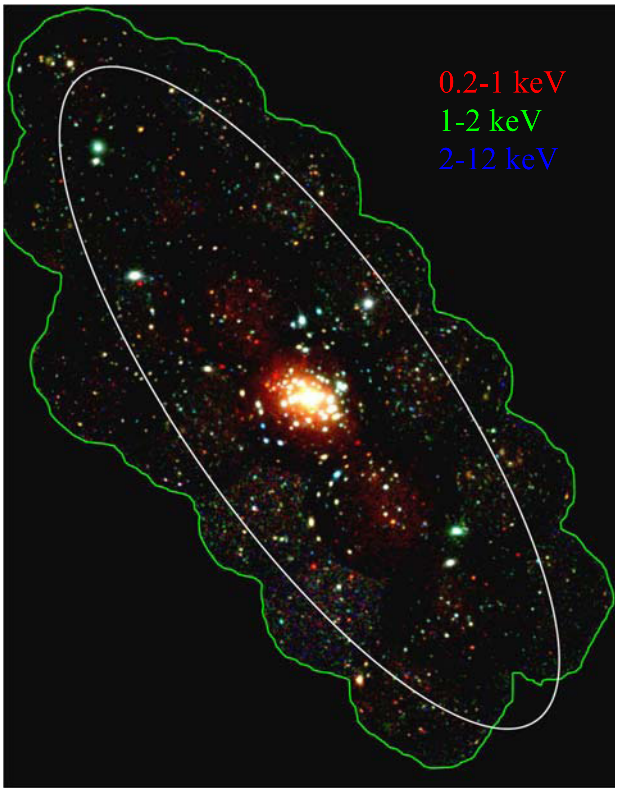

The left panel shows a deep optical image of M31 overplotted with the XMM-Newton fields of the survey. Covered area of individual EPIC observations is approximated by circles with 14' radius. Newly observed fields of the survey are marked as bold. The right panel shows a three-colour XMM-Newton EPIC low background image combining PN, MOS1 and MOS2 of the new and archival data. Red, green and blue show the 0.2-1, 1-2 and 2-12 keV bands respectively. The optical extent of the galaxy is indicated by the D_{25} ellipse. The image is smoothed with a Gaussian of 20" FWHM. The green line indicates the boundary of the observed area. Observation S3 totally drops out due to high background. In some observations individual noisy MOS1 and MOS2 CCDS are omitted.

H. Stiele, V. Burwitz, M. Freyberg, J. Greiner, F. Haberl, W. Pietsch, G. Sala

The Superwind of NGC 253 with XMM-Newton

We present a study of the nuclear outflow of the starburst galaxy NGC 253 with XMM-Newton. We analyzed spectra from different regions of the outflow with different distance to the starburst nucleus that drives this superwind. We derived temperatures, electron densities, the ionization mechanism and the spatial distribution of several elements.This is the first time that the hot wind fluid has been directly detected in X-rays.

The edge-on (i = 78.5°) galaxy NGC 253 is one of the best nearby (2.58 Mpc) paradigms of a nuclear starburst galaxy, where a superwind emanates from its nuclear region. This outflow is driven by the wind of hot stars and supernovae that frequently explode in this region. First results from XMM-Newton data were published by Pietsch et al. (2001, A&A, 365, 174). We here take a closer look at the Reflection Grating Spectrometer (RGS) spectra (for more details see Bauer et al., 2006, astro-ph/0610302).

We obtained spectra (cf. Fig. 1, right) from different regions along the outflow with the RGS. The spectra change with distance from the nucleus; emission lines at high energies weaken in intensity while lines at lower energies get stronger. From emission line ratios we derived temperatures for different regions and elements. The temperature ranges between 0.21 and 0.79 keV. The Fe XVII line ratio shows that the plasma is predominantly collisionally ionized; in region SE 1 we also see an indication for a plasma that is not in equilibrium. Here the Fe XVII line ratio is inverted either because the plasma is underionized or due to delayed recombination of Fe XVIII. Electron densities range between 0.1 cm^{-3} in the centre and 0.03 cm^{-3} in the outflow.

We also produced narrow emission line images from the RGS data. The image in the O VIII line (Fig. 1, left, inlet) is the only line image that shows the morphology of an outflow. We see a clumpy distribution that is not limb brightened and conclude that this emission originates from the hot wind fluid.

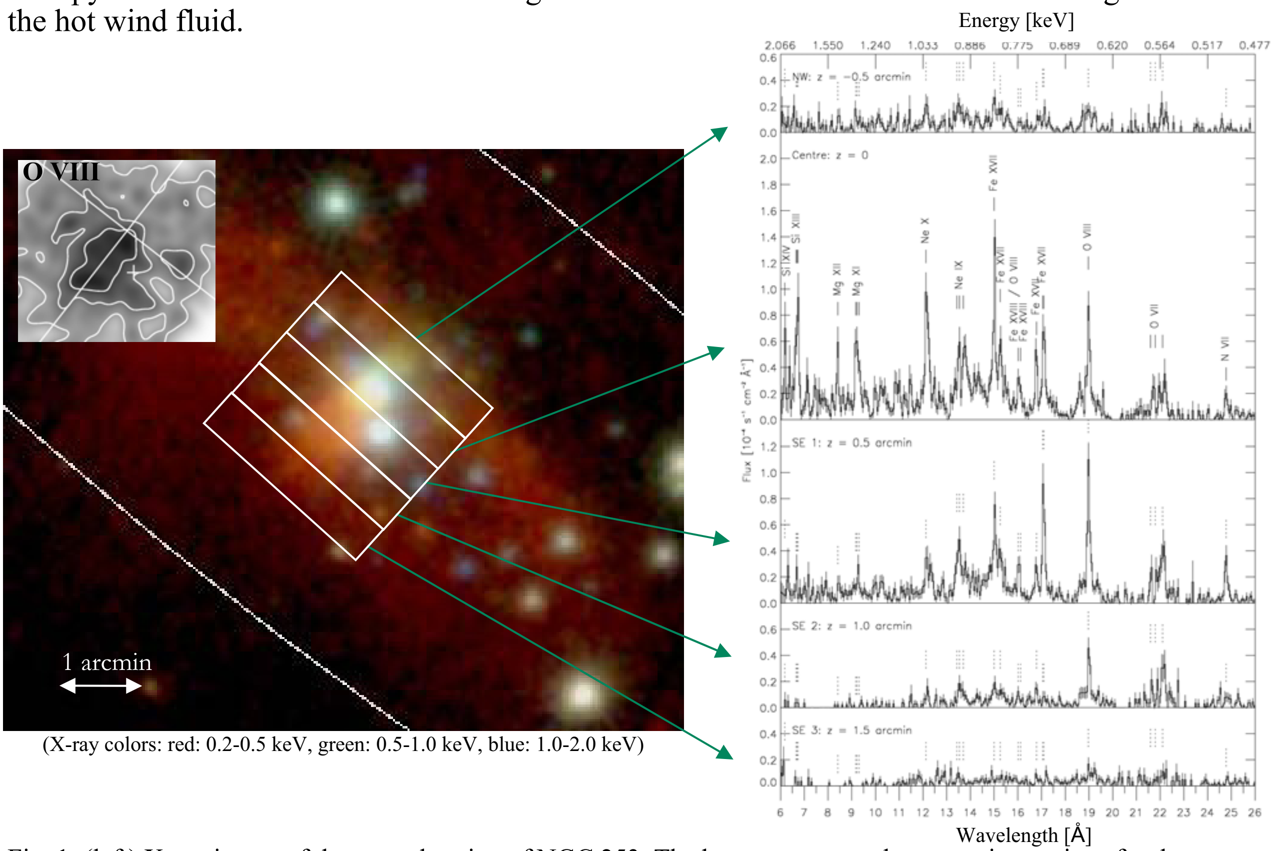

(X-ray colors: red: 0.2-0.5 keV, green: 0.5-1.0 keV, blue: 1.0-2.0 keV)

Fig. 1: (left) X-ray image of the central region of NGC 253. The boxes represent the extraction regions for the spectra and the D25 ellipse is indicated. The inlet is an images in the O VIII emission line with the same scale. (right) Spectra of different regions along the outflow.

M. Bauer, W. Pietsch

A Multiwavelength Map of NGC 1365

We present results from a new multiwavelength study of the central 1-2 kpc of NGC 1365. NGC 1365 is a nearby barred spiral galaxy (D=21Mpc) with a strongly variable and heavily absorbed active nucleus, a nuclear starburst ring, and a number of X-ray bright point sources. Our ultimate goal is to characterize the processes that give rise to the observed X-ray (Chandra and XMM-Newton), optical/IR (HST, NTT, VLT), and radio (ATCA) emission. In addition, we use the X-ray observations to study the spectral and photometric variability of NGC1365-X1 ─ one of the most variable ultraluminous X-ray sources.

Fig 1. Smoothed Chandra contours overlay the FORS2-VLT image of NGC1365 shown on the right. The extended central X-ray emission is associated with the nuclear starburst ring and the inner spiral (see Figs. 2 & 3); while the majority of the X-ray point sources, which loosely follow the spiral structure, are likely X-ray binaries within the galaxy. NGC 1365-X1 in particular, is a highly variable ultraluminous X-ray source (ULX) whose luminosity has varied by a factor of 40 (see Fig 5. below) over a decade.

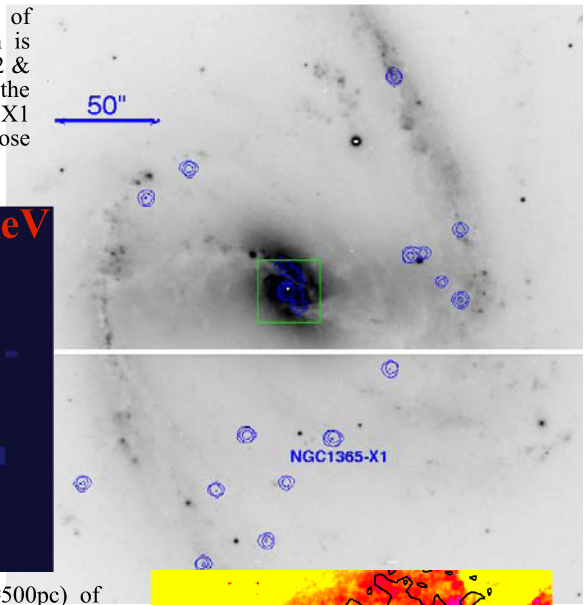

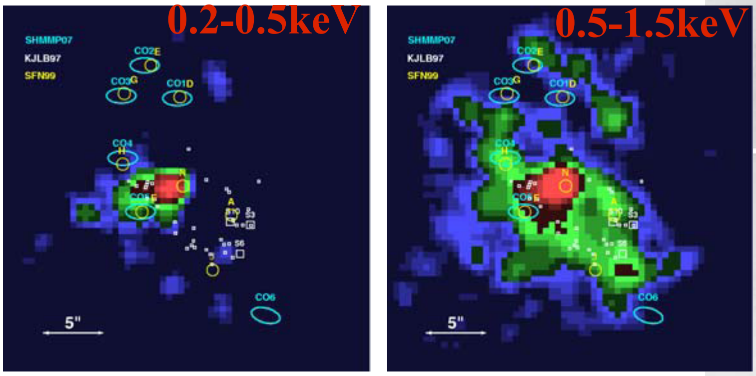

Fig 3. The central region (5″≈500pc) of NGC 1365 imaged with Chandra in three energy bands. The circum-nuclear starburst ring is traced by individual hotspots in the radio (ATCA, yellow circles; SFN99), super-star clusters in the optical (HST, white squares; KJLD97), and molecular emission ($C^{12}O$, cyan ellipses; SHMMP07). The softest X-ray emission is concentrated in the direction of the radio jet (radio spot F) and traces the highly-ionized outflow cone (HL96). The hardest X-ray emission traces well the starburst ring, while the 0.5-1.5keV emission traces the full inner spiral.

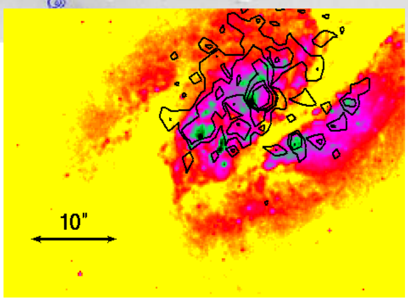

Fig 2. HST WFPC2 image of the inner spiral. The contours represent the Chandra 0.3-10keV emission.

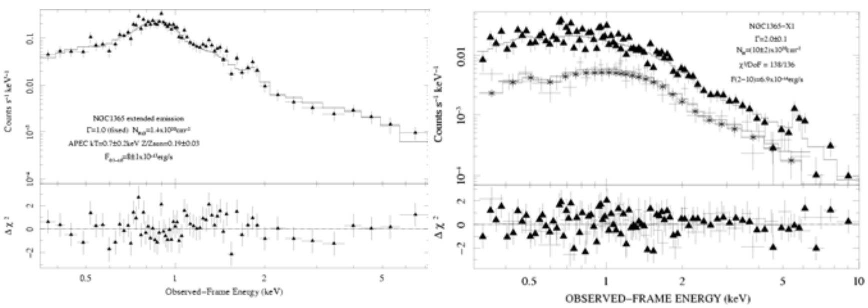

Fig 4. *Left:* NGC 1365 extended emission Chandra spectrum modelled with a 0.7keV thermal plasma with subsolar abundance (APEC model in XSPEC, $L_{0.3\text{-}10}$=2.3x10^{40}erg/s) and power-law emission dominating above 2keV ($L_{0.3\text{-}10}$=2.0x10^{40}erg/s). *Right:* The best NGC1365 X-1 XMM-Newton spectrum modelled with an intrinsically absorbed ($N_{H,i}$=10±2x10^{20}cm^{-2}) power-law with photon index Γ=2.0±0.1.

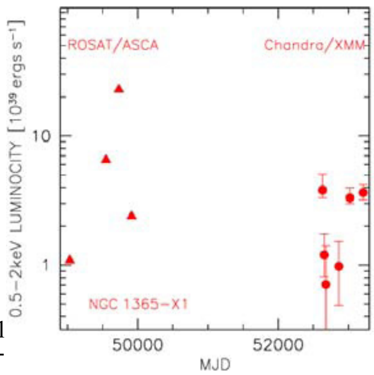

Fig 5. Soft band luminosity variability of NGC 1365-X1.

•**References:**
•Hjelm & Lindblad 1996, A&A, 305, 727 [HL96]
•Sakamoto et al. 2007, ApJ, 654, 782 [SHMMP07]
Kristen et al. 1997, A&A, 328, 483 [KJLD97]
Stevens et al. 1999, MNRAS, 306, 479 [SFN99]

Iskra Strateva, Stefanie Komossa

Mid Infrared diagnostic of LINERs

We report SPITZER results from the first MIR spectroscopic study of a comprehensive sample of 33 *low-ionization-nuclear-emission-line-region* galaxies (LINERs).We compare the properties of two different LINER populations: IR-faint LINERs and IR-luminous LINERs. We show that their ionization sources can be easily distinguished by their MIR spectra in different ways.

INTRODUCTION

Optical spectra of LINERs are characterized by enhanced narrow emission lines of low-ionization species. At least one third of galaxies in the nearby Universe exhibits LINER spectra. Nevertheless, the nature of their ionization sources is still matter of debate. Some LINERs seem to be powered by accretion onto a massive black hole at low rate and for this reason they are believed to constitute the low-luminosity end of the AGN class. On the other hand, other LINERs can be explained with excitation by a nuclear starburst or by shock heating. Determining which fraction of LINERs are low luminous AGN and which fraction is powered by other ionization processes, is crucial for understanding the growth history in central black holes and the relation between AGN and galaxy formation/evolution. Any observational tool capable to distinguish between these two LINER categories is therefore very important, in particular if LINERs at high z are as numerous as LINERs in the nearby Universe.

RESULTS

Our sample was observed with IRS on board of SPITZER. Our main results are the following.

=The SEDs of the two LINERs populations are different. Fig.1 shows IR bright and IR faint averaged spectra, with the latter further divided into the three subgroups. IR bright LINERs show starburst-like emission, i.e. strong PAHs and

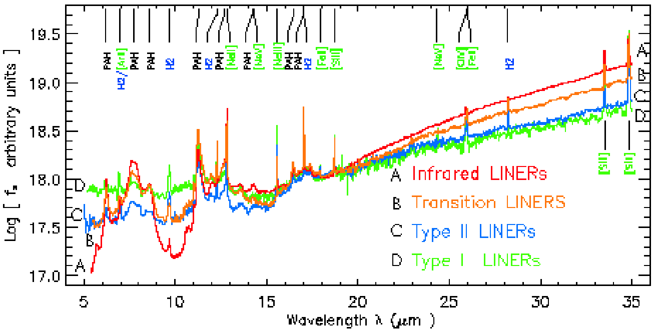

Figure 1.

silicate absorption, while faint IR sources are much bluer, have weaker 5-8 micron PAH emission but stronger 11.2 PAH micron emission.

Fig. 2b shows the 6.2/11.2 μm *versus* the 12.7/11.2 μm PAH emission ratios. IR faint LINERs have a 12.7/11.2 (and 6.2/11.2) lower than IR-bright LINERs. Since these PAH ratios are believed to increase with PAH ionization degree, this result suggests a less ionizing environment in IR-faint LINERs than in IR-bright ones.

=The two LINER populations also occupy two different regions of the Fe[II]26.0/[OIV]25.9 vs. [OIV]25.9/[NeII]12.8 diagnostic diagram (Fig. 2c) presented by Lutz et al. (2003). IR bright sources all lie on the linear relation connecting starburst and Seyfert galaxies, which might be explained by a minor AGN contribution in addition to the star-forming regions. The IR faint LINERs are clearly off this line and lie in a region populated by SNRs which might indicate that shock heating processes play an important role in these sources.

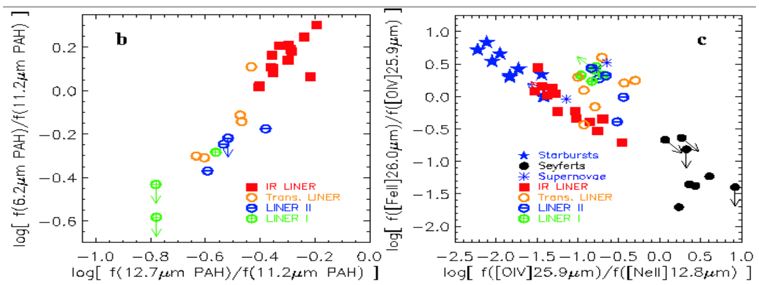

Figure 2

References:
- Lutz, D., et al., 2003, A&A, 409, 867
- Sturm et al. 2006, ApJL, 653, L13

A.Contursi, E.Sturm, D. Rupke,D.-C. Kim,D. Lutz,H. Netzer,R. Genzel,M. Lehnert, L.J. Tacconi,D. Maoz,J. Mazzarella,S. Lord,D. Sanders, and A. Sternberg

Bulges and the Bimodalities in Galaxy Properties

We show that the type of bulge a galaxy has predicts where that galaxy will fall in the red-blue and structural galaxy dichotomies. Galaxies with pseudobulges (or no bulge) lie in the blue cloud and have lower global Sérsic index and higher central surface brightness, while galaxies with classical bulges lie on the red sequence, irrepective of bulge-to-total ratio. Thus, the location in the bimodality reflects differring evolutionary paths of the whole galactic system – not merely different emphasis of the disk and bulge subcomponents.

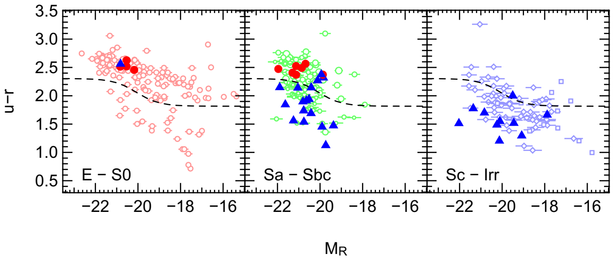

Figure 1. The location of three different galaxy populations is shown in color magnitude space, from left to right: early-type (E-S0), intermediate-type (Sa-Sbc), and late-type (Sc-Irr). Galaxies identified as having pseudobulges are represented by filled triangles, galaxies with classical bulges are shown as filled circles. Galaxies without bulge identification are shown as open symbols for comparison. The dashed line separates the red sequence from the blue cloud.

The global colors and structural properties of galaxies have been shown to follow bimodal distributions. Galaxies separate into a "red sequence", populated prototypically by early-type galaxies, and a "blue cloud", whose typical objects are late-type disk galaxies. Intermediate-type (Sa-Sbc) galaxies populate both regions. It has been suggested that this bimodality reflects the two-component nature of disk-bulge galaxies. However, it has now been established that there are two types of bulges: "classical bulges" that are dynamically hot systems resembling (little) ellipticals, and "pseudobulges", dynamically cold, flattened, disk-like structures that could not have formed via violent relaxation. Alas, given the different formation mechanisms of these bulges, the question is whether at types Sa-Sbc, where both bulge types are found, the dichotomy separates galaxies at some value of disk-to-bulge ratio, B/T, or, whether it separates galaxies of different bulge type, irrespective of their B/T.

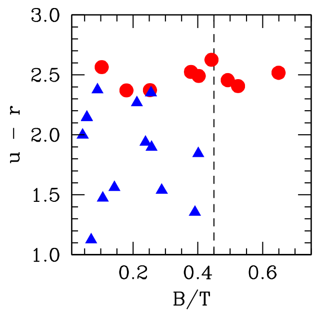

Figure 2. The distribution of bulge-to-total ratios, B/T, of intermediate type (Sa-Sbc) galaxies with pseudobulges (blue triangles) and classical bulges (red filled circles) with respect to $u-r$ color.

We identify classical bulges and pseudobulges morphologically in HST images of RC3+SDSS galaxies. We show that (1) The red – blue dichotomy is a function of bulge type: at the same B/T, pseudobulges are in globally blue galaxies and classical bulges are in globally red galaxies (Figure 1, Figure 2). (2) Bulge type also predicts where the galaxy lies in other dichotomous global structural parameters: global Sérsic index and central surface brightness (Figure 3). (3) The red – blue dichotomy is not due to decreasing bulge prominence.

This argues that the type of bulge a galaxy has is a signpost of the evolutionary history of the whole galaxy, and that the location of a galaxy with respect to the bimodality reflects differring evolutionary paths of the whole galactic system. It is not merely a reflection of different emphasis of the disk and bulge subcomponents.

Classical bulges indicate that a galaxy has suffered a major merger (of smaller fragments) in its past. This is more likely to have happened early, in higher-density environemts, when there was still enough gas to subsequently form the disk. Therefore, these galaxies are likely to be red today. Pseudobulges are disk components and therefore indicate a disk-only galaxy. Such a galaxy has not suffered a major merger since its disk formed. This more likely at later epochs, when the merger rate is lower and in low-density environments. Therefore, these are likely to be younger, blue galaxies.

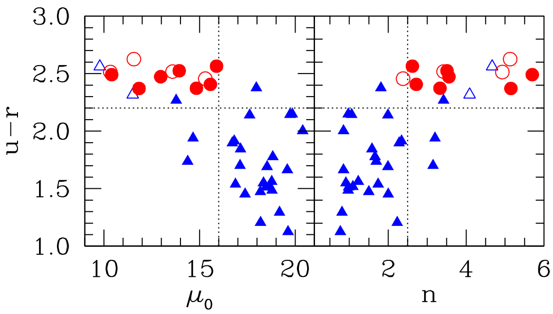

Figure 3. Dependence of bulge type on global structure for all galaxies in the bulge sample. Blue triangles represent pseudobulges, red circles represent classical bulges; S0 galaxies are plotted as open symbols. In both panels the horizontal line denotes $u-g=2.2$. The vertical line in the left panel denotes $\mu_0=16$, and the horizontal line in the right panel denotes $n=2.5$.

Niv Drory & David B. Fisher

Statistical Photometry of MgII-absorbing Galaxies

The photometric properties and the impact parameter distribution of galaxies responsible for the MgII absorption revealed in the spectra of distant QSOs are investigated by means of an **advanced image stacking technique**, applied to a sample of **~2800** systems (0.4<z<1) from the SDSS. The average MgII absorbing galaxy is ~0.5 L* and can be as far as ~100 kpc away from the absorbed line of sight (35 kpc median). On average, stronger absorbers are found closer to their parent galaxies than weaker ones. Also, galaxies associated to stronger absorptions have colours of star forming galaxies, while galaxies associated to weaker systems have colours typical of passive early type galaxies. These results suggest that MgII systems are generated and ejected from galaxies by galactic winds, which are powered by intense star formation.

Although they are difficult to identify in individual images, galaxies linked to MgII absorptions in background QSOs produce systematic excesses of light around those QSOs. Such excesses can be clearly seen by stacking the absorbed QSOs images, after subtracting the light of the QSO itself (PSF), as shown in the images below (the *right panel* displays the tiny residuals with respect to a pure PSF for reference unabsorbed QSOs, due to the QSO hosts).

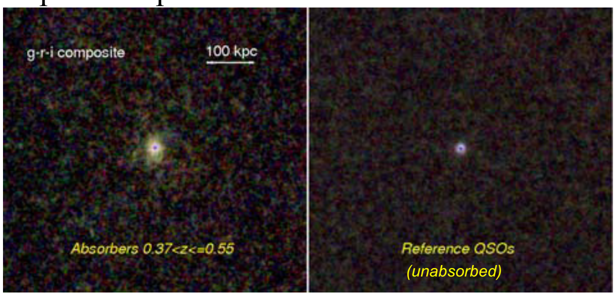

The surface brightness of the light excess is proportional to the light-weighted impact parameter distribution of absorbing clouds around galaxies. The flux in different bands (SDSS g, r, i, and z) can be used to estimate the rest-frame luminosity and Spectral Energy Distribution of the absorbing galaxies.

The overall properties of absorbing galaxies are well represented by a single power-law with index ~-1.5 for the impact parameter distribution, and SED typical of intermediate spirals with a total luminosity of ~0.5 L*(g).
Stronger MgII absorbers are more strongly clustered around their parent galaxies than weaker systems, as shown by the slope of the SB profiles in the two top panels of the figure aside.
Also stronger absorption implies "later" type SED (more star formation and younger stellar populations), while weaker absorptions (EW[2796]<1.1Å) are mainly associated to red, passive galaxies. This is demonstrated by comparing local SED templates (bottom panels) with the observed colours (data points), after shifting and convolving the templates with the actual redshift distribution of absorbers (line and shaded area in the top panels).

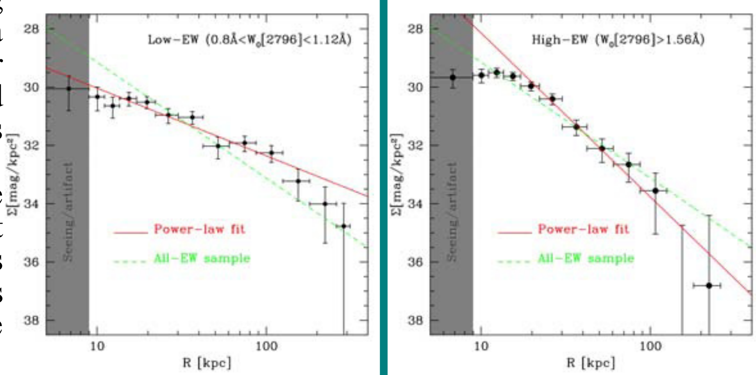

Low-EW High-EW

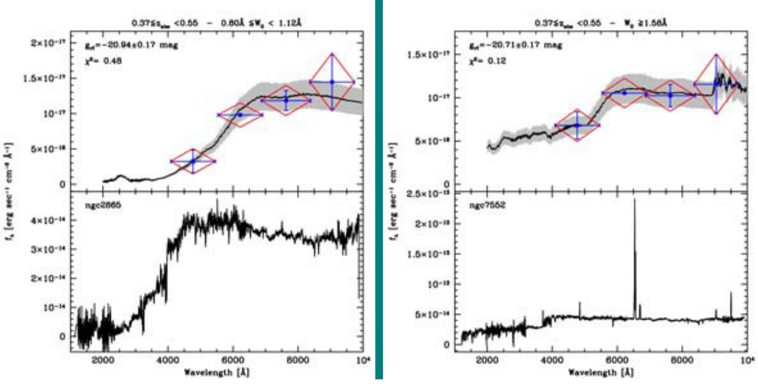

References:
- Zibetti, S. et al., 2005, ApJ, 631, L105
- Zibetti, S. et al., 2007, ApJ, 658, 161

Stefano Zibetti – B. Ménard – D. Nestor – S. Rao – A. Quider – D. Turnshek

Galaxy Dust Properties at 1 < z < 2.5

Fundamental properties of the extinction curve are investigated for a sample of 108 star-forming galaxies at 1 < z < 2.5, selected from the FDF Spectroscopic Survey, the K20 survey, and the GDDS. The sample galaxies indicate dust properties in between those of the SMC and the LMC.

Nearby starburst galaxies do not show a significant, broad dust absorption feature at 2175 Å (the UV bump) in their spectra [1], which is consistent with SMC-type dust properties. Is it possible to find spectral evidence of UV bumps, such as present in the LMC and Milky Way extinction curves, in vigorously star-forming (distant) galaxies? Or do these environments destroy and/or not make the carriers of the UV bump?

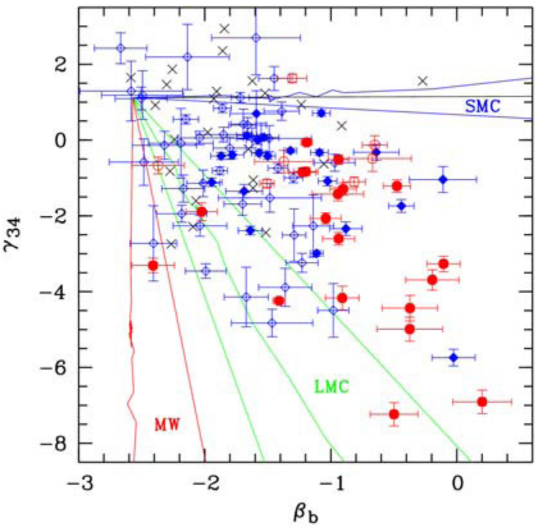

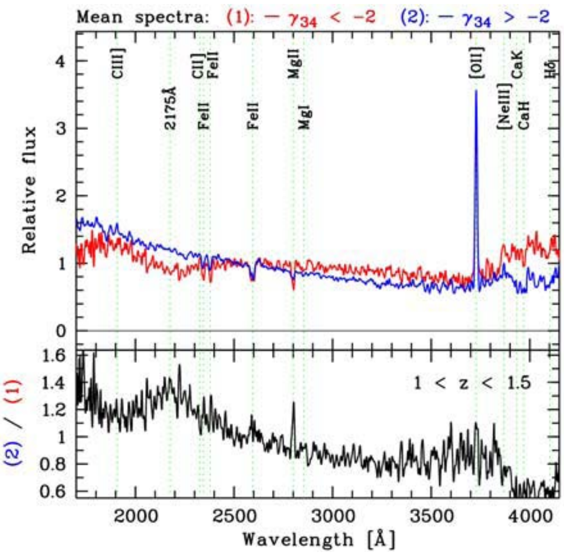

In order to answer this question we study the UV continua of 108 UV-bright galaxies at 1 < z < 2.5, most of them located in the FDF and the CDFS [2,3,4]. The strength of the 2175 Å feature is traced by γ_{34} (the more negative the stronger), while the continuum slope in the UV-bump region is indicated by β_b (the more negative the bluer).

The left figure shows γ_{34} versus β_b for the FDF (blue) and K20 (red) galaxies in the redshift ranges 1 < z < 1.5 (filled symbols) and 1.5 < z < 2.5 (open symbols) in comparison to local starburst galaxies (crosses) and models for SMC- (blue curves, Calzetti law in black), LMC- (green), and Milky Way-type (red) dust. We find a robust evidence for extinction curves in between those of the SMC and the LMC, independent of the redshift. The right figure illustrates the differences in the spectroscopic properties of galaxies at 1 < z < 1.5 showing weak (blue) and strong (red) 2175 Å features.

Galaxies with strong UV bumps at z < 1.5 tend to have lower masses, SFRs, and a more regular morphology (mostly disc galaxies) than those at z > 2. In general, strong UV bumps seem to be associated with a metallicity close to solar, high dust column densities (allowing efficient dust self-shielding), and the presence of a relatively large amount of dust-producing AGB stars.

References:
- [1] Calzetti, D., Kinney, A.L., & Storchi-Bergmann, T. 1994, ApJ, 429, 582
- [2] Noll, S. & Pierini, D. 2005, A&A, 444, 137
- [3] Noll, S., Pierini, D., Pannella, M., & Savaglio, S. 2006, astro-ph/0612080 (proceedings)
- [4] Noll, S., Pierini, D., Pannella, M., & Savaglio, S. 2007, A&A, submitted

S. Noll, D. Pierini, M. Pannella, & S. Savaglio (all MPE)

The Three Types of Galaxy Disk

A study of the surface-brightness profiles of more than 100 S0–Sb galaxies points to a strong connection between bars and the structure of galaxy disks. We find three profile types: pure exponential (Type I); profiles which are steeper beyond a "break radius" (Type II; Freeman 1970); and profiles which become *shallower* beyond a break radius (Type III; Erwin et al. 2005). Most Type II profiles are probably related to the outer Lindblad resonance of bars, and do *not* represent truncations due to star-formation thresholds (common in late-type spirals). Type III profiles are most often changes in disk structure, not excess light from spheroids. They may represent the evolved counterparts of "extended UV disks" seen by GALEX, and are strongly *anti*-correlated with bar strength: the weaker the bar, the more likely the galaxy has a Type III profile.

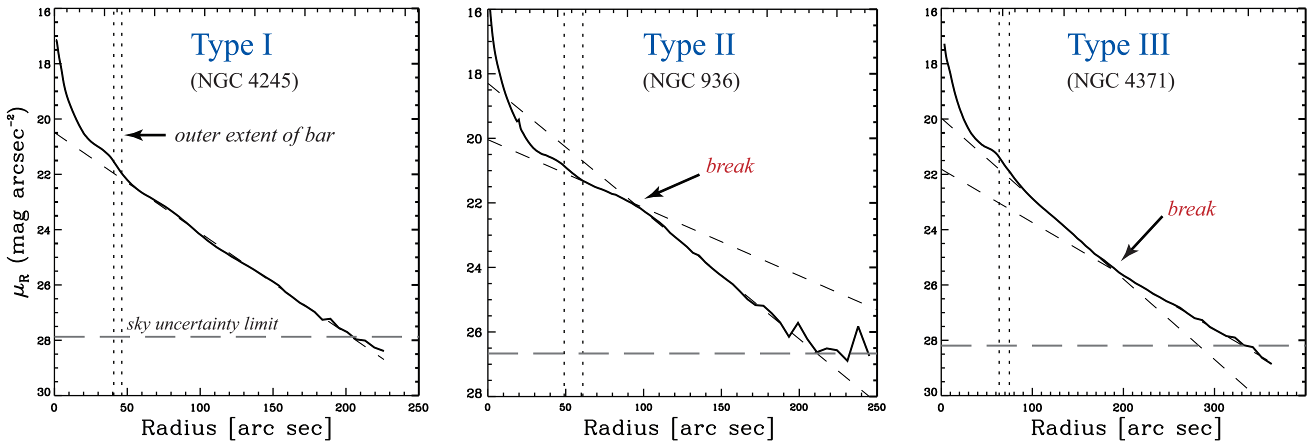

The frequency of profile types in S0–Sb galaxies is: Type I = 32%; Type II = 37%; Type III = 44% (includes galaxies with inner Type II profiles). This compares with frequencies of 11%, 66%, and 33% for late-type spirals (Pohlen & Trujillo 2006). In late types, Type II profiles appear to be mostly due to star formation thresholds; but in S0–Sb disks, Type II profiles are usually associated with outer rings in barred galaxies and may be a result of bar-driven secular evolution.

Most Type III profiles are like NGC 3982 (**right**), with outer light part of the disk, not the spheroid; here, we can see that excess light beyond the break (blue arrow and dashed blue circle) is due to spiral arms. Type III profiles may thus be similar to "extended UV disks" seen by GALEX (e.g., Gil de Paz et al. 2005).

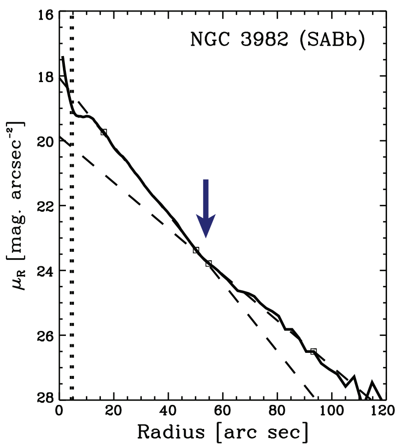

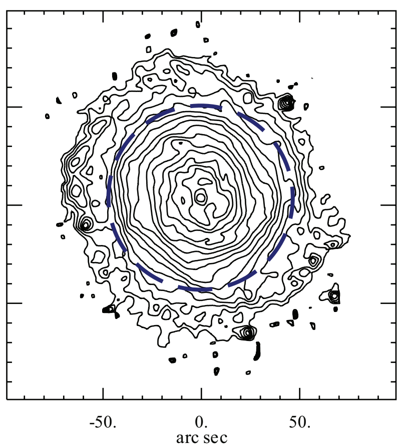

References:
- Erwin et al. 2005, ApJL, 626, L81
- Freeman 1970, ApJ, 160, 811
- Gil de Paz et al. 2005, ApJL, 626, L29
- Pohlen & Trujillo 2006, A&A, 454, 759

Peter Erwin - Michael Pohlen - John E. Beckman

The Halos of Elliptical Galaxies

The complicated intrinsic shape and orbital structure of elliptical galaxies makes it notoriously more difficult to constrain their gravitational potentials and dark matter concentrations in comparison to spiral galaxies. Gerhard et al. (2001) found that their halo core densities were at least 25 times larger than those found in spiral galaxies of the same circular velocity. Romanowsky et al. (2003) however found several elliptical galaxies with more diffuse haloes, contesting the current cosmological paradigm. We aim to address this discrepancy by obtaining a more detailed picture of haloes of elliptical galaxies through the combination of stellar kinematic, planetary nebulae (PNe) and X-ray data. Here we report on the spherical modelling of PNS (Douglas et al., 2007) and SAURON (Emsellem et al., 2004) data for NGC 3379 using NMAGIC (de Lorenzi et al., 2007). Our results confirm that its halo is relatively diffuse or alternatively the galaxy is flattened along the line-of-sight. Modelling of the X-ray luminous galaxy NGC 5846 is currently in progress.

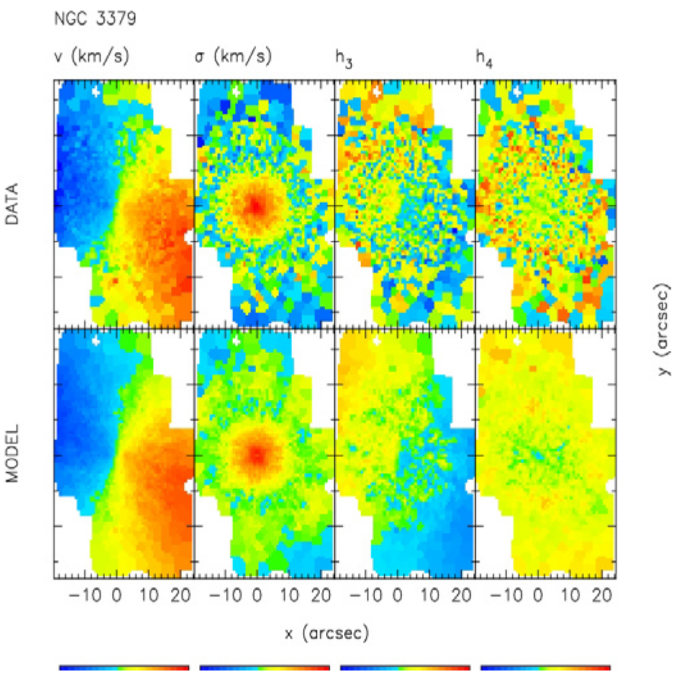

Fig 1: The top panels show SAURON kinematics and the lower panels show the NMAGIC fit to the data.

We construct N-particle models for NGC 3379 using NMAGIC. We combine SAURON data (Fig. 1) and PNS data (Fig. 3), extending to a radius of about 7 R_e. We find that the data is consistent with a more diffuse dark matter halo (Fig. 2, 3).

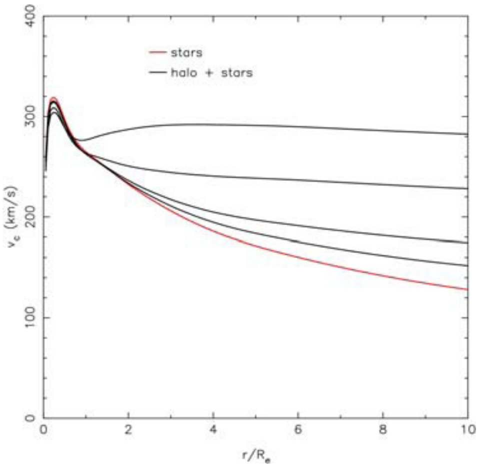

Fig 2: Circular velocity curves for mass models consisting of the stellar mass distribution of NGC 3379 plus various logarithmic dark matter profiles.

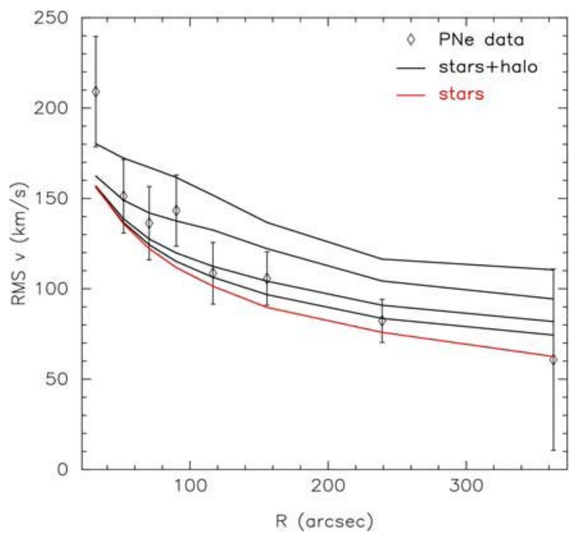

Fig 3: PNe velocity dispersion data for NGC 3379 superimposed with NMAGIC fits using the mass models in Fig. 2.

References:
- Gerhard et al., 2001, AJ, 121, 1936
- Romanowsky et al., 2003, Sci, 301, 1696
- de Lorenzi et al., 2007, MNRAS, 376, 71
- Emsellem et al., 2004, MNRAS, 352, 721
- Douglas et al., 2007, ApJ, in press

Payel Das, Flavio de Lorenzi, Ortwin Gerhard et al.

Modeling Galaxy Observations Using Particles

We have extended the M2M algorithm of Syer and Tremaine for constructing N-particle models of stellar systems to model real observational data. We have implemented this algorithm in a parallel code NMAGIC and carry out a sequence of tests to illustrate its power.

I. NMAGIC (Fig. 1) works by varying the weights w_i of the particles moving in the global potential, until the model fits the observations. The „force-of-change“ is:

$$\frac{dw_i(t)}{dt} \propto -w_i(t)\sum_j K_{ji}\Delta_j(t)$$

K_{ji} is the contribution of particle i to the observable j and Δ_j is a measure of the mismatch to the data.

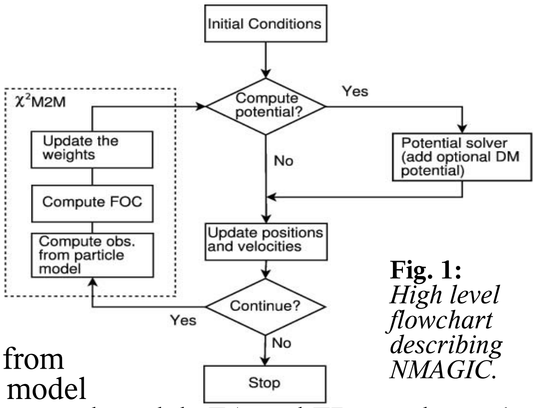

Fig. 1: *High level flowchart describing NMAGIC.*

II. Isotropic Hernquist Model: The aim of this experiment is to recover a spherical isotropic Hernquist (SIH) model using different initial conditions (ICs), made from distribution function (DF). We started with a Plummer (P) model and a different Hernquist model (SIH-2). The final, reconstructed models FA and FB are shown in Fig. 2.

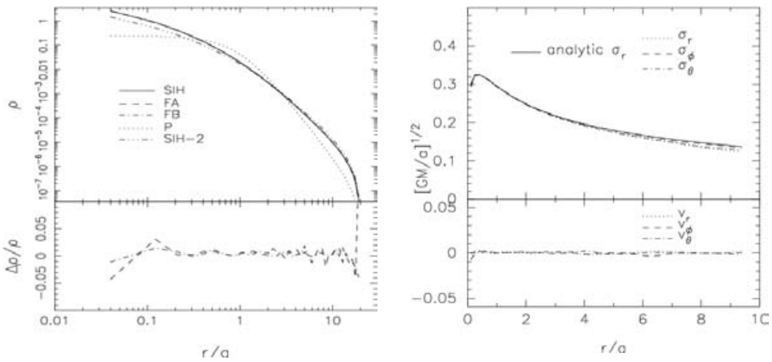

Fig. 2: Top left: *Density profiles. FA and FB reproduce the SIH target perfectly. Bottom left: Relative density deviations. Right: Internal kinematics of model FA. It is very nearly isotropic and has negligible rotation, despite starting from anisotropic ICs.*

III. Oblate 3I Maximum Rotator Model: This experiment shows that we are able to recover a DF with steep gradients, and how the final model depends on the amount of observational data available. Target: Max. rotating 3I Hernquist model (axis ratio q=0.6). ICs: spherical isotropic Hernquist model. Observables: Density and (a) slit or (b) integral field kinematics.

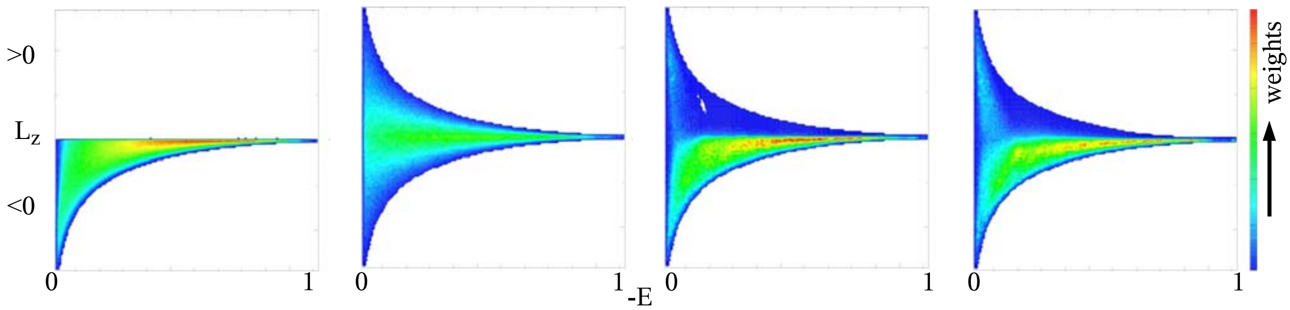

Fig. 3: *Projected weight distributions in the energy-angular momentum plane. From left to right: Target, ICs, model reconstructed from (a), model reconstructed from (b).*

NMAGIC works well, especially in case (b), where the weights of the counter rotating particles have been reduced by a factor ~50.

References:
- Syer D. & Tremaine S. (1996), MNRAS 282
- Gerhard O. E. (1993), MNRAS 265
- van der Marel R. P. & Franx M. (1993), ApJ 407
- Hernquist L. (1990), ApJ 356
- Debattista V. P. & Sellwood J. A. (2000), ApJ 543
- De Lorenzi F. etal (2007), MNRAS 376

F. De Lorenzi, V. P. Debattista, O. Gerhard, N. Sambhus

Polarised infrared emission from SgrA*

Sagittarius A*, the supermassive black hole in the Galactic Centre, shows occasional outbursts of NIR emission. Beginning in 2004, we have been able to detect linearly polarised radiation, giving new insights into the physics behind the infrared light from SgrA*.

Using the NIR camera NAOS/CONICA at the VLT in Chile in polarimetry mode, we were able to observe polarised emission from SgrA* three times (in 2004, 2005, and 2006). The so far most outstanding event was the outburst of May 2006, showing a maximum polarisation of ~40%. A variability on time scales of ~15 minutes could be observed in several parameters like flux, polarised flux, and polarisation fraction. Additionally the polarisation angle showed a spectacular swing of about 70° within 15 minutes at the end of the flare.

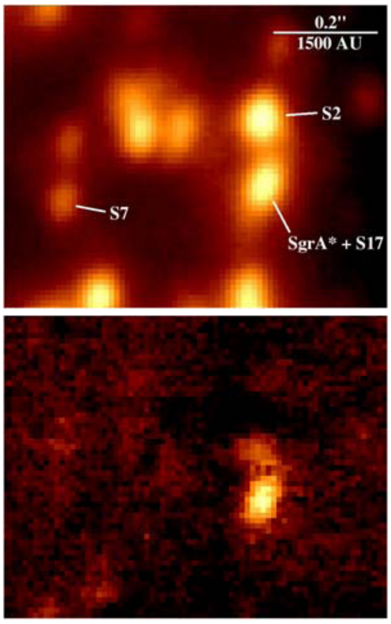

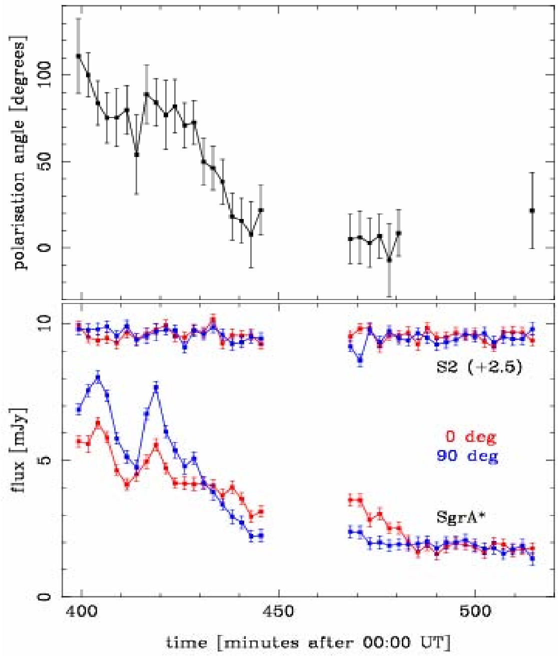

Observations of the polarised flare in May 2006. *Top left*: Sum image of the polarimetric channels 0 and 90 degrees obtained during the flare peak. *Bottom left*: Difference image of these two channels. The residual flux at the position of SgrA* nicely illustrates the strong polarisation (up to ~40%) of the light. *Right*: Evolution of polarisation angle (*top*) and source flux *(bottom)* with time. The strong polarisation and the swing in polarisation angle are clearly visible.

These recent observations allow a deeper understanding of the emission from SgrA*. They support the dynamical emission model of a plasma hot spot orbiting the black hole at (or close to) the innermost stable circular orbit. In this picture a plasma bubble arises from the accretion disk due to infall of matter or magnetic reconnection. This bubble orbits the black hole with a period about 15-20 min, gets sheared, cools down and vanishes after few cycles. But the observed polarimetric properties, especially the time evolution of the polarisation angle, also tell us that a "pure" plasma spot model is probably too simple; there might also be a jet component.

References:
• Genzel R., et al. 2003, Nature, 425, 934
• Eckart A., et al. 2006b, A&A, 455, 1
• Trippe S., et al. 2007, MNRAS, 375, 764

S. Trippe, T. Ott, S. Gillessen, F. Eisenhauer, F.Martins, R. Abuter, R. Genzel

SINFONI in the Galactic Center: Young stars and infrared flares in the central light month

We report on 75 mas resolution, near-IR imaging spectroscopy within the central 30 lt-days of the Galactic center, taken with the new adaptive optics–assisted integral-field spectrometer SINFONI on the ESO VLT. Nine of 10 stars in the central 0.4", and 13 of 17 stars out to 0.7" from the central black hole are B0–B9 main-sequence stars. Based on the 2.1127 µm HeI line width, all brighter early-type stars have normal rotation velocities, similar to solar neighborhood stars. We combine the new radial velocities with SHARP/NACO astrometry to derive improved three-dimensional stellar orbits for six of these ''S stars''. Their orientations in space appear random. Their orbital planes are not co-aligned with those of the two disks of massive young stars 100–1000 from SgrA*. We can thus exclude the hypothesis that the S stars as a group inhabit the inner regions of these disks. They also cannot have been located/formed in these disks and then migrated inward within their planes. We conclude that the S stars were most likely brought into the central light-month by strong individual scattering events. The updated estimate of distance to the Galactic center from the S2 orbit fit is R_0 = 7.62 +/- 0.32 kpc, resulting in a central mass value of (3.61 +/- 0.32) x 10^6 $M_\odot$. We happened to catch two smaller flaring events from SgrA* during our spectral observations. The 1.7–2.45 µm spectral energy distributions of these flares are fit by a featureless, ''red'' power law of spectral index α'= -4 +/- 1 ($S_\nu \sim \nu^{\alpha'}$). The observed spectral slope is in good agreement with synchrotron models in which the infrared emission comes from accelerated, nonthermal, high-energy electrons in a radiatively inefficient accretion flow in the central R ~ $10R_S$ region.

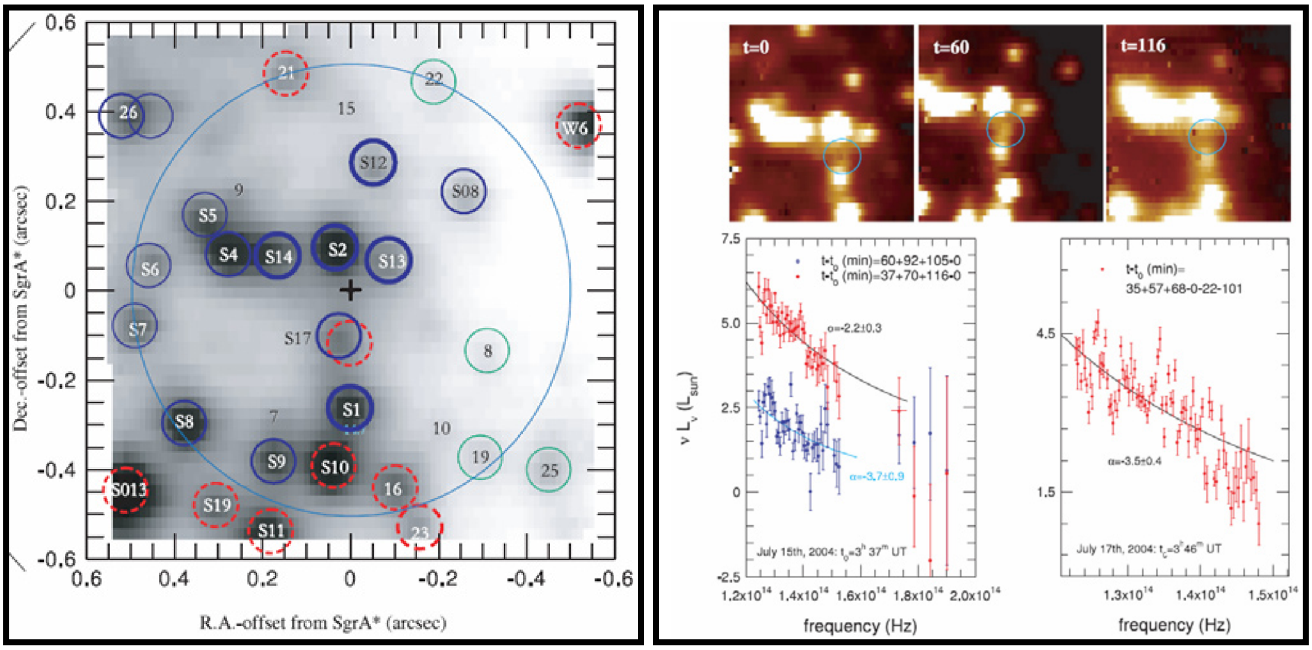

Figure: left: K-band image constructed from the 3D spectral data cube. The central light month is dominated by young, massive, early type stars (blue circles). Right: observation of infrared flares from Sgr A* (top). The near infrared SED indicates synchrotron emission from a radiatively inefficient accretion flow close to the black hole.

References:
• Eisenhauer et al. 2005, ApJ, 628, 246

Eisenhauer, Genzel, Alexander, Abuter, Paumard, Ott, Gilbert, Gillessen et al.

XMM-Newton emission-line imaging of the Galactic centre

X-ray imaging of the central part of our Galaxy with *XMM-Newton* is presented. The images with selected emission-lines (Sxv, FeI, Fexxv and Fexxvi) suggest the composite nature of the diffuse emisison of distinct origins.

We present narrow-band imaging of the Galactic centre region within 12' of SgrA*, obtained from *XMM-Newton* EPIC cameras. The X-ray spectrum of the diffuse emission is characterised by strong emission lines, including the Fe K complex. Fig. 1 shows the broad-band and three narrow-band images centred on Sxv, Fe I and Fexxv, obtained from the total ~360 ks exposure.

The three narrow-band images show clearly different morphology. In general, the North-East side of the image (or the *b*>0 side of the Galactic plane) is brighter and shows complex morphology, while the Fexxv image is smooth and spherical around SgrA*.

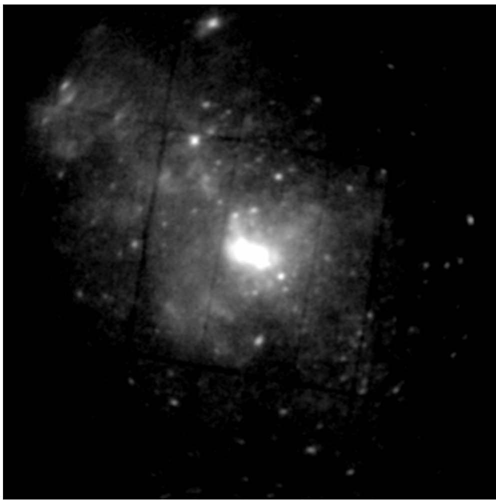

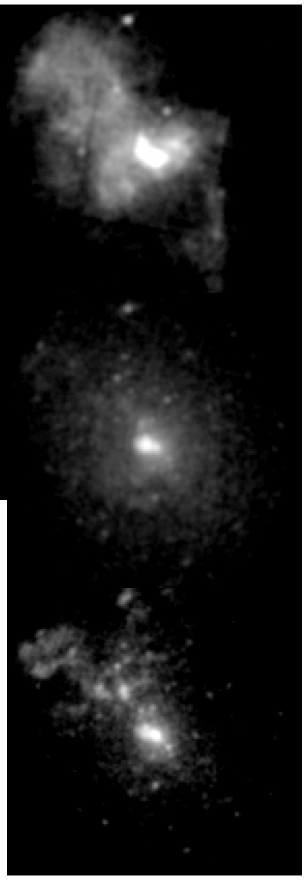

Fig.1: Main picture: The broad band (2.5-7.8keV) image; Side pictures (from top to bottom): The three narrow-band images centred on SXV (2.6keV), FeXVV (6.7keV) and Fe I (6.4keV). The size of each image is 12x12 arcmin^2.

Suggested origin of these emission lines are:

Fe I: this is fluorescence emission from cold gas, illuminated by nonthermal emission, perhaps of the past brightening of the black hole at Sgr A*. It could trace illuminated surface of molecular clouds.

Fexxv: along with Fexxvi, this emission originates from hot gas with T~6x10^{7}K. Its spherical distribution traces the stellar distribution peaking at the Galactic centre, and supports the collective stellar origin (Revnivtsev et al 2006).

Sxv: this line comes from cooler gas with T~(1-2)x10^{7}K, and its complex morphology suggests that it does not originate from unresolved stars but spatially extended gas. The effect of obscuration on the apparent morphology has to be investigated further.

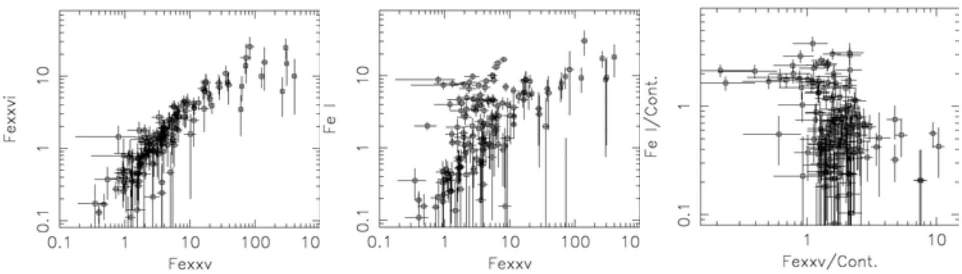

Fig. 2: An analysis of the continuum-subtracted emission-line images from part of the EPIC pn data gives following results. 1) Constant FeXXV/FeXXVI ratio, indicating a constant temperature; 2) Apart from the FeI enhanced regions, FeXXV is usually accompanied by FeI at a similar ratio; 3) Similar equivalent width of FeXXV, suggesting a common mechanism at work. *Note that Sgr A East emits unusually strong FeXXV.*

References:

• Revnivtsev M.,Sazonov S., Gilfanov M., Churazov E., Sunyaev R., 2006, A&A, 452, 169

K.Iwasawa and Y. Tanaka

Direct Observation of the Molecular Torus in NGC1068

We report the first direct observations of the torus in NGC1068 using SINFONI near-infrared integral field spectroscopy. At a resolution of 0.077", we have resolved the molecular gas close around the nucleus and measured its extension, for which a size of 17 x 7 pc is found. Our observations are consistent with the predictions of small and clumpy torus models.

There are several pieces of evidence that support the association of the H_2 morphology with the molecular torus. At first, the orientation of the major axis of the torus ~120 deg is consistent with that of the line of maser spots (Greenhill et al. 1996), the 20mas scale radio continuum in the nuclear component S1 (Gallimore et al. 2004), and the 300K dust emission (Jaffe et al. 2004). Figure 2 shows the map of VLBA 5 GHz radio continuum of the component S1 in contours, with maser positions overplotted. The nuclear radio source S1 marks the location of the central engine and resolves into an extended, approx 0.8 pc long structure oriented nearly perpendicular to the jet axis but more closely aligned to the axis of H_2O maser disk.

Additional evidence comes from the size scale of the nuclear gas, which is remarkably similar to those of static torus models, in particular the more recent clumpy model of Hoenig et al. (2006), for which a size of 15 x 7 pc (diameter) is predicted for the H_2 distribution in this galaxy (Mueller Sánchez et al. 2007a).

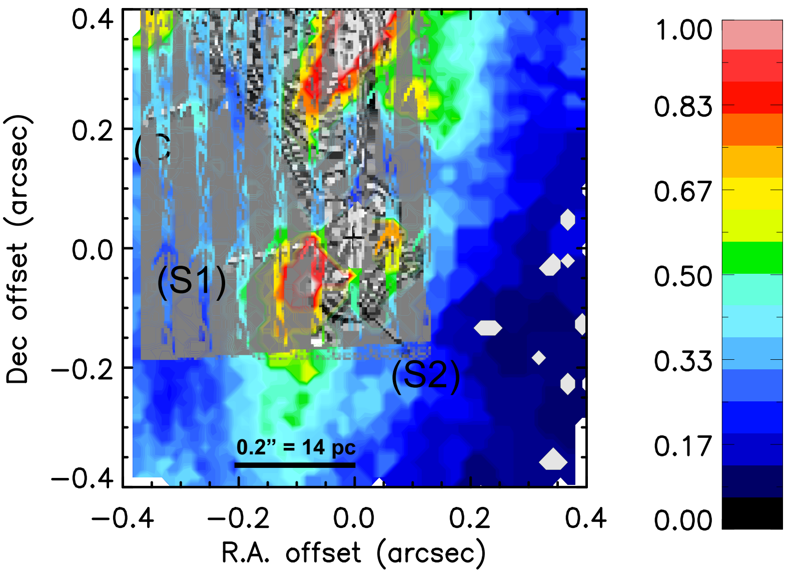

Fig. 1. Morphology of the H_2 1-0S(1) emission in the central 55 pc^2 of NGC1068 with a resolution of 5 pc. The peak of the non-stellar continuum is represented by a cross. The image is smoothed using Voronoi binning. The 5 GHz radio continuum image is overplotted showing the position of the nucleus S1 and the jet-cloud interaction at the position of component C (Mueller Sánchez et al. 2007b).

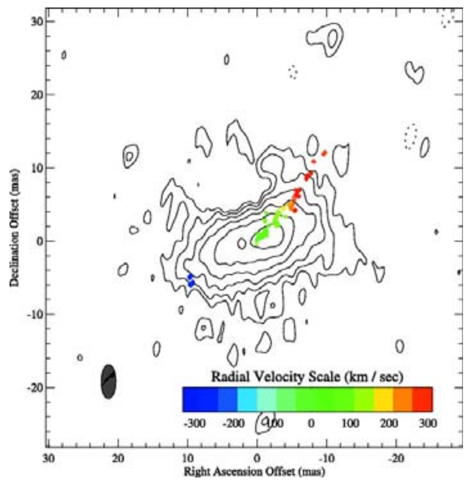

Fig. 2. S1 maser spots and VLBA 5 GHz radio continuum image in contours, showing that the P.A. of the major axis of this component and that of the maser spots is consistent with that of the torus (Fig. 1).

References:

- Gallimore J., Baum S., O'Dea P., 2004, ApJ, 613, 794
- Greenhill L., Gwinn C., Antonucci R., Barvainis R., 1996, ApJ,472, L21
- Hoenig S., Beckert T., Ohnaka K., Weigelt G., 2006 A&A, 452, 459
- Jaffe W., et al., 2004, Nature, 429, 47
- Mueller Sánchez F., et al., 2007a, in prep.
- Mueller Sánchez F., et al., 2007b, in prep.

Mueller Sánchez F., Davies R., Genzel R., Tacconi L., Hicks E., Friedrich S.

A Close Look at Star Formation around AGN

Star formation in the nuclei of 9 Seyfert galaxies has been analysed using SINFONI data with resolutions down to 0.085" (10 pc in some objects). The stellar light profiles typically have size scales of a few tens of parsecs. In two cases there is unambiguous kinematic evidence for stellar disks on these scales. In the nuclear regions there appear to have been recent – but no longer active – starbursts in the last 10-300 Myr. The stellar luminosity is less than a few percent of the AGN in the central 10 pc, whereas on kiloparsec scales the luminosities are comparable. The surface stellar luminosity density follows a similar trend in all the objects, increasing steadily at smaller radii up to ~10^{13} L_{sun} kpc^{-2} in the central few parsecs, where the mass surface density exceeds 10^4 M_{sun} pc^{-2}. These intense starbursts may be Eddington limited and hence inevitably short-lived, implying that they occur in multiple short bursts. The data hint at a 50-100 Myr delay between the onset of star formation and subsequent fuelling of the black hole. The role that stellar ejecta (winds and supernovae) may play in fuelling the black hole is explored.

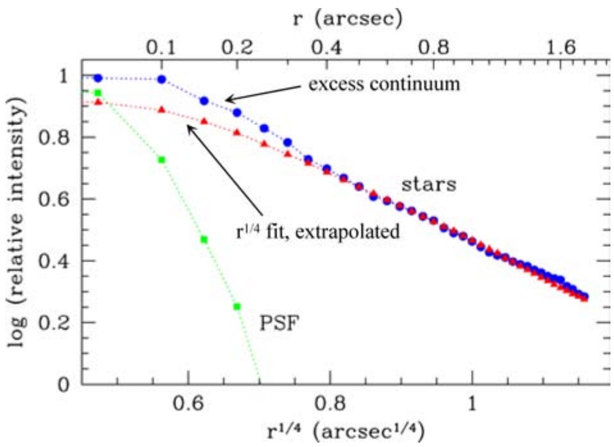

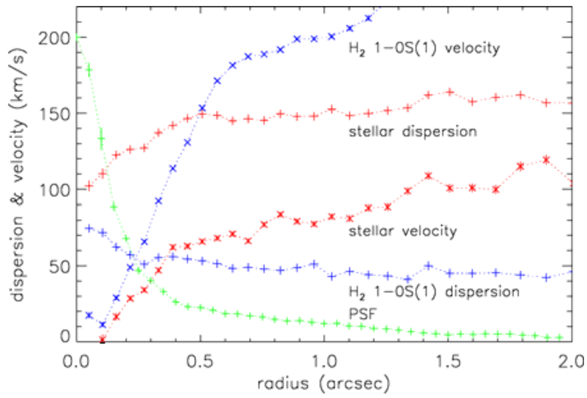

Evidence for the nuclear stellar disk in the central arcsec of NGC1097 comes from the excess stellar continuum (above left) and the drop in stellar velocity dispersion (above right) which together imply a distinct stellar population with distinct kinematics.

The delay between the onset of star formation and the onset of AGN activity is shown at right. Turbulence induced by supernova may halt accretion until the star formation has ceased. Subsequently, winds from AGB stars may provide the necessary fuel.

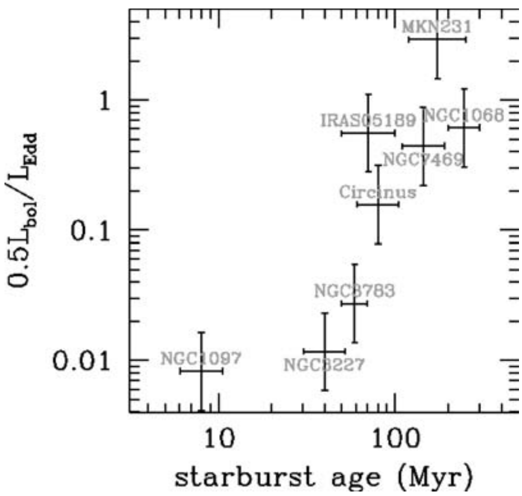

References:
- Davies, Mueller Sánchez, Genzel, Tacconi, Hicks, Friedrich, Sternberg, 2007, ApJ submitted
- Davies, et al., 2006, ApJ, 646, 754
- Mueller Sánchez, Davies, Eisenhauer, Tacconi, Genzel, 2006, A&A, 454, 481
- Davies, Tacconi, Genzel, 2004, ApJ, 613, 781
- Davies, Tacconi, Genzel, 2004, ApJ, 602, 148

R. Davies, F. Mueller Sánchez, R. Genzel, L. Tacconi, E. Hicks, S. Friedrich, A. Sternberg

High z obscured AGN: Spitzer and Mambo view

MAMBO 1.2mm photometry of 24μm bright but optically obscured Spitzer sources indicates warm rest frame infrared SEDs, implying that these galaxies represent a significant population of obscured high redshift AGN.

Using the IRAM 30m telescope, we have obtained MAMBO 1.2 mm photometry of 40 extragalactic sources from the 4 square degree Spitzer First Look Survey that are bright in the mid-IR ($S_{24\mu m}$>1mJy) but optically obscured $\log_{10}(\nu F_\nu 24\mu m/\nu F_\nu 0.7\mu m)>1$. We use these observations to search for cold dust emission, probing the similarity of their spectral energy distributions to star-forming infrared galaxies or obscured AGN. The sample as a whole is well detected at mean $S_{1.2mm}$=0.70±0.09mJy and $S_{1.2mm}/S_{24\mu m}$=0.15±0.03. Seven (three) of the sources are individually detected at >3σ (>5σ) levels. Mean millimeter fluxes are higher for sources with the reddest mid-IR/optical colors.
Optically faint but with relatively low millimeter–to–mid-IR ratios, the typical SEDs are inconsistent with redshifted SED shapes of local star-forming infrared galaxies or redshifted unobscured AGN. They also differ from SEDs of typical high redshift submillimeter-selected galaxies, with the 24μm sources that are individually detected by MAMBO possibly representing intermediate objects. Compared to star-forming galaxies, a stronger but optically obscured mid-IR component without associated strong far-IR emission has to be included. This component may be due to luminous optically obscured AGN. Based on infrared luminosities and first redshift measurements from Spitzer spectra of such obscured 24μm sources, they may represent a significant part of the high redshift luminous AGN population, rivaling QSOs of similar luminosity in number density.
While classical submillimeter surveys detect predominantly star forming objects, the new obscured Spitzer selection identifies an only partly overlapping AGN dominated population.

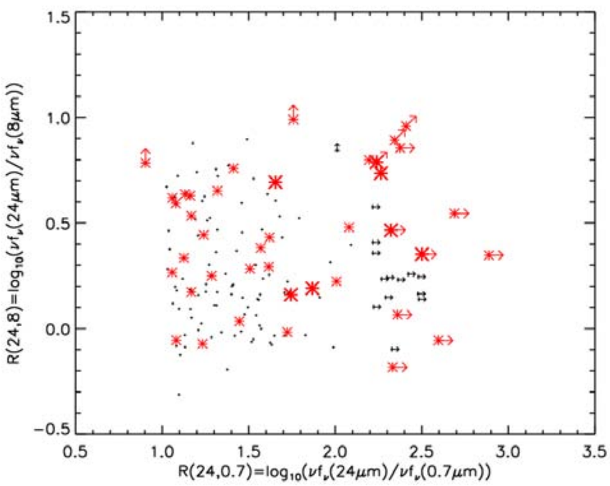

Optical/mid-infrared color-color plot for mid-infrared bright but optically faint 24μm sources from the Yan et al. (2004) Spitzer FLS sample. Small asterisks indicate the sources observed with MAMBO at 1.2mm, big asterisks the ones individually detected at that wavelength

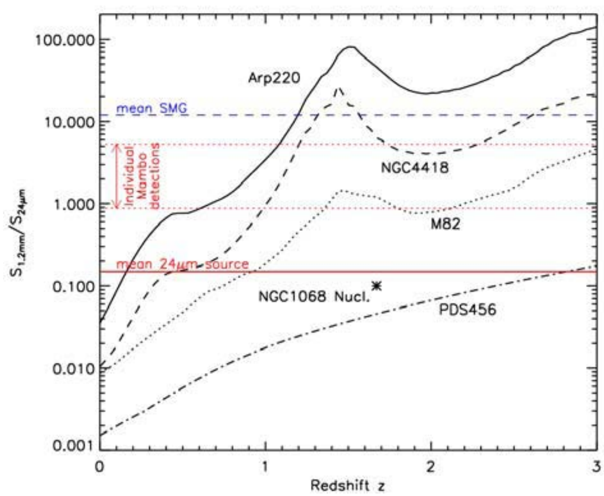

Ratio of 1.2mm to 24μm flux density as a function of redshift for local SED templates, ranging from star forming infrared galaxies (M82, Arp 220) to obscured compact objects (NGC 4418) and AGN (PDS 456). The solid red line shows the mean for our sample, indicative of warm and likely AGN heated dust

References:
• Lutz, D., et al. 2005, ApJ 632, L13
• Yan, L., et al. 2004, ApJS, 154, 60

Dieter Lutz, Linda Tacconi, Reinhard Genzel

Silicate Emission in AGN

Emission from the Torus or (and) the NLR ?

Long sought silicate emission features in AGN have been recently detected by Spitzer spectroscopy, but it remains uncertain how they can be interpreted in unified scenarios. We present our recent results from Spitzer and SUBARU observations concerning silicate emission in AGN which suggest that the emitting region is more extended then the torus. We identify the narrow line region as a possible candidate for the extended silicate emitting region.

Silicate Emission in Type1 QSOs

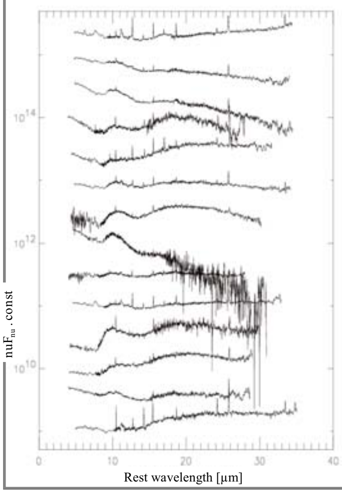

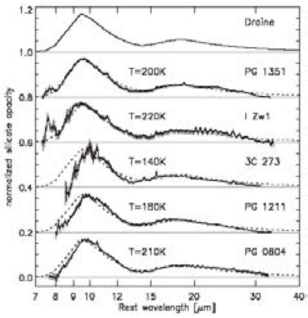

left: IRS spectra of QUEST PG-QSOs showing the frequent presence of silicate emission

right: estimated temperatures for the silicate dust in QSOs using the product of a BB and the ISM silicate opacities (dashed line) (Hao et al. 2005).
{dust sublimation temperature between 800-1500 K (Kimura et al. 2002)}

Silicate Emission in Type 2 AGNs

From the AGN unification model one would expect to see silicates in absorption for type 2 sources. The presence of silicate emission in type 2 sources may indicate a larger extension for the silicate emission region then predicted by the torus model.

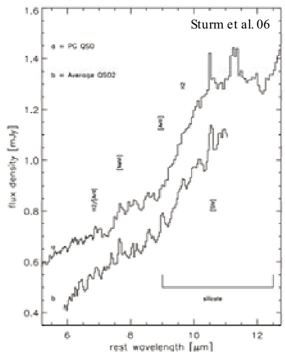

Silicate Emission Masked by Starformation !

The presence of starformation is able to mask out the underlying silicate emission features due to PAH emission which fills up the gaps around 8 and 12 µm. This has to be considered in a study of silicate emission features.

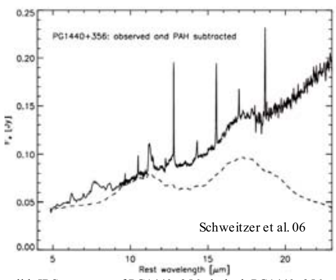

solid: IRS spectrum of PG1440+356, dashed: PG1440+356 minus M82 (scaled with respect to PAH emission)

Silicate Emission in the LINER NGC 3998

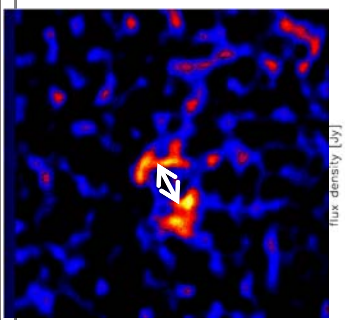

Residual extended silicate emission in NGC 3998 observed with SUBARU. Image size ~ 200 x 200 pc^2

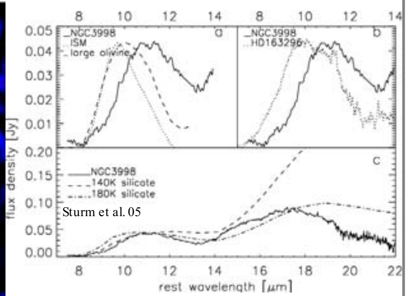

(a): Comparison of the NGC 3998 10 µm feature to the standard ISM Emission of amorphous silicates (dotted, Kemper et al. 2004), and to olivines of larger grain size (dashed, van Boekel et al. 2005). (b): Comparison to the Herbig Be star HD163296 (dotted,Meeus et al. 2001). (c): Dashed (dash-dotted): the product of a 140 K (180K) blackbody and the ISM silicate opacities, produced as in Hao et al. (2005)

We observed the LINER NGC3998 with COMICS on the SUBARU telescope with two different filters. One filter was centered on the silicate emission bump located around 11 µm and the other filter was located on the continuum emission to subtract the underlying continuum. The image shown above is the continuum subtracted silicate emission after subtraction of the PSF. The residual emission clearly indicates, that the silicate emission has been spatially resolved and that it is extended on a scale of roughly 30 pc.

Three Reasons Against the Simple Toruspicture + an Alternative Picture

1 – The silicate emission is too cool to be explained by a torus origin.
2 – Silicate emission has been detected also in type 2 sources.
3 – In the LINER NGC3998 we found silicate emission extended on a scale of roughly 30 pc.

An alternativ origin of the silicate emission may be cooler dust which is located further away from the central heating source. The NLR would be a candidate for such a silicate hosting, cooler region.

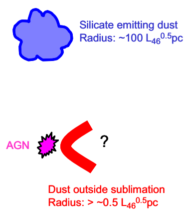

References :
Hao et al., 2005, astro-ph/0504423
Kemper et al., 2004, ApJ, 609, 826
Kimura et al.,E.K. 2002, Icarus, 159, 529
Meeus et al., 2001, A&A, 365,476
Schweitzer et al., 2006, ApJ, 649, 79S
Sturm et al., 2005, ApJ, 692, L21
Sturm et al., 2006, ApJ, 642, 81S

M. Schweitzer for the Spitzer QUEST team

Host galaxy colors of moderate-luminosity AGN

MAX-PLANCK-GESELLSCHAFT

MPE

We present results (Silverman et al. submitted, ApJL) that may explain why the rest-frame optical colors of X-ray selected AGN have a broad distribution (Nandra et al. 2006) dissimilar to the non-active galaxies. We have identified a sample of 96 moderate-luminosity ($41.9<\mathrm{Log}\sim L_{0.5\text{-}8\,\mathrm{keV}}<43.7$) AGN found in the Extended *Chandra* Deep Field-South Survey and drawn from a parent sample of 5555 galaxies (i.e. no optically selected QSOs) from the COMBO-17 (Wolf et al. 2004) survey with $0.4<z<1.1$. The color distribution of AGN hosts appears to be a result of the (1) strong color evolution of the luminous ($M_V<-20.7$) galaxy population from z~1 to the present, and (2) the influence of ~10 Mpc scale structures. Galaxies with AGN at z~0.9 preferentially have blue (U-V<0.7) colors in contrast to those at z~0.5 that are redder with many falling along the red sequence. There is tantalizing evidence to suggest that *within large-scale sheets, host galaxies reside in the color 'valley' and are evolving rapidly towards the red sequence*. We find that within the redshift interval $0.63<z<0.76$, which is dominated by two major redshift spikes at z=0.67 and z=0.73, luminous host galaxies primarily have rest-frame colors 0.6<U-V<1.1 with an AGN fraction reaching 15%. We further show that *the color distribution of AGN host galaxies, outside these redshift spikes, has a bi-modality similar to the parent galaxy sample* with an AGN fraction of ~5%. We claim that larger scale structures are important in driving the evolution of galaxies by triggering AGN activity with the physical mechanisms yet to be determined.

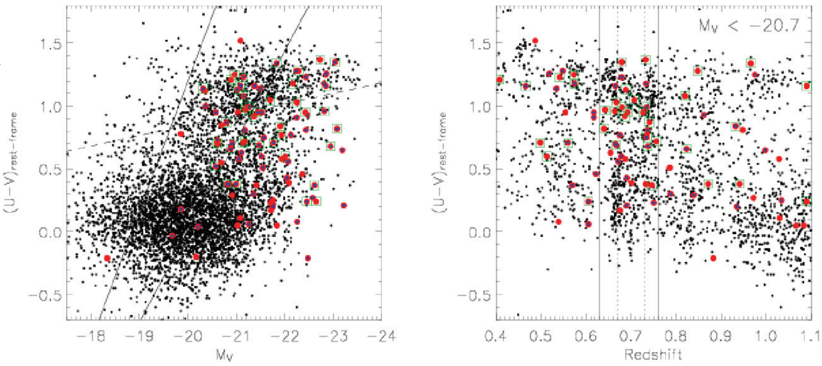

Rest-frame color (U-V) - magnitude (M_V) diagram *(LEFT)* of 96 galaxies hosting AGN compared their parent sample of 5,555 galaxies. All galaxies are marked with a small black dot and those hosting X-ray selected AGN are highlighted by large red circles. Solid lines denote the approximate limits for galaxies with $R_{ap}<24$ at z=1 and z=0.8. The division between red and blue galaxies implemented by Bell et al. (2004) is shown by the dashed line. AGN hosts classified as early-type (Sersic index >3) galaxies by the HST/ACS morphology (Caldwell et al. 2005) are marked by a small blue dot. ***Right*** Color versus redshift for the most luminous galaxies. The vertical solid lines denote the redshift interval (0.63<z<0.76) with the dotted lines marking the redshift spikes at z=0.67 and z=0.73. AGN with spectroscopic redshifts are shown by a smaller blue dot. In both panels AGN with hardness ratio (H-S/H+S) >-0.2 are marked by a green box.

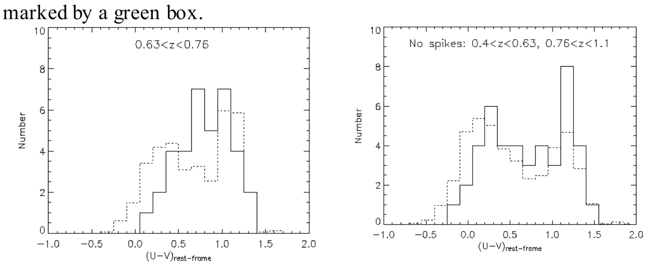

LEFT Rest-frame color (U-V) histogram for the galaxies that host AGN (solid line) with absolute magnitude $M_V<-20$ in the narrow redshift range (0.63<z<0.76) centered on the redshift spikes. ***Right*** The distribution of AGN host galaxies over the two redshift intervals (0.4<z<0.63, 0.76<z<1.1) that do not include those in the *Left* panel. For comparison, we have plotted, in both panels, the distribution of all galaxies (dotted line) above this absolute magnitude and renormalized to match the number of AGN.

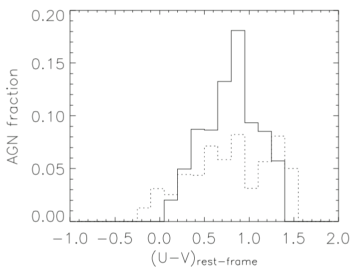

Fraction of galaxies ($M_V<-20.7$) with AGN as a function of rest-frame optical color (U-V). The solid histogram specifically pertains to the redshift interval 0.63<z<0.76 whereas the dotted histogram includes objects at redshifts other than this narrow range.

We find that the host galaxy colors to be determined by the following:

- Color evolution of the underlying galaxy population, de-population of the red sequence and increase in the mean SFR with redshift (Faber et al. 2006)
- Transitional colors associated with large-scale sheets (Gilli et al. 2003), a higher incidence of AGN activity (~15%) compared to a 'field' value (~5-6%) and possible quenching of star formation (e.g. Di Matteo, Springel & Hernquist 2005)

References:

- Bell et al. 2004, ApJ, 608, 752
- Caldwell et al. 2005, ApJS, astro-ph/0510782
- Gilli et al. ApJ, 592, 721
- Nandra et al. 2006, ApJL, astro-ph/0607270
- Faber, S. et al. 2006, ApJL, astro-ph/0506044
- Wolf et al. 2004, A&A, 421, 913
- Di Matteo, Springel, & Hernquist 2005, Nature, 433, 604

J. Silverman, V. Mainieri, G. Hasinger, R. Gilli, J. Bergeron, G. Szokoly, W. N. Brandt, P. Rosati, P. Tozzi, D. Alexander, B. Lehmer, A. Koekomoer, F. Bauer & the entire E-CDF-S team

AGNs and large scale structure

We present results from studies of AGN clustering in the ROSAT-NEP and XMM-COSMOS surveys. We detect strong auto-correlation signal of AGN and strong cluster-AGN cross correlation. We derived and estimate of the relative bias of AGN and galaxies together with an estimate of the bias factor of AGNs and its evolution.

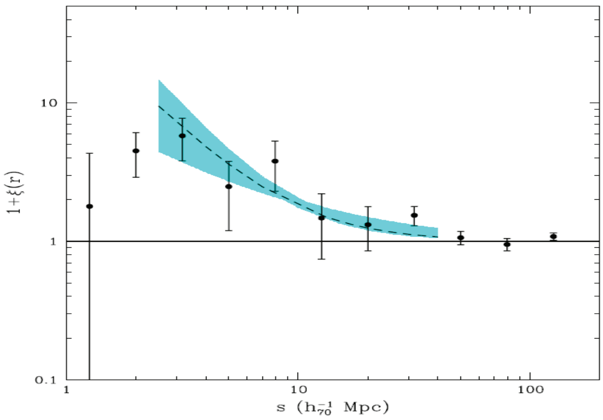

The cluster-AGN soft X-ray cross correlation function plus one. The error bars are quoted at 1σ level. The dashed line represents the best fit maximum-likelihood power-law fit s_0=8.7 Mpc and Γ~1.7. The shaded region illustrates the 1σ confidence region of the power-law fit in the distance range in which it was performed.

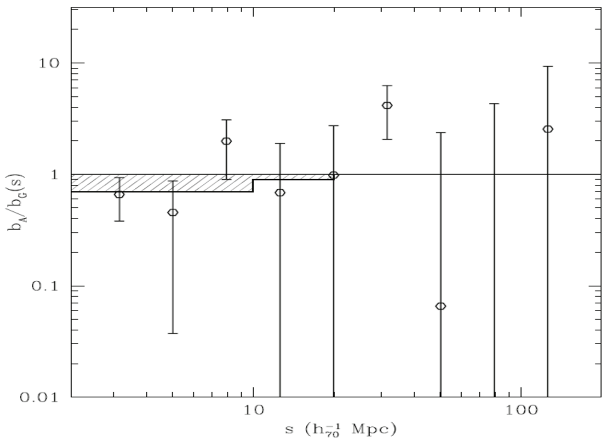

The ratio between the observed ROSAT- NEP ξ(s) and the best fit cluster-galaxy cross -correlation function
In the linear biasing theory it returns the ratio of the bias factor of AGNs and galaxies.
Errors are quoted at the 1σ level. The shaded region shows the expected level of b_A / b_G(s)=1.

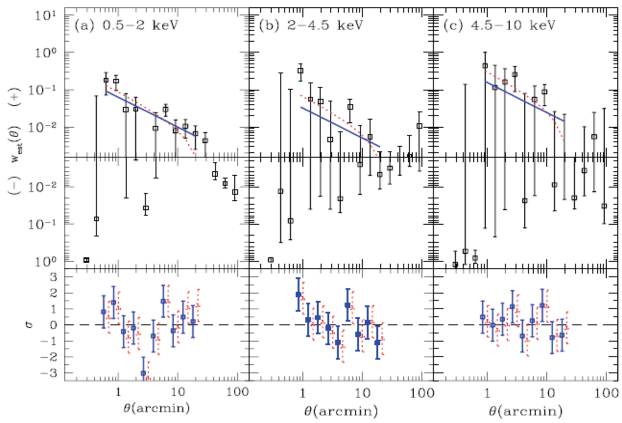

The binned estimated angular auto correlation of the X-ray sources detected in the first-year XMM-COSMOS data in three standard energy bands as labeled. The blue-solid and red-dotted lines show the best-fit power-law models for Γ-1=0.8 without and with an integral constraint respectively. The models
are plotted in the range where the fits are made.
Fit residuals in terms of σ has been also plotted in the lower panels for the two models in the same line styles (colors) as the models.

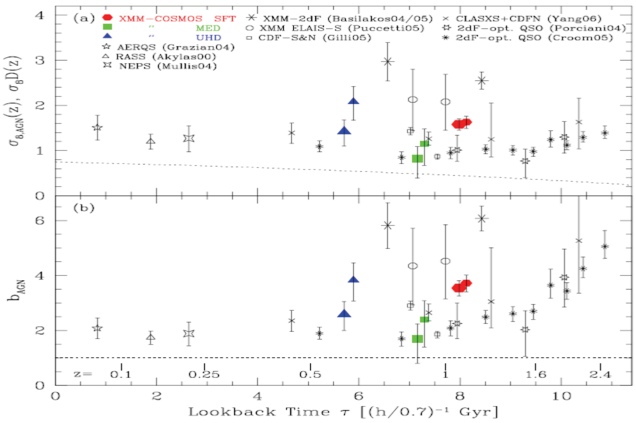

(a) The $\sigma_{8,AGN}$ of the X-ray sources/AGNs inferred by the power-law fits to the correlation functions from this work and literature are plotted against the look back time corresponding to the effective median redshift of the samples. The dotted line shows $\sigma_{8,AGN}$ for the mass in the linear theory normalized to 0.9 at z=0.
(b) The bias parameter b_{AGN} are plotted as a function of the effective redshift.

Nico Cappelluti and the XMM-COSMOS and NEP teams

Tidal disruption events discovered with XMM-Newton

The paradigm that the nuclei of non-active galaxies are occupied by concentrated dark objects was predicted long ago by theory. This conjecture can be proved by the discovery of giant-amplitude, non-recurrent X-ray flares from such non-active galaxies and explained in terms of outburst radiation from stars tidally disrupted by a nuclear dormant supermassive black hole. Two sources classified as optically non-active galaxies have been detected with XMM-Newton during slew observations in full agreement with the tidal disruption model.

Through comparison of the XMM-Newton Slew Survey (XMMSL1) with the ROSAT All-Sky Survey (RASS) five new tidal disruption candidates arise showing high variability and soft X-ray spectra (Esquej et al. 2007). Optical observations revealed that three of these sources show signs of optical activity and need further investigation within the transient galactic nuclei phenomena. The two other objects, XMMSL1 J111527.3+180638 and XMMSL1 J132342.3+482701 (whose NED counterparts are NGC 3599 and SDSS J132341.97+482701.3 respectively), meet all known criteria (Komossa 2002) for objects within the tidal disruption scenario.

Follow-up pointed XMM-Newton observations performed on NGC 3599 and SDSS J132341.97+482701.3 roughly two years after the slew observation show that both sources have faded by factors of 50 and 70 respectively leaving a residual steep soft spectrum. A posterior follow-up Swift observation on NGC 3599 showed that its flux experimented a further decrease following a $t^{-5/3}$ decline law (as can be inferred from the light curve in Fig. 1), consistent with efficient accretion to the supermassive black hole from a thick disk. For SDSS J132341.97 +482701.3, that was very faint at the time of the Swift observation and only a few counts were detected, the flux did not decrease as expected. Nevertheless, its light curve can be also fitted by a $t^{-5/3}$ decline law.

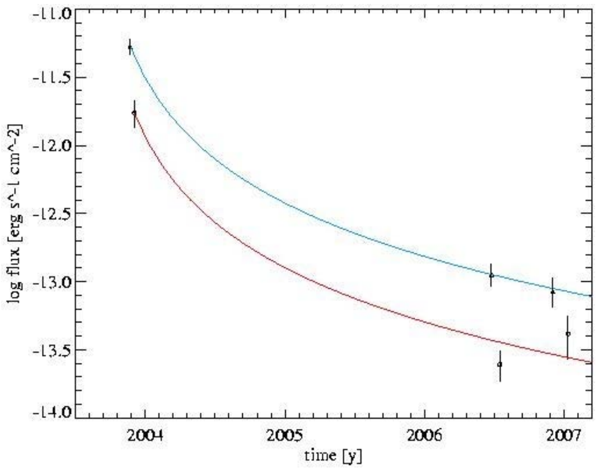

Fig.1. X-ray light curves of the two tidal disruption events. Triangles: NGC 3599. Circles: SDSS J132341.97+482701.3. The points come from the XMM slew, XMM pointed and Swift observations respectively. A $t^{-5/3}$ law has been fitted for both sources.

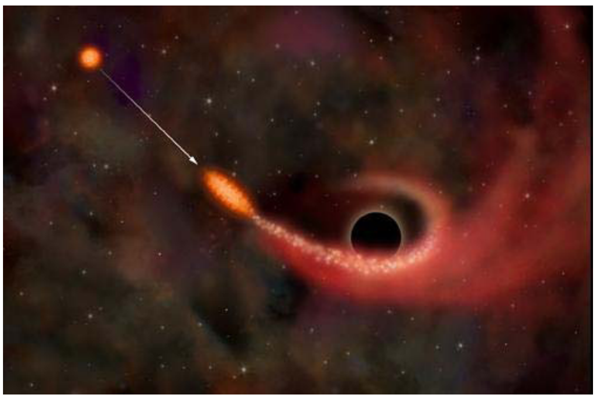

Fig.2. Artist's sketch of the stellar disruption and accretion by a supermassive black hole.

Although previously detected tidal disruption events support theoretical predictions, the sample is not big enough to allow conclusions to be drawn about the feasibility and mechanisms involved in the phenomenon. The detection, confirmation and follow-up of each new case is needed to strengthen the theory through observational data.

References:
- Esquej, P., Saxton, R.D., Freyberg, M.J., et al. 2007, A&A 462, L49
- Komossa, S. 2002, Rev. Mod. Astron., 15, 27

P. Esquej et al.

Chandra LETGS spectroscopy of MR 2251-178 and its warm absorber

We analyse the *Chandra*Low Energy Transmission Grating Spectrometer (LETGS) observation of the QSO MR 2251-178. The warm absorber of MR 2251-178 is well described by a hydrogen column density of ~1021atoms/cm2and an ionization parameter log(ξ) ~ 1. We find in the spectrum evidence of narrow absorption lines coming from highly ionized species of C, N, O,Mg and Fe showing a highly stratified material outflowing with velocities ~ 0-3000 km/s. We also find evidence of having emission lines comingfrom a higher ionization state. We conclude that they could be located at *different distances from the nucleus*. We note changes (in time) on the O VII and O VIII K-edges at different periods of the observation. They could be explained through changes in the ionization state of the absorber on timescales of hours.

Scientific Motivation

MR 2251-178 was the first quasar observed in X-rays (Ricker et al. 1978). Also, it was the first Active Galaxy (AGN) reported to host a "Warm Absorber" ($T \sim 10^{4-5}$ K, Halpern 1984). Now, found in ~ 50 % of the AGN spectra, the warm absorber is key to constrain physical conditions, ionization states, kinematics and evolution of the nuclear environment in the centre of galaxies, and it is an important component in the unification picture of AGN.

Detection of Absorption and Emission Lines

By dividing the 4-60 Å range in small pieces of ~ 0.5 Å, we were able of finding absorption lines in the (negative+positive orders) LETGS spectrum of MR 2251-178 (Fig 1). The best photoionization model that accounts for these lines as well as a global representation of the spectrum has $N_H \sim 10^{21}$ atoms/cm^2 and log(ξ) ~ 1. Figure 2 shows several portions of the spectrum where **absorption** lines are present. Fig 3 shows **emission** lines, which (on average) can be represented by a higher ionization state of log(ξ) ~ 2.4.

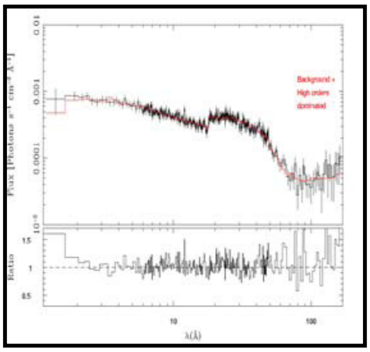

Fig. 1 4-60 Å spectrum of MR 2251-178.

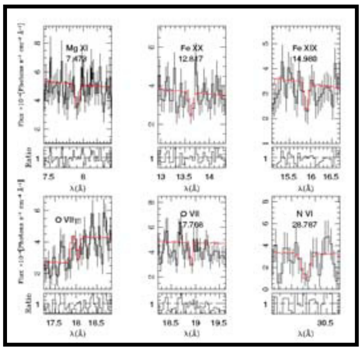

Fig.2 X-ray absorption lines.

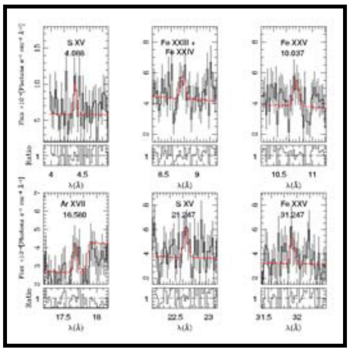

Fig. 3 X-ray emission lines.

Variability of the OVII and OVIII K-edges. Fig 4 shows how changes in the ionization state of the warm absorber can be explained in terms of changes of the ionization parameter. These changes occur on a timescale of ~ hours.

Conclusions. We find evidence of narrow absorption lines coming from highly ionized species of C, N, O, Mg and Fe showing a highly stratified material outflowing with velocities ~ 0-3000 km/s. The warm absorber of MR 2251-178 is well described by a hydrogen column density of $\sim 10^{21}$ atoms/cm^2 and an ionization parameter log(ξ) ~ 1. The emission material is well described by log(ξ) ~ 2.4.

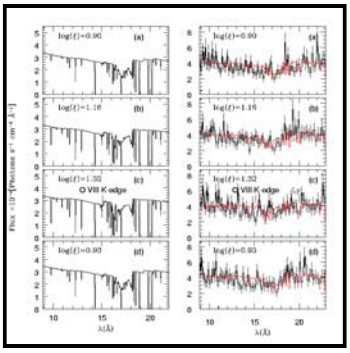

Fig. 4 Time variability of the Oxygen edges.

References:
- Ricker, G. R., et al. 1978, Nature,271,35
- Halpern, J. P. 1984, ApJ, 281, 90.

JM. Ramírez, Stefanie Komossa and Vadim Burwitz (MPE)
and Smita Mathur (Dep. of Astronomy, Ohio SU)

Spitzer spectra of X-ray selected QSO2s

We have performed a spectroscopic study of 7 Type 2 QSOs using the mid-infrared spectrometer *IRS* on board the *Spitzer Space Telescope*. These are the first mid-IR spectra of X-ray selected QSO2s taken. The spectra strongly differ from template spectra of Type 2 AGN at lower luminosities. They also do not resemble the spectra of other previously used QSO2 templates, such as Ultraluminous Infrared Galaxies (ULIRGs). X-ray selected QSO2s are instead characterized by powerful AGN in hosts with a luminosity due to star formation < 10^{11} $L_{\odot}$. The dominance of the AGN light in the mid-IR spectra of QSO2s together with their flatter spectral energy distributions (SEDs) places important constraints on models of the cosmic infrared background and of the star formation history of the universe.

Intrinsically luminous, but highly obscured active galactic nuclei (AGN), the Type 2 QSOs (QSO2s), have long been sought as a crucial (and necessary) component of AGN unification theories and of models that explain the cosmic X-ray and infrared background by the growth of obscured supermassive black holes throughout cosmic history. The existence of obscured QSOs, however, remained controversial until very sensitive and deep hard x-ray imaging and spectroscopy campaigns became feasible with the advent of Chandra and XMM-Newton. In the X-ray domain the QSO-2 population is characterized by high intrinsic absorption and high intrinsic X-ray luminosity. Based on these criteria we have selected a sample of 7 QSO2s for the first mid.infrared spectroscopic study of such objects, with the aim of studying their physical properties.

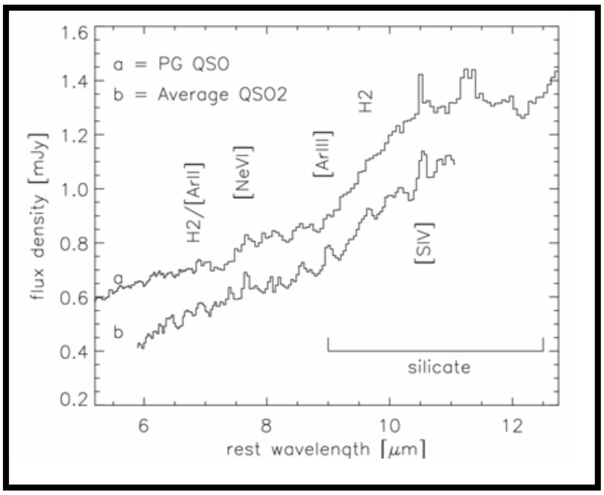

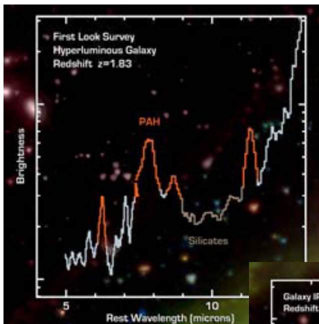

Left: A typical Mid-IR ULIRG spectrum with strong PAH emission. *Below:* deeply embedded ULIRG nucleus with strong ice and silicate absorption

Left: average QSO2 (b) compared to a typical Type 1 QSO (a)

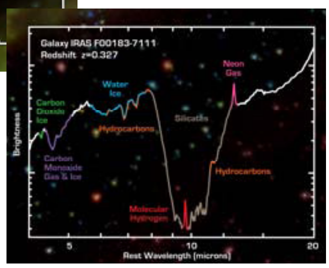

QSO2 mid-IR spectra do not exhibit strong PAH dust emission features from circum-nuclear star forming regions, typical for lower luminosity Type 2 Seyfert galaxies or other previously used QSO2 templates, such as ULIRGs. They also do not show the ice and silicate absorption features of highly luminous but deeply embedded compact nuclei seen in some ULIRGs. Instead they reveal a relatively featureless, rising continuum similar to luminous Type 1 AGN. We also find evidence for a 10 μm silicate feature in *emission*. Models of dusty tori in the AGN unification scenario predict this only for Type 1 AGN.

The mid-IR SEDs of QSO2s are on average warmer than for Type 2 template objects of lower luminosity, probably with only a weak (rest-frame) far-IR peak, due to a strong AGN contribution as revealed by the mid-IR spectra. Based on the strength (limits) of the PAH features we derive values (limits) of the star formation related far-IR luminosity of a few x 10^{11} $L_{\odot}$, a range which is very typical for local starburst galaxies but well below ULIRGs.

Reference: Sturm et al. 2006, ApJ 642, 81

Hasinger, G., Sturm, E., Lehmann, I., Mainieri, V., Genzel, R., Lehnert, M.D., Lutz, D., & Tacconi, L.J.

Star formation in QSO hosts

Using Spitzer mid-infrared spectroscopy of a sample of PG QSOs at redshifts z<0.3 we have detected a widespread presence of PAH emission as tracers of the star-forming QSO hosts. Similar PAH/FIR and [NeII]/FIR ratios are found in QSOs and in starburst dominated ULIRGs and lower luminosity starbursts. We conclude that the typical QSO in our sample has at least 30% but likely most of the far-infrared luminosity ($10^{10\ldots12}$ $L_\odot$) arising from star formation, providing strong constraints on the long standing question about the excitation source of the far-infrared continuum in AGN.

To investigate the link between AGN activity and star formation and the extent to which they occur simultaneously, it is important to quantify the star formation activity in QSO hosts. Detecting star formation tracers in the presence of extremely powerful AGN emission is, however, notoriously difficult. In the mid-infrared, the contrast between the emission from possibly dust-obscured star formation and from the central AGN is favourable, and established star formation tracers are available. In the Quasar and Ulirg Evolution STudy (QUEST) we are studying QSOs, ultraluminous infrared galaxies, and the possible evolutionary connection between the two using the infrared spectrograph *IRS* onboard the *Spitzer Space Telescope*.

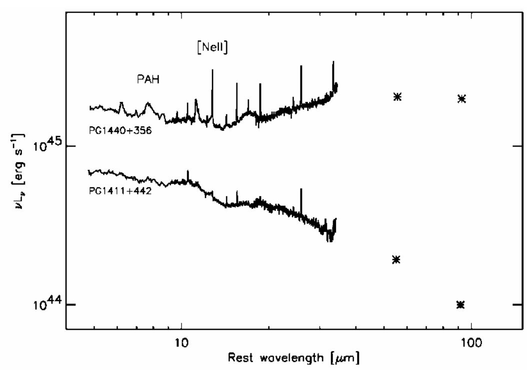

Left: *(scaled) IRS spectra of two PG QSOs illustrating the full range of PAH, [NeII], and far-infrared emission within the sample.* **Right:** *Average IRS QSO spectrum. Main emission lines and features are marked*

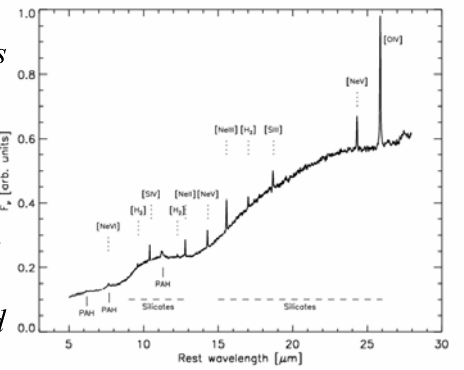

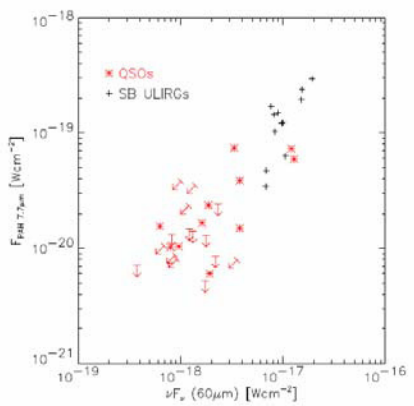

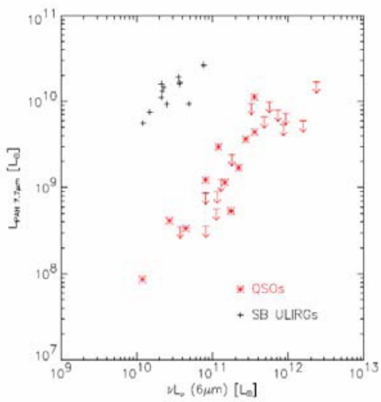

Far Left: *Correlation of PAH (7.7µm) and far-infrared for the QSOs and for starburst dominated ULIRGs.*
Left: *Correlation of PAH (7.7µm) and mid-infrared for the same QSOs and starburst dominated ULIRGs.*

Similar PAH/FIR ratios are found in QSOs and in starburst dominated ULIRGs, indicating the star-formation origin of the far-infrared continuum. While there is also a correlation between PAHs and mid-infrared (6 µm, AGN-dominated) continuum, this correlation is different between starbursts and QSOs, and hence only reflecting a general AGN-starburst connection

Reference: Schweitzer et al. 2006, ApJ, 649, 79

E. Sturm, M. Schweitzer, D. Lutz, A. Contursi, L.J. Tacconi, R. Genzel., S. Veilleux, H. Netzer, et al.

Observation of the blazar Mrk 421 in its active state with INTEGRAL

A ToO observation of the TeV-emitting blazar Mrk 421 with INTEGRAL was triggered in June 2006 by an increase of the RXTE count rate to more than 30 mCrab. The source was then observed with IBIS, JEM-X and OMC of INTEGRAL for a total exposure of 829 ks. During this time several outbursts were observed. Multi-wavelength observations were immediately triggered and the source was observed from radio up to TeV energies. The data obtained during these observations are analysed with respect to spectral evolution and correlated variability. Preliminary results of the analyses are presented in this poster.

Mrk 421 was detected by all 3 instruments with a high significance (up to 160σ between 20 – 50 keV). In Figures 1 & 2 the ISGRI and the OMC lightcurves are shown. Whereas the optical light-curve of OMC scatters around a mean value of 2.6×10^{-14} erg/(cm² s Å) four strong flares are observed at X-rays. The strongest flare is a factor of 4 more intense than the quiescent level of ~4 cts/s. The time interval was split into phases with a quiescent and an active emission. The data of the two phases were then spectrally investigated.

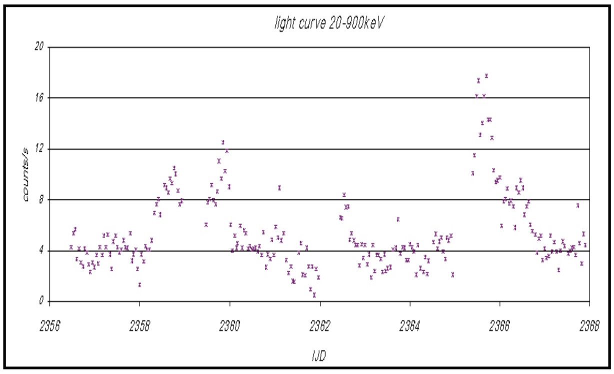

Figure 1. The ISGRI light-curve of Mrk 421 in the energy range 20 – 900 keV.

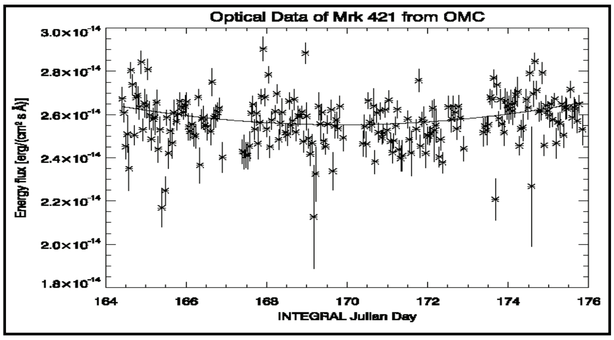

Figure 2. The OMC lightcurve of Mrk 421.

References:
1 Maraschi et al., Ap. J. **526**, L81, 1999
2 Blazejowski et al., Ap. J. **630**, 130, 2005

Different spectral models were fitted (XSPEC) to JEM-X and ISGRI data, covering quiescent and flaring periods, to find the function which fits the data best. A broken power law (PL) could be best fitted in both cases (χ^2_{red} = ~1.9). With the exception of the low-energy PL index, which shows a slight spectral hardening during the active state, the parameters are consistent within the errors.

Parallel to the INTEGRAL observations a multiwavelength campaign was initiated at radio (Metsähovi and VLBA radiotelescopes), at optical (KVA telescope) and at TeV energies (Whipple). The data from these observations were averaged over the observation time and then compiled in an energy-density spectrum (Figure 3). They are compared with the theoretical models of Maraschi et al.[1] and Blazejowski et al.[2] which were adapted to the IBIS data. The models fit the RXTE, IBIS and Whipple data reasonably well, However, the spectra measured by JEM-X in both states are flatter than predicted by the models. The peak energy is at ~1 keV.

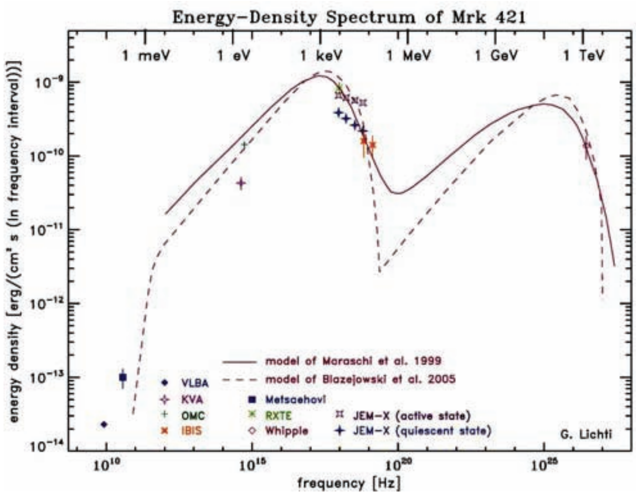

Figure 3. The νF_ν spectrum for quasi-simultaneous data of Mrk 421 in June 2006.

G. Lichti, E. Bottacini, P. Charlot, W. Collmar, D. Horan, A. von Kienlin et al.

Multifrequency Observations of the γ-Ray Blazar 3C 279 at different Optical Flux Levels

We compare multifrequency (radio to hard X-rays) measurements of the the variable γ-ray blazar 3C 279 from an optical low-state in June 2003 to an optical high-state in January 2006. The surprising result is, that the two SEDs differ only in their high-energy synchrotron emission.

The prominent γ-ray blazar 3C 279 was observed by INTEGRAL in June 2003 and in January 2006. These hard X-ray observations were supplemented by multifrequency campaigns from radio and mm bands (e.g. Effelsberg, Metsähovi, IRAM, SMA), via near-IR, optical and UV bands (Siding Spring and Tuorla in 2003, a WEBT campaign and Swift in 2006), up to X-rays (Chandra and Swift).

In 2003 we measured an optical low-state spectral energy distribution (SED) (Collmar et al. 2004) of 3C 279, and in 2006 an optical high-state one (Collmar et al. 2007). Both SEDs show the typical shape of non-thermal synchrotron and inverse-Compton (IC) emission. The surprising result is, that - despite a significant flux change in the high-energy synchrotron emission (near IR/optical/UV) – the rest of the spectra remain the same. In particular, the low-energy IC emission (X- and hard X-rays) is unchanged, proving that the two emission components do not vary simultaneously. This unexpected behavior – the optical band in high- and the X- and hard X-rays in low state - provides new constraints on the modeling of the broadband emission of the source. It most likely points to time-shifts occurring between the different spectral bands.

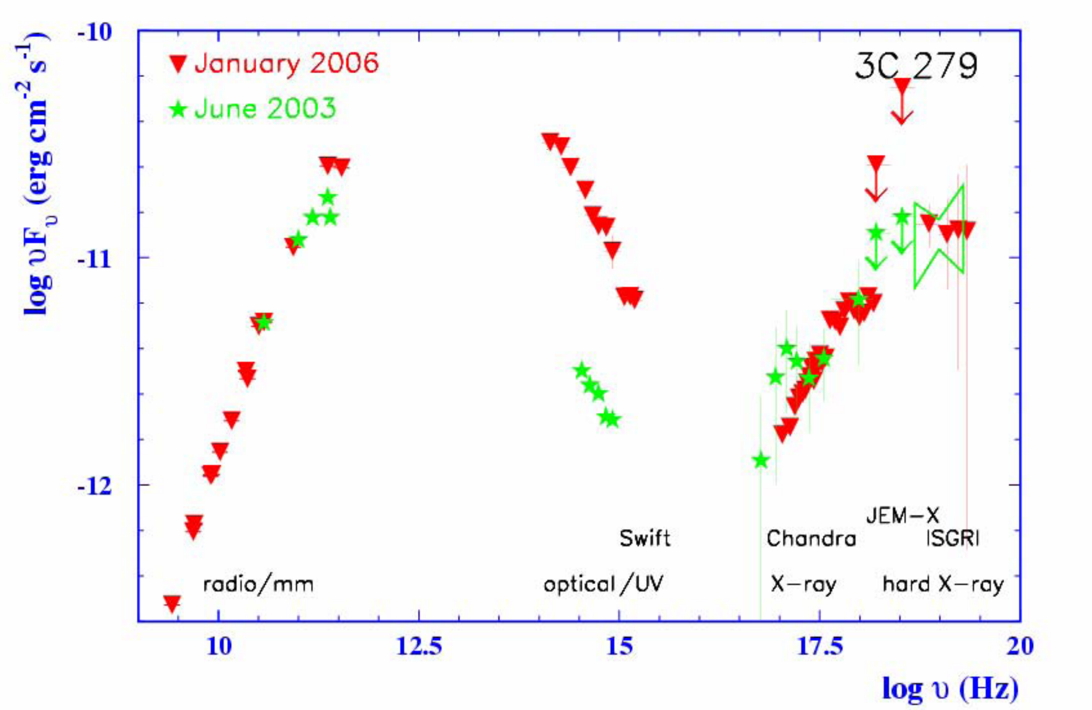

Quasi-simultaneous spectral energy distributions (SEDs) for 3C 279 from radio to the hard X-ray band (~100 keV) were compiled by multifrequency measurements. Both SEDs show the typical two-hump shape. The January 2006 SED (red symbols), having the best X- and hard X-ray coverage to date, is compared to the one measured in June 2003 (green symbols). Surprisingly, despite a significant change in the optical/near-IR flux of 3C 279, the spectrum in the other observed bands, in particular the X- and hard X-ray bands, remains the same.

References:

• W. Collmar, M. Böttcher, et al., 2004, ESA SP-552, 555

• W. Collmar, et al., 2007, accepted

W. Collmar, M. Böttcher, T. Krichbaum, E. Bottacini, V. Burwitz, et al.

Gravitationally redshifted emission lines

The gravitational pull of black holes (BHs) deforms emission in their vicinity such as spectral emission lines. Depending on distance the emission lines are shifted and even distorted close to the BH. This is a common feature of all BHs of arbitrary mass. We show that gravitationally redshifted emission lines can be used to probe BH properties such as mass and spin. We demonstrate that relativistic ray tracing simulations are consistent with optical and X-ray observations of the active galactic nucleus (AGN) Mrk 110. High-resolution observations allow in principle for probing gravitational redshift at unexpectedly high distances amounting to several 10000 gravitational radii (several 100 light days for an AGN with a 100 million solar mass BH).

In a simple model we assume that the emission lines originate from thin Keplerian rotating rings that lie in the equatorial plane of a Kerr BH. Gravitational redshift of the spectral lines can be studied by shifting the rings successively towards the BH. The left figure below shows the deformation of emission lines by gravitational redshift for highly inclined rings (inclination angle of 75°) around a fast spinning Kerr BH with specific angular momentum of a = 0.998M. The ring radius with maximum emission is denoted as R_{peak} (in units of gravitational radii, $r_g = GM/c^2$). In this theoretical analysis there is no line specified, i.e. the line energy (horizontal axis) is specified by the general relativistic (GR) Doppler factor satisfying $g = \nu_{obs}/\nu_{em}$. The line flux (vertical axis) is normalized to unity for the line exhibiting maximum flux. Two effects are visible from the plot: First, the line flux is suppressed as the ring approaches the BH. At the event horizon the line vanishes (not shown here). Second, the line profile is deformed successively as the emitting ring comes closer to the BH. This is a typical signature of GR.

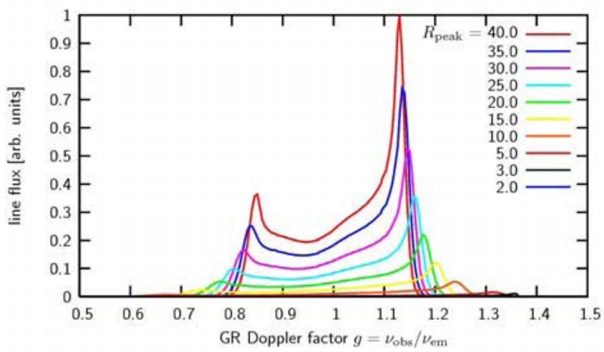

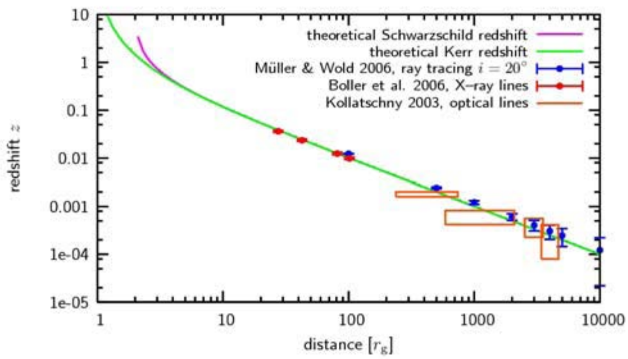

The right figure shows the comparison of ray tracing simulations (blue dots) and redshift functions from theory (purple and green curves) with observational data (boxes: optical lines from broad line region; red dots: soft X-ray lines). Each simulated line is attributed with a centroid GR Doppler factor or centroid redshift according to $g = (1+z)^{-1}$. Redshift z increases as the emitting ring approaches the hole. Observations and simulations are consistent. The plot shows that BH rotation can only be probed very close to the BH ($r < 4\ r_g$), e.g. with X-ray iron K lines.

References:
- Kollatschny, W., A&A 412, L61, 2003
- Müller, A. & Wold, M., A&A 457, 485, 2006
- Boller, T., Balestra, I., & Kollatschny, W., accepted by A&A, astro-ph/0612491

Andreas Müller (MPE)

Stellar Evolution

and Interstellar Medium

Massive Stars in the Galaxy

Recent massive-star nucleosynthesis is traced throughout the Galaxy with radioactivity gamma-rays of ^{26}Al and now also ^{60}Fe. Precision spectroscopy measurements of ^{26}Al gamma-rays with the SPI spectrometer on INTEGRAL along the plane of the Galaxy reveal Doppler shifts and broadenings. The large-scale Galactic rotation and the kinematics of interstellar gas in the massive-star regions are responsible for these signatures. Different magnitudes of Doppler shifts and broadenings for different parts of the Galaxy can provide new information on in the inner spiral-arm and bar regions of the Galaxy.

The imaging resolution of the SPI Ge spectrometer instrument (~2.7°) allows space-resolved spectroscopy. SPI's Ge detectors maintain a record spectral resolution of ~3 keV at 1809 keV over years of measurements. From data of the first two mission years, we found that the gamma-ray line is not significantly broadened, in contrast to an earlier measurement which had suggested kinematic broadening corresponding to ISM velocities of ~500 km s^{-1}. Furthermore, we found that the ^{26}Al line centroid varies across the inner region of the Galaxy, in a way which was expected from the Galaxy's large-scale rotation.

^{26}Al radioactivity is seen along the plane of the Galaxy, and attributed to massive star nucleosynthesis within the last few Myr (τ_{26Al}~1 My). The best image still is from the COMPTEL 9-year measurements. INTEGRAL/SPI now made a precision measurement resolving the ^{26}Al gamma-ray line.

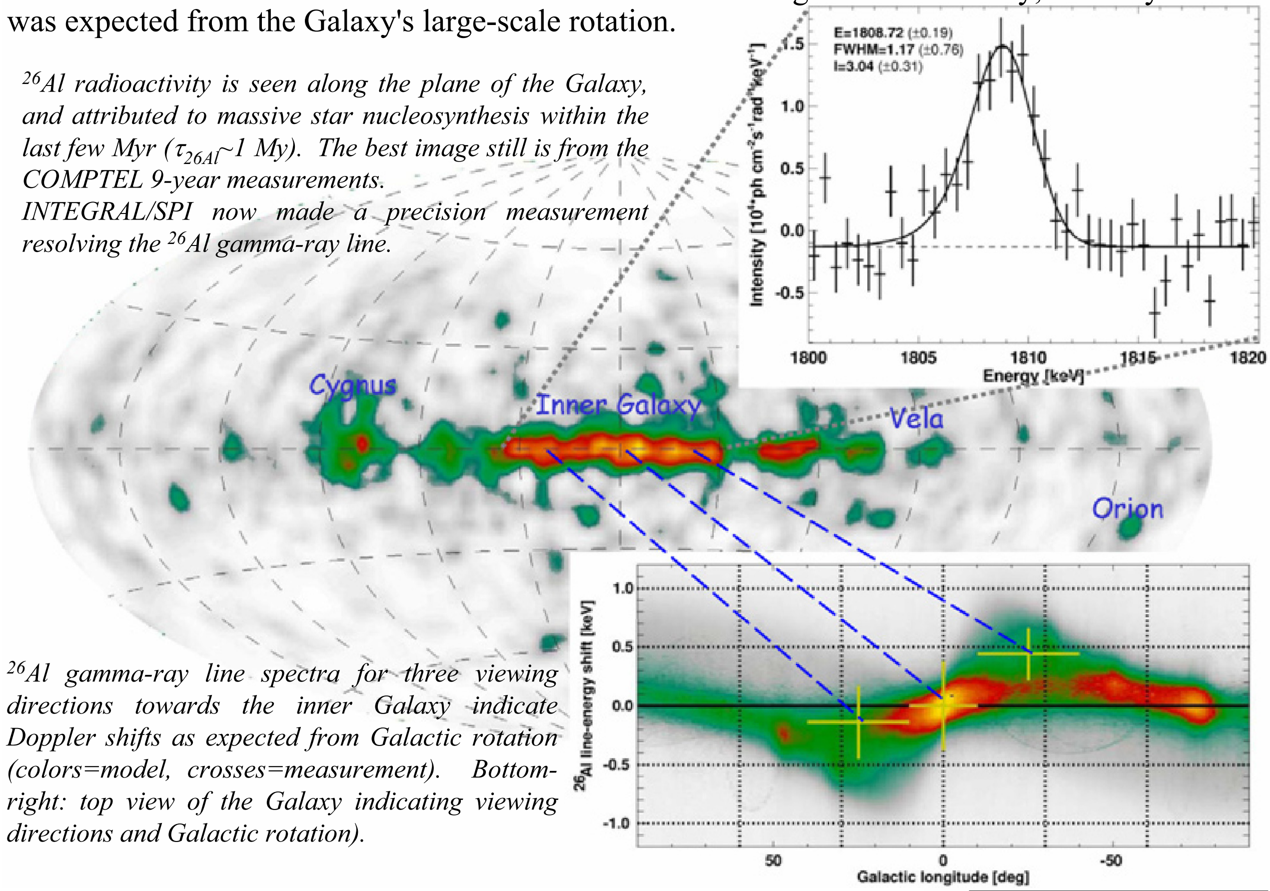

^{26}Al gamma-ray line spectra for three viewing directions towards the inner Galaxy indicate Doppler shifts as expected from Galactic rotation (colors=model, crosses=measurement). Bottom-right: top view of the Galaxy indicating viewing directions and Galactic rotation).

This demonstrates that ^{26}Al gamma-rays sample massive-star nucleosynthesis throughout the Galaxy. Thus, a new and independent massive-star census is obtained. It translates into a core-collapse supernova rate of 1.9 ± 1.1 SN per century. With more exposure, separation into finer directional pixels will allow to study the structure of inner-Galaxy spiral arms and bar through ^{26}Al radioactivity.

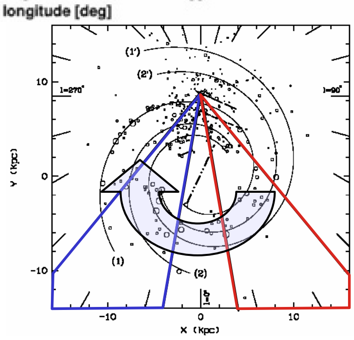

• Diehl R., Halloin H., Kretschmer K., et al., 2006. Radioactive ^{26}Al from massive stars in the Galaxy. Nature, 439, 45

Roland Diehl, Hubert Halloin, Karsten Kretschmer, Wei Wang

20 years of SN 1987A – the soft X-ray evolution

Unlike any other supernova the X-ray lightcurve of SN 1987A has increased with time since the first discovery of a soft X-ray signal in 1991 until today at a steadily accelerating pace. X-rays below 10 keV are produced by the circumstellar gas heated by the explosion shock wave. The emission is dominated by the inner ring matter with peak densities around 10^4 cm^{-3}, a total mass of about 0.5 M_{sun} and an overabundance of Si and S, which supports the ring matter being dredged up from the inner zones of the supernova progenitor star.

On the 23rd of February1987 a massive star exploded as a supernova in theLarge Magellanic cloud. Despite the very close monitoring over the full electromagnetic spectrum a couple of scientific questions still remain unresolved, among which are the evolution of the progenitor and how it got rid of matter during its life when it supposedly turned from a red supergiant to a blue supergiant. For sure, the progenitor lost mass about 20000 years ago and the inner ring with the two apparently plane parallel outer rings were produced. This mass ejection may be the result of a binary merger or an event associated with a luminous blue variable single star. Both the origin and the intra-stellar site of the ring(s) may be traced by measuring the elemental abundances with X-rays.
We have compiled the complete soft X-ray lightcurve until January 2007 (c.f. Fig. 1) from measurements with ROSAT, Chandra, XMM-Newton and Suzaku. From the X-ray flux the ambient matter density can be derived. It turns out that a Gaussian density distribution inside the ring and an exponential distribution ouside, both decreasing with increasing distance from the ring (torus) center, reproduce the X-ray lightcurve quite well, both for the 0.5-2 keV and 3-10 keV band (c.f. Fig. 1). This requires that the shock wave has already passed the center of the ring and if there are no high density regions upstream, like the base of the red supergiant wind, the lightcurve will significantly flatten over the next few years, which is already indicated in the most recent Suzaku and XMM-Newton data points.

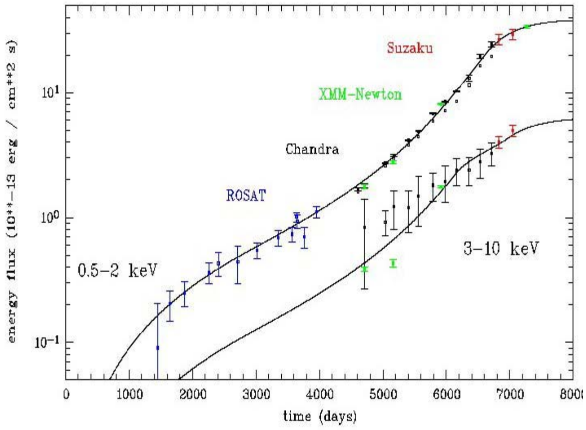

Fig.1: X-ray lightcurves of SN 1987A.

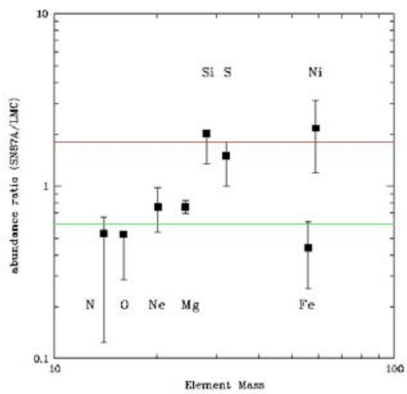

Fig.2 : Elemental abundance ratios.

With the availability of medium resolution CCD spectra and high resolution grating spectra elemental abundances have been determined. If normalized to the abundances typical for the LMC the elemental abundances of the inner ring and the matter in between the ring and the explosion site are distributed as shown in Fig. 2. Si, S and possibly Ni are overabundant, whereas the lighter elements but including Fe are slightly underabundant, which is supporting a deep layer stellar origin and excludes models attributing the rings to a interaction of the red and blue supergiant winds.

Ref.: Haberl, F., et al., A&A 460, 811 (2006)

Bernd Aschenbach, Frank Haberl, Günther Hasinger

Chandra LETGS High-Resolution X-ray Spectra of the Super Soft Source RX J0512.9-6954

The results from the detailed analysis of high resolution X-ray spectra of the super soft X-ray source RX J0513.9-6954 obtained with Chandra LETGS are presented here. The target of opportunity observations RX J0513.9-6954 during its X-ray bright states were triggered by a long term optical monitoring using the SMARTS consortium telescopes. The new X-ray data shows that RX J0513.9-6954 along with other supersoft X-ray sources all have highly structured and complex X-ray spectra, deviating strongly from simple Planckian distributions. These high resolution spectra appear to be a combination of temperature structured optically thick heated white dwarf spectra with forests of absorption lines, overlayed with optically thin spectra from a surrounding hot corona. Results obtained from the analyses of the X-ray spectra RX J0513.9-6954 are shown below and compared with theoretical models.

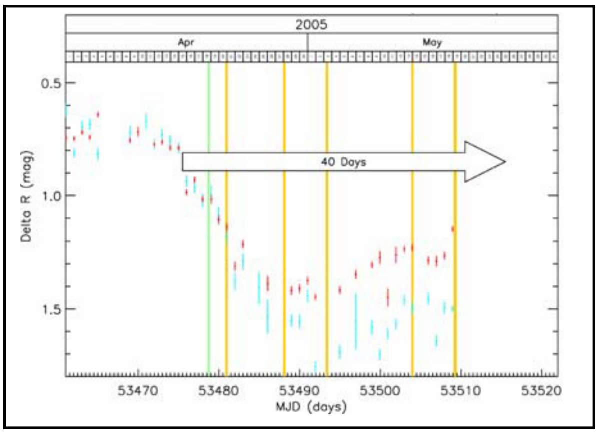

Fig. 1 Shows the optical low state of the super soft X-ray source RX J0513.9-6954 Apr./May 2005. Indicated in yellow are the times of the X-ray observations.

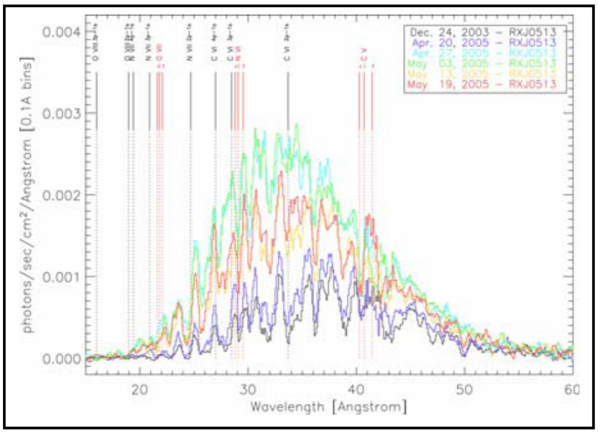

Fig. 2 shows the complexity of the spectral features present in the Chandra LETGS X-ray data as well as their temporal evolution.

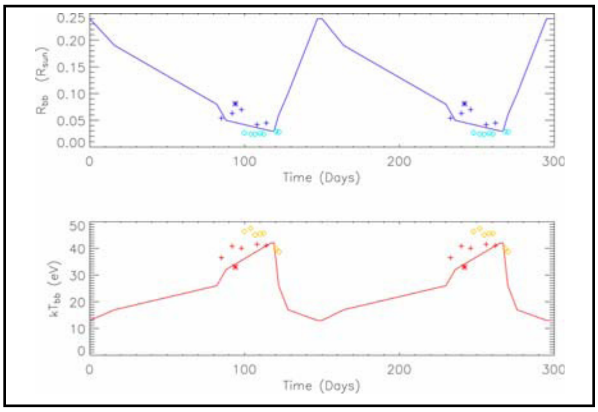

Fig. 3 The temporal evolution of measured photospheric Radius and Temperature is shown compared to the model be Hachisu and Kato 2003. The (*) depicts Chandra data obtained in Dec. 2003. Fits by McGowen et al. 2005 to XMM data of the Apr./May 2004 X-ray bright state are shown as diamonds.

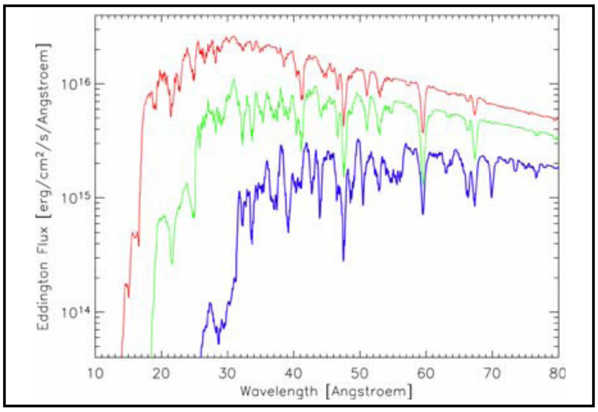

Fig. 4 Sample of LTE white dwarf models used for fitting the X-ray spectra at log g=8.5 for 440 (blue), 560 (green), and 680 kK (red).

References:

• Burwitz V., Reinsch K. , Greiner J. , et al. 2007 Advances in Space Research, in press
• Hachisu & Kato 2003, ApJ 590, 445
• McGowan, K.E. et al. 2005, MNRAS 364, 462

Vadim Burwitz, Jochen Greiner et al.

RX J0720.4-3125, a precessing isolated Neutron star?

In the nineties of the last century ROSAT discovered a group of seven nearby isolated neutron stars with temperatures which indicate ages around one million years. Observations of one of these objects with XMM-Newton revealed a surprising discovery: variations in the X-ray spectrum of RX J0720.4-3125 were found over only a few years, indicating changes in the surface temperature. A likely conclusion is that the pulsar (RX J0720.4-3125 rotates with a spin period of 8.4 seconds) precesses, i.e. the rotation axis itself moves around a cone. Therefore, we see sometimes hotter and sometimes cooler spots on its surface. RX J0720.4-3125 is the best case to study the precession of a neutron star via its X-ray emission directly visible from the stellar surface. Precession may be a powerful tool to probe the neutron star interior.

Isolated neutron stars are detectable in X-rays due to their thermal emission as long as their temperature has not decreased significantly below one million degrees. Seven neutron stars discovered by ROSAT (often called “The Magnificent Seven”) were investigated with the extremely sensitive instruments on board of the X-ray observatory XMM-Newton. One of them is the pulsar RX J0720.4-3125 which rotates with a spin period of 8.4 s at a distance of about 300 pc. In a detailed analysis of the X-ray spectra the surprising discovery was made that the spectra of the neutron star changed over a few years: between May 2000 and May 2004 the contribution of hard X-rays in the spectral measurements increased. Afterwards this contribution decreased again (Figure 1). This apparent temperature variation (Figure 2) can likely be explained by viewing different areas of the stellar surface at different times. If the rotation axis does not rest stable in space but slowly moves around a cone the viewing geometry changes over years. This precession first moves one magnetic pole and then the other into our view. If the polar caps have different temperatures and are of different size they emit unequal shares of hard X-rays.

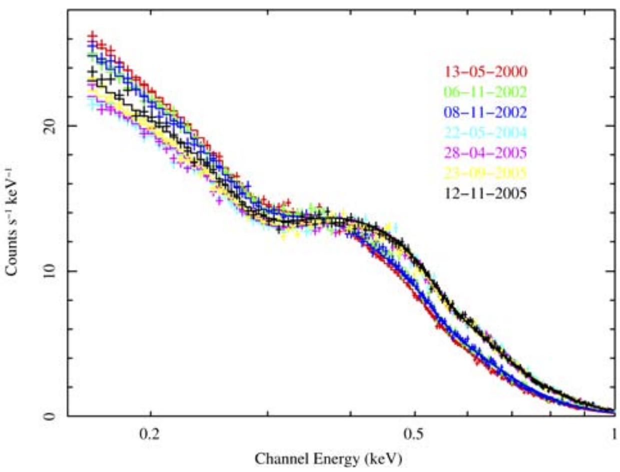

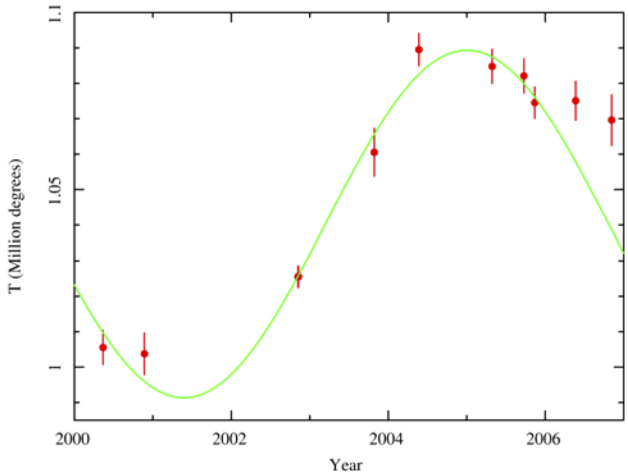

A timing analysis of the X-ray pulses of RX J0720.4-3125 reveals deviations from a gradual braking of the neutron star rotation which is consistent with the precession model. Both analyses indicate cyclic changes with a period of 7-8 years which is naturally interpreted as the precession period. The precession model can explain the observed variations in temperature and in size of the emission region as well as their anti-correlation. Further X-ray monitoring of the object by XMM-Newton is granted and will show if the observed behavior is indeed cyclic.

References:
- Haberl F., Motch C., Buckley D.A.H., et al. 1997, A&A 326, 662
- Haberl F., Turolla R., de Vries C.P., et al. 2006, A&A 451, L17

Frank Haberl

X-ray Emission Properties of Old Pulsars

We have studied the X-ray emission properties of old rotation-powered pulsars with XMM-Newton in order to probe and identify the origin of their X-radiation. The X-ray emission from these old pulsars is found to be largely dominated by non-thermal processes. All spectra are best fitted by a simple power law model. None of the observed spectra required adding a thermal component (representing either a hot polar cap or surface cooling emission) to model the data. For PSR B1929+10 -- which in X-rays is the brightest among the old rotation-powered pulsars -- the contribution from thermal emission of heated polar caps is inferred to be at most ~ 7%. The new results invalidate the ROSAT based picture in which old pulsars emit X-rays from heated polar caps and show sinusoidal pulse profiles. All lightcurves are markedly different from broad sinusoidal pulse profiles but show two or more peaks and/or narrow distinct features.

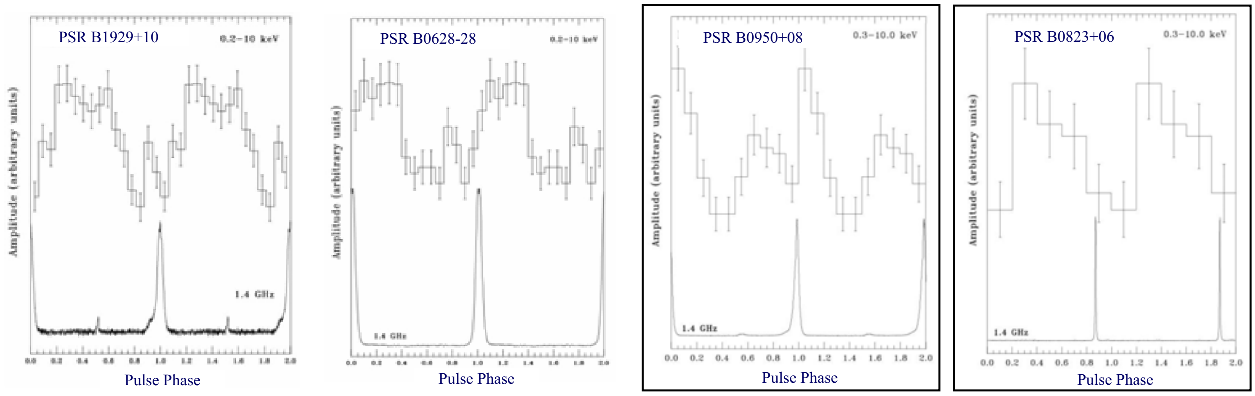

Fig.1 Integrated pulse profiles of the old pulsars PSR B1929+10, B0628-28, B0950+08 and B0823+26 as observed with the EPIC-PN aboard XMM-Newton (top) and at 1.4 GHz with the Effelsberg radio telescope (Becker et al. 2004; 2005; 2006). X-ray and radio profiles are phase aligned. Two phase cycles are shown for clarity. All pulsars which are detected with sufficient photon statistics show narrow pulse components. All lightcurves are markedly different from broad sinusoidal pulse profiles which are expected for thermal hot polar cap emitters! Pulsed fractions are in the range 30-50 %. Small energy dependences in the profiles are observed for B1929+10 and B0950+08.

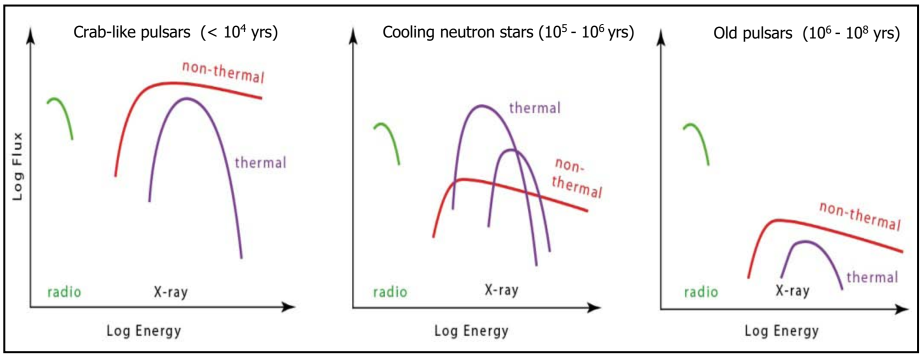

Fig.2 Emission properties of rotation-powered pulsars are varying with age. Magneto-spheric emission dominates in young and old pulsars, thermal emission in middle aged neutron stars. The hot polar caps observed in the latter may be formed by internal anisotropic heat flow rather than from high energy particles bombarding the polar caps. Hot polar cap emission may then decrease along with the cooling surface component so that old (cooled down) neutron stars have no observable heated polar caps.

References:
• Becker, W., Kramer, M., Jessner, A., et al. 2006, ApJ, 645, 1421
• Becker, W., Jessner, A., Kramer, M., et al., 2005, ApJ, 633, 367
• Becker, W., Weisskopf, M.C., Tennant A.F., et al., 2004, ApJ, 615, 908

W. Becker (MPE), C.Y. Hui (MPE), H.H. Huang (MPE)

Central Dynamics of Globular Clusters

Various observations, such as surface brightness profiles that deviate from the classical predictions, evidences for central rotation in some clusters, and the possible presence of a central black hole, challenge the classical view in which the central dynamics of globular clusters are dominated by two-body relaxation processes.

Introduction

Globular clusters have been classified into two groups due to their dynamical state. Clusters are classified as post-core-collapse when they show concentrated surface brightness profiles, with a steep central cusp; while pre-core collapse clusters are less concentrated and have flat central cores. Baumgardt et al. (2005) predict shalow central cusps for clusters containing a central black hole.

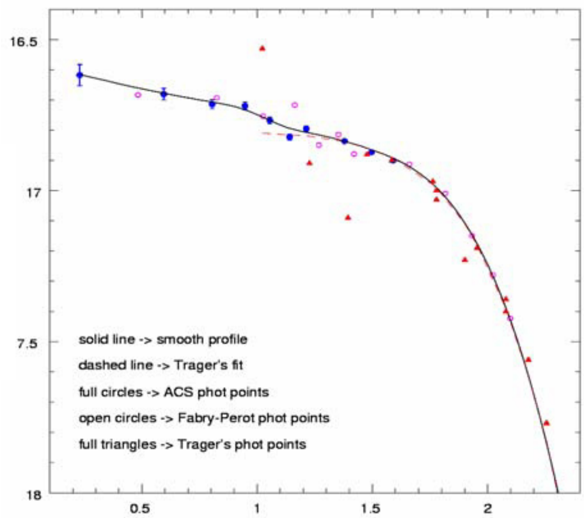

Fig 1. Surface brightness profile for Omega Centauri measured from integrated light using a F435W HST-ACS image.

Various observational results

Noyola & Gebhardt (2006) observe central surface brightness slopes with values intermediate between the expected for flat and cuspy cases. Rotation and flattening have been observed by van den Bosch et al. (2005) and Gebhardt et al (2002) in the central region of M15 and G1. Unusual pulsar configurations predict a central mass concentration for NGC 6752 (D'Amico, 2002) as well as a large central M/L value for the center of the cluster. These observations are inconsistent with expectations from two-body relaxation and could be explained by the presence of a single or a binary intermediate mass black hole in the center of the clusters.

Omega Centauri

When the surface brightness and the velocity dispersion profiles of Omega Centauri are compared with various dynamical models, they suggest the presence of a central intermediate mass black hole of 40,000 solar masses. Such a black hole places the cluster on the low mass extrapolation of the MBH-sigma correlation known for large galaxies.

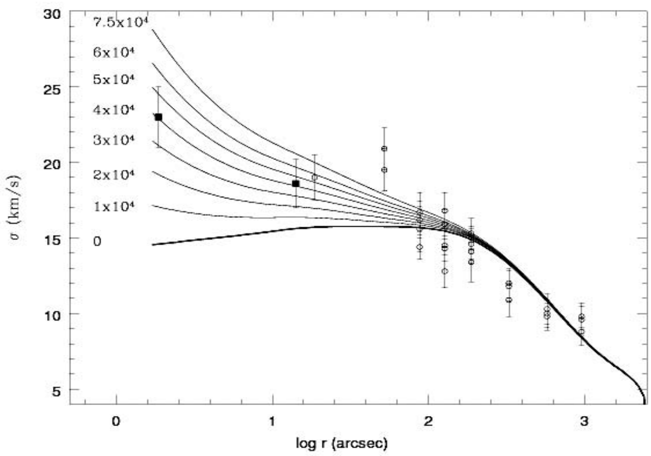

Fig 2. Observed velocity dispersion profile compared with spherical models with various black hole masses.

References:
- Baumgardt et al. 2005, ApJ, 620, 238
- D'Amico et al. 2002, ApJ, 570,89
- Gebhardt et al. 2002, ApJL, 578, 41
- Noyola & Gebhardt, 2006, AJ, 132, 447
- van den Bosch et al. 2006, ApJ, 641,852

Eva Noyola

The first stellar mass determination in the Galactic Center: the binary IRS16SW

We have photometrically and spectroscopically monitored the variable star IRS16SW in the Galactic Center. The detection of periodic modulations in its radial velocity combined to a periodic light curve clearly identifies this star as an eclisping binary. The orbital solution leads to a mass of ~ 50 $M_\odot$ for both components.

IRS16SW is one of the brightest source in K band images of the Galactic Center. From its spectroscopic morphology, it is classified as an Ofpe/WN9 star. It is thought to be related to Luminous Blue Variables, a class of stars displaying photometric and spectroscopic variability. Photometric studies have indeed revealed that the star is a regular variable with a period of 19.45 days. But its nature – binary or pulsating star – was not established.
To solve this problem, we have obtained spectroscopic data covering the photometric period. We have used the instrument SINFONI on the VLT. It was immediately clear that the star also showed spectroscopic variations, as seen In Fig. 1. The determination of radial velocities from the HeI 2.11 μm line unambiguously established the binary nature of the star. Fig. 2 indeed reveal a nice periodic variation of the radial velocities.
The mass of the components was estimated from fits of the light and radial velocity curves: both stars have a mass of about 50 $M_\odot$. This places them among the most massive stars known. This is also the first stellar mass determination in the Galactic Center, showing, if it was still needed, that the bright sources close to SgrA* are young, massive stars.

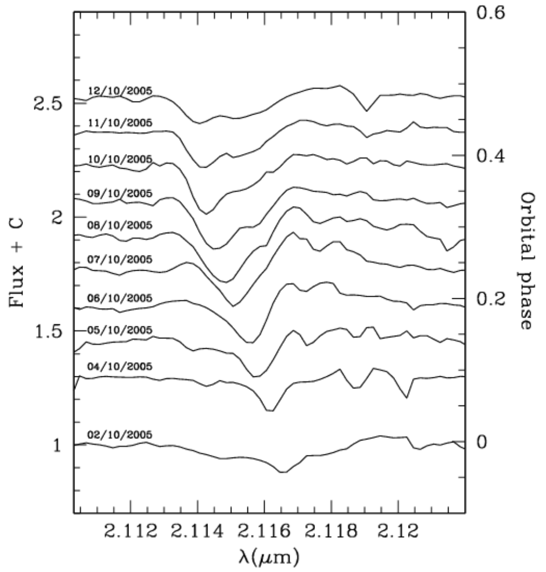

Fig. 1: Variation of the HeI 2.11 μm line as a function of orbital phase. The change in radial velocities is obvious.

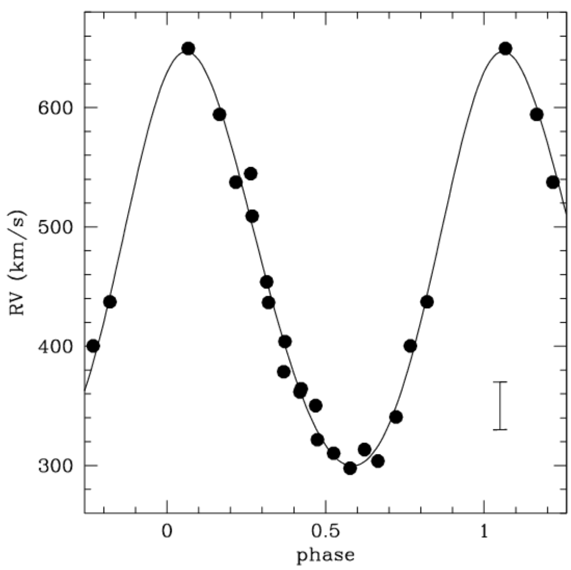

Fig. 2: Radial velocities derived from the HeI 2.11 μm feature together with the best orbital solution (solid line).

Reference:
• Martins, F, Trippe, S., Paumard, T., et al., 2006, ApJ, 649, L103

T. Ott, F. Martins, S. Trippe, T. Paumard, R. Genzel, G. Rauw, F. Eisenhauer, S. Gillessen, H. Maness, R. Abuter

X-ray monitoring of optical novae in M 31

We identified 34 X-ray counterparts for optical novae in M 31 based on ROSAT, XMM-Newton and Chandra archival observations, most of which can be classified as super-soft sources (SSS). This establishes optical novae as the major class of SSS in M 31. We determined X-ray light curves and spectra. Some novae unexpectedly showed short X-ray outbursts starting within fifty days after the optical outburst and lasting only two to three months. On the other hand two novae were still detected as SSS more than nine years after the optical outburst. The number of optical novae detected in X-rays is much higher than previously estimated (>30%). From the X-ray light curves we estimate the burned masses on the White Dwarf and the masses of the ejecta.

In contrast to our Galaxy, observing optical novae in the Andromeda galaxy M 31 offers the unique chance to learn more about the duration of the SSS state in novae with minimal effort. M 31 is the only nearby galaxy with many (more than 100 novae that exploded over the last five years) reported optical novae within the field of view of one XMM-Newton or Chandra observation. The left panel of the figure shows a contour plot of the inner area of the merged Chandra HRC-I archival observations of the M31 core from December 2004 to February 2005 overlaid on a Hα image from the Local Group Survey. All the optical novae are marked that

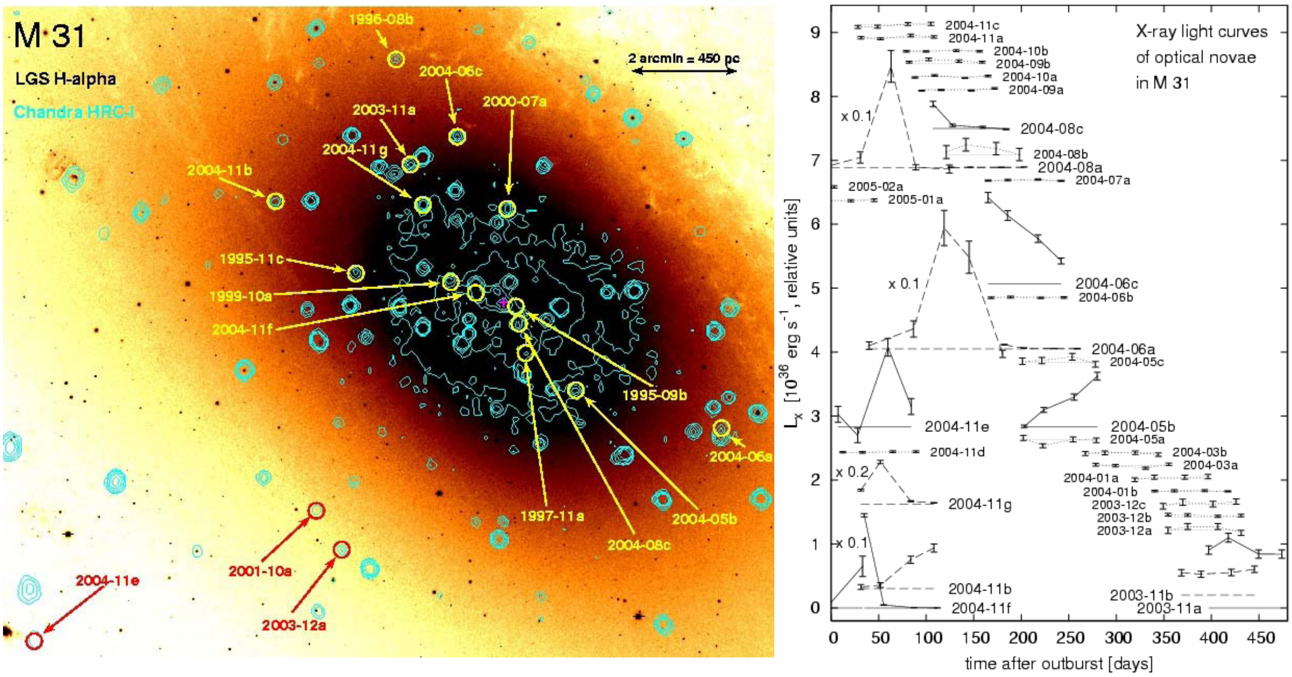

were detected in the X-ray observations. In the right panel, we show X-ray light curves for the optical nova counterparts observed with the Chandra HRC-I and ACIS-I instruments during 2004/5 within about a year after outburst. Detected sources are indicated by solid or dashed lines, not detected novae by dotted lines. Zero level for the individual light curves are indicated and have been shifted for clarity. Typical ejected masses derived from the start date of the SSS phase are 10^{-5} M_{sun}, the burned mass derived from the turn-off time of the SSS phase for most of the novae is below a few times 10^{-6} M_{sun}. Dedicated nova monitoring observations of the core of M 31 with XMM-Newton and Chandra are in progress.

References:

• Pietsch W., Fliri J., Freyberg M.J., Greiner J., Haberl F., Riffeser A., Sala G. 2005, A&A 442, 879
• Pietsch W., Haberl F., Sala G., et al. 2007, A&A in press (astro-ph 200612596)

W. Pietsch, R. Bender, V. Burwitz, M. Freyberg, J. Greiner, F. Haberl, G. Sala

Optical Polarization of the Crab Pulsar with extreme time resolution

We derived the polarization of the Crab pulsar and its environment with very fine time resolution (~10 μsec) and high statistics based on about 14 hours (selected out of 25 hours) of observations with the high-speed photo-polarimeter OPTIMA at the 2.5m Nordic Optical Telescope (NOT). This allowed the derivation of details in the degree and angle of linear polarization never before resolved. We compare the phase resolved optical polarization to the phase structure at radio wavelengths and find a surprising correspondence of optical polarization and radio emission. This subtle connection between presumed coherent and non-coherent emissions, which has also been detected between the giant radio pulses and the optical intensity of Crab, require more elaborate theoretical models than those available in the current literature.

Polarization of pulsed component

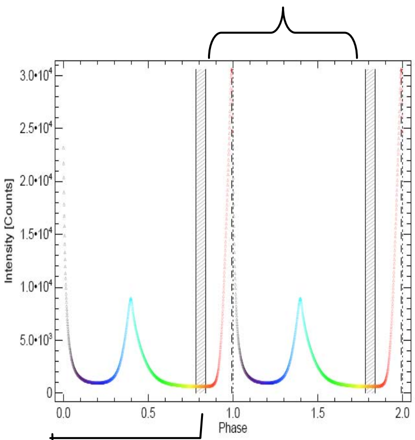

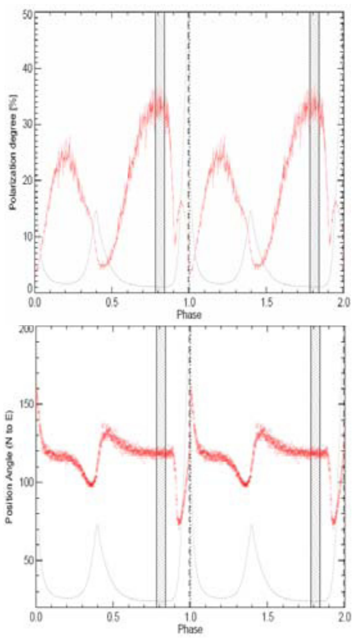

Zoom to Main Pulse

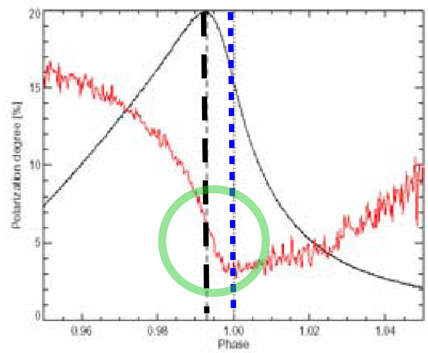

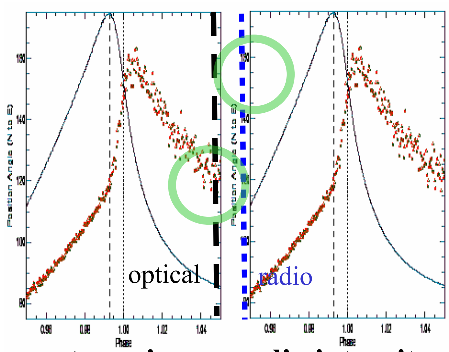

Results:

- **optical emission from the Crab pulsar is highly polarized, especially in the bridge and the 'off-pulse' phases.**

- **polarization minimum at maximum radio intensity; NOT aligned with the optical peaks**
- **optical LC and polarization extremely stable in time**
- **large swings of polarization angle**

Polarization of near Nebula (PSR-DC)

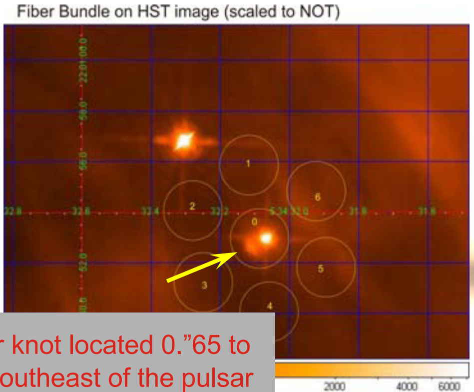

Inner knot located 0.”65 to the southeast of the pulsar (HST image)

OPTIMA fiber array pick-up

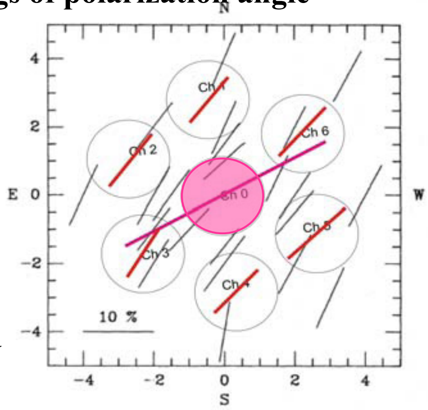

A. Słowikowska, G. Kanbach, A. Stefanescu

GRO J1655-40: from ASCA and XMM-Newton Observations

We have analysed three ASCA observations (1994, 1995 and 1997) and three XMM-Newton observations (2005), in all of which the source was in high/soft state. We modeled the continuum spectra with relativistic disk model *kerrbb*, estimated the spin of the central black hole, and constrained the spectral hardening factor f_{col} and the source distance. If *kerrbb* model applies, for normally used value of f_{col} (1.7), the distance cannot be very small, and f_{col} changes with observations.

Background **1.** The microquasar GRO J1655-40 underwent X-ray out-bursts in 1994-1995, 1996-1997 and 2005. Its geometric parameters are considered best determined: mass M_{BH}=7.0±0.2M_{sun}, inclination angle θ=69.50°±0.08[1], distance D=3.2±0.2kpc[2], which makes it a good laboratory of studying black holes and the environments. **2.** The spin of the central black hole has been estimated by various authors with various methods (see, e.g., [3][4][5] [6]), and the reported values range from 0.2[4] to 0.996[5]. **3.** In estimating black hole spin from continuum spectral modeling, most disk models treat the disk as multi-temperature black-body rings and the derived spin value depends on the color correction factor $f_{col}=T_{col}/T_{eff}$. The normally used value of f_{col} is 1.7, following Shimura & Takahara [7], but it should not be constant (see, e.g., [8]). **4.** The widely accepted distance 3.2±0.2 kpc was challengedby Foellmi et al.[9], who gave an upper limit of 1.7 kpc. This will also change the spin estimation.

Observations, data reduction and model fitting

In the six selected observations (three ASCA observations in 1994-09-27, 1995-08-15 and 1997-02-26, and three XMM-Newton observations in 2005-03-14, 2005-03-15, and 2005-03-16, respectively), the source was in high/soft state. For ASCA, only GIS2 data were used, after gain correction and deadtime correction. For XMM-Newton, only Epic-pn data were used, after correction for rate-dependent Charge-Transfer-Efficiency[10].

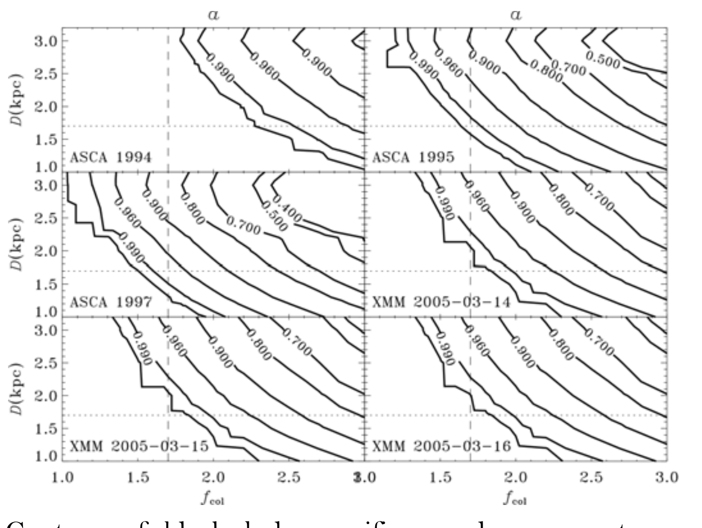

Contour of black hole specific angular momentum a versus distance D and f_{col}. The dotted lines and dashed lines indicate D=1.7kpc, and f_{col}= 1.7, respectively.

The relativistic disk model *kerrbb* in *XSPEC* was used in the fitting. We let f_{col} vary from 1.0 to 3.0, and distance D vary from 1.0 kpc and 3.2 kpc. For each combination of f_{col} and D, we fitted each data set and obtained a spin value a, if the fit was acceptable ($\chi^2/dof<2$). The contour of the derived spin a over D and f_{col} are shown in the figure.

Conclusion

1. for the normally used f_{col} value 1.7, *kerrbb* model does not favor small distance;

2. because the black hole spin and the source distance should be constant in such a short time span, f_{col} changes dramatically between these observations.

References

[1] Orosz, J. A., & Bailyn, C. D. 1997, ApJ, 477, 876
[2] Hjellming, R.M. & Rupen, M.P. 1995, Nat, 375, 464
[3] Zhang, S. N., Cui, W., & Chen, W. 1997, ApJ, 482, L155
[4] Abramowicz, M. A., & Kluźniak, W. 2001, A&A, 374, L19
[5] Aschenbach, B. 2004, A&A, 425, 1075
[6] Shafee, R., et al. 2006, ApJ, 636, L113
[7] Shimura, T. & Takahara, F. 1995, ApJ, 445, 780
[8] Merloni, A., Fabian, A.C., Ross, R.R. 2000, MNRAS, 313, 193
[9] Foellmi, C., Depagne, E., Dall, T. H., & Mirabel, I. F. 2006, A&A, 457, 249
[10] Sala, G., et al 2006, A&A, 461, 1049

Xiao-Ling Zhang, Shuang Nan Zhang, Gloria Sala, Jochen Greiner, Yuxin Feng, Yangsen Yao

The black-hole candidate XTE J1817-330 as seen by XMM-Newton and INTEGRAL

The galactic black hole candidate XTE~J1817-330 was discovered in outburst by RXTE in February 2006 (Remillard et al. Atel#714). We present Target of Opportunity Observations performed with XMM-Newton (13 March 2006) and INTEGRAL (15-18 February 2006) aimed at confirming the existence of a black hole in this X-ray binary and determining its main properties.

A typical black-hole binary X-ray spectrum: The joint XMM-Newton and INTEGRAL spectra, covering from optical to soft gamma rays, are fit with the standard two-component model for black hole binaries, consisting of a thermal accretion disk model (with kT_{max}= 0.65(+/-0.01) keV, R_{in}=13(+/-5)R_G=13(+/-5)GM/c^2) plus a power law (Γ=2.7+/-0.3)), accounting for the hot corona (fig. 1). Both the maximum disc temperature and the inner most disc radius point to a black hole as the compact accreting object.

Fig 1: XMM-Newton and INTEGRAL spectra (**upper panel**) and best-fit model (**lower panel**).

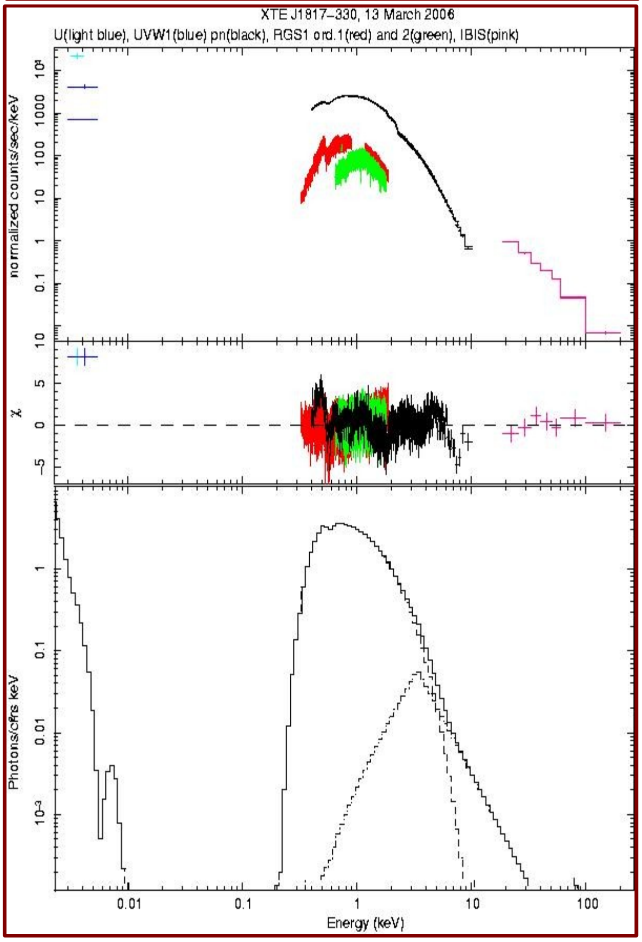

ISM absorption: The soft X-ray spectrum, together with the optical and UV data, show a low hydrogen column density towards the source, N_H=1.86(+/-0.01)x$10^{21}cm^{-2}$. Several interstellar absorption lines are detected in the RGS spectrum (fig 2.): OIK-alpha, OIK-beta, OII, OIII and OVII, which trace both cold and hot components of the ISM. The absorbing column density is compatible with the interstellar value, which locates the source behind the galactic slab of ISM, i.e., sets a lower limit for the distance of 1 kpc.

Fig 2: RGS spectrum showing several ISM lines.

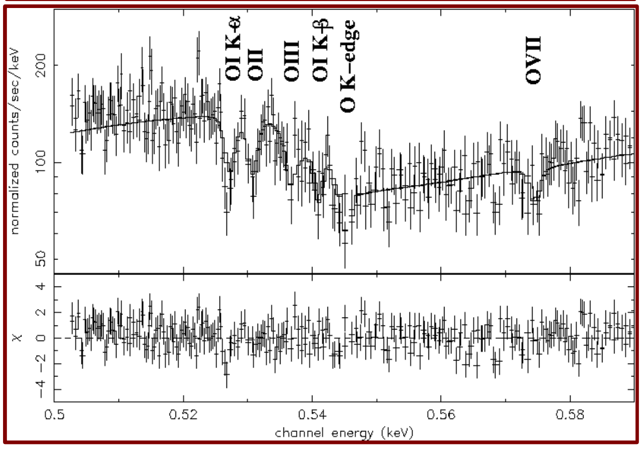

Fig 3: Accretion rate vs black hole mass.

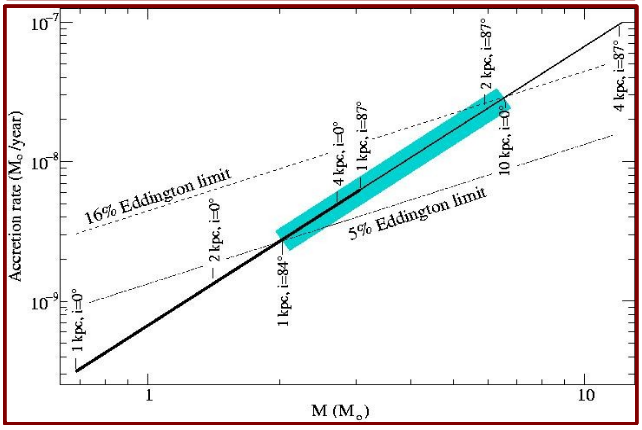

Black-hole mass and distance:
The comparison of the accretion rate vs. black-hole mass derived from the best-fit disc model normalization for several distances and inclinations with the Eddington limit (fig 3.) provides an upper limit for the distance of 10 kpc, and constraints the black hole mass to be in the range 3-6.5$M_\odot$.

References:

• Sala. Greiner, Ajello, Bottacini, Haberl, A&A, submitted

Gloria Sala, Jochen Greiner, Marco Ajello, Eugenio Bottacini, Frank Haberl

Polarisation studies of GRB041219a

Linear polarisation in γ-ray burst prompt emission is an important diagnostic with the potential to significantly constrain models. The spectrometer aboard *INTEGRAL*, SPI, has the capabilty to detect the signature of polarisation from a bright γ-ray source. GRB041219a is the most intense, bright burst localised by *INTEGRAL* with a fluence of 5.7×10^{-4} erg cm^{-2} and is an ideal candidate for such a study. Our results over several energy ranges and time intervals are consistent with a polarisation level of about 60%, but at a low level of significance (~2σ).

Aims

Polarisation can be measured using multiple events scattered into adjacent detectors because the Compton scatter angle depends on the polarisation of the incoming photon. Linearly polarised γ-rays preferentially scatter perpendicular to the incident polarisation vector. A search for linear polarisation in the most intense pulse of duration of GRB 041219a (Fig 1) was performed in the 100-350 keV, 100-500 keV and 100 keV-1 MeV energy ranges. It was possible to divide the events into six directions in the first two energy ranges using the kinematics of the Compton scatter interactions.

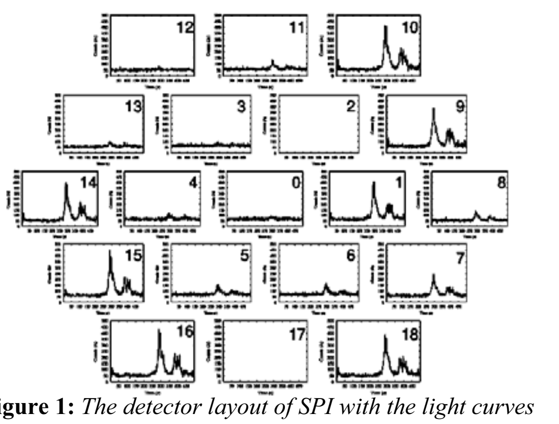

Figure 1: *The detector layout of SPI with the light curves of GRB041219a showing the count rate per detector. Detectors #2 and #17 are not operational.*

Method

The multiple event data from the spectrometer was analysed and compared with the predicted instrument response obtained from Monte-Carlo simulations using the GEANT 4 INTEGRAL mass model. The χ^2 distribution between the real and simulated data as a function of the percentage polarisation and polarisation angle was calculated for all three energy ranges. The degree and angle of polarisation were obtained from the best-fit value of χ^2.

Results

A weak signal consistent with polarisation was found throughout the analyses. The degree of linear polarisation in the brightest pulse of duration 66 s was found to be 63(+31/−30) % at an angle of 70(+14/-11) degrees in the 100-350 keV energy range. The degree of polarisation was also constrained in the brightest 12 s of the GRB and a polarisation fraction of 96(+39/-40) % at an angle of 60(+12/-14) degrees was determined over the same energy range. However, despite extensive analysis and simulations, a systematic effect that could mimic the weak polarisation signal could not be definitively excluded.

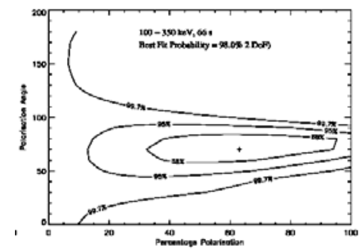

Figure 2: *Contour plots of the polarisation as a function of polarisation angle showing the 68%, 95 % and 99.7% contours for the 100-350keV energy range.*

Conclusions

Our results over several energy ranges and time intervals are consistent with a polarisation signal of about 60% at a low level of significance (~2σ). The procedure described here demonstrates the mehod of using SPI as a polarimeter.

References:

• McBreen et al 2006, A&A,455, 433

McGlynn et al 2007, A&A, in press.

S. McBreen, S. McGlynn, D. Clarke, L. Hanlon, A. J. Dean, B. McBreen, D. Willis

PROBING GRB ENVIRONMENTS
through emission lines

The energy output by the Gamma-Ray Burst (GRB) is expected to **photoionise** the surrounding medium out to large radii, which then cools and **produces line emission** that is particularly strong in the optical. The variability of these emission lines is a **strong diagnostics of the gas density and geometry** in the close environment of the burst, which is not easily accessible by, i.e. absorption lines.We present the results of a **spectral time-series analysis** of the host galaxy of **GRB 990712** observed up to ~6 years after the burst.
We find that the emission line fluxes show no variation within the uncertainties up to 6 years after the burst, and we use the measured line intensities to **set a limit on the density** of the gas **within a few parsecs of the burst location**. This is the first time that emission from cooling GRB remnants is probed on time scales of years.

One of the indicators about the nature of the GRB progenitor is the density of the circumburst environment. The GRB radiation is expected to photoionise the circumburst environment and thus, lead to time dependent absorption, emission and recombination line features. The line fluxes and recombination time-scale depend on the density and temperature of the circumburst environment, which are expected to be different than the normal interstellar medium values, around massive stars. If a region of radius R is heated and ionized by the burst radiation, the maximum emission will occur after a time t ~R/c ~3 yr (R/pc), due to light travel times from different parts of the region.
We present the spectroscopic observations of GRB 990712 (z = 0.433). Our observations, up to 6 years after the burst, allow us to probe an emitting region of at most 2 pc in size. All of the observed lines have constant fluxes over ~6 years after the burst.

Table 1. Log of observations.

Date	Instrument	Grism	Coverage (nm)	Exposure time (s)
14 Jul. 1999	FORS1	150I	370–770	2400
11 Nov. 1999	EFOSC	Gr6	400–800	1800
06 Jun. 2002	FORS1	600R	525–745	4320
17 Jul. 2004	FORS2	600RI	512–845	2400
05–06 Jul. 2005	FORS2	300V	445–850	7200

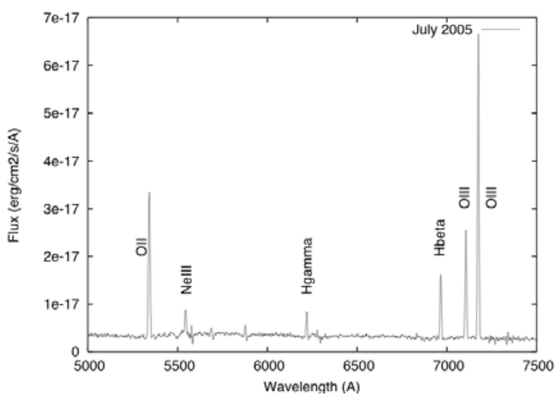

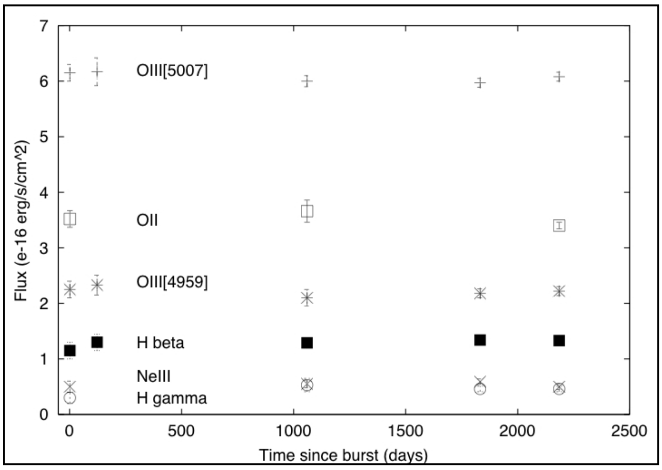

Since the line fluxes are constant, the contribution of the emission from the cooling gas to the OIII (5007) line luminosity has to be below the flux uncertainty level (10%, corresponding to a luminosity of about 3×10^{40} erg/s).

Comparing this luminosity with the luminosity of OIII line obtained from numerical simulations of cooling GRB remnants (Perna et al. 2000), we set **a density upper limit of 6000 cm^{-3}** within a region of about **2 pc surrounding the burst**. This is the first time that the density of a circumburst environment is constrained based on host galaxy emission line fluxes.

References:
• Küpcü Yoldas, A., Greiner J., Perna, R. 2006, A&A 457, 119 (and references therein)

Aybüke Küpcü Yoldaş (MPE), Jochen Greiner (MPE), Rosalba Perna (JILA)

The Gamma-Ray Burst Host Galaxy Population

GHostS – GRB Host Studies – is the largest public database including spectroscopic and photometric information on galaxies hosting gamma-ray bursts (GRBs). At this time it contains 39 galaxies (blue histogram), i.e. 2/5 of all GRBs with known redshift (99 objects, empty histogram).

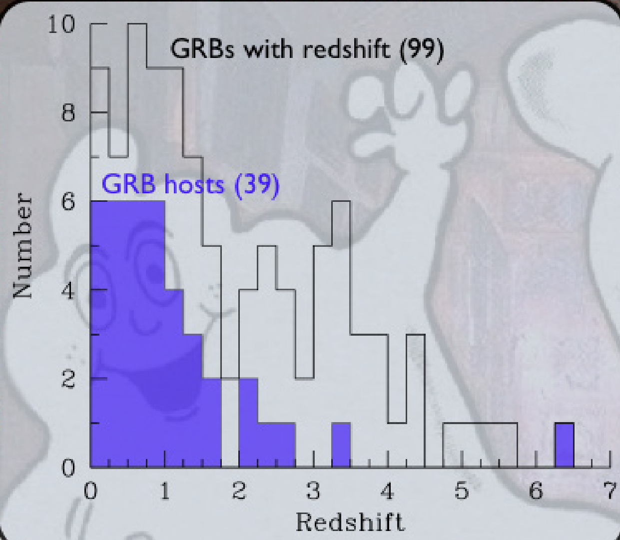

The total Stellar Mass of GRB host galaxies (blue histogram) was derived by fitting the optical-NIR SED, using a complex set of star formation histories (Glazebrook et al. 2004). 87% of the hosts have stellar masses $M_* \leq 10^{9.8}$ $M_\odot$. The empty histogram is from the 262 LBGs at 1.4<z<3 complete for $M_* > 10^{10.0}$ $M_\odot$ (Reddy et al. 2004) normalized to the GRB histogram for $M_* > 10^{10.0}$ $M_\odot$. GRB science is unique in identifying a large fraction of low-mass high-z galaxies. It is now widely recognized that low-mass galaxies had a major role in the star-formation history of the universe for z<1.5 (Juneau et al. 2005; Savaglio et al. 2005).

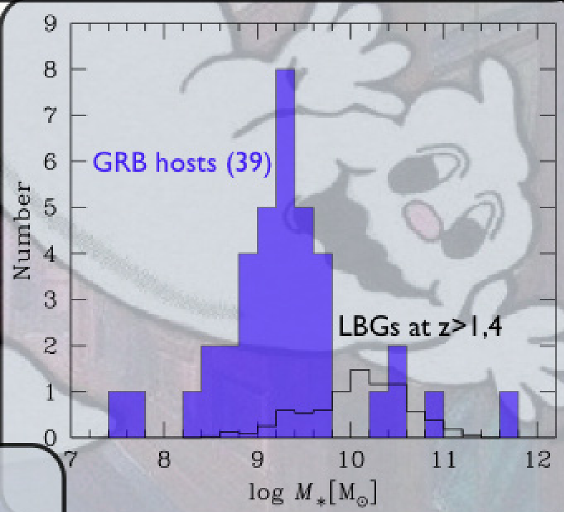

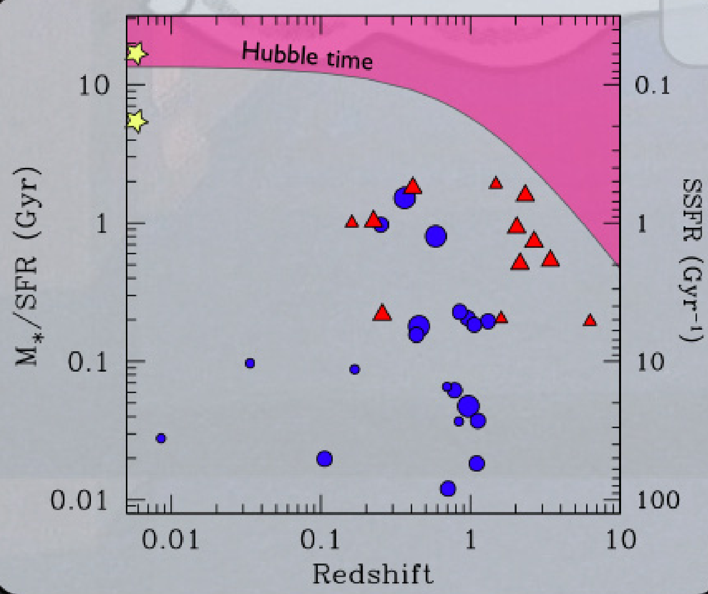

The Growth Time Scale $\rho_* = M_*/SFR$ (specific star formation rate SSFR on the left y-axis) is the time required by a galaxy to build its observed stellar mass, assuming the observed SFR is constant over its past history. The SFR is measured using [OII] or Hα emission line (blue dots) or UV emission from SED best fit (red triangles). The size of the symbols is proportional to the stellar mass of the galaxy, and show that small galaxies tend to be more starforming than big galaxies. The yellow stars mark the SSFR for MW and LMC. In 63% of the GRB hosts ρ_* is shorter than 250 Myr (SSFR higher than 4 Gyr^{-1}). These galaxies can be considered bursty. The curve marks the age of the universe as a function of redshift.

References:
http://www.grbhosts.org
Glazebrook et al. 2004, Nature, 430, 181
Juneau et al. 2005, ApJ, 619, L135
Reddy et al. 2006, ApJ, 653, 1004
Savaglio et al. 2005, ApJ, 635, 260

S. Savaglio (MPE) - K. Glazebrook (Swinburne University)- D. Le Borgne (Saclay)

Testing the inner Galaxy structure ...

... with spectroscopy of the ^{26}Al 1.8 MeV line

We analyse observations of the inner Galaxy performed with the Spectrometer on INTEGRAL (SPI) and compare them with models of the spatial distribution and the kinematics of the radioactive isotope ^{26}Al. We use the SPI data to judge the plausibility of different models that differ in the presence or absence of components such as the thick disk or thin disk and the shape of the Galactic rotation curve.

^{26}Al is produced mainly in massive stars. Its presence therefore indicates that star formation was active sometime during approximately the previous few tens of million years. Because of the penetrating nature of the 1.8 MeV gamma rays from its decay, we can receive radiation from sources throughout the Galaxy. Measurements of the Doppler shift help localise the source regions along the line of sight. Doppler broadening of the line tells us about the source kinematics.

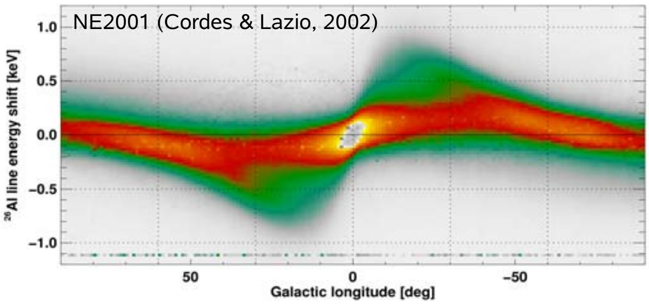

Model prediction of the ^{26}Al 1.8 MeV intensity as a function of Galactic longitude and Doppler shift.

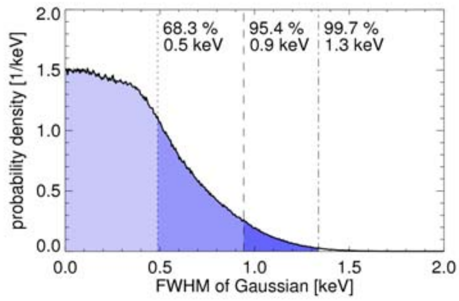

Probability distribution of the width of the 1.8 MeV emission from the inner radian of the Galaxy.

The figure to the right shows three reference templates used to model the SPI data. We use two different approaches for comparing our data with these models:

- Measure the width of the line seen from a particular source region (figure at top right)

  In this approach, the instrumental data are modelled as the sum of a model describing the instrumental background and one describing the spatial distribution of the ^{26}Al emission. This yields a spectrum which is in turn modelled as a combination of the instrument energy response (in the case of SPI, this is a distorted Gaussian peak whose detailed shape is calibrated with continuously measured background lines) and the shape of the emission from the sky.

- Observe source regions of emission in narrow energy intervals and compare the observed spectra with the model predictions.

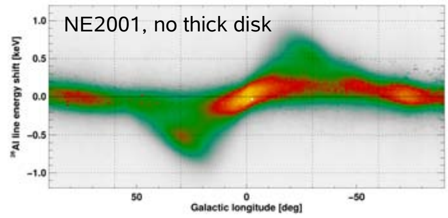

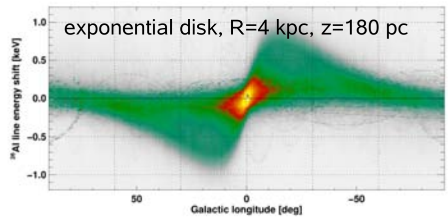

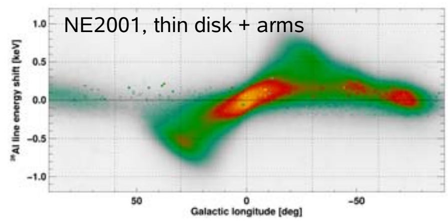

References:
• Kretschmer, K., Diehl, R. & Hartmann, D. H., 2003, A&A, 412, L47-L51
• Cordes, J. M. & Lazio, T. J. W., 2002, astro-ph/0207156

K. Kretschmer, R. Diehl, W. Wang, H. Halloin

SPI Observations of Diffuse ^{60}Fe in the Galaxy

We analyzed the three years of data on gamma-ray emission from the Galactic plane accumulated by the spectrometer SPI on board INTEGRAL. We detect the γ-ray lines from ^{60}Fe decay at 1173 and 1333 keV, obtaining an improvement over our earlier measurement of both lines with now 5 σ significance for the combination of the two lines. The average flux per line is (4.4 ± 0.9) x 10^{-5} ph cm^{-2} s^{-1} rad^{-1} for the inner Galaxy region. Deriving the Galactic ^{26}Al gamma-ray line flux with using the same set of observations and analysis method, we determine the flux ratio of ^{60}Fe/ ^{26}Al gamma-rays as 0.148 ± 0.06, which can constrain the present theoretical predictions.

Origin of 60Fe sources in the Galaxy

^{60}Fe is the long-lifetime radioactive isotope, with the mean decay time of 2x10^6 years. It is produced through successive neutron captures on Fe isotopes, e.g. ^{56}Fe, in neutron-rich environment (see Fig. 1). Hence, ^{60}Fe is mainly produced and ejected by supernovae.

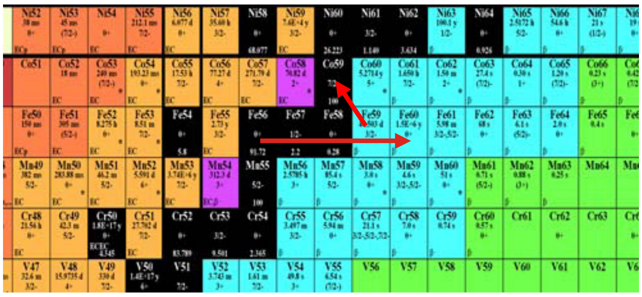

Fig. 1: ^{60}Fe production by n-capture on Fe isotopes. ^{59}Fe β decay would produce a leak.

Ratio of ^{60}Fe / ^{26}Al

Using the same data but different energy bands, we can derive the flux ratio of ^{60}Fe/^{26}Al in a self-consistent way:
F(^{60}Fe)/F(^{26}Al) ~ (14.8±6.0)%

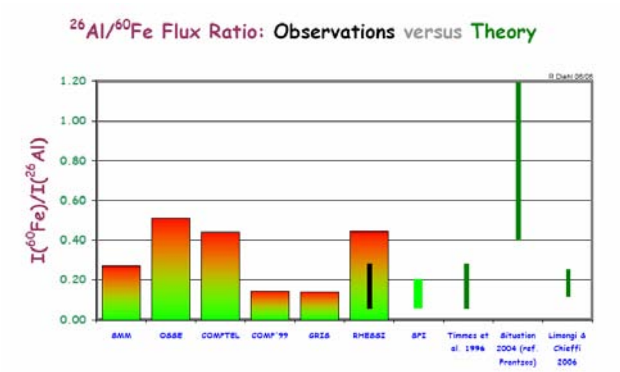

Fig. 4: Comparison between predictions and observational limits. Improved models agree with present limits on ^{60}Fe/^{26}Al gamma-ray flux ratio. Uncertainties are still large, improvements are needed.

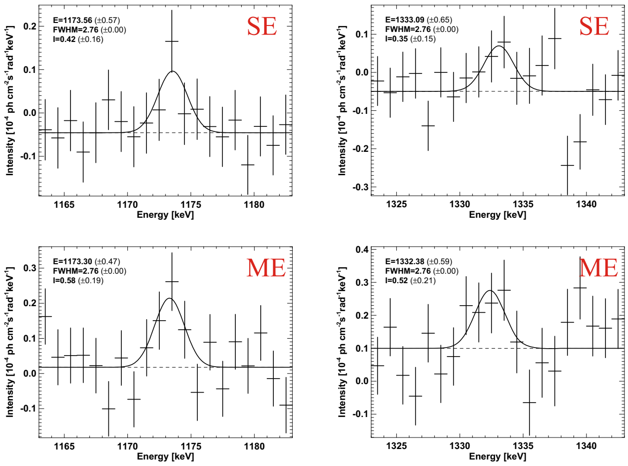

Fig. 2: The spectra of two gamma-ray lines from ^{60}Fe with 3-year SPI data (single-events SE and multiple-events ME databases, from Wang et al. 2007).

Result from Summed ^{60}Fe Lines

Superimposed bins are for zero at 1173 and 1333 keV with the detection of significance 5 σ, which is better than previous results (Smith 2004; Harris et al. 2005).

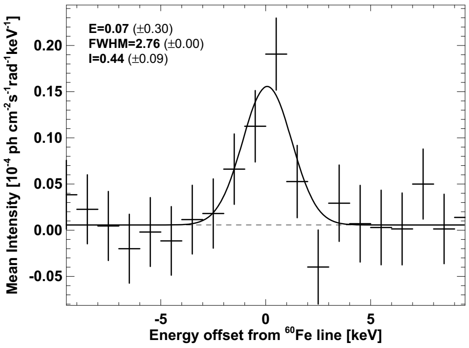

Fig. 3: Combined spectrum of ^{60}Fe from the inner Galaxy. The narrow line feature is similar to the 26Al line (Diehl et al. 2006).

References:

- Diehl, R. et al. 2006, A&A, 449, 1025
- Harris, M. et al. 2005, A&A, 433, L49
- Smith, D. 2004, ESA-SP, 552, 45
- Wang, W. et al. 2007, A&A, submitted

Wei Wang, and M. Harris, R. Diehl, et al.
wwang@mpe.mpg.de

Galactic γ-ray emission and source populations

Gamma-ray emission from the plane of the Galaxy shows a prominent excess around 1 GeV above that predicted from interstellar processes. While it is possible to explain this by some - rather extreme - variations in the cosmic-ray spectrum, or by more exotic processes involving e.g. dark matter, a more natural explanation may be populations of undetected compact sources. These could be for example pulsars. We present a population synthesis study of the EGRET sources and show how the GeV excess could arise in this case. This is combined with the latest predictions from the GALPROP cosmic-ray propagation project for interstellar emission to give a satisfactory account of the emission without special assumptions. The upcoming GLAST mission should resolve the issue by detecting many more of the sources in the Galaxy and measuring their spectra.

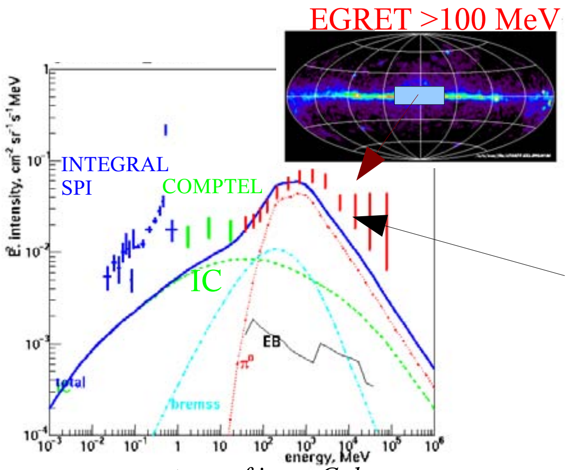

γ-ray spectrum of inner Galaxy: data compared with prediction using locally measured cosmic-ray spectra

The diffuse continuum gamma-ray emission from the Galactic plane above 100 MeV is produced by cosmic-ray interactions in the interstellar medium via pion-decay and inverse-Compton scattering. However detailed modelling using the GALPROP code and the directly-observed proton and electron spectra fails to reproduce the EGRET data > 1 GeV: this is known as the GeV excess. It is possible to explain it if the cosmic-ray spectra in the solar vicinity are not typical, or by more exotic processes involving e.g. dark matter.

Populations of undetected hard-spectrum compact sources, in particular pulsars, may offer a viable alternative.

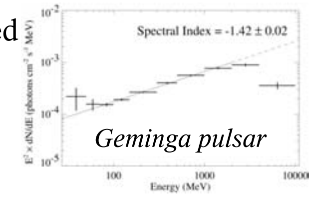

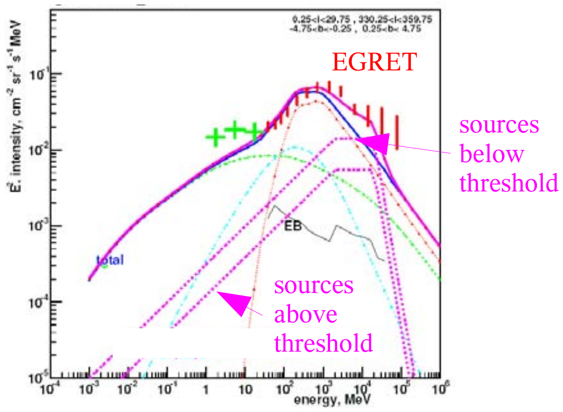

γ-ray spectrum of inner Galaxy: interstellar emission model with emission from population of hard-spectrum sources added

Population synthesis of sources with spectra based on known γ-ray pulsars having a luminosity function which is consistent with the 3rd EGRET source catalogue can explain the emission.

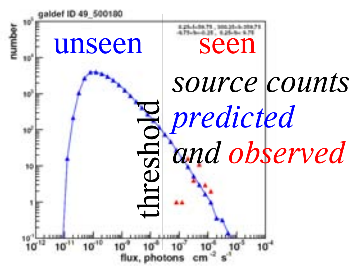

GLAST, to be launched later this year, will detect large numbers of pulsars and other source populations, and this should allow their contribution to the GeV excess to be determined precisely.

•**References:**
•Strong et al. 2004 ApJ 613, 962
•Strong, Moskalenko & Ptuskin, 2007, Annual Reviews of Nuclear and Particle Science, Vol 57.

A. Strong

Physics of the Solar System

Plasma Convection in Earth's Magnetosphere

Measurements by the Electron Drift Instrument on board the Cluster spacecraft at large distances within the Earth's magnetosphere have been used to construct detailed maps of the plasma convection in Earth's ionosphere. The derived patterns are exactly what is expected from magnetic reconnection between the interplanetary magnetic field and Earth's magnetic field, with the addition of some feedback from the ionosphere.

When the interplanetary magnetic field (IMF) that is carried by the solar wind reconnects with the terrestrial magnetic field, flux tubes are carried by the solar wind over the poles into the magnetotail, where they eventually reconnect once more and are transported sunward, until they again meet the IMF, allowing the whole process to repeat. The result is a large-scale internal circulation of the magnetospheric plasma and magnetic flux that extends all the way down to the ionosphere, forming a two-cell pattern, with anti-sunward flow over the polar caps, returning at lower latitudes to the dayside. Since plasma flow across a magnetic field produces an electric field, this convection is equivalent to an electric potential across the polar caps, We have used vector measurements of the plasma velocity made by the Electron Drift Instrument on Cluster between February 2001 and March 2006, to derive statistical maps of the convection as a function of the IMF orientation.

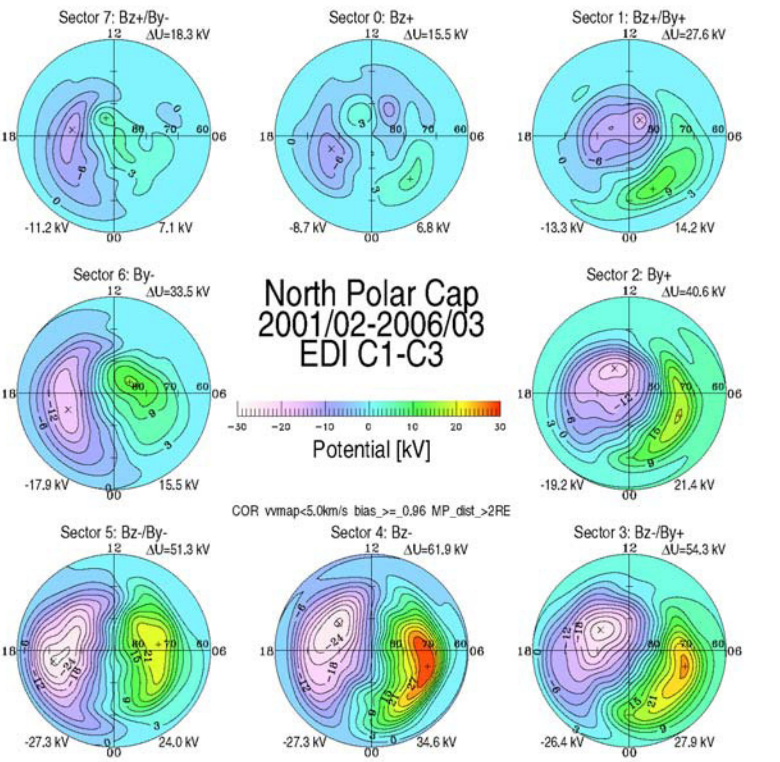

Fig.1: Polar cap electric potentials, obtained by mapping the velocity measurements made on Cluster into the ionosphere, for eight 45-degree sectors of the IMF in the plane transverse to the Sun-Earth line, starting from northward (Sector 0) and continuing in a clockwise sense, with Sector 4 for southward IMF. The background colour shows the value of the potential. Lines are drawn at fixed values of the potential. The minimum and maximum potentials are listed at the bottom, and the total potential drop at the upper right of each map. Because of the equivalence between convection and electric potentials, the contours can also be interpreted as showing the direction of the convective flow.

Cluster measurements are obtained at distances up to 19 Earth-radii, and are therefore mapped down to ionospheric altitudes, assuming that the magnetic field lines threading the Cluster orbit are equipotentials. Fig.1 shows the derived electric potential maps for the northern hemisphere for 8 directions of the IMF. In general, these maps are very similar to what is known from direct ionospheric measurements, confirming that the magnetic field lines are indeed equipotentials. For southerly IMF (Sectors 3-5), the expected two-cell convection pattern is clearly evident. When the IMF lies in the ecliptic plane (Sectors 2 and 6), the pattern becomes skewed, as expected from the tension in the reconnected field lines. The lack of mirror symmetry between the patterns for Sectors 2 and 6, as well as the skewing already apparent for southward IMF (Sector 4), can be understood in terms of the day-night drop in ionospheric conductivity. This shows that the convection at Cluster is a combination of solar wind and ionospheric effects. For northward IMF (Sector 0) two new cells appear on the dayside that have not been observed before. They are evidence for reconnection occurring with terrestrial field lines that are extending into the magnetotail.

G.Paschmann, S. Haaland and M. Förster, with the entire EDI team

Ionic Charge States of Solar Energetic Particles: a Clue to the Source

Measurements of the energy dependence of the ionic charge of heavy ions in solar energetic particle events allow to infer the location of the source. In *impulsive* events, directly related to solar flares, the acceleration takes place in the low corona, at altitudes < 0.3 R_S. In *gradual* events, the particles are accelerated at the coronal and interplanetary shock. High charge states at high energies suggest a contribution of flare particles in the accelerated population that are accelerated near the Sun.

New measurements of ionic charge states with advanced instrumentation onboard the SAMPEX, SOHO, and ACE spacecraft showed that the mean ionic charge of heavy ions in solar energetic particle (SEP) events is varying with energy (Klecker et al., 2006a). In ^{3}He- and Fe-rich events (*impulsive events*), directly related to the flare process, the mean ionic charge, <Q>, of heavy ions increases significantly with energy in all events, for Fe from ~12 to ~20 in the small energy range of 0.10 to 0.55 MeV/n (Fig. 1). This systematic increase of $<Q>$ can only be explained by ionisation in a dense environment. Model calculations including ionization and recombination processes in the solar corona show that $<Q>$ approaches asymptotically the equilibrium upper limit $<Q>_{eq}$ (Fig.1, dotted lines). The equilibrium mean charge depends on the density N and the acceleration time scale τ , with $(N\tau)_{eq}$ ~10^{10} - 10^{11} s cm^{-3} for ~0.2–1.0 MeV/n Fe ions. For acceleration time scales of ~10 to 100 s, compatible with X-ray and electron measurements in these events, this corresponds to densities of ~10^8 - 10^{10} cm^{-3}, i.e. ionization and acceleration of the particles take place very low in the corona, at altitudes <0.3 R_S. It has been demonstrated recently that the apparent difference between the observed and predicted energy dependence of Q can be explained by interplanetary propagation effects: low energy particles loose a significant fraction of their energy between the Sun and 1AU. Models combining acceleration, charge stripping and propagation at the Sun with interplanetary propagation are able to reproduce the observed energy dependence of the ionic charge of iron (Fig. 2, Dröge et al., 2006).

In large SEP events related to coronal mass ejections (CMEs) and coronal/interplanetary shocks (*gradual events*), the mean ionic charge at energies < 1 MeV/n is generally constant and consistent with solar wind charge states. At higher energies a large event-to-event variability is observed, with $<Q>$ of Fe often as high as ~18-20 at energies of 10s of MeV/n (Klecker et al., 2006b). This can be explained by a contribution of flare particles, further accelerated to high energies by the coronal or interplanetary shock.

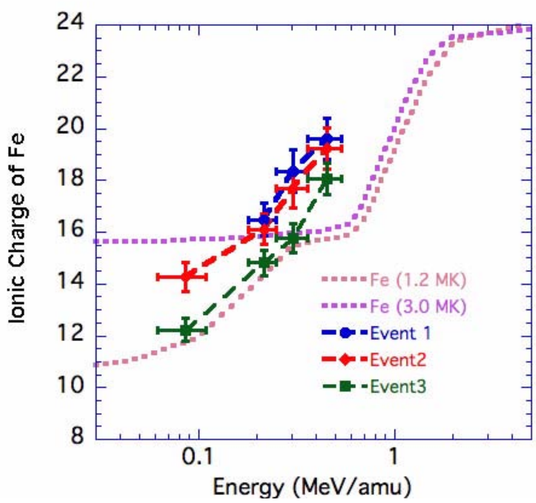

Fig. 1: The energy dependence of <Q> of Fe in three representative impulsive events. Also shown is the energy dependence of $<Q>_{eq}$ due to ionization effects in a dense environment for a temperature of 1.2 10^6 K and 3 10^6 K (Klecker et al., 2006c).

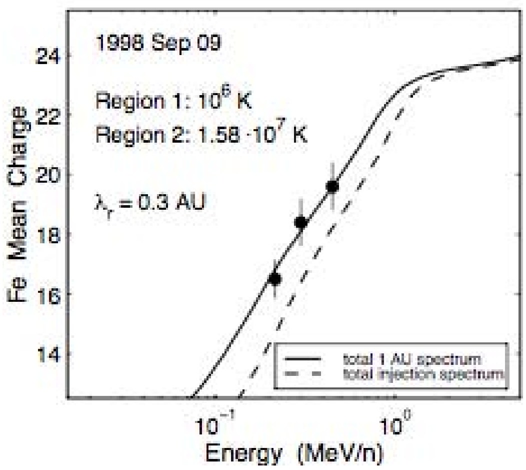

Fig.2: Calculated mean charge of iron at r_0 =0.05 AU (dashed line) and at 1 AU after the interplanetary transport, assuming a constant radial mean free path λ_r= 0.3 AU (solid line). Filled circles denote ACE observations of the 1998 September 9 event (Dröge et al., 2006).

References:
- Dröge, B., Y.Y. Kartavykh, B. Klecker, and G. M. Mason, *Ap. J.,* 645, 1516 – 1524, 2006.
- Klecker, B., E. Möbius, M.A. Popecki, Space Science Rev., 124, 289-301, 2006a.
- Klecker, B., H. Kunow, H.V. Cane, et al., Space Science Rev., 123, 217-250, 2006b.
- Klecker, B., E. Möbius, M. A. Popecki, et al., Adv. Space Res. 38, 493–497, 2006c.

B. Klecker (in collaboration with E. Möbius, M.A. Popecki, UNH)

γ-rays from halos around the Sun and stars

We study the Sun as an extended source of gamma-ray emission, produced by inverse-Compton scattering of cosmic-ray electrons with the solar radiation. This emission contributes to the diffuse gamma-ray background even at large angular distances from the Sun. Analyzing the EGRET database, we find clear evidence for the emission from the Sun and its vicinity, compatible with our predictions. Considering the same process from the regions around stars, we expect the inverse Compton gamma-ray emission, to be clumpy, and some of the most luminous stars could possibly be detectable by GLAST.

The inverse Compton (IC) emission from the Sun has been computed using the modulated cosmic-ray electron spectrum, the solar photon field and the Klein-Nishina cross section with the anisotropic formulation. The figure on the right shows the IC intensity as a function of angular distance from the Sun, compared with the extragalactic background (EGB) for different solar modulation values.

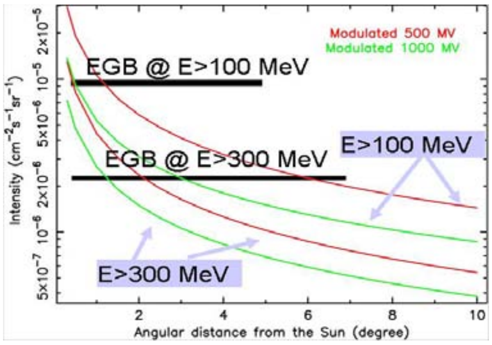

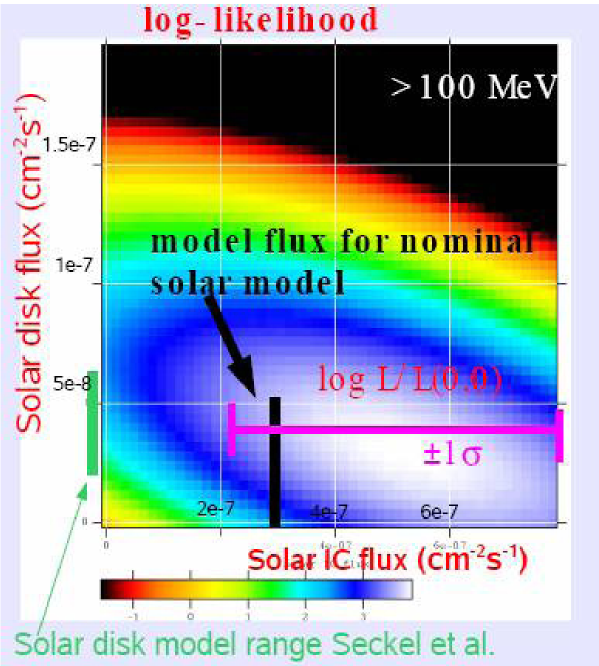

We have analyzed the EGRET data for the solar emission (for details see poster by Petry et al.). The log-likelihood is displayed as a function of solar disk flux and extended flux compared with the predicted model of solar inverse Compton flux for E >100 MeV.

The solar emission is detected at a level of about 5.3σ. There is evidence for the extension of the emission at a level of 2.7σ; the maximum logL indicates a positive extended component with a flux compatible with the IC model. The total flux from the Sun is more than expected for the disk source, so this is clear evidence for the IC emission even without the proof of extension. The measured extended flux is fully consistent with the model. In future work we will make a detailed spectral analysis. This is important for future missions such as GLAST and for studying solar modulation.

A rough estimate of the gamma-ray flux expected from some luminous stars is given in the figure on the right. Among the 70 most luminous stars within 600 pc from Hipparcos catalogue, some could possibly be detected by GLAST. OB associations will be even more promising as possible candidates for detection.

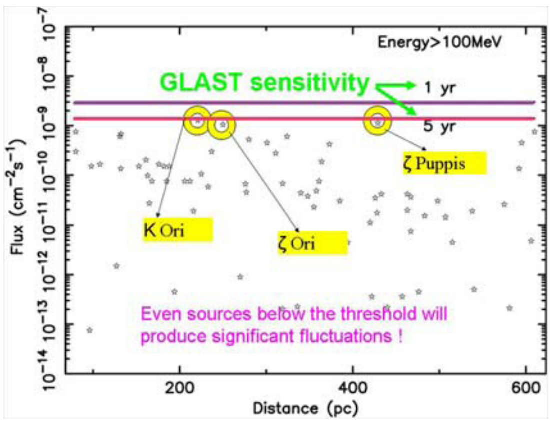

References: Orlando and Strong, Ap&SS in press

Elena Orlando - Dirk Petry - Andrew Strong

MAX-PLANCK-GESELLSCHAFT

Spokes in Saturn‘s rings

The spokes are intermittently appearing radial markings in Saturn’s B ring which are believed to form when micron sized dust particles are levitated above the ring by electrostatic forces. First observed by the Voyagers, the spokes disappeared between October 1998 and September 2005, when the Cassini spacecraft saw them reappear. The trajectories of the charged dust particles comprising the spokes depend critically on the background plasma density above rings, which is a function of the solar elevation angle. Due to the rings being more open to the sun now than when Voyager flew by, the charging environment above the ring has prevented the formation of spokes until very recently.

The Voyager and Cassini spacecraft have collected images of Spokes at Saturn (Fig.1). These features are typically 10,000 km in length and 2000 km in width, and although they last for hours, they seem to form in minutes[1]. Hubble Space Telescope observations monitored the spoke activity since 1995, until they vanished in 2004. The spokes were observed to fade as the ring’s opening angle increased, and the changing light-scattering geometry was thought to explain their total disappearance. Hence, it was surprising that even Cassini could not find spokes for over a year in orbit around Saturn. Cassini first spotted spokes in September 2005, indicating that their activity has a strong seasonal variation[2].

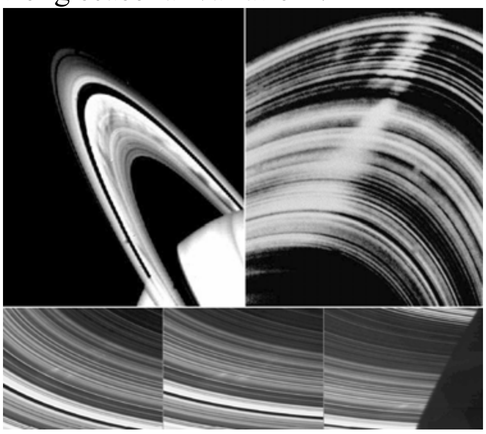

Fig.1 *Top:* Voyager images of spokes in backscattered *(left)* and forward scattered light *(right)*. *Bottom:* Cassini images.

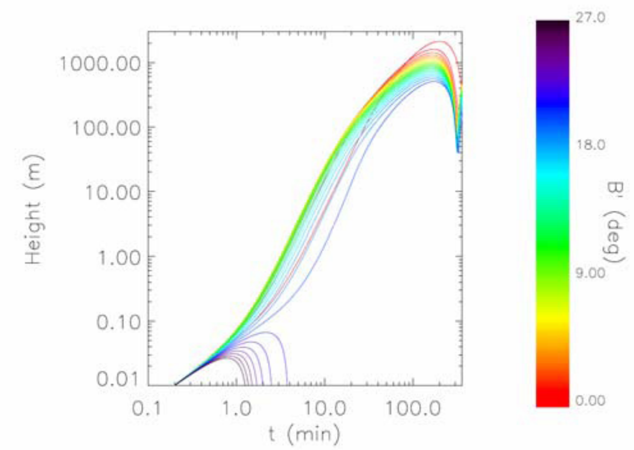

Fig.2 Calculated trajectories of 0.5 μm radius dust grains started with a single *e* charge at different values of the ring’s opening angle *B’*.

The intermittent lift-off of small grains requires a dense, transient plasma environment, that could be triggered by meteorite impacts[3] or ionospheric electron beams[4], for example. Regardless of the triggering mechanism, grains will be exposed to the permanently present background plasma once they leave the short-lived dense plasma cloud. Their subsequent charging history and their trajectory will be determined by the properties of the background plasma environment Because the rings changing opening angle *B’*, the background plasma density is expected to show a large seasonal variation, possibly explaining the lack of spokes for large values of *B’* when the background plasma density is high (Fig.2). The Cassini observations since 2006 seem to verify the prediction of this model. The exact nature of the triggering mechanism of spoke formation remains an open issue and is the subject of ongoing investigations[5].

References:

[1] B.A. Smith *et al*., *Science 212*, 163, 1981; and *Science 215*, 504, 1982
[2] C.J. Mitchell, M. Horányi, O. Havnes, C.C. Porco, *Science 311*, 1587, 2006
[3] G.E. Morfill, C.K. Goertz, *Icarus 55,* 111, 1983
[4] G.H. Jones *et al., Geophys. Res. Lett. 33*, L21202, 2006
[5] M. Horányi, G.E. Morfill*, in preparation*

M. Horányi, G.E. Morfill

Generator Regions Observed by the Cluster Spacecraft in the Terrestrial Magnetosphere

With its four satellites in tetrahedral configuration, the Cluster mission provides for the first time a platform for the *in-situ* investigation of energy conversion in the magnetosphere, by evaluation of the power density, **E•J**. Cluster data from the CIS, EFW, and EDI experiments can be used to infer the electric field, **E**, while the current density, **J**, can be derived form the FGM magnetic field measurements. When **E•J**<0, mechanical energy is locally converted into electromagnetic energy, part of which can propagate as Poynting flux and dissipate in the auroral ionosphere. *Marghitu et al. (2006)* and *Hamrin et al. (2006)* identified four concentrated generator regions (CGRs) in the plasma sheet boundary layer, conjugate with low altitude electron precipitation measured by the auroral satellite FAST.

The plasma sheet boundary layer is an active location, where electric fields are associated with plasma motion caused by the dynamics of the plasma-sheet/lobe interface, while electric currents are induced by pressure gradients. In the event illustrated by the figure below, the electric field and current have the right relative phase to support generator processes in the four regions indicated by yellow bands. The current (b1), obtained by the Curlometer method, and the electric field (c1), derived from CIS proton data, are used to compute **E•J** (d1, red). The CGRs are clearly visible (e1) as sharp gradients in the cumulative sum of **E•J**. The CIS and EFW results are in good agreement (e1), and the CGRs are found to correlate with electron precipitation near the polar cap boundary when conjugate FAST data are available (a2). The Poynting flux (d1, black) is dominantly directed to the Earth and, when mapped to ionosphere, is comparable to the electron energy flux (c2).

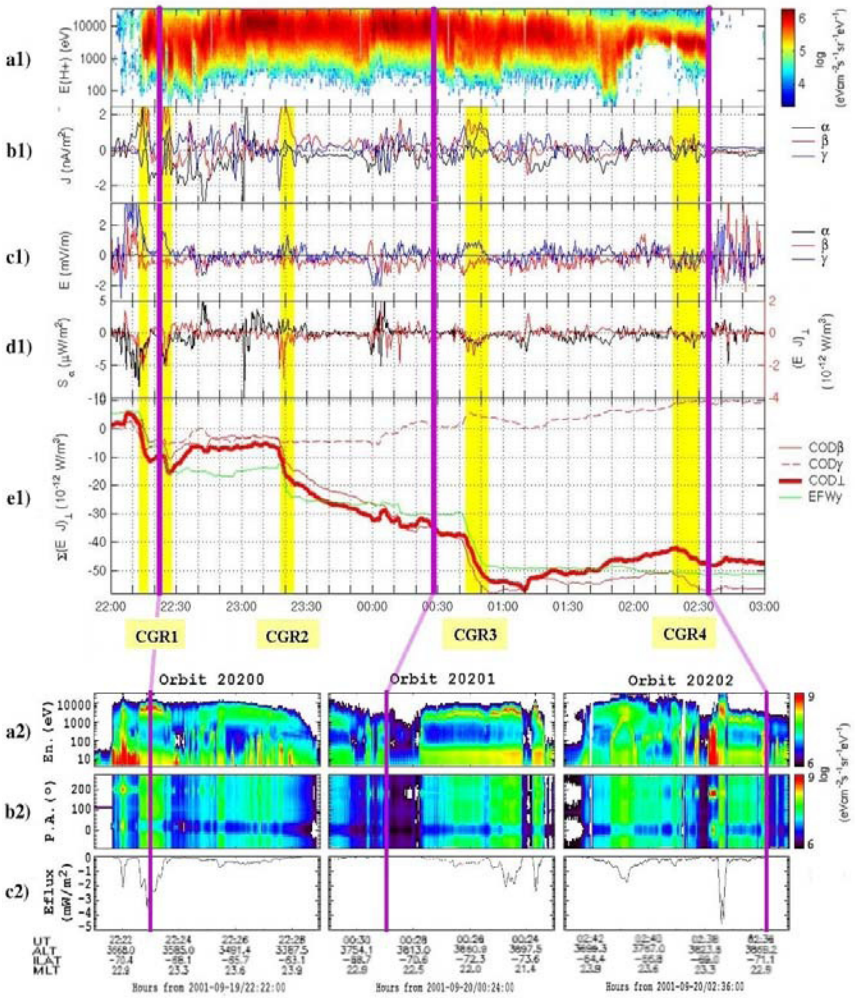

Top: Cluster data from September 19–20, 2001. (a1) Proton energy spectrogram for SC1. (b1) Current density. (c1) Electric field, averaged over spacecraft. (d1) Power density (red) and Poynting flux (black) averaged over spacecraft. (e1) Cumulative sum of the power density computed by using CIS (red) and EFW (green) data. The thin red lines show the contributions of the components perpendicular to the magnetic field, $E_\beta J_\beta$ (solid) and $E_\gamma J_\gamma$ (dashed). The concentrated generator regions CGR1–CRGR4 are indicated with yellow bands. The conjunctions with FAST are shown with magenta lines. **Bottom:** FAST data for three conjunctions, at 22:23, 00:29, and 02:36 UT. (a2, b2) Energy and pitch-angle spectrograms. (c2) Energy flux into the ionosphere, at the satellite level. The time runs from right to left for the second and third conjunctions, in order to emphasize the correlation between the CGRs and the precipitating energetic electrons.

References:

- O. Marghitu, M. Hamrin, B. Klecker, et al., Ann. Geophys., 24, 619, 2006.
- M. Hamrin, O. Marghitu, K. Rönnmark, et al., Ann. Geophys., 24, 637, 2006.

O. Marghitu and B. Klecker, in collaboration with M. Hamrin and K. Rönnmark

Cluster survey of the mid-altitude cusp

We have performed a statistical study based on four times three months of Cluster data taken in the dayside magnetosphere, representing 120 orbits. Out of 960 possible cusp crossings only 261 passes were actually identified as cusp crossings according to our criteria. From those crossings and from the 3D capability of the Cluster mission, we have had access to a wealth of information on the dynamics of the cusp, its morphologies and its particle content.

The cusp regions play a major role in solar wind-magnetosphere coupling. In fact, they are the regions through which the magnetosheath plasma has direct access to the magnetosphere and the ionosphere. The polar cusps were one of the main scientific objectives of ESA's Cluster mission (left-hand side figure).

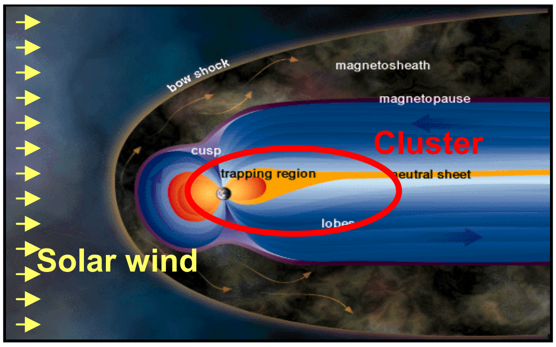

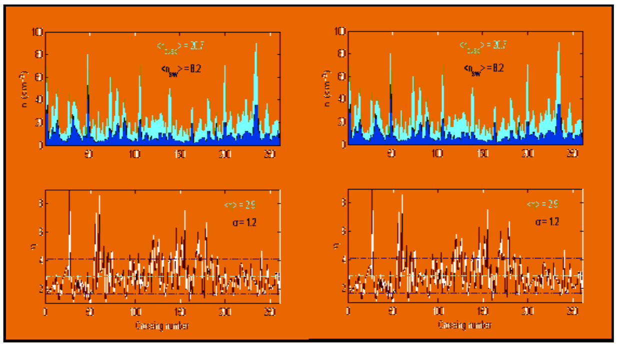

For the first time, the multipoint capability of Cluster has allowed us to study *in situ* the response of the cusp to changes in interplanetary magnetic field (IMF) orientations: the time required for the cusp width to fully adjust is larger than 20 minutes and the motion of the cusp triggered by the rotation of the IMF has a velocity proportional to the variation in Bz: Vcusp = 0.024 ΔBz, the cusp velocity being in °/min and ΔBz in nT.

We have compared the ion densities in the solar wind and in the cusp (right-hand side figure). It appears that the normalized density in the cusp, η, is around 3 on average. The average density in the cusp is found to be higher under northward IMF while the normalized density is smaller for northward IMF than for southward IMF, suggesting that the efficiency of reconnection is greater under southward IMF.

Regarding the morphology, the occurrence of nicely dispersed ion structures in the cusp is 34%. Not less than 56% of the cusp crossings fall in our "discontinuous" or "irregular" categories. A few cases of discontinuous cusps occurring under stable IMF conditions have been spotted. They all occur when the IMF is dominated by its East-West component, which is expected for both anti-parallel and component reconnection hypotheses but their wide in local time and latitudinal distributions is *a priori* not compatible with the anti-parallel reconnection hypothesis solely.

References:

• Pitout F., C.P. Escoubet, B. Klecker, H. Rème, Cluster survey of the middle altitude cusp: 1. size, location, and dynamics, *Annales Geophys*., 24, 3011-3026, 2006.

F.Pitout, C.P. Escoubet, H.Rème, B. Klecker

Magnetic field cross-calibration using **CAA**

Multispacecraft studies of magnetic fields depend very much on the precise knowlegde of the measurements accuracy. The **C**luster **A**ctive **A**rchive (**CAA**) gives access to the whole data base of the Cluster mission and facilitates this way the cross-calibration of the instruments. The magnetic field is measured on the four Cluster spacecraft by **F**lux-**G**ate **M**agnetometers (**FGM**). Two other instruments **EDI** (the **E**lectron **D**rift **I**nstrument, built in **MPE**) and **WHISPER** (**W**aves of **HI**gh frequency and **S**ounder for **P**robing of **E**lectron density by **R**elaxation) determine the magnetic field magnitude B by measuring the gyrofrequencies of the electrons in the ambient magnetic field. The distributions of the differences and ratios of the magnitudes measured by the three instruments are used to characterize the absolute error of the magnetic field measurement. The absolute accuracy of B is around 0.2 % on the four spacecraft.

The gyrofrequency of a charged particle in an homogeneous magnetic field is a direct measure of the magnetic field magnitude: $B = ct * f_{gyro}$, where $ct = 2 \pi q/m$, q is the charge and m the mass of the charged particle.

EDI measures the direction and time-of-flight of injected electrons.The EDI electron gyrofrequencies (time-of-flight) were used systematically for the FGM calibration check on Cluster [1]. This check was limited to the periods where EDI measurements were available. Due to the lack of EDI data on Cluster 4, only indirect methods were used to calibrate the FGM measurements.

WHISPER is measuring high frequency wave spectra. The density of the electrons in the plasma sphere is high enough to allow the determination of the electron gyrofrequencies. This depends on the visibility of the gyrofrequency and its harmonics in the spectra, since image processing methods are used. The two figures show distributions for the EDI - FGM comparison for Cluster 1 (Fig.1) and WHISPER - FGM for Cluster 4.(Fig.2)

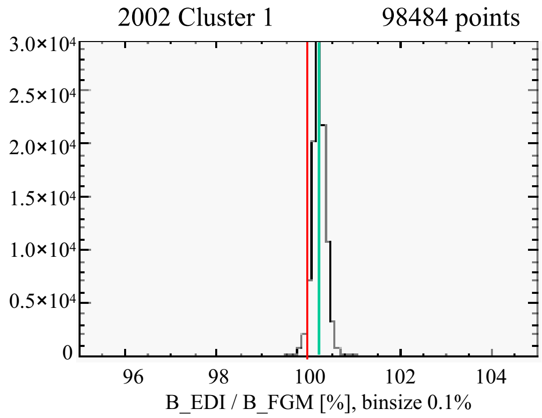

Figure 1

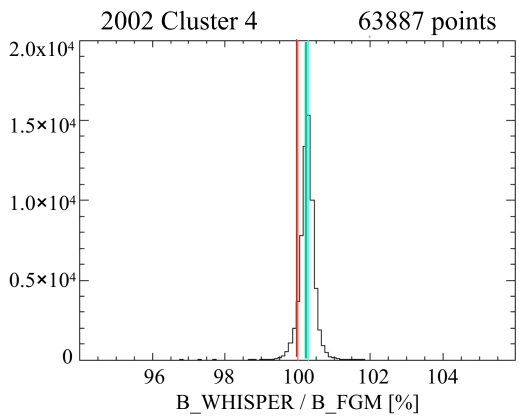

Figure 2

The histograms of the ratios between EDI (resp. WHISPER) and FGM in percent, binsize 0.1% are centered at 100.2% and have a standard deviation of 0.6%

The 0.2 % shift of the distributions center could be due to an FGM scaling error .

Acknowledgement for data usage to the ESA Cluster Active Archive and the FGM, EDI and WHISPER teams.

References:

• Georgescu E. et al, Use of EDI time-of-flight data for FGM calibration check on CLUSTER, *Proceedings of the Cluster and Double Star Symposium 5th Anniversary of Cluster in Space,* ESA SP 598,P6.9,2006.

E. Georgescu in collaboration with J. Gloag (IC, UK), A. Rochel (LPCE, Fr)

Determining the crossing parameters for a 2D, non-planar magnetopause by the use of timing technique

Since the Cluster mission became operational we benefit from correlated measurements taken simultaneously at four points in space. The differences in the position and time of the satellites' encounter with the terrestrial magnetopause (MP) can be fed into a timing technique and used to infer the MP orientation, thickness and velocity. This multi-spacecraft technique, which assumes a planar MP, proves reliable and offers an independent check for various single spacecraft techniques (*Haaland et al., 2004*).

We extended the timing method in order to accommodate situations when the MP behaves like a two-dimensional, non-planar discontinuity (*Blăgău, A., 2007*). This is the case, for example, when the single-spacecraft technique relying on minimum variance analysis of the magnetic field (MVAB) provides different individual MP normals, all of them contained approximately in the same plane (see **Fig. 1**). Such a configuration is not necessarily related to experimental errors, but can have natural causes, like a local bulge/indentation in the MP or a large amplitude traveling wave on this surface. We illustrate our technique with a test case and compare the results with those based on the planar MP assumption.

In one implementation of the method, the MP is locally modeled as a layer of constant curvature and thickness, oriented along the invariant direction $\vec{l}$ (introduced in **Fig. 1**) and moving along two perpendicular directions. Knowing the times when each satellite detects the MP leading and trailing edge, we can solve a system of equations for determining the spatial scale of the structure (radius of curvature and thickness), the direction of movement and its evolution in time, assuming a polynomial dependence for the displacement (a total of 8 model parameters).

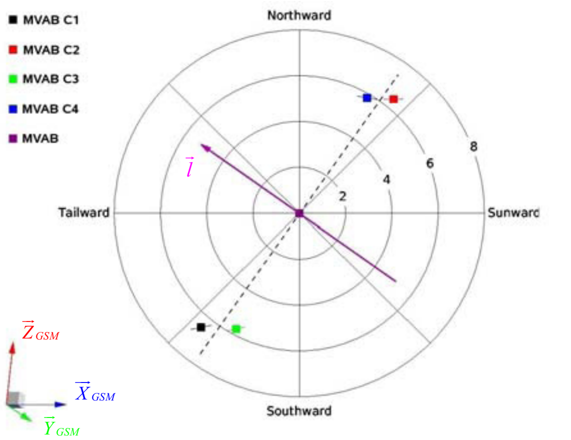

Fig. 1 Polar plot showing the orientation of the four individual normals (MVAB C1-C4) with respect to their average, taken as reference direction in space (symbol MVAB; the circles designate directions of equal inclination, in degrees). The individual normals are located roughly in one plane (dashed line) indicating a two-dimensional MP with the invariant direction oriented perpendicular (unit vector $\vec{l}$).

The solution we found is presented in **Fig. 2**. In contrast to the planar situation, the instantaneous, non-planar normals at each spacecraft location are linked through the MP geometry and dynamics.

We found that the global (over the 4 satellites) magnetic variance along the instantaneous, 2D MP normals is less than the same quantity computed based on planar results. This is an independent confirmation that, indeed, we model correctly the MP behaviour for this event.

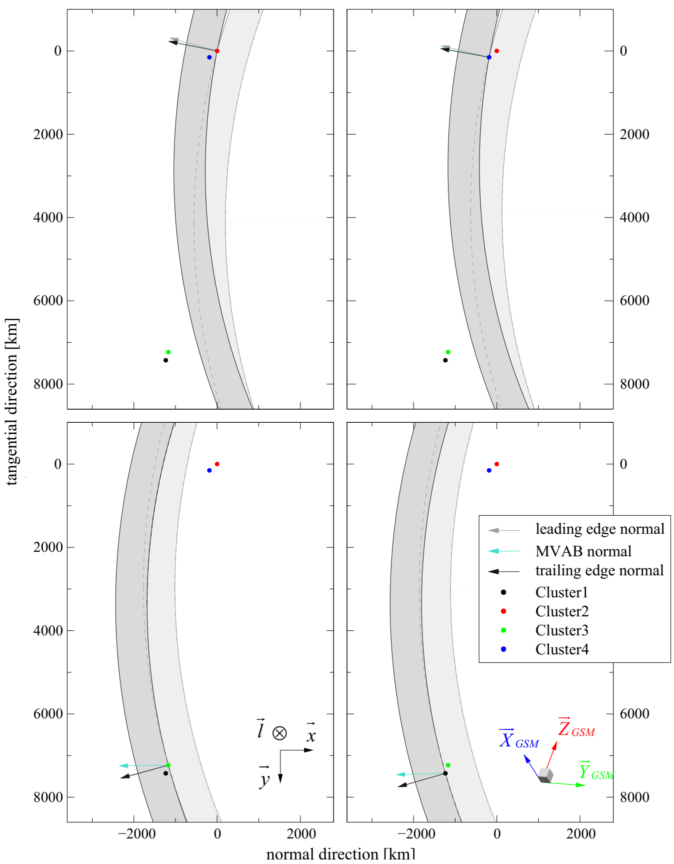

Fig. 2 Graphical representation of the obtained solution. The drawings are MP cuts in a plane perpendicular to the invariant direction $\vec{l}$ (which is pointing into the page). The satellite positions are indicated by the colored dots and the MP moves along $-\vec{x}$ with constant velocity, whereas along $\vec{y}$ it has a more complicated, back and forth motion. Each of the four panels is associated with one satellite and shows the MP configuration at two times: when the respective satellite enters the layer (light gray) and when it leaves the layer (darker gray). The MP geometrical normals at the satellite position and for these two times are shown, together with the individual normals obtained from the MVAB technique (green arrows).

References:
• Haaland, S. et. al.Annales Geophysicae, 22, 1347, 2004
• Blăgău, A. Ph. D. Thesis (to be submitted)

A. Blăgău, B. Klecker, G. Paschmann, M. Scholer, S. Haaland, and O. Marghitu

A Model Auroral Arc

Auroral arcs can be regarded as by-products of the plasma convection in ionosphere and magnetosphere. Pressure forces in the outer magnetosphere drive the convection against the frictional forces of the ionosphere and generate shear stresses in the magnetic field, i.e. strong field-aligned currents. The auroral mechanism is a way to release such shear stresses and convert the liberated magnetic energy into kinetic energy of electron and ion beams. This is achieved by the generation of U-shaped potential structures in the low magnetosphere, if the attending field-aligned currents are sufficiently intense. The electrons produce the auroral luminosity in the lower ionosphere by collisional excitations. This chain of events has been cast into an analytical model in a distorted-dipole magnetic field. It generates a simple set of relations for the main characteristics of auroral arcs and the right magnitudes for high-beta (~1-3) generator plasma.

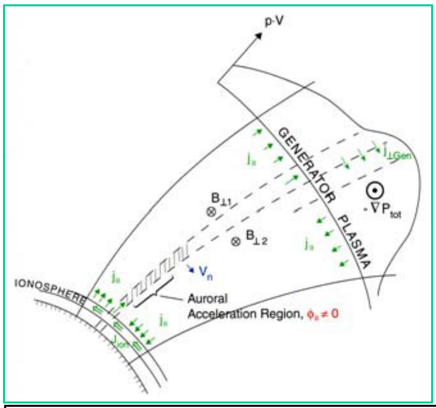

High-latitude current system with pressure profile of the generator plasma. Ledges in this profile are sources of the auroral current sheet.

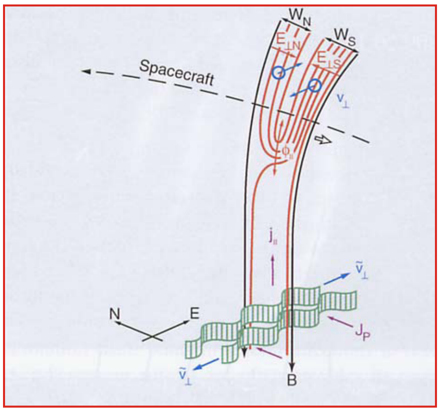

U-shaped potential distribution of a quasi-electrostatic potential generated by an upward directed intense auroral current. The transverse electric field components release the magnetic shear stresses, the parallel components accelerate the particles.

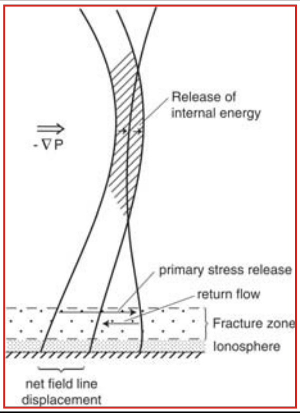

Visualizing the stress relief: The low sections of the field-lines decouple from the ionosphere, move fast in the direction of the driving force, overshoot, and return to a lower stress position, while the source plasma expands.

Auroral characteristic parameters

Transverse field jump: $$\Delta B_{y,arc} = \frac{\delta}{2}\cdot\hat{B}\cdot\Gamma$$

Energy flux: $$\dot{W}_{arc} = \delta\cdot\frac{\hat{B}^2}{\mu_0}\cdot\frac{R_E L}{2\tau_A}$$

Potential drop: $$\Phi_\parallel = \hat{B}\cdot\frac{R_E L}{2\tau_A}\cdot w_{arc}\cdot\Gamma^{-1}$$

Arc width: $$w_{arc} = \left(\frac{\delta\tau_A}{\mu_0 R_E L K}\right)^{\frac{1}{2}}\cdot\Gamma$$

Proper motion: $$v_n = \frac{w_{arc}}{4\tau_A} \qquad \Gamma \approx 1$$

R_E = Earth's radius, L = equatorial distance, τ_A = Alfvén wave transit time, K^{-1} = effective parallel resistance in acceleration region.

δ is the differential pressure jump at the ledge of the generator plasma.

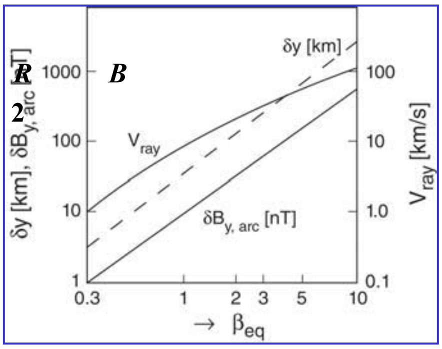

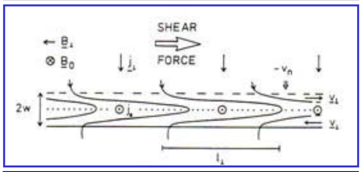

Foot-point motion during stress relief seen from above. While stored energy is consumed, arc and current sheet propagate into the region of higher stresses.

The motion of the frequently seen auroral rays is a manifestation of the stress release process (v_{ray}). δy is the net displacement of the field lines, and δB_y the jump of the transverse field through the current sheet and thus a measure of the differential shear stresses. The process depends strongly on the plasma beta of the generator plasma.

This process may as well operate in stellar magnetic fields pervaded by high-beta plasma and generate very high energy particles in relation to field strength, spatial dimensions and critical current density.

References:

•G. Haerendel: Auroral arcs as sites of magnetic stress release, submitted to *J. Geophys. Res.* (2007).

•G. Haerendel: Acceleration from field-aligned potential drops, *APJ Suppl., 90*, 765-774 (1994).

Gerhard Haerendel

Generic Residue Analysis

Generic residue analysis is a method to determine the orientation and motion of plasma structures. The method is an extension of the classical minimum variance technique. Using plasma and field data from the ESA Cluster mission, the feasibility of the method has been demonstrated for the first time.

One of the prime objectives of the Cluster mission was to study boundary layers and discontinuities in the Earth's magnetosphere. In this poster, we show an application of a new method, generic residue analysis, to establish the orientation and motion of the Earth's magnetopause. Generic residue analysis essentially provides a frame of reference where a measured quantity (e.g., B-field, mass flow, energy) best satisfy the conservations law applicable to that quantity (e.g., conservation of magnetic poles, mass conservation, energy conservation).

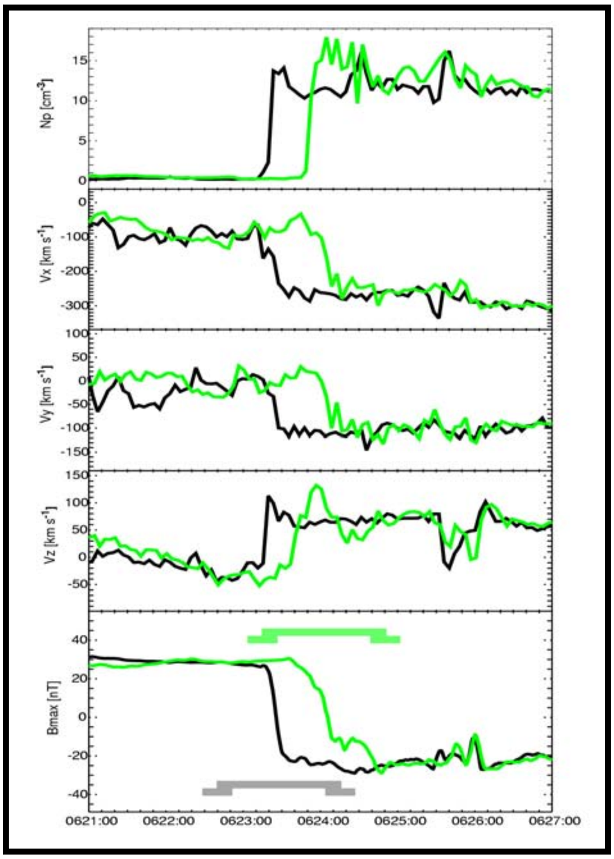

The above figure shows selected plasma and field measurements from the Cluster spacecraft C1 (black) and C3 (green) during a magnetopause crossing on 5 July 2001. Using the time segments indicated by the horizontal bars in the lower panel, we applied the generic residue method to establish the orientation and motion of this discontinuity.

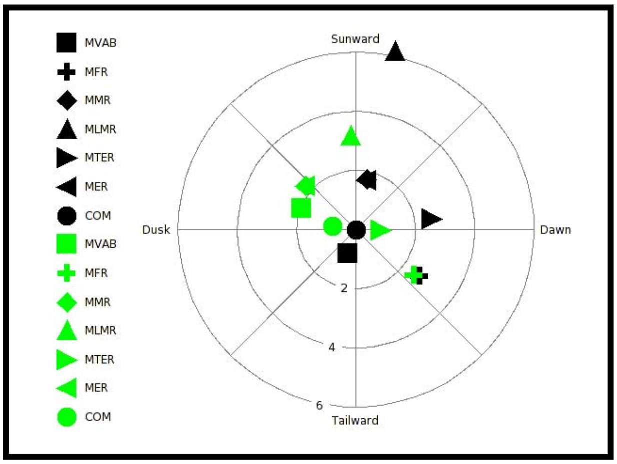

The orientation of a discontinuity is usually described by its boundary normal. The above figure shows normals, projected into a polar plot, obtained from generic residue analysis of various measurements from Cluster C1 (black) and C3 (green). Each symbol represent the result from a particular conservation law :

- MVAB – absence of magnetic poles
- MFR – conservation of magnetic flux
- MMR – conservation of mass flux
- MVAJ – conservation of charge
- MTER – conservation of energy
- MLMR – conservation of linear momentum
- MER – conservation of entropy
- COM – weighted combination of above

For this particular events, all methods give orientations that agree to within a few degrees, thus validating the technique.

References:

Sonnerup et al, 2006 : Orientation and Motion of a Plasma Discontinuity from Single-Spacecraft Measurements of Plasma Velocity and Density: Generic Residue Analysis , JGR, A10, 1996
Haaland et al, 2006 : Discontinuity Analysis With Cluster, ESA SP 596,

S. Haaland, B. Sonnerup, G. Paschmann, Cluster CIS & FGM teams

Collective Processes in Space Dusty Plasmas: dissipative instability in planetary rings

The dissipative forces can crucially change the stability of dust-density perturbations in dusty plasmas of planetary rings. Inside the co-rotation distance the ion drag force is responsible for the excitation of dust-acoustic waves, while for the region outside the synchronous orbit this mode can hardy be excited (at the radial distances corresponding to the main rings). The instability due to the ion drag force could be of some importance for formation and evolution of Saturnian's "spokes" occurring in the vicinity of the synchronous orbit.

We demonstrate that the ion drag force related to the momentum transfer from the moving ions to the charged dust grains can be an important factor, which affects stability of the low–frequency dust acoustic waves (DAW) in the dusty plasmas of Saturn rings. Two features determine the exceptional role of the ion drag force in planetary rings - the occurrence of a ring atmosphere/ionosphere and of a relative motion between the plasma and dust particles. The relative velocity causes the existence of radial zones of transparency for dust - density waves propagation and regions where these waves are damped. We found that inside the co - rotation distance (where the plasma ions move slower than the dust grains) the ion drag force can be responsible for the excitation of dust-acoustic perturbations. According to our model the growth rate of this dissipative instability is strongly dependent on the radial distance from the planet. Reasonable estimations of the plasma parameters based on the Cassini measurements show that the boundary for the onset of the dissipative instability located in the direct vicinity of the synchronize orbit ($x > x_{cr} \sim x_{synchr}$). Note that the strong neutral gas damping (associated with dust-neutral momentum transfer) can quench the instability and move the boundary for the onset of the instability inside the co-rotation distance ($x_{cr,L} > x_{cr,U}$ in Fig.1). Outside the co-rotation distance (where the plasma ions overtake the dust grains) the collisional process lead to damped perturbations, and thus DAW can hardy be excited at radial distances corresponding to the main Saturn's rings.

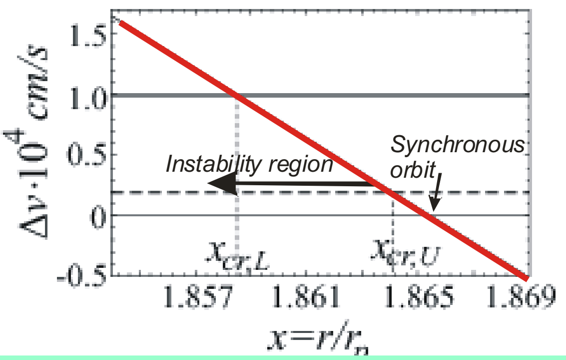

Fig.1 The instability domain in parameter space: relative distance from the planet (x); relative dust velocity

Fig.2 "Spokes" in Saturn rings observed by Voyager 2 inside the synchronous orbit

***Results:* (i) The boundary for the onset of the dissipative instability located in the direct vicinity of the synchronize orbit; (ii) The smaller the charged particles are, the larger the growth rate of the instability; (iii) The discovered instability can be of importance for the formation and evolution of Saturn's "spokes" (Fig. 2) occurring in the vicinity of the synchronous orbit and formed by micron and submicron-sized dust particles.**

V. V. Yaroshenko and G. E. Morfill in collaboration with F. Verheest

Mars in X-rays: a novel view of an ancient world

After our discovery of X-rays from Mars with Chandra (Dennerl 2002), we studied the origin of the X-ray emission in more detail, using the higher sensitivity and spectral resolution provided by XMM-Newton (Dennerl et al. 2006, 2007). This pioneering observation confirmed our previous findings that the X-ray flux consists of two components, caused by two different processes: scattering of solar X-rays in the upper Martian atmosphere, and charge exchange interactions between highly charged heavy solar wind ions and atoms in the Martian exosphere. Here we briefly summarize the novel results, which include the ***first unambiguous discovery of extended X-ray emission from the exosphere of another planet.***

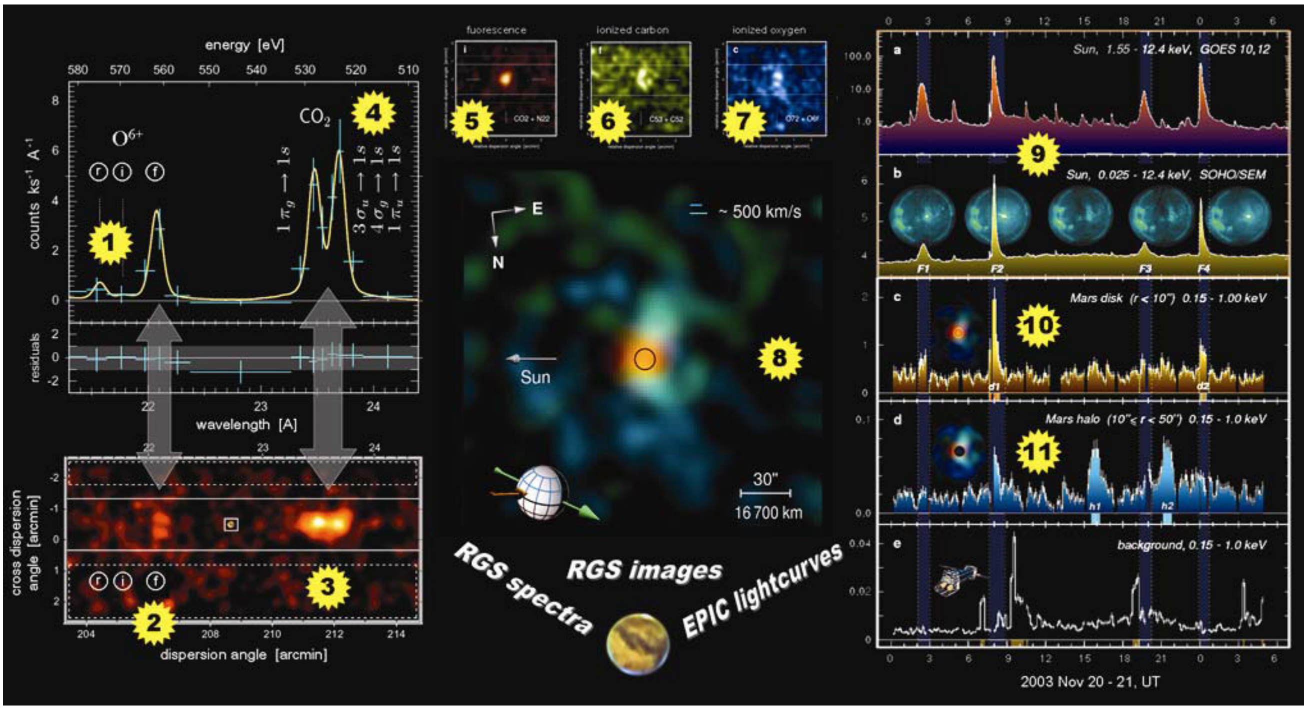

The RGS spectrum of the O^{6+} multiplet 1 clearly shows the spin-forbidden $2\,^3S_1 \rightarrow 1\,^1S_0$ transition to dominate, proving that charge exchange is indeed the origin of this emission. The corresponding RGS image 2 reveals that the O^{6+} emission originates above the Martian poles (a small optical image at the center illustrates the apparent size of Mars). In contrast, the RGS image of neutral oxygen 3 looks very different, consisting of two blobs along the dispersion direction. This is caused by X-ray fluorescence of the Martian CO_2 atmosphere, where fine-structure due to molecular transitions 4 is observed for the first time. Fluorescence is also detected from neutral nitrogen. The superposition of all the fluorescent images 5 shows a morphology which is consistent with the position and size of Mars, in contrast to the charge exchange images of highly ionized carbon 6 and oxygen 7. The combination of these three images to the first ever X-ray color image of Mars and its exosphere 8 reveals surprising structure which is still unexplained. During the observation, the Sun was highly active, exhibiting several intense X-ray flares 9. These flares are mirrored in the X-ray lightcurve of the Martian atmosphere 10. The X-ray lightcurve of the Martian exosphere exhibits also bright flares 11. They are not related to the solar X-ray flux, because they were powered by the solar wind ions.

References:
- Dennerl, K. et al., 1997, ***Science*** 277, 1625-1630
- Dennerl, K., 2002, ***A&A*** 394, 1119-1128
- Dennerl, K. et al., 2006, ***A&A*** 451, 709-722
- Dennerl, K. et al., 2007, in preparation

K. Dennerl, V. Burwitz et al.

25143 Itokawa: The Power Of Ground-Based Mid-IR Observations

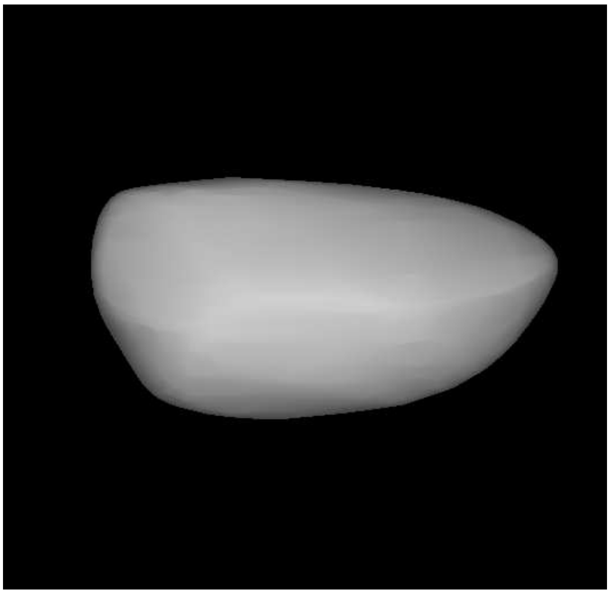

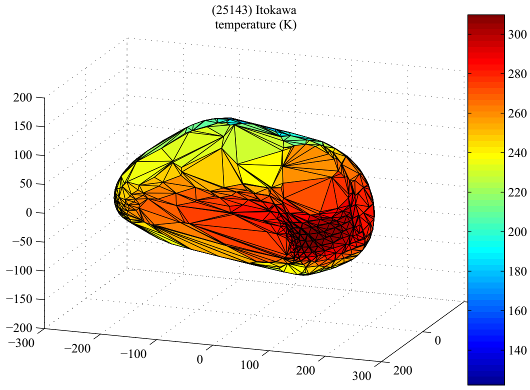

Pre-encounter ground-based thermal observations of NEA 25143 Itokawa at 10 µm led to a size prediction of 520(± 50) × 270(± 30) × 230(± 20) m, corresponding to an effective diameter of D_{eff}^{TPM} = 318 m (Müller et al. 2005). This is in almost perfect agreement with the final in-situ results 535 × 294 × 209 m ($D_{eff}^{Hayabusa}$ = 320 m; Demura et al. 2006). The corresponding radar value, based on the same shape model (Kaasalainen et al. 2005), were about 20% too high: 594 × 320 × 288 m (D_{eff}^{Radar} = 379 m; Ostro et al. 2005). The very simple N-band observations revealed a surface which is dominated by bare rocks rather than a thick regolith layer. This prediction was nicely confirmed by the Hayabusa mission (e.g., Fujiwara et al. 2006; Saito et al. 2006). The ground-based measurements covered three different phase angles which enabled us to determine the thermal properties with unprecedented accuracy and in excellent agreement with the results from the touch-down measurements (Okada et al. 2006; Yano et al. 2006). These thermal values are also key ingredients for high precision Yarkovsky and YORP calculations (mainly the rotation slowing) for Itokawa (e.g., Vokrouhlický et al. 2004; Vokrouhlický et al. 2005;). In addition to the above mentioned properties, our data allowed us to derive the surface albedo and to estimate the total mass. We believe that with our well-tested and calibrated radiometric techniques (Lagerros 1996, 1997, 1998; Müller & Lagerros 1998, 2000, 2000a) we have tools at hand to distinguish between monolithic, regolith-covered and rubble pile near-Earth objects by only using remote thermal observations (Müller et al. 2007). This project also emphasizes the high and so far not yet fully exploited potential of thermophysical modeling techniques for the NEA/NEO exploration.

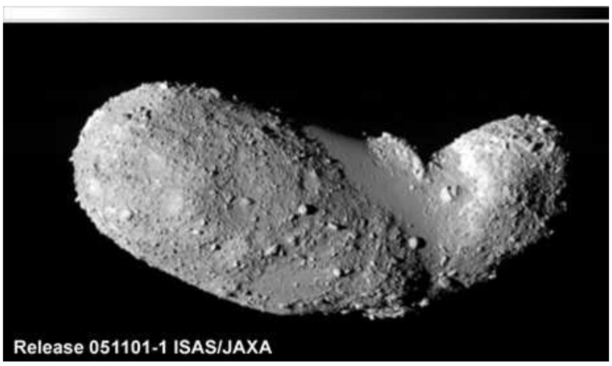

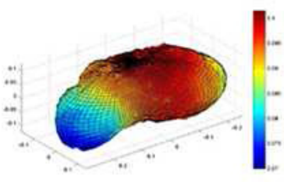

Gravity Map (Modell-A)

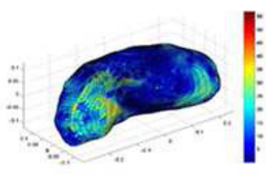

Slope Map (Model-B)

T.G. Müller, T. Sekiguchi, M. Kaasalainen et al.

The Herschel Asteroid Preparatory Programme

The goal of the Herschel Asteroid Preparatory Programme is to establish a set of about 50 asteroids as far-IR/submm/mm calibrators for Herschel. The selected asteroids will fill the flux gap between Mars, Uranus and Neptune and the mid-IR calibration stars. ISO used 10 of these asteroids successfully for far-IR calibration, Spitzer integrated the fainter ones in the MIPS calibration scheme, Akari uses meanwhile the full target list and several groundbased observatories established observing programmes either in support for the space projects or for own calibration purposes.

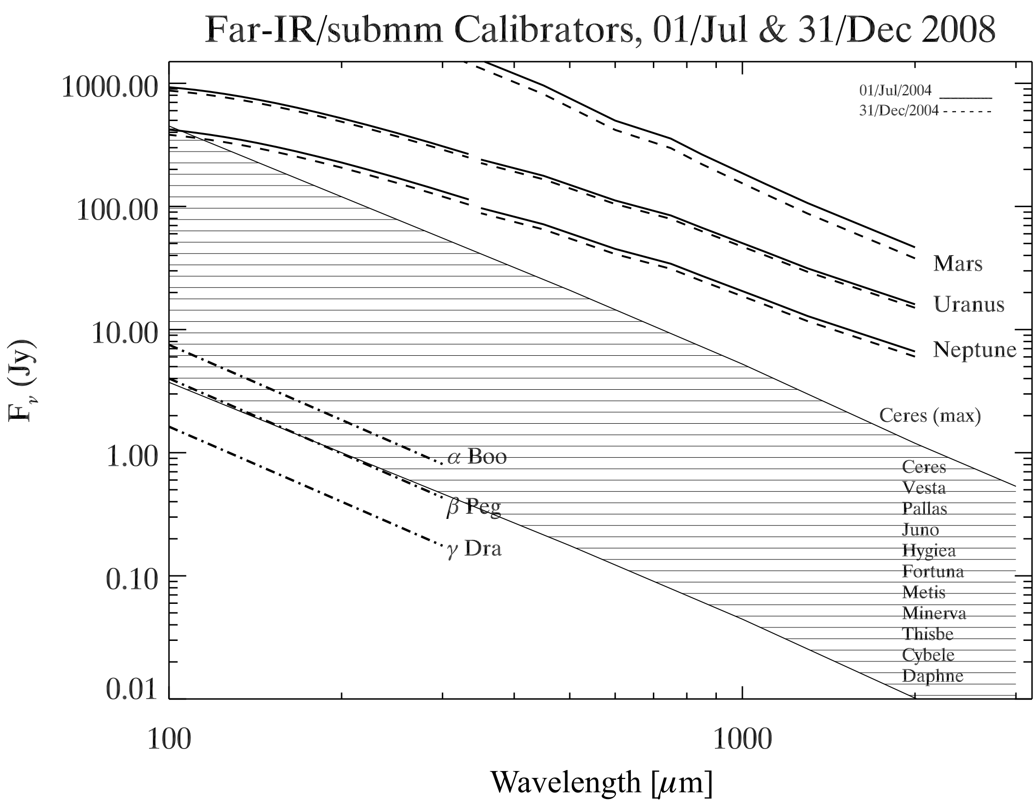

Celestial standards play a major role in astronomy. They are needed to characterise the performance of instruments and they are an important prerequisite for accurate photometry. With the access to the far-IR, submm and mm wavelength range through satellites, airborne and groundbased instruments, it became necessary to establish new calibrators for these wavelengths. The traditional far-IR/submm/mm calibrators, the outer planets, are too bright or cause nonlinearity problems for instruments on upcoming sensitive. Stellar standards are quite faint in this range and pose problems of their own. The large flux gap between these two types of calibrators can be filled by a set of asteroids (Müller & Lagerros, A&A 1998, 2002, 2003). The ”Herschel Asteroid Preparatory Programme” (Müller et al. 2005; Müller et al. 2007) is currently conducted together with the Herschel and Akari calibration teams. We investigate the physical and thermal properties of about 50 asteroids. All of them are large, almost spherical and belong the the main-belt. They cover the flux range between about 1 and several hundred Jansky at 100 μm and at 1 mm they still reach up to 10 Jy. Thermophysical model predictions (light curves, SEDs or monochromatic fluxes) are accurate on the 5-20 % level, depending on the object, the observing and the illumination geometry.

T.G. Müller & Herschel CalSG & Akari calibration team

Gamma-rays from the Sun

In 2006, two teams of theorists independently predicted that the vicinity of the Sun should emit high energy gamma-rays due to the inverse Compton scattering of solar photons on cosmic-ray electrons. Using specially developed methods, we reanalyse the archival EGRET dataset to search for the emission. We detect it above 100 MeV at the 5 σ level compatible with the predictions and previous upper limits.

Motivation: Orlando & Strong (2006) and Moskalenko, Porter & Digel (2006) predict the Sun as extended steady gamma source due to inverse Compton (IC) scattering of solar photons on cosmic ray electrons. Thompson et al. (1997) investigated the lunar and solar gamma emission for the first time based on Morris (1984) and Seckel et al. (1991): using EGRET data, they observed a flux of 4.7×10^{-7} cm^{-2}s^{-1} above 100 MeV from the Moon, but could only provide an upper limit of 2×10^{-7} cm^{-2}s^{-1} for the emission from the Sun. The predicted IC emission is below this upper limit and comes from an extended region. Thompson et al. were looking for a <u>point</u> source. Can we detect the extended Sun in the EGRET data knowing better what we are looking for?

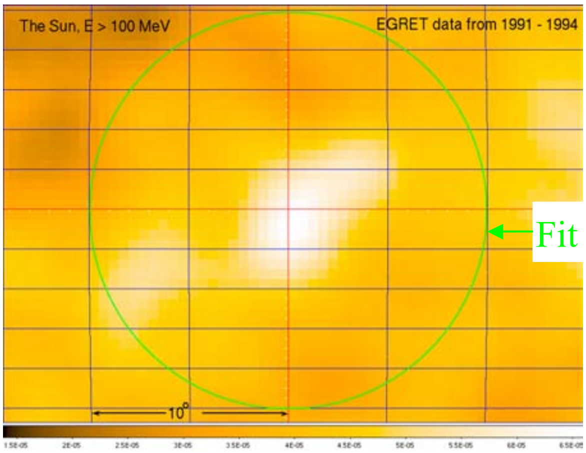

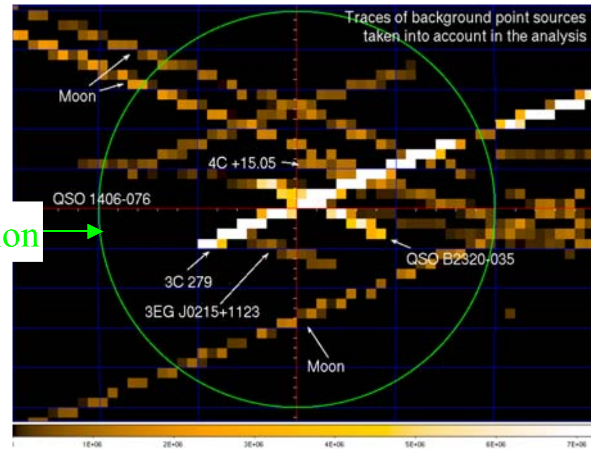

The problem: To follow a faint source moving quickly with respect to all other celestial objects through the entire EGRET dataset (5 million events) taking into account changing calibration parameters and background conditions (diffuse background and passing point sources).

The method: We use data analysis code developed for the moving target "Earth" (Petry, 2005) and add necessary features (solar and lunar ephemerides, occultations, close encounter detection, source trace calculation). The diffuse background is reduced by a cut on the galactic latitude (this also eliminates the detected solar flare from 11 June 1991). We treat close encounters with point sources by including them into the overall background model (3C 279, Moon, several quasars). We then perform a maximum likelihood fit of combined solar and background model leaving as free parameters (a) the solar IC flux (model by Orlando & Strong), (b) the solar point source flux (inspired by Seckel et al. 1991), (c) an isotropic background, and (d) the flux of the dominant background point source (3C 279).

Results: The fit result in terms of the fit parameters (a) and (b) is shown in figure 2 of the partner poster by Orlando, Petry & Strong (this conference). Figure 1 (left) on this poster shows the flux map of the solar emission obtained in this analysis (background not subtracted). The units are photons cm^{-2}s^{-1}sr^{-1}. Figure 2 (right) shows the exposure traces of the several point sources which are passed by the Sun as it travels across the sky. The units are those of an exposure (cm^{2}s). - In order to verify our method, we confirm that we reproduce the fluxes of well-known sources like the Crab Nebula, 3C 279, and in particular the Moon, and that we do not detect the Sun if we deliberately alter its ephemeris. Further work on this subject will investigate the spectrum of the solar emission and refine the determination of systematic errors.

References:

- Orlando & Strong, 2006, Ap&SS in press
- Thompson et al., 1997, J. Geophys. Res., 102, 14735
- Morris, 1984, J. Geophys. Res., 89, 10685
- Moskalenko, Porter & Digel, 2006, ApJ, 652, L65
- Seckel, Stanev & Gaisser, 1991, ApJ, 382, 652
- Petry, 2005, AIP conf. proc., 745, 709

Dirk Petry - Andrew Strong - Elena Orlando

Physics of Complex Plasmas

String Fluids in Complex Plasmas

"String fluids" occur naturally when an anisotropic external force is applied to a fluid system and causes the interparticle interaction to be anisotropic, too. Such rheological fluids exist, e.g. in strong magnetic or electric fields, where the charge-dipole interaction force becomes important. The interest in such systems stems from the ease with which external control of phases (and hence properties) can be achieved. Recently, we were able to create electrorheological complex plasma fluids in the PK-3 Plus laboratory on the ISS, and observe the phase transition from a normal fluid state at the individual particle level for the first time. Such information - especially the dynamics - was not available so far (using e.g. colloidal systems). Investigating phase transitions in different types of fluid systems allows us a fundamental insight into the generic properties of such nonlinear (and in part critical) phenomena.

Conventional fluids with dipolar interaction

Such fluids consist of particles having dipole moments. If dipole is induced by an external field they are called electrorheological fluids. The resulting interaction energy is

$$W(\mathbf{r}) = W_{\text{iso}}(r) + W_{\text{an}}(\mathbf{r})$$

$$W_{\text{an}}(\mathbf{r}) = -d^2\,\frac{3\cos^2\theta - 1}{r^3}$$

Complex plasmas in external AC fields are identical to electrorheological fluids with dipoles $d \sim 0.5Q\lambda M_T$

Q: charge, λ: sreening length
M_T: thermal Mach number of ions in AC field

Electrorheological (ER) colloids

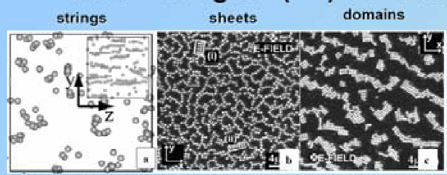

By increasing the field at moderate densities, one observes **(a)** formation of vertical strings, **(b)** merging into sheets, and **(c)** appearance of crystalline domains.

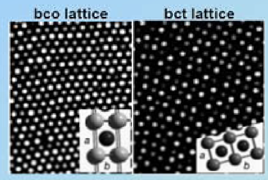

At higher densities, the ***second-order*** phase transition from bct to bco lattice occurs.
(Yethiraj & van Blaaderen, Nature 2003; Hynninen & Dijkstra, PRL 2005)

Snapshots of the transition to a string fluid in **PK-3 Plus** (with different AC fields)

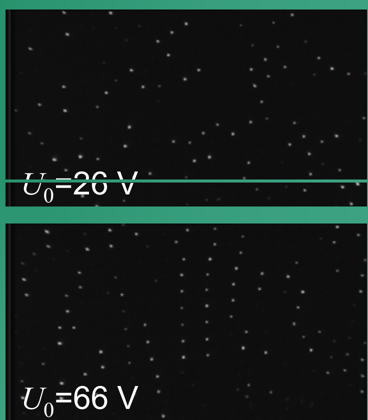

Phase Diagramm for String Fluids

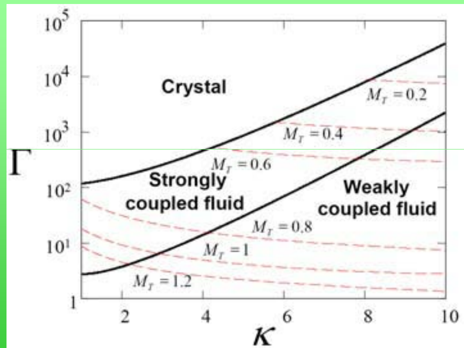

Transition to string fluid occurs above dashed line.

Conclusions
- Field-induced anisotropic interactions in complex plasma are identical to those in classic electrorheological fluids.
- There is a number of structural second-order phase transitions, like lattice bct-bco transition and fluid isotropic-to-string transition.
- Structural second-order phase transitions in complex plasma can be observed with the PK-3 Plus setup, and should be observed with PK-4 as well.

H. Thomas, A. Ivlev, R. Kompaneets, G. Morfill, C. Räth

Recrystallization of a 2D Plasma Crystal

A monolayer plasma crystal was melted by application of a short electric pulse. During the following recrystallization, a liquid-like phase was followed by a transient state characterized by energy release and the restoring of long range translational order. No long range orientational order was found, though highly ordered domains - separated by strings of defects - formed locally. Numerical simulations revealed the same regimes of recrystallization as the experiment.

The experiment was performed in a weakly ionized argon plasma generated by a capacitively coupled radio-frequency discharge. Melamine-formaldehyde spheres formed a 2D plasma crystal with a hexagonal structure which was melted by an electric pulse applied to two wires mounted in the particle plane to both sides of the crystal (Fig. 1a). The particles were illuminated by a horizontally spread laser sheet and the recrystallization was recorded from the top view with a high speed CCD camera at 500 fps. Particle temperatures, defects fractions, the bond order parameter as a local measure for order and the pair- and bond correlation functions were calculated from the images. Exponential fits to the correlation functions yield the correlation lengths as a measure for long range translational and orientational order.

Fig. 1

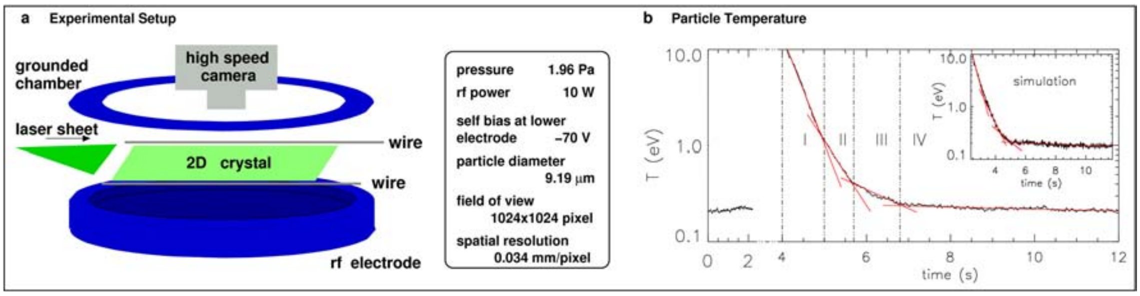

The exponential temperature decay !"ig. 1b, solid lines are exponential fits) changes fro pure Epstein damping due to friction with neutral gas atoms (regime I) to a slower decay rate (II,III) until a constant temperature of ~ 0.22 eV is reached (IV), when defect fraction and translational order are restored to the initial state before melting. Both defect fractions and the correlation lengths ξ and ξ_6 can be fitted by power laws ~ $(T-T_c)^\alpha$ during all regimes (Fig. 2a,b). Color-coded maps of the bond order parameter, which is 1 for an ideal hexagonal unit cell, are shown in Fig. 2c,d. The arrows represent the orientation of unit cells. 5- and 7-folds are marked by red and blue dots. One can see the forming of adjacent ordered domains with non-uniform orientation, which destroys the long range orientational order. Similar behaviour is found in the simulation (Fig. 2e). The regime of additional heating could be either due to the release of latent heat (dissolution of lattice defects, tilting of nearest neighbor bonds), or due to the strong coupling between the particles, which would simulate successively larger "effective" particles.

Fig. 2

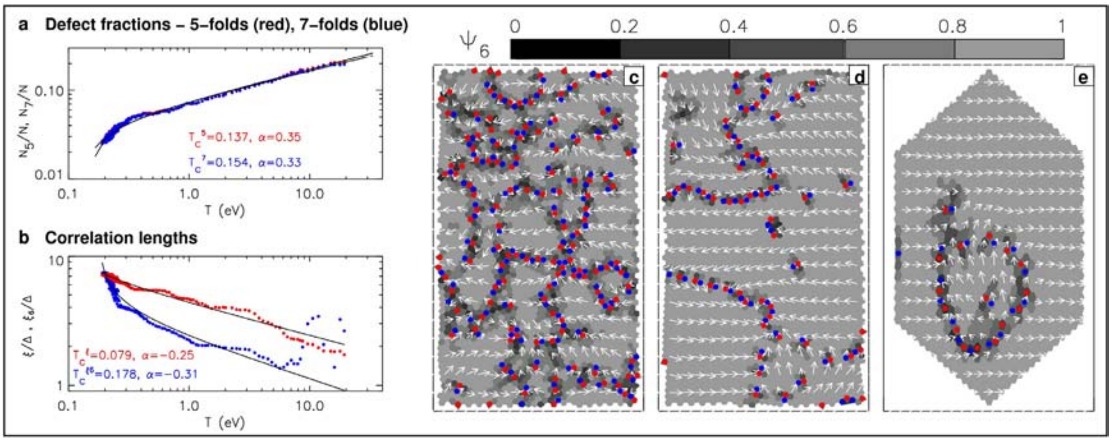

References:

• C. A. Knapek, D. Samsonov, S. Zhdanov, U. Konopka, G. E. Morfill, Phys. Rev. Lett. 98, 015004 (2007)

C. A. Knapek, D. Samsonov, S. Zhdanov, U. Konopka, G. E. Morfill

Interaction among particles in 3D plasma clusters

Small particles injected in laboratory plasmas form different structures, which obey discharge conditions and the force of gravity. The influence of gravity always stresses these structures and relatively stress-free 3D clusters are obtained only under microgravity conditions. Using the specific shape of the discharge with a 'secondary plasma' inside the main plasma sheath, it was possible to build 3D plasma clusters in gravity. In such assemblies the particles are strongly coupled and the characteristics of individual interactions as well as the properties of the whole structure (as a macro-system) can be investigated.

The interaction among particles in three-dimensional plasma clusters obtained inside a 'secondary plasma' of very small size ($64 mm^3$) have been studied. A suitable combination of dc and rf applied to a chosen segment of the so-called ‚adaptive' electrode provided gravity compensation, uniform over dimensions much larger than the cluster itself. The forces acting on the particles could be reconstructed due to unique three-dimensional diagnostics, which allow us to obtain coordinates and velocities of all the particles simultaneously.

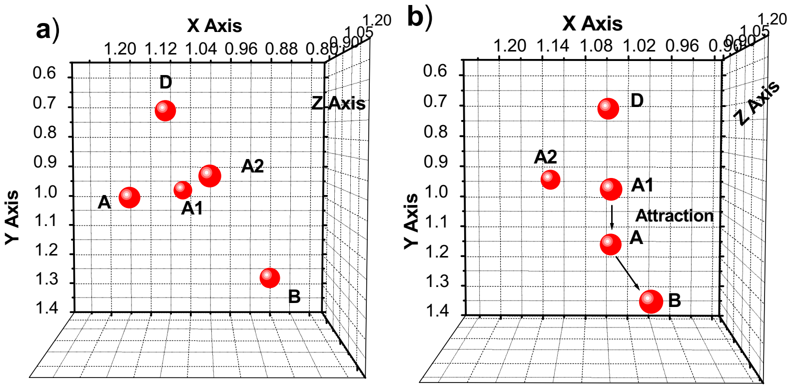

Fig.1 A cluster of 4 particles. (a) Particles before interaction, (b) particle A is attracted by the orbital particle B. Units on the axis are in millimeters. (P=57 Pa, peak-to-peak voltages are Vrf pixel=120V, Vrf driven electrode=300V).

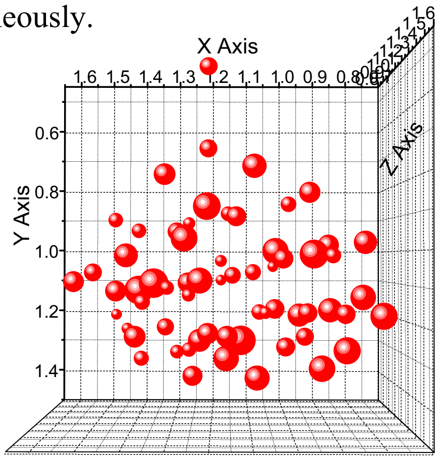

Fig.2 The 3D structure of the cluster with 63 particles and one particle leaving from the top during restructuring.

From the analysis of the spontaneous motion in a small 4 particle cluster the interaction force has been calculated (Fig.1). The measurements yield a maximum (external) confinement force of $1.4 \cdot 10^{-15}$N and interparticle force that is repulsive at short distances and attractive at larger distances, with a maximum attractive force of $2.4 \cdot 10^{-14}$N at particle separation 195 μm. Thus, the attractive part of interaction force turned out to be stronger than the surrounding confinement electric field. This makes it possible for the first time to conduct high accuracy kinetic studies of generic importance [1]. The attractive part of this force may be due to the shadow effect and it is compatible with dipole-dipole interaction, as shown in [2]. The restructuring of 3D plasma clusters containing 17 and 63 particles has been analyzed as well (Fig.2). Our estimates show the tendency of the systems to approach the states with minimum energy by rearranging particles inside. The measured 63 particles' cluster vibrations demonstrate a suitable agreement with vibration of a drop with surface tension. This indicates that even a 63 particle cluster already exhibits properties normally associated with the cooperative regime [3].

References:

1. T. Antonova, B.M. Annaratone, D.D.Goldbeck, V. Yaroshenko, H.M. Thomas and G.E.Morfill, Phys. Rev. Lett. 96, 115001 (2006)
2. V. Yaroshenko, B.M. Annaratone, T. Antonova, H. M. Thomas, and G. E. Morfill, New J. Phys. 8(9), 1 (2006)
3. T. Antonova, B.M. Annaratone, H.M. Thomas, G.E. Morfill, submitted to Phys. Rev. Letters, 2007

T. Antonova , B.M. Annaratone, V. Yaroshenko, H.M. Thomas, G.E. Morfill

Potential around a charged dust particle in a collisional sheath

By employing a self-consistent kinetic approach, an analytical expression is derived for the potential of a test charge in a weakly-ionized plasma with drifting ions. The drift is assumed to be due to an external electric field, with the velocity being mobility-limited and much larger than the thermal velocity of neutrals. The expression is proved to be in excellent agreement with existing measurements performed in the sheath region of a rf discharge.

Model assumptions

✓Only the charge-exchange collisions are taken into account, i.e., gas-kinetic and polarization collisions are neglected;
✓the ion-neutral cross-section is velocity-independent;
✓for the state without the dust particle, a mobility-limited ion drift in a homogeneous electric field is assumed (note that the time-averaged electric field is considered, as ions are assumed not to respond to the time variations of the rf field);
✓the ion flow velocity substantially exceeds the thermal velocity of neutrals (therefore we consider the velocity distribution of neutrals to be the delta-function);
✓charged dust particle is considered to be a non-absorbing point charge;
✓the non-linear screening region near the dust particle is negligibly small (therefore we employ the linear response formalism);
✓the electron response is negligible.

No assumption is made about the ratio of the ion-neutral "mean" free path to the effective length of charge screening.

Comparison with experiment of Refs. [1,2]

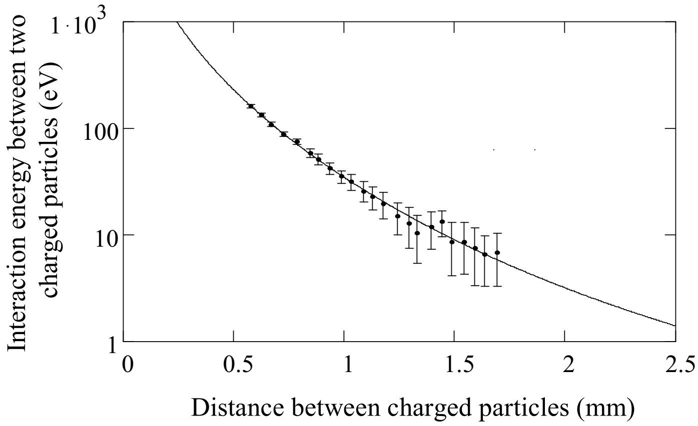

(The line connecting the particles was perpendicular to the direction of the ion drift).

Conclusion

Our model attributes screening of a charged grain to ions only. Assuming a mobility-limited ion drift with velocity much larger than the thermal velocity of neutrals, we derived an analytical expression for grain screening which appeared to be generally not of the Yukawa form. Both our expression and the Yukawa potential are in excellent agreement with the experiment of Refs. [1, 2]. At the same time, our expression strongly suggests that measurements performed in a broader range of distances should reveal significant deviations from the Yukawa potential. Hence, experiment [1, 2] **cannot** be used for justification of either the Yukawa potential or the dominant role of electrons in grain screening, and more experiments are necessary to resolve the issue.

References:
• U. Konopka, G. E. Morfill, and L. Ratke, Phys. Rev. Lett. **84**, 891 (2000).
• U. Konopka, Ph.D. thesis, Ruhr-Universitat Bochum, 2000.
• R. Kompaneets et al., submitted to Phys. Plasmas.

R. Kompaneets, U. Konopka, A. V. Ivlev, V. Tsytovich, and G. Morfill

Effect of plasma absorption on the electrostatic potential Behind an absorbing dust grain in highly collisional plasma

Considering Boltzmann electrons and hydrodynamic description of slowly drifting ions, the potential and electric field have been calculated behind a small absorbing floating dust grain in highly collisional plasma. Both the isotropic and anisotropic parts of the potential are influenced by plasma absorption. Long range potential is completely dominated by absorption. At moderate distance the attraction between grains takes place in certain parameter regime whereas the short- and long-range asymptotes of potential are always repulsive.

A stationary, negatively charged, spherical, absorbing dust grain is immersed in a highly collisional quasineutral plasma where ions are drifting with subthermal velocity while electrons form stationary background. Linear response technique has been applied to get an expression for the potential downstream from the grain. The amplitude of the anisotropic part of the potential is decreased by the absorption effect and even changes its sign. At large distances, the dominant contribution comes from the isotropic part associated with the absorption i.e. the long-range asymptote is completely determined by absorption.

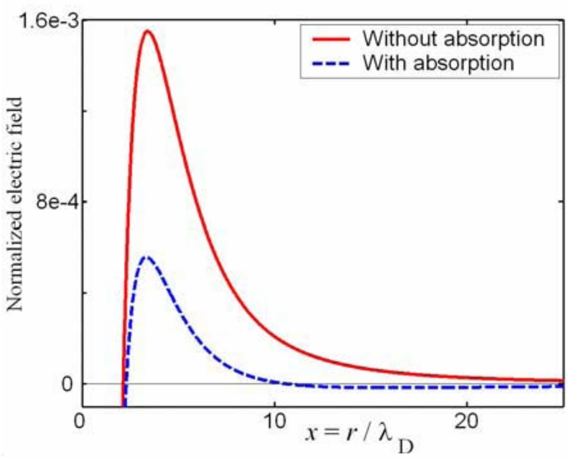

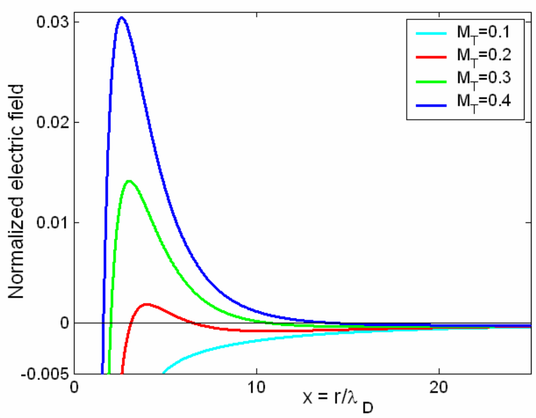

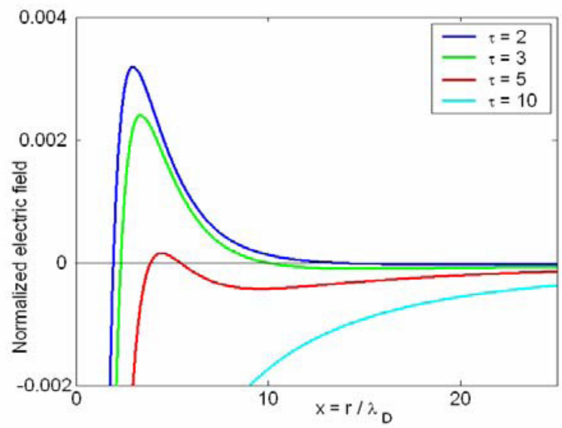

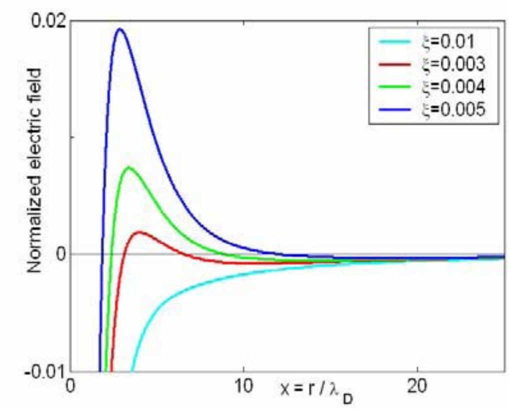

The ion drag force which is associated with the anisotropy induced by flowing plasma has been calculated. It is shown that the effect of plasma absorption reduces the magnitude of the force in the highly collisional plasma. The figures show the variation of the normalized electric field with normalized distance for different plasma parameters. Here, M_T is the thermal mach number for drifting ions, ξ is the normalized ion mean-free path and τ is the electro-to-ion temperature ratio.

References:
Chaudhuri et. al., Phys Plasmas 14, 022102 (2007)
Khrapak et. al., J. Appl. Phys. 101, 033307 (2007)

M. Chaudhuri, S. A. Khrapak, G. E. Morfill

Grain charge in the bulk of gas discharges

A series of experiments has been dedicated to investigate the effect of ion-neutral collisions on grain charging in bulk plasma of gas discharges. It is demonstrated that ion-neutral collisions represent very important factor, which significantly reduces the charge under typical conditions. A simple analytical model is proposed which fits reasonably the results from experiments and simulations. Application of the obtained results is briefly discussed.

Traditionally, it had been believed that collisionless orbital motion limited (OML) theory adequately describes electron and ion collection by a small grain in plasmas when ion and electron mean free paths are long compared to the plasma screening length. In a series of recent papers it was pointed out, however, that ion-neutral charge exchange collisions can considerably increase the ion flux to a grain (or probe) even when the latter requirement is fulfilled. This motivated us to experimentally determine grain charge in a bulk discharge plasma in a wide range of neutral gas pressures.

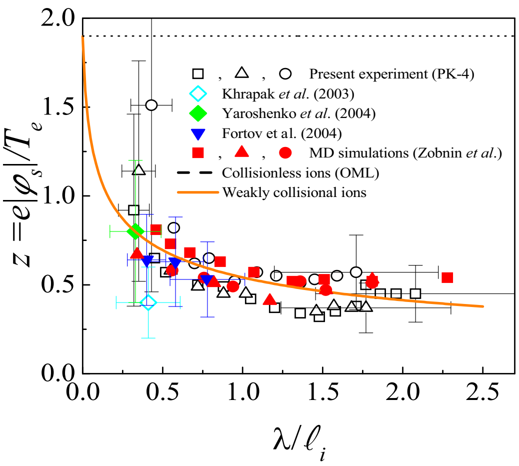

The experiment was performed with the PK-4 facility in ground-based conditions. Grain flows in a horizontal dc discharge tube filled with neon gas at pressures 20-150 Pa were studied. The charges were estimated by two methods: from the force balance condition at high pressures and from the analysis of linear dispersion relation describing the transition to an unstable grain flow at lower pressures [1-3]. In Figure the obtained experimental results are shown along with the results from numerical simulation and other available experimental data. The experimentally determined charges are considerably smaller than those predicted by OML (dotted line), which proves the significant effect of ion-neutral collisions on grain charging in plasmas.

A simple analytical approximation for the ion flux to the grain in the weakly collisional regime (ion mean free path is larger than the characteristic length scale of ion-grain interaction) has been also proposed. This approximation (solid curve) provides a reasonable fit for the available experimental and numerical data, especially taking into account experimental errors. The above mentioned approximation has recently been successively used to improve the understanding of void formation in experiments with PKE-Nefedov onboard ISS [4], to estimate conditions for critical point existence in complex plasmas [5], to refine the model for grain surface temperature [6], to analyze electrostatic interactions between particles [7], etc.

References:

1. S. Ratynskaia, S. Khrapak, A. Zobnin, M. H. Thoma, M. Kretschmer, A. Usachev, V. Yaroshenko, R. A. Quinn, G. E. Morfill, O. Petrov, and V. Fortov, Phys. Rev. Lett. **93**, 085001 (2004).
2. S. A. Khrapak, S. V. Ratynskaia, A. V. Zobnin, A. D. Usachev, V. V. Yaroshenko, M. H. Thoma, M. Kretschmer, H. Hofner, G. E. Morfill, O. F. Petrov, and V. E. Fortov, Phys. Rev. E **72**, 016406 (2005).
3. S. A. Khrapak, S. V. Ratynskaia, M. H. Thoma, A. V. Zobnin, A. D. Usachev, V. V. Yaroshenko, M. Kretschmer, H. Hofner, G. E. Morfill, O. F. Petrov, and V. E. Fortov. AIP Conference proceedings **799** (Melwill, NY 2005), pp. 177-180.
4. M. Kretschmer, S. A. Khrapak, S. K. Zhdanov, H. M. Thomas, G. E. Morfill, V. E. Fortov, A. M. Lipaev, V. I. Molotkov, A. I. Ivanov, and M. V. Turin, Phys. Rev. E **71**, 056401 (2005).
5. S. A. Khrapak, G. E. Morfill, A. V. Ivlev. H. M. Thomas, D. A. Beysens, B. Zappoli, V. E. Fortov, A. M. Lipaev, and V. I. Molotkov, Phys. Rev. Lett. **96,** 015001 (2006).
6. S. A. Khrapak and G. E. Morfill.. Phys. Plasmas **13**, 104506 (2006).
7. S. Ratynskaia, U. de Angelis, S. Khrapak, B. Klumov, and G. E. Morfill. Phys. Plasmas **13**, 104508 (2006).

S. Ratynskaia, S. Khrapak, V. Yaroshenko,
M. Thoma, M. Kretschmer, H. Hoefner G. Morfill,

Liquid-vapor critical point in complex plasmas

The occurrence of liquid-vapor phase transition and possible existence of a critical point in complex plasmas - systems that consist of charged micrograins in a neutralizing plasma background - is investigated theoretically. An analysis based on the consideration of the intergrain interaction potential suggests that under certain conditions systems near and at the critical point should be observable. Measurements under microgravity conditions would appear to be required. The analysis aims at determining plasma parameter regime most suitable for experimental investigations.

The purpose of this investigation is to ascertain that complex plasmas can exhibit a liquid-vapor critical point. To do this we have analyzed basic grain-grain interactions and derived the binary interaction potential in isotropic weakly collisional bulk plasma of gas discharges. The interaction potential turns out to be similar to that in usual gases, i.e. it is repulsive at short distances and attractive at larger distances (see sketch). Repulsion is caused by electrostatic interaction between like charged grains, the attraction is due to the so-called shadowing force, which is the resultant of the drag force experienced by neighboring grains continuously absorbing plasma on their surfaces. The resulting long-range interaction potential is $U(r)=4U_0[(R/r)^2-(R/r)]$, where U_0 is the depth of the potential and R is the distance at which the potential crosses zero. The effective length scale of this interaction is determined by spatial scale of ion Maxwellization, i.e., by the mean free path of ion-neutral collisions.

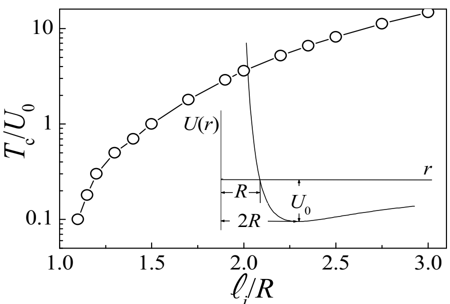

The qualitative similarities in the interaction compared to conventional gases indicate that complex plasmas can have a liquid-vapor critical point. There is, however, an important difference: The characteristics of the potential U_0 and R are not fixed but depend on a variety of complex plasma parameter (e.g., grain size and charge, plasma density, ion and electron temperatures). The question is, therefore, whether the critical point can occur for realistic plasma parameters, i.e., whether it is observable.

To get further insight into this problem we used arguments similar to those in the Van-der-Waals theory of liquid-vapor critical point and calculated critical parameters. Figure shows the calculated dependence of the critical temperature (normalized to the depth of the potential U_0) on the ion mean free path l_i (normalized to the distance R). As expected, the critical temperature drops considerably upon narrowing the range of attraction (with decreasing the ion mean free path). There can be about 1 order of magnitude deviations (in both directions) from the simplest estimate $T_c \sim U_0$. The critical grain density can be roughly estimated as $n_c \sim 0.3R^{-3}$.

The requirements for observing the critical point in complex plasmas within the chosen paradigm are: (i) isotropic plasma conditions (at least subthermal ion drift); (ii) weak confinement (the intergrain distance should be somewhat larger than R, where $R\sim(2\text{-}4)\lambda$ under usual conditions); (iii) low enough neutral gas pressure ($l_i>R$ so that the attractive branch in the potential exists) (iv) High enough critical temperature (higher than the neutral gas temperature, which is the lower limit for the grain kinetic temperature due to Brownian motion).

Isotropic plasma conditions with weak confinement require experiments with complex plasma under microgravity conditions. We have performed estimates of the plasma conditions for PKE-Nefedov, PK-3 Plus, and PK-4 facilities operating/prepared for operation onboard ISS. Altogether these estimates indicate that the critical point of complex plasmas can be observable, although fine tuning of plasma parameters might be necessary.

References:

•S. A. Khrapak, G. E. Morfill, A. V. Ivlev. H. M. Thomas, D. A. Beysens, B. Zappoli, V. E. Fortov, A. M. Lipaev, and V. I. Molotkov, Phys. Rev. Lett. 96, 015001 (2006).

S. A. Khrapak, G. E. Morfill, A. V. Ivlev, H. M. Thomas

Non-Newtonian viscosity of complex plasma fluids

Fluids exhibit rich variety of rheological properties. Along with conventional Newtonian fluids that have constant viscosity, there exists a broad class of non-Newtonian fluids with the rheology that strongly depends on the flow conditions. Classic examples encountered in everyday life include ketchup, gelatine, paint, etc. Other fluids such as molten polymers and slurries are of considerable technological importance. Using the PK 4 setup, we measured shear flow profiles induced in complex plasma fluids either by an gas flow or by a laser beam, compared the results with theory and showed that complex plasmas exhibit strong non-Newtonian behavior.

According to a theoretical model of non-Newtonian viscosity of complex plasmas, there are three distinct shear flow regimes: If shear rate γ is small enough, the viscosity ν does not depend on γ and the shear stress $\sigma \propto \gamma$ (regime I). At larger γ the behavior becomes non-Newtonian: $\nu(\gamma)$ falls off showing shear thinning (regime II), so that $\sigma(\gamma)$ may also decrease. As γ grows further, $\nu(\gamma)$ and hence $\sigma(\gamma)$ increase again (shear thickening, regime III). Such behavior is typical to conventional non-Newtonian fluids.

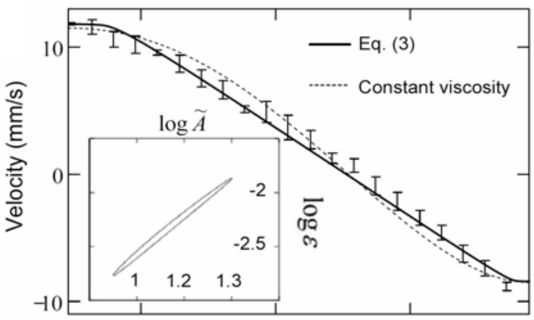

Fig. 1 0 2 4 x(mm)

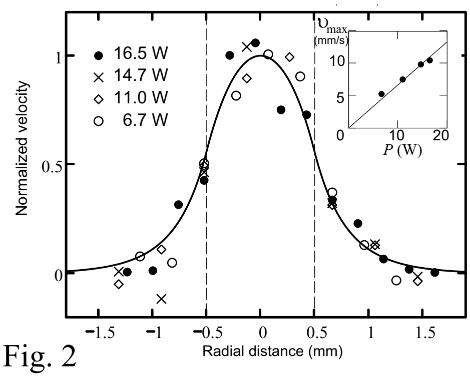

Fig. 2

Typical example of measured velocity curve for the 1D gas-induced flow is shown in Fig. 1 (transverse coordinate x equals zero at the discharge tube axis). Substantial part of the curve has quasi-linear profile, which is common peculiarity for all measurements performed at different conditions. We performed a two-parametric fit of the curve with solutions of the Navier-Stokes equation for (i) our non-Newtonian viscosity model and (ii) conventional constant-viscosity case. One can see that the non-Newtonian viscosity yields extended region of quasi-linear profile and thus provides good agreement. In contrast, for the constant-viscosity model the curve is of fairly different shape, which makes qualitative distinction with the non-Newtonian case. Thus, the range of shear rates achieved in these experiments was sufficiently broad to reveal non-Newtonian behavior of complex plasmas. At the same time, the shear was small enough to expect hydrodynamics to be applicable.

In contrast, inhomogeneity of the laser-induced flows shown in Fig. 2 was very high – the velocity changed significantly at the scale of the interparticle distance. In this case, we measured the cylindrically symmetric velocity profiles for different values of laser power P and normalized to the maximum velocity at the center v_{max}. Qualitatively one can see that the normalized profiles seem to be similar for different P, and v_{max} grows linearly with P. This suggests that – if the hydrodynamics still works – the effective viscosity in such "extreme" flows should tend to some constant value. Such hypothesis is well confirmed by the corresponding fit shown in Fig. 2.

Combination of both methods of the flow generation made it possible to span entire range of γ up to the edge where complex plasmas cannot be considered as a continuous medium. The derived magnitude of the kinematic viscosity in the Newtonian regime is ~ 100 mm^2/s, which is about the viscosity of, e.g., glycerin. The observed shear thinning, however, diminishes the viscosity by factor of 10, making it close to the viscosity of air at atmospheric pressure. Hence, in terms of viscosity the fluid complex plasmas are very similar to ordinary classic fluids.

A. Ivlev, R. Kompaneets, H. Höfner, I. Sidorenko, G. Morfill

Crystallization of 3-dimensional complex plasmas

Pk-3 Plus is the subsequent experiment of PKE - Nevedov. Due to changes of geometric features, as the bigger size of the electrodes, it is possible to grow larger crystals. They are also more stable and show less fluctuations. So we are able to observe crystallization in lab for more than an hour. Using the orientation of the next neighbors of each particle we characterize the type of the crystal structure on a local scale. It is found, that crystallization reaches a high state after a few minutes. But crystalline structure continues to change from hcp to fcc for much longer time because of the lower energy of fcc, as it is predicted in simulations.

For this experiment we inject particles of 2,55µm in size at a pressure of 0.40 mbar in a radio-frequency (rf) Argon plasma. The particles are levitated in the sheath region of the plasma but extend far into its bulk region. At appropriate plasma parameters the dusty plasma cloud starts to form a plasma crystal. By increasing and decreasing the rf power, the crystal gets melted and crystallization restarts at a well defined time. Then we accomplish several scans at different times up to 40 minutes after crystallisation started.
By the scans we obtain three dimensional information of the cloud. This 3D positions of the particles we can use for local order analysis. In that method the orientation of the next neighbors of a particle is compared to ideal crystal. So it is possible to distinguish the type of neighborhood a particle sits in. In our case we used fcc and hcp to compare. All other local structures are assumed as liquid.

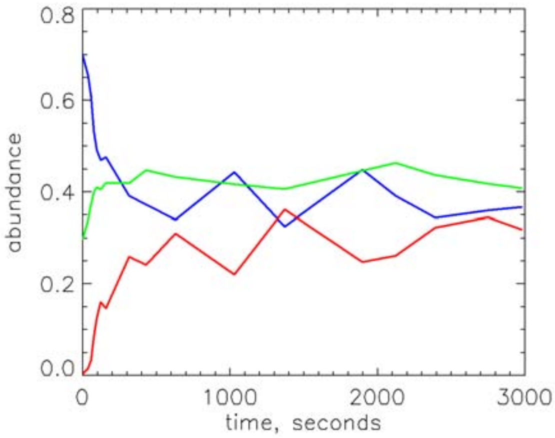

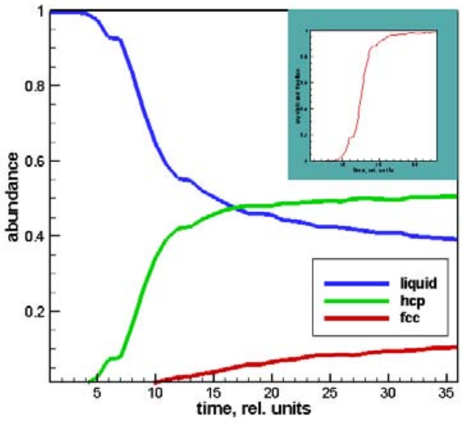

The left figure shows the fraction of certain struc-tures for the ex-perimental data. The fraction of hcp (green) starts at 30% increasing and reaches saturation soon. The fraction of fcc (red) starts at zero and reaches saturation later than hcp. It even seems to continue increasing. The strong variations in at 1000 seconds and 2000 seconds come from gas renewing, which is necessary for long time measurements. The right figure shows simulation data according to a similar situation. You can clearly see, that hcp increases soon and fcc follows when hcp almost reached saturation. This is due to the fact, that the energetic state of fcc lies below hcp. So when the cloud cools down by neutral gas friction it first settles down in hcp state and then, continuing cooling down, reaches fcc. Comparing the two figure it is visible that experiment and simulation match very well. So few minutes after starting most of the complex plasma crystallized, but changes in the type of crystalline structure can be observed for much longer time.
Comparing experiments at different plasma parameters to simulations should give us information about crystal parameters such as damping or coupling parameter.

P. Huber, V. E. Fortov, A. V. Ivlev, B. Klumov, A. M. Lipaev, V. I. Molotkov, G. E. Morfill, M. Rubin-Zuzic, H. M. Thomas

Complex plasma 'void' characteristics in microgravity

Most complex plasma experiments in microgravity exhibit a particle-free region in the center of the discharge plasma, the so called 'void'. Also 'PKE-Nefedov' – MPE's complex plasma experiment facility onboard the International Space Station in 2001 - 2005 [1] – shows in most experiments this feature.
In a dedicated experiment session on the ISS we injected particles into the void at different gas pressures and by analyzing their outward trajectories we can conclude on the forces acting on the particles.
Together with computer simulations we now assume that the force that is responsible for the void formation is the drag force of the ions that are produced in the center of the discharge, streaming outwards to the rf electrodes. This tells us something about the dynamics of the ion component inside a complex plasma.
Since 2006, a new plasma experiment facility is onboard ISS, 'PK-3 Plus'. First results of void measurements with PK-3 Plus are compared to those of PKE-Nefedov.

The analysis of the trajectories of the particles emitted from the void (see figures on the right side: 1) reveals a linear dependency of the velocities in x (2a) and y direction (2b) with respect to the center. By integrating the equation of motion

$$m\ddot{x}_i + R\dot{x}_i + \nabla\Phi(x)\big|_{x_i} = 0$$

with $x_i=x$, y and using the linear behaviour $v(x_i)=a_i x_i$ we get the effective potential energy of the particles

$$\Phi(x_i) = \Phi_0 - \frac{1}{2}(m a_i^2 + R a_i) x_i^2$$

which is of parabolic shape (3). Calculating the (not electrical!) potential at the boundary of the void we get roughly the same value in x and y which reveals the boundary to be a equipotential surface.

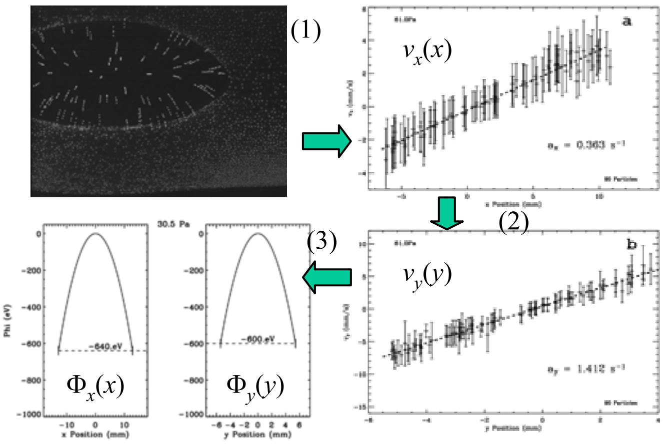

A set of experiments on the ISS focused on the void at different pressures. The size and position change with the pressure as shown in fig. (4). The values of a_x and a_y as shown in (5).

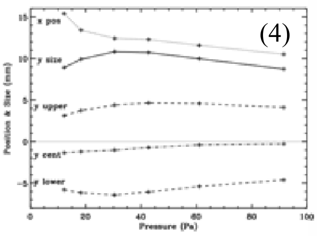

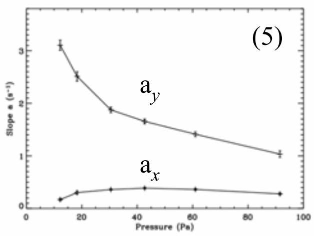

Simulations show that the trajectories of the particles (dark blue dots, 6) can be well fitted with parabolas (light blue) through the center of the void. The dotted ellipses depict the equipotential lines, nicely fitting the actual shape of the void.

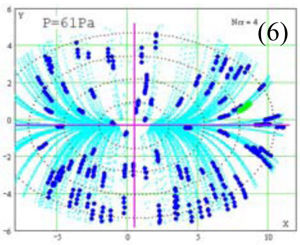

SUMMARY:

- The analysis shows that the structure of the void is independent from the presence or distribution of the particles.
- The effective potential energy that drives the particles out of the void is found to be of parabolic shape with the void boundary being an equi-potential surface. This is true for the total void volume, in extension to [2].
- The absence of gravity reveals weak forces, as the ion drag force - which we assume is mainly responsible for the void formation - and also thermophoretic forces.
- This results may help to understand the void - a prominent feature in complex plasmas, never seen on Earth before - and thus learn about the basics of complex plasmas.
- First experiments with the new 'PK-3 Plus' facility onboard ISS show a total different behaviour with more than 10 times lower particle velocities inside the void. This needs further investigation.

References:
[1] http://www.mpe.mpg.de/pke, PKE-Nefedov Homepage
[2] Kretschmer, et al, Phys. Rev. E 71, 056401 (2005)

M. Kretschmer, U. Konopka, S. Zhdanov, H. Thomas, G. Morfill, ISS Crew "Exp.8"

The 'classical tunnelling effect' - observations and theory

In ground-based laboratory experiments, in experiments under microgravity conditions and in parabolic flight experiments, it is often observed that individual microparticles appear sometimes to simply pass through a strongly coupled complex plasma without affecting the fabric (the structure) of the penetrated cloud. We have termed this new effect 'classical tunnelling' in analogy to its quantum mechanical counterpart.

The tunnelling in strongly coupled complex plasmas occurs at a typical microparticle velocity range of 1- 15mm/s, at least 5-10 times faster than the particle velocities in the surrounding strongly coupled environment. To explain this anomalous transport, a 'geometrical model for charge variation' of moving and stationary ordered particles is proposed[1]. This model qualitatively is applicable both in cases of large (H~1) or small (H<<1) values of the Havnes parameter ($H=Z/N_e$, Z is the particle charge, and N_e is the number of free electrons per particle). Theoretical predictions are in good qualitative agreement with observations and numerical simulations, and show that the phenomenon can be considered as a consequence of the non-Hamiltonian character of complex plasmas.

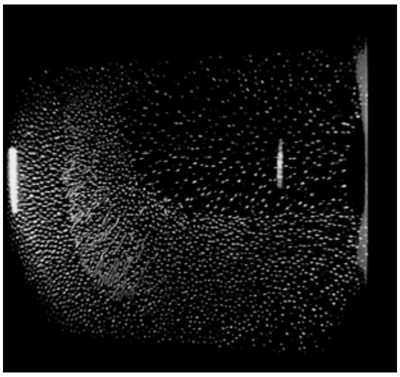

Parabolic flight experiments: Chains of particles (r=1.69μm) passing through a cloud of larger particles (r=3.45μm, H>1).

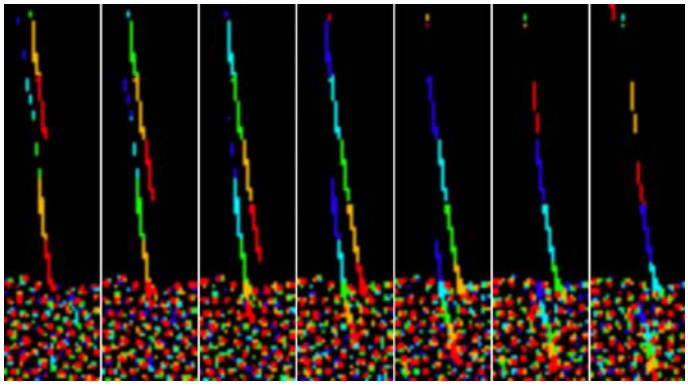

Ground-based laboratory experiments: Anomalous transport of particles under gravity conditions. Particles are of the same size (r=0.6μm, H<<1).

Experiments on board of the ISS: Formation of a dense cloud of coupled particles (r=3.45μm) at the boundary of the sheath region (shown at left), and example of anomalous transport observations (shown at right; 1-3 are the trajectories of penetrating particles, H<1).

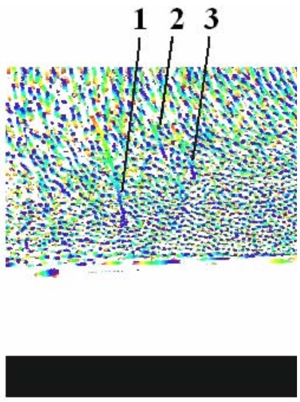

References:
1. G.E. Morfill, U. Konopka, M. Kretschmer, M. Rubin-Zuzic, H.M. Thomas, S. Zhdanov, and V. Tsytovich, New Journal of Physics, 8, 7 (2006)

G.E. Morfill, U. Konopka, M. Kretschmer, M. Rubin-Zuzic, H.M. Thomas, S. Zhdanov, and V. Tsytovich

Nonlinear Waves in 3D Complex Plasmas

Experimental results on dark solitons (solitary rarefaction waves) in a three-dimensional complex plasma containing monodisperse microparticles are presented. The waves are exited by a short voltage pulse applied to one of the electrodes of the rf discharge chamber. The particles are levitated by thermophoresis. For this purpose, a gas temperature gradient of 400K/m is applied.

The experiments were performed in a 13.56 MHz symmetrically driven RF discharge. Spherical melamin-formaldehyde particles with a diameter of 3.42 microns were injected by a dispenser. To establish the temperature gradient we heated the lower electrode (ΔT=12K). For wave excitation we used a voltage jump method, applying a voltage pulse (5-50V) to the lower and/or the upper electrode. A vertical slide of the complex plasma was illuminated by a laser diode and the scattered light was then recorded by a high-speed camera with a frame rate of 1000Hz. Setup details are shown in the picture.

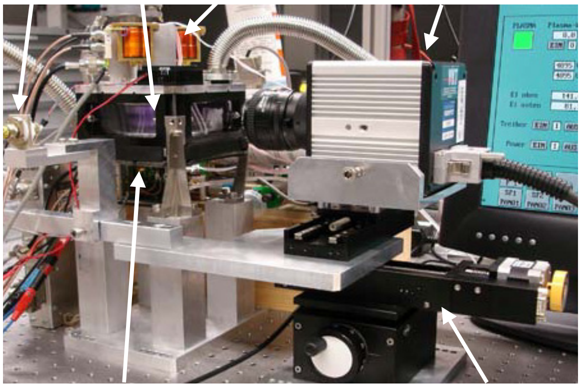

The excited waves were supersonic. For instance, in an experiment performed at higher pressure (50 Pa, see pictures below) the measured wave speed was c=(17.0±1.1)mm/s and exceeds approximately two times the calculated dust acoustic wave speed (c_{DAW}=8mm/s). The decompression factors of the observed waves were of the order of 10. The amplitude damping factor was 8.69 s^{-1},which is ten times lower than the Epstein damping rate (123 s^{-1}) for the given conditions. The wave fronts consisted of a rarefaction zone and a sedimentation front. Particles coming from the rarefaction zone and then crossing the sedimentation front were counter streaming the particles within the sedimentation front. These multidirectional flows were observed below 20Pa.

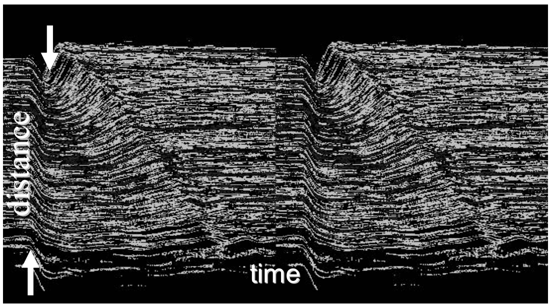

Time dependence of the average intensity of the horizontal pixel lines which are parallel to the electrodes. The Arrows mark the time of excitation.

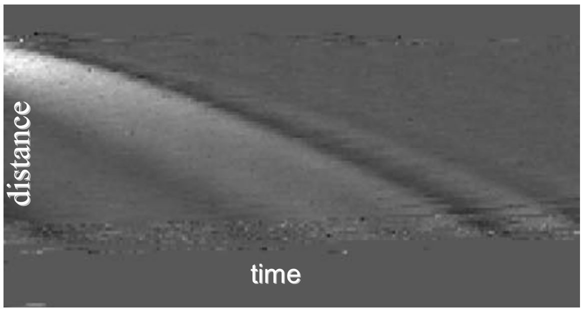

Vertical velocity component versus time. White colors represent positive z-velocity (rarefaction zone) whereas black represents neg. z-velocities (sedimentation front)

Complex plasmas give us the unique chance to explore highly nonlinear waves such as dark solitons at the most fundamental kinetic level. Such kind of detailed experimental investigation is almost impossible in other (atomic) systems.

R. Heidemann, H. Thomas, S. Zhdanov, R. Sütterlin, G. Morfill

Excitation of Ion Acoustic Soliton

Excitation of IAS and its interactions with fast burst ions were studied. IAS evolves from the normal fast ion-beam mode. Burst ions are created by applying a positive ramp voltage to the grid. Their velocity changes with the rise time and/or amplitude of the applied signal. Strong interactions between the burst ions and soliton arise via the effect of inverse Landau damping.

The experiments were carried out on a inhomogeneous double plasma device (Fig. 1). The ion-acoustic soliton (IAS) was excited by applying an positive ramp voltage to the grid (SG), the wave signal was received by a positively biased probe (CP). The potential structure and ion flow around SG is shown in Fig. 2.

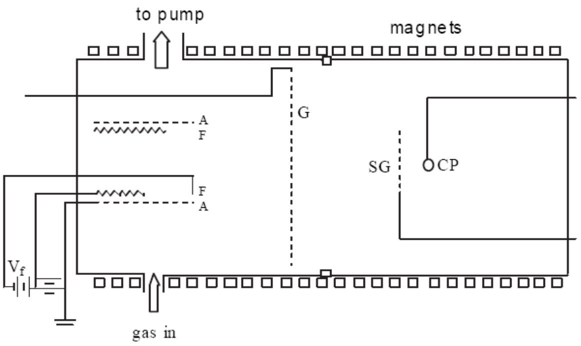

Fig. 1

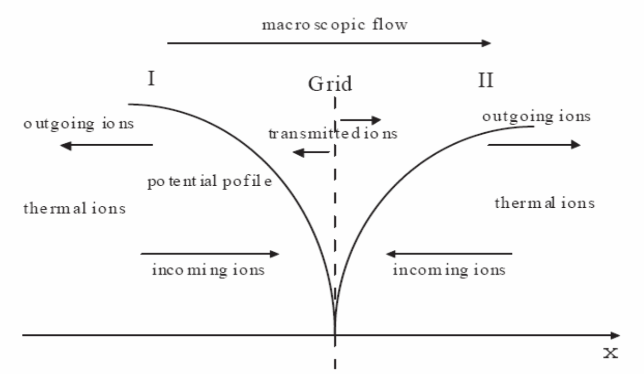

Fig. 2

Perturbation of the electron saturation current versus time at the probe 7 cm away from SG.
Fig. 3 fixed Vpp=20 (amplitue of applied voltage on SG) and variable rise time τ
Fig. 4 fixed τ=2.5μs and variable Vpp

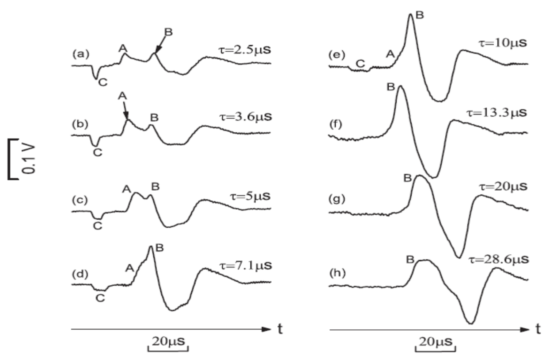

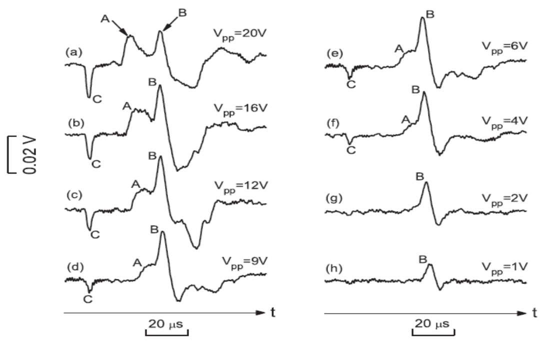

Estimate of the velocity of the burst ions can be deduced by energy conservation:

$$v_{\max} \sim c_s \left(M^2 + \frac{2eV_{pp}}{T_e} \frac{1}{\omega_{pi}\tau} \right)^{1/2} \quad \text{for the rise time longer} \quad = c_s\sqrt{M^2 + 2eV_{pp}/T_e}$$

shorter than the ion oscillation time scale.

References:
•Y. F. Li, J. X. Ma, Y. R. Li, D. L. Xiao, and K. E. Longgren, *Phys. Lett. A* 358, 297 (2006).
• J. X. Ma, Y. F. Li, D. L. Xiao, J. J. Li, and Y. R. Li, *Rev. Sci. Instrum.* 76, 062205 (2005).

Yang-fang Li, J. X. Ma, De-long Xiao, Yi-ren Li, and M. Y. Yu

Cutoff wave number for shear waves in a two-dimensional liquid complex plasma

Liquids generally support compressional (longitudinal) waves. However, shear (transverse) waves can only propagate if their wavelength is as short as a few molecular spacings. Thus, the dispersion relation of the shear waves in a liquid has a cutoff wave number. This cutoff is well known for molecular liquids, and it has been predicted theoretically for strongly-coupled plasmas as well. We report the first experimental observation of the cutoff wave number for shear waves in a liquid dusty plasma.

The cutoff wave number for shear waves in a liquid-state strongly-coupled dusty plasma was measured experimentally [1]. The phonon spectra of random particle motion were measured at various temperatures in a monolayer dusty plasma. In a liquid state of this particle suspension, shear waves were detected only for wavelengths smaller than 20 to 40 Wigner-Seitz radii, depending on the Coulomb coupling parameter.
In the experiment, a monolayer suspension of polymer microspheres was levitated in the sheath above a horizontal electrode in a radio-frequency plasma. The particles interacted with a Yukawa potential, and formed a triangular lattice.

To melt this lattice and form a liquid, we used a laser-heating method [2]. Laser manipulation was used to apply random kicks to the particles. Two focused laser beams were moved rapidly, drawing Lissajous figures in the monolayer. The kinetic temperature of the particles increased with the laser power applied, and above a threshold a melting transition was observed. This laser-heated dusty plasma has some characteristics of a thermal equilibrium.

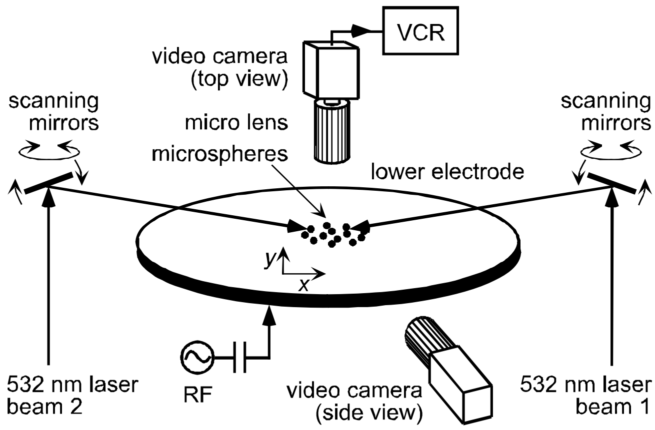

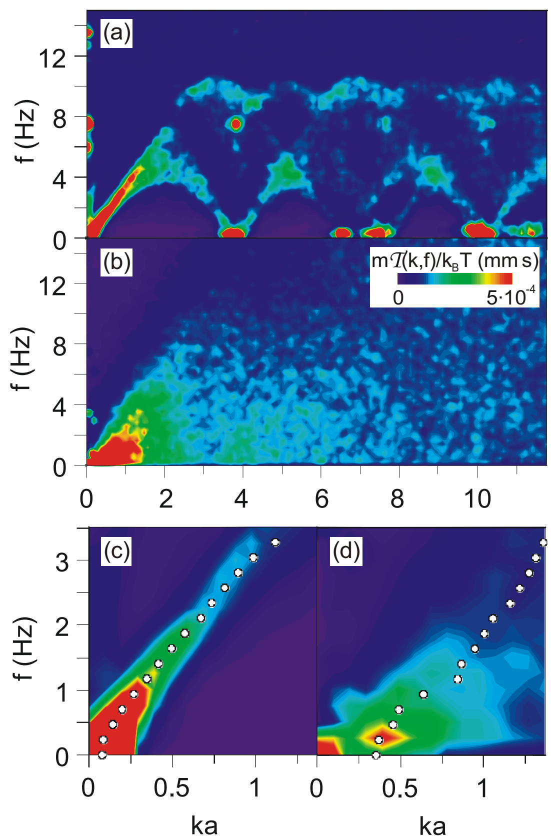

Left figure: Experimental setup, including two rastered laser beams for heating.
Right figure: Power spectrum of shear waves for: crystal (a,c) and liquid (b,d). The cutoff in a liquid is identified as a lack of wave energy at the smallest wavenumbers.

References:
1. V. Nosenko, J. Goree, and A. Piel, Cutoff wave number for shear waves in a two-dimensional Yukawa System (Dusty Plasma), Phys. Rev. Lett. **97**, 115001 (2006)
2. V. Nosenko, J. Goree, and A. Piel, Laser method of heating monolayer dusty plasmas, Phys. Plasmas **13**, 032106 (2006)

V. Nosenko, J. Goree, and A. Piel

Highly resolved density waves self-excited in a complex plasma

We report an investigation of self-excited density waves appearing in a complex (dusty) plasma under the influence of thermophoresis at low pressures. The waves propagate either up- or downwards depending on the position of the dust cloud in the plasma chamber. The critical pressure for the onset of the self-excited waves and the wavelength depend on the temperature gradient applied. The wave frequency, phase velocity and wavelength were measured as a function of the height above the lower electrode of the setup. Using a high speed camera (1000 frames per second) we analyzed the behavior of the microparticles under the influence of the waves at a high time and space resolution.

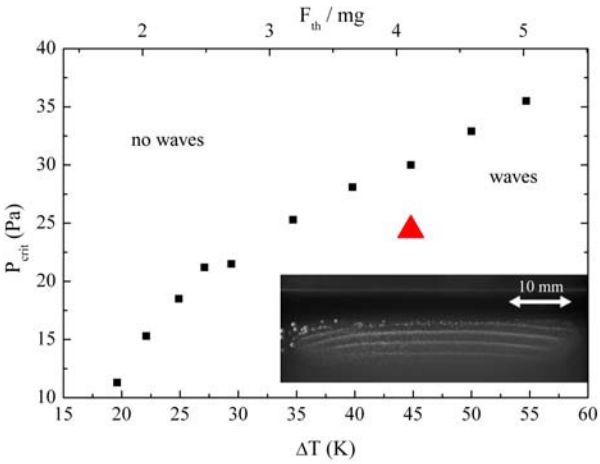

Fig.1: The critical pressure for the onset of the excitation in argon with 1.28 μm particles as a function of the temperature difference between the electrodes resp. the thermophoretic force acting on the microparticles. The inset shows a photograph of the waves (red triangle) which are analyzed in detail.

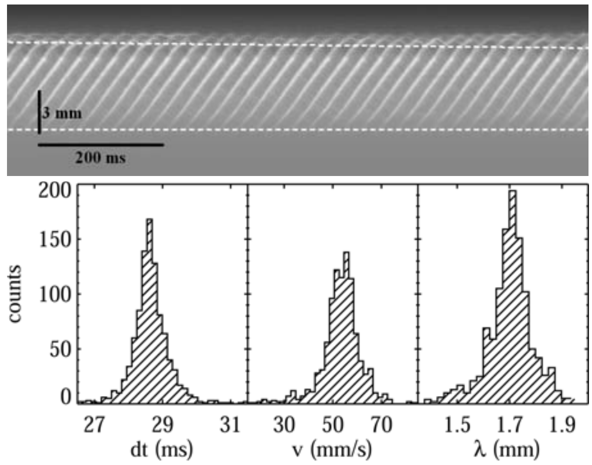

Fig.2: Pixel intensities summed over 100 pixels horizontally in the central cloud plotted next to each other for appr. 900 frames *(top)*. The wave ridges are clearly visible. From this, we determined wave parameters *(bottom)*: period <dt> = 28.77 ± 0.01 ms, phase velocity <v> = 55.5 ± 0.2 mm/s, and wavelength <λ> = 1.74 ± 0.01 mm

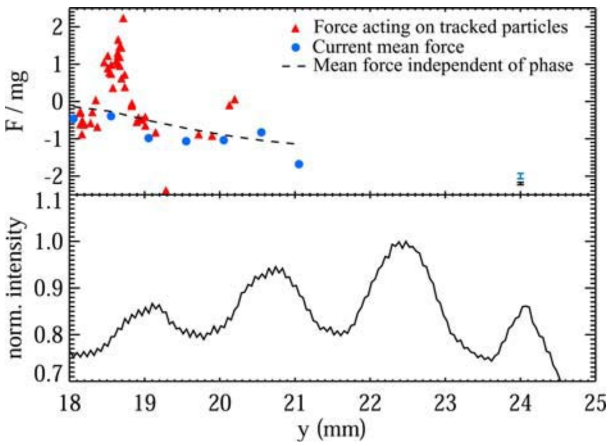

Fig.3: Net force acting on the particles in a single phase of the wave *(top)* and normalized pixel intensity in the same phase vs. the height above the electrode *(bottom)*

We performed experiments in a dusty ccrf-discharge (Ar, 30 V peak-to-peak, 3 cm electrode distance, 1.28 μm MF-particles). The lower electrode was heated, so that the vertical temperature gradient was adjustable. Below a critical pressure, self-excited waves appeared, propagating vertically. We measured the critical pressure as a function of the temperature gradient (Fig. 1). For the case shown in red in Fig. 1 (p = 24 Pa, ΔT = 45 K) we determined the wavelength, frequency and phase velocity (Fig. 2). The phase velocity increased slightly with the height. We also tracked the microparticles from frame to frame and calculated the net force acting on them (one wave phase shown in Fig. 3). A periodical rise in the force is visible, correlated with the rise in pixel intensity.

M. Schwabe, M. Rubin-Zuzic, S. Zhdanov, and G. E. Morfill

Streamlines: Particle lanes in fluids

The GEC-rf-reference cell is used to produce a complex plasma. With two glass-rings a circular path is formed. Particles are accelerated by applying a slow varying electric field to the additional electrodes mounted to the outer glass-ring. A quasi-infinite particle stream can be observed that behaves like a liquid crystal.

Setup: Two glass-rings (r=2/4cm) and a screw nut (obstacle) on the rf electrode (3W at 13.56MHz). Particles (Melamine-Formaldehyde d=6.8µm) in Argon plasma at 17 Pa, no gas-flow. Acceleration by 9 electrodes: slow varying EM field (freq. 0.9 Hz, ampl. 50V, last electrode -40V offset, phase shift 120° between electrodes.

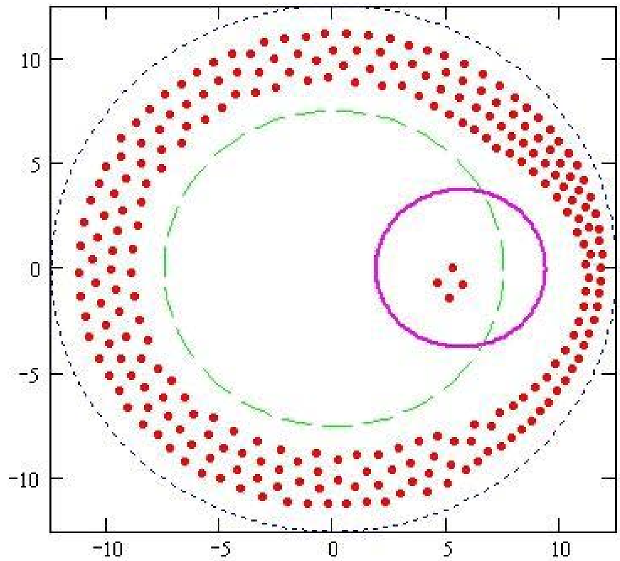

Simulations: Acceleration by constant force at any position. The obstacle is a hard sphere. Particles get compressed before the obstacle and thus are pushed out of the center of the confinement potential.
Particles behave more like a liquid crystal as displacements occur seldom and particles mostly arrange in a 6-fold symmetry like in crystalls.

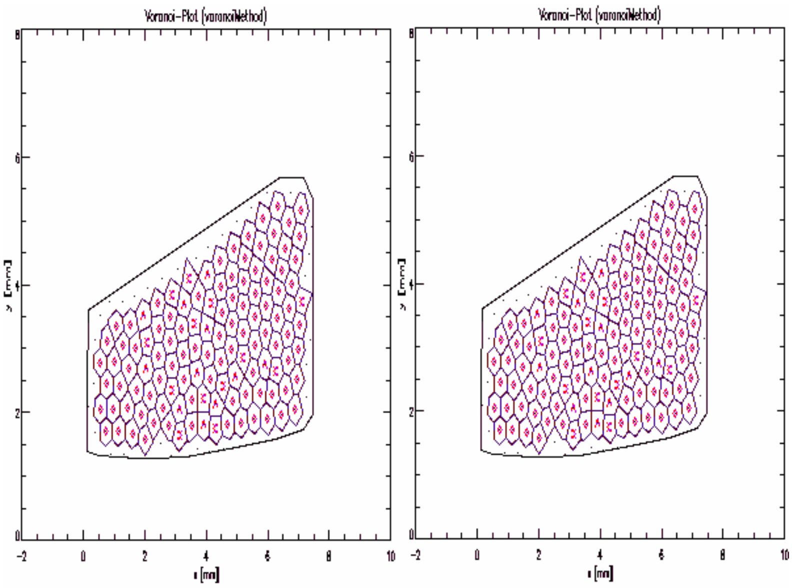

Structural analysis: Particle flow behind the obstacle. Direction of flow is from left to right.
Three regions can be observed: A region (most left), where particles stream fast around the obstacle in a 6-fold symmetry. The transition region (center) where lanes split up from 8 to 12 lanes. Here the 6-fold symmetry breaks up and particles have 5, 6 or 7 neighbours. A stable region again (most right) where particles stream slow, with a 6-fold symmetry, after the particles have rearranged again to a broader stream.

M. A. Fink, S. Zhdanov, G. E. Morfill

Microparticles as Probes in a filamented Plasma

Low-pressure, low-temperature radio-frequency plasmas are studied in external magnetic fields. At magnetic field strengths higher than the corresponding ion magnetization field the plasma breaks up into filaments. Simultaneously, the dynamical behaviour of embedded microparticles is changing with the strength of the magnetic field and the related modification of the plasma density structure. The dynamic changes from a collective rotation at moderate field strengths to a localized rotation in several small vortices centred at the filaments at high fields.

In experiments on complex plasmas in a high magnetic field environment we observed that the plasma itself starts breaking up into separated filaments that are aligned with the magnetic field. The transition from the homogeneous to the structured plasma is observed when the ions in the plasma become magnetized. The transition is smooth, starting with a weak enhancements of the plasma glow at some locations. With increasing field more regions of enhanced plasma glow columns (filaments) appear starting to form regular structures themselves. Fig.1 shows a typical view of the structured plasma glow at fields higher than the magnetization field for the ions.

Microparticles that were injected into the plasma acquire a high negative charge Q. As a result the particles are levitated at the edge of the lower sheath where $QE_S=mg$ to form a regular lattice or liquid-like structure. Horizontally, the particles are confined by a weak radial electric field E_C. By applying a vertical magnetic field the plasma ions are subjected to the $\boldsymbol{E}_C\times\boldsymbol{B}$ force, resulting in a azimuthal ion flow. Its drag on the particles causes an overall rotation of the particle cloud. At higher magnetic fields, when filamentation take place, the horizontal confinement is continuously altered. A substructure dedicated to the localized filaments is superposed. The microparticles probe these inhomogeneities by being attracted or repelled from this region and by a localized rotation around them (see Fig. 2). The appearance of filamentation is seen by a change in the structure of the particle cloud even before a plasma glow structuring can be observed. If the charge of the particles is known and an appropriate theory for the ion-drag force is selected, the electric fields around the filaments can be measured. Thus, the particles behave as plasma micro probes.

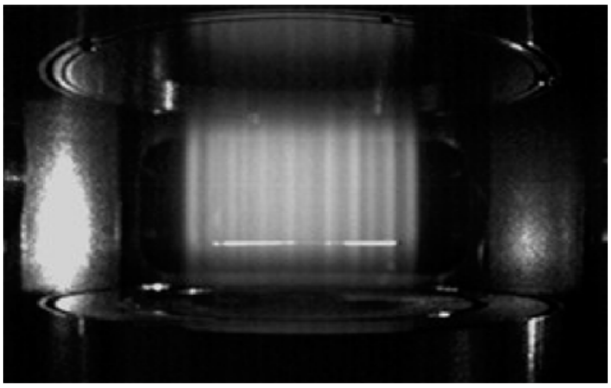

Fig.1: The plasma glow, seen from a side view camera at a magnetic inductance of 1.6T. The glow shows a filamentation of the plasma where the filaments are aligned with the magnetic field. The horizontal bright line is produced by the laser light reflection on introduced microparticles that are levitated close to the lower sheath edge.

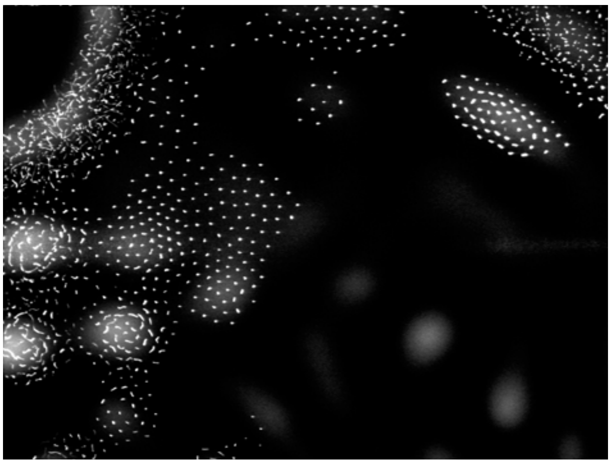

Fig.2: Top view of the plasma glow and the embedded particles at a magnetic inductance of 1.6T. The plasma filaments are seen in cross section (bright areas). Microparticles rotate around the filaments.

References:

• Konopka et. al., *Complex Plasmas in Strong Magnetic Field Environments*, AIP Conf. Proc. 799, 181 (2005)

U. Konopka, M. Schwabe and G.E. Morfill

MAX-PLANCK-GESELLSCHAFT

Dust impact on the coma plasma chemistry

The cometary coma consists of neutral gas, plasma, and dust grains. Dust grains can influence both the neutral and charged coma's constituents. Usually, presence of dust particles in a plasma results in additional losses of both electrons and ions due to the plasma recombination on the particle surfaces. Solar radiation makes the impact of dust even more complicated, depending on the solar flux, the dust number density, photoelectric properties of the dust particles, the dust particle composition, distribution of sizes, etc. We propose a simple kinetic model evaluating the role of dust particles in the coma plasma chemistry and demonstrate that this role can be crucial resulting in a nontrivial behavior of both the electron and ion densities of the plasma. We show that coma's dust particles can be negatively as well as positively charged depending on their composition. These opposite charges of the grains can result in fast coagulation of dust particles forming complex aggregate shapes of cometary grains.

Effects of dust particles on the ionization balance in the cometary coma can be estimated from the system of the continuity equations for the number densities of electrons and positive ions, as well as for the grain charge. Similar model previously has been used to describe the formation and evolution of noctilucent clouds [Ref. 1]. Case study presented on the figure.

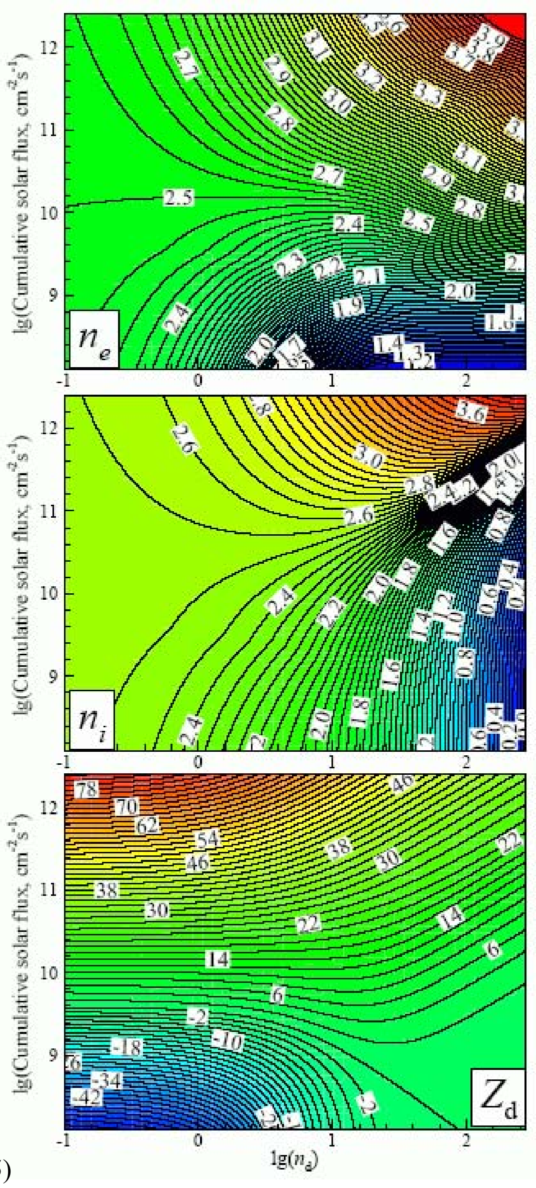

The Figure shows dust particle charge (bottom panel), the electron density (top panel), and the molecular ion density (middle panel) versus the grain number density and the effective cumulative solar flux. We note that strong influence of dust particles on the plasma composition occurs at fairly moderate values of dust number densities. As a result, both depletion and increase of the electron density can be observed in the dusty coma (depending on the grain properties and number density of dust particles) complemented by complicated behavior of the molecular ion component. This ion behavior can be explained by competition of ionization/recombination processes.

It can be shown that dust particles, depending on the particle size, number density and photoelectric properties, can strongly affect plasma composition of the dusty cometary coma. It is important that positively as well as negatively charged dust particles can appear in the coma. These opposite charges result in coagulation of dust particles. The shape of these aggregated grains can be complex.

References:

• Klumov B., S.Vladimirov, G. Morfill, JETP Lett., **82**, 10, 632,(2005)

Boris Klumov, Sergei Vladimirov and Gregor Morfill

Microcrystalline diamond growth on seed particles and thermophoretic effects on levitated fine particles in an rf plasma sheath

We describe an approach to diamond growth on levitated seed diamond particles (ϕ = 2~4 μm) in a capacitively coupled parallel-plate rf plasma. This deposition, not on a planner substrate (two-dimensional, 2-D) but on levitated particles (3-D) is technologically interesting. In order to enhance crystalline growth, we apply a hot filament chemical vapor deposition (HFCVD) technique in which one can expect: 1) high density of atomic hydrogen and 2) effective heating of the particles due to heat radiation. Both are essential factors for successful diamond growth. In addition, we studied the control of particle levitation against a thermophoretic effect at high temperatures.

1. Diamond growth using HFCVD

Diamond growth on the diamond seed particles placed on a Si substrate (2-D) using HFCVD was investigated to obtain proper growth conditions. A methane to hydrogen gas ratio is 1 %, temperatures of the substrate and the filament are 750 °C and 2000 °C, respectively, and total pressure is 300 Pa which is equivalent to that of a levitation condition. After 3 h deposition, small grains on seed particles' surfaces were observed by a scanning electron microscope (SEM). Their micro-Raman spectrum shows the clear peaks assigned to microcrystalline diamond [1, 2]. The microcrystalline diamonds growth on seed particles is successful.

SEM **Micro-Raman spectroscopy**

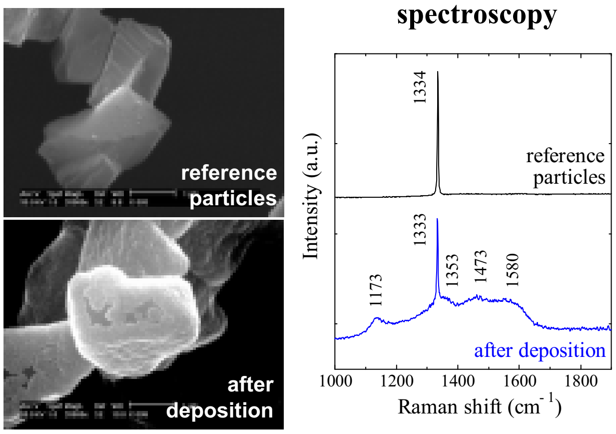

Thermophoretic effect on levitated particles

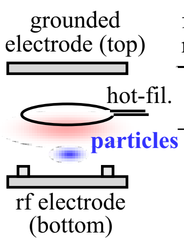

Temperatures of the electrodes and the filament. (H_2 = 30sccm, He = 1sccm, 50Pa, rf power = 50W, with Al_2O_3 particles)

Fig.	top el. °C	bottom el. °C	filament °C
(a)	RT	RT	RT
(b)	800	800	1000
(c)	800	800	2000

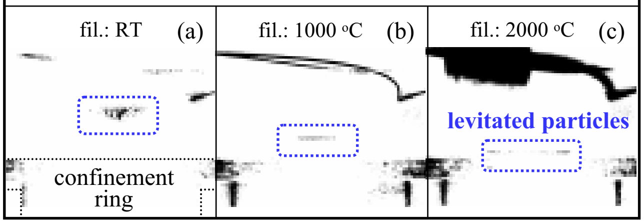

2. Thermophoretic effect on levitated particles

Levitated fine particles with diameters of a few micrometers in a plasma sheath are sensitive to the balance of several forces, e.g., electrostatic, gravity, ion drag, thermophoretic and others [3, 4]. Among all, a thermophoretic force is very strong in the substrate temperature range of diamond growth (~ 800 °C), which disturbs successful particle levitation. In a parallel electrode rf plasma chamber, we investigated the particle levitation with changing electrodes temperatures. The levitation conditions are the following: pressure = 60 Pa, H_2 flow = 50 sccm, and rf power = 40 W. We found that it is important to keep the top electrode temperature high enough to compensate the thermophoretic effect. In our case, the top electrode temperature should be 200 °C higher than that of the bottom electrode to maintain the levitation.

Moreover, we confirmed particle levitation in the hot filament equipped rf plasma chamber. In this case, a position of the levitated particles changes according to a temperature of the filament placed above the levitation region. Proper control of surrounding temperatures is necessary for successful levitation, which is required for 3-D diamond growth.

We acknowledge F. Jamitzky for the use of micro-Raman spectroscope in the Department für Geo- und Umweltwissenschaften der Ludwigs-Maximilians-Universität München (Institut für Kristallographie), and S. Lindig for the SEM measurements in IPP.

References:

[1] A. C. Ferrari et al, Phys. Rev. B **63**, 121405 (2001).
[2] F. Piazza et al, Diamond Relat. Mater. **15**, 109 (2006).
[3] H. Rothermel et al, Phys. Rev. Lett. **89**, 175001 (2002).
[4] C. Zafiu et al, Phys. Plasmas **9**, 4795 (2002).

S. Shimizu, T. Shimizu, B. M. Annaratone, W. Jacob, H. Thomas, N. Sato, G. E. Morfill

Hardware Projects

Detector Developments

Software Projects

eROSITA – Science & Instrument

eROSITA (extended ROentgen Survey with an Imaging Telescope Array) will be one out of three instruments on the Russian Spectrum-Roentgen-Gamma mission which is planned for launch in 2011 into a low earth orbit with ~30° inclination. The other two instruments are the wide field X-ray monitor Lobster (Leicester University, UK) and ART (IKI, Russia), an X-ray concentrator based on a Kumakhov optics. The primary scientific goal of eROSITA is the detection of ~100 thousands Clusters of Galaxies up to redshifts z > 1 in order to study the large scale structure in the Universe and test cosmological models including the Dark Energy. For achieving this goal a four years lasting all-sky survey supplemented by one year of pointed observations is needed.

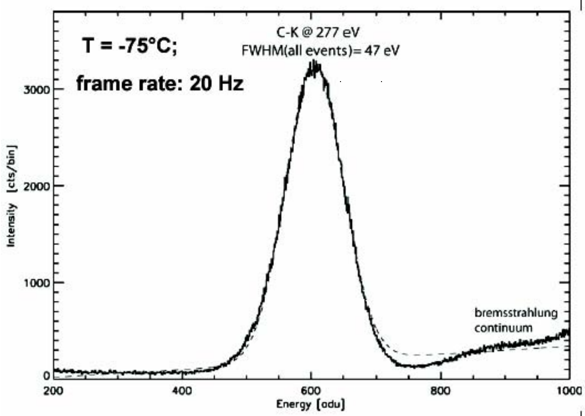

eROSITA consists of seven Wolter-I X-ray mirror modules with 54 paraboloid / hyperboloid shells each. A baffle in front of each mirror module suppresses X-ray and optical stray light, and acts as thermal baffle. The diameter of each mirror module is 36 cm, the focal length is 160 cm, the on-axis angular resolution is 15 arcsec (at 1.5 keV). In the focus of each mirror module is a pnCCD camera with a sensitive area of 3×3 cm^2 providing a field of view with more than 1° diameter. The CCD has to be cooled to -80°C. Therefore, the cameras are connected to the two radiators by heatpipes. Each of the seven cameras has its own electronics box (not shown) for controlling the camera and readout of camera signals. The advanced version of the XMM-Newton pnCCD camera shows superb performance, e.g. regarding its low energy response.

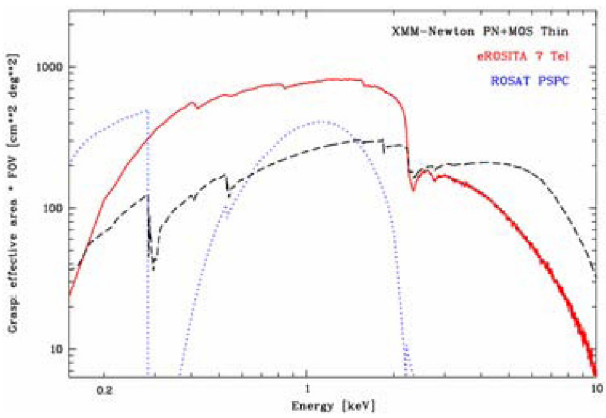

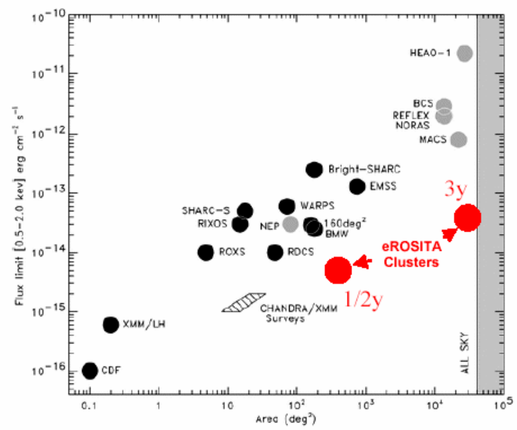

eROSITA will have substantially more grasp (effective area × field of view) than ROSAT or all three XMM-newton telescopes together. This is also reflected in a comparison of the sensitivity of the eROSITA galaxy cluster survey (red dots) with previous surveys. The eROSITA flux limit of the survey in the 0.5 to 2 keV band will be about 4 ×10^{-14} erg s^{-1} cm^{-2} over most of the sky and about ten times deeper in the poles of the survey scan pattern.

P. Predehl on behalf of the eROSITA-team at MPE

FIFI LS – a FIR Spectrometer for SOFIA

We present FIFI LS, an instrument that will provide a unique tool for astronomical 3D spectral imaging of line emission in the far-infrared (FIR). Observing in the FIR, which is largely unaffected by dust extinction and contains a large number of important emission lines, will allow FIFI LS to make significant contributions to a number of astrophysical problems. It will utilize the high angular resolution and sensitivity of SOFIA (the Stratospheric Observatory for Infrared Astronomy) to adress many key questions in modern astronomy like the relation between AGN‘s and starburst galaxies or the powering mechanism of ULIRGs. As a state-of-the-art astronomical instrument, FIFI LS will enable simultaneous 3D observations in two separate bands (42-110 and 110-210 µm). The instrument will allow diffraction-limited spectral imaging at R=1400 to 6500, depending on wavelength, with two separate Littrow mounted grating-spectrometers. To achieve spatial information effectively a 5 x 5 pixel spatial field of view is rearranged to a 25 x 1 pixel slit. This slitimage is dispersed to a 25 x 16 pixel, 2D detector array. The detectors are two large format Ge:Ga arrays, axially stressed in the Red channel to achieve a longer wavelength response and slightly stressed in the Blue channel.

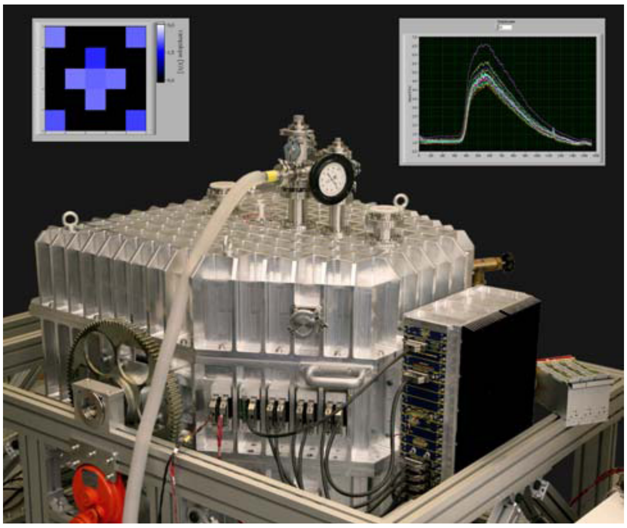

FIFI LS cryostat with electronic rack: upper left: 5 x 5 pixel field of view (detector partially assembled)
upper right: (first light) black body spectrum measurement

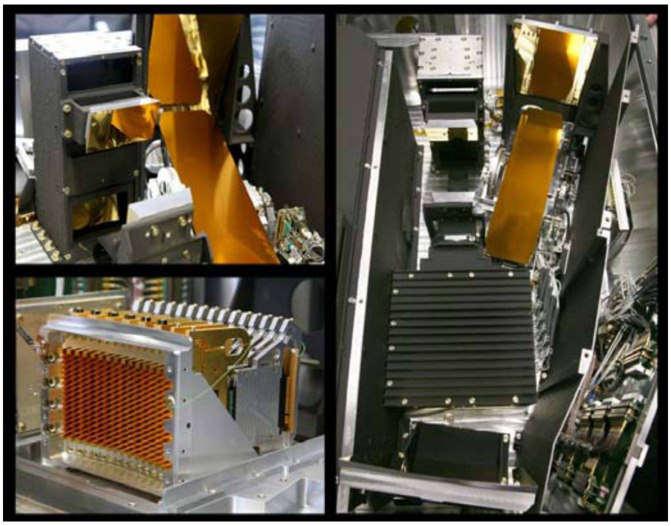

FIFI LS red channel optics and detector:
upper left: image slicer, lower left: 16 x 25 (Ge:Ga) pixel array , right: top view on grating and detector housing

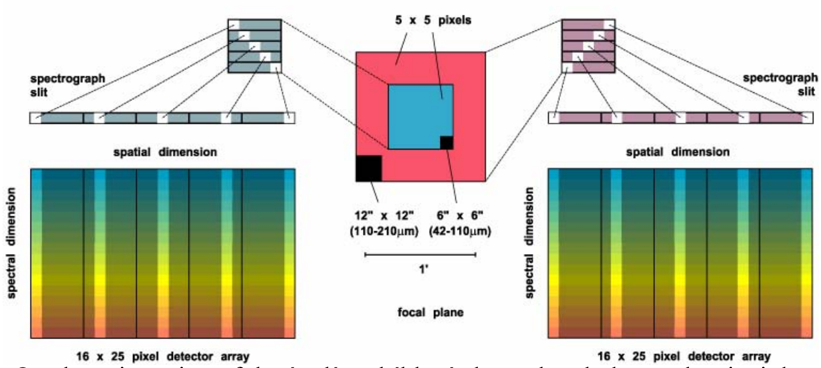

On sky orientation of the ´red´ and ´blue´ channel and the work principle of the image sclicer

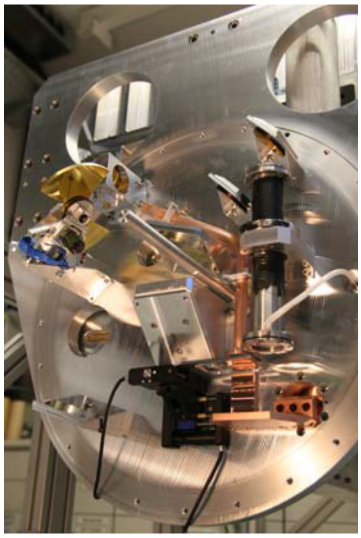

telescope simulator to characterize FIFI LS in the FIR.

References:
- Klein et al., 2006, Proceedings of SPIE, Vol. 6269, pp. 62691F
- Raab et al., 2006, Proceedings of SPIE, Vol. 6269, pp. 62691G
- Raab et al., 2004, Proceedings of SPIE,Vol. 5492, pp.1047-1085
- Looney et al., 2003, Proceedings of SPIE, Vol. 4857, pp. 47-55

M. Schweitzer for the FIFI LS team

ESI: A Far-Infrared Imaging Spectrometer for the Japanese SPICA space observatory

The Japanese Aerospace Exploration Agency (JAXA) is currently planning the next generation Infrared Space Observatory SPICA. Equipped with a cryogenic 3.5 m mirror this observatory will provide a unique platform for high resolution, high sensitivity observations in the Mid- and Far-Infrared region. A European-based consortium will propose the imaging Far-Infrared Spectrometer ESI operating in the 35 – 210 µm wavelength range. Covering the peak of the cosmic infrared background emission as well as the important cooling lines of the interstellar medium, this instrument will provide crucial new data to address astrophysical key topics.

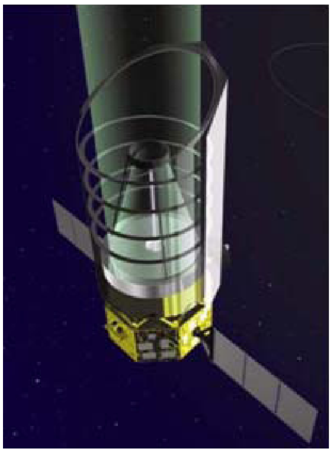

The large aperture of SPICA cooled to 4.5 K gives the possibility for unprecedented levels of sensitivity in the mid to far infrared, especially in spectroscopy where SPICA will be 10 – 20 times more sensitive than Herschel and will become more sensitive than JWST beyond 20 µm. SPICA is the only planned facility to observe in the 28 – 60 µm band. ESI will cover this band with a sensitivity two orders of magnitude greater than ISO and with a spatial resolution ~6 times better.

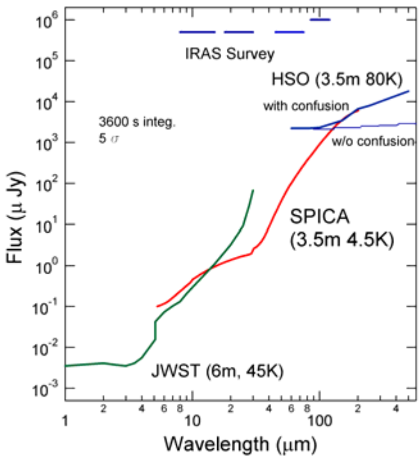

The basic instrument concept is an imaging Fourier Transform spectrometer with a spectral resolution of ~2000 at 100µm and a spatial field of view of at least one arcmin. The FoV will be restricted by the number of pixels available as well as by thermal restrictions on the arrays. Two possible detector technologies are currently under study: Photoconductors as used on Herschel/PACS operating at temperatures around 1.7 K and Transition Edge Superconducting (TES) bolometers with operating temperatures of ~100 mK. The spectrometer will cover the wavelength range from 35 to 210 µm to match other instruments on SPICA. The wavelength coverage will be ultimately restricted by the responsivity of the detector arrays and the beam splitter/filter performance respectively.

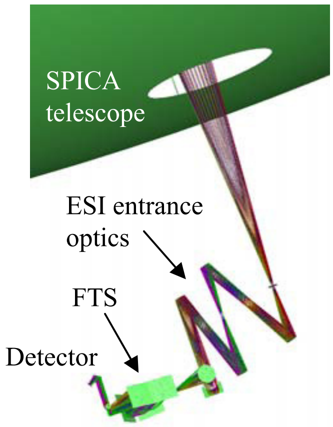

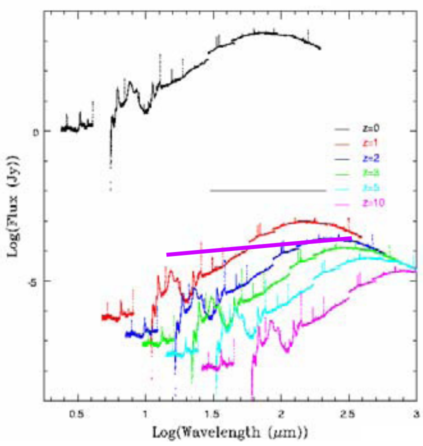

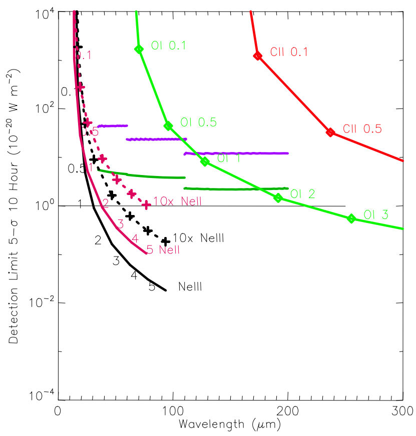

Estimated sensitivities of ESI for broad band observations (left) and line spectroscopy (right). Purple lines show results based on state of the art photoconductors, while green lines use possible 10^{-19} W/√Hz detectors. High sensitivity detectors are one of the central goals of the ESI study and development phase.

Reference:

• **ESI: the far-infrared instrument for the SPICA mission**, Proceedings of SPIE, Volume 6265, pp62650L (2006)

W. Raab, A. Poglitsch

GRAVITY - Resolving the event horizon

Sgr A*, the super-massive compact object at the centre of the Galaxy, is known to exhibit so called flares in the near infrared. These events are likely due to energetic events very close to the central object, on a scale of a few Schwarzschild radii (10 μas). The Very Large Interferometer is in principle able to deliver astrometry with an accuracy of order 10 μas. In order to consequently continue our long-term research program of the Galactic Centre we have proposed a 2nd generation VLTI instrument, called "GRAVITY", that aims at resolving for the first time the event horizon of a black hole.

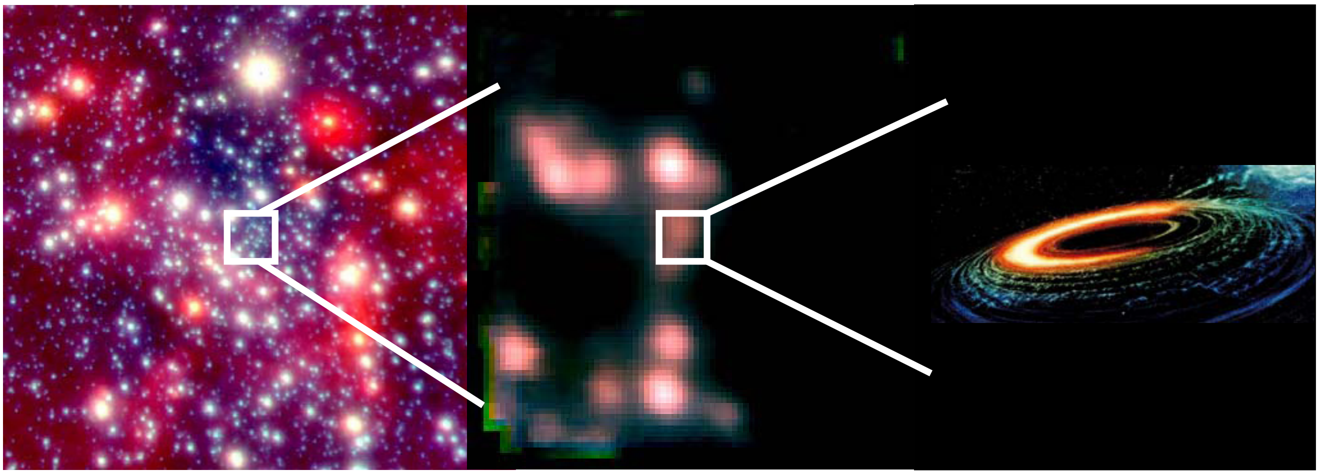

The Galactic Center in the near infrared – a success story in angular resolution. Left: NACO image. Middle: Zoom into the central arcsecond. SgrA* is the red source in the white square. Right: The orbiting hot spot scenario - a likely model for the emission seen during near infrared flares. The hot spot orbits the black hole in 20 minutes. GRAVITY aims at resolving this proper motion.

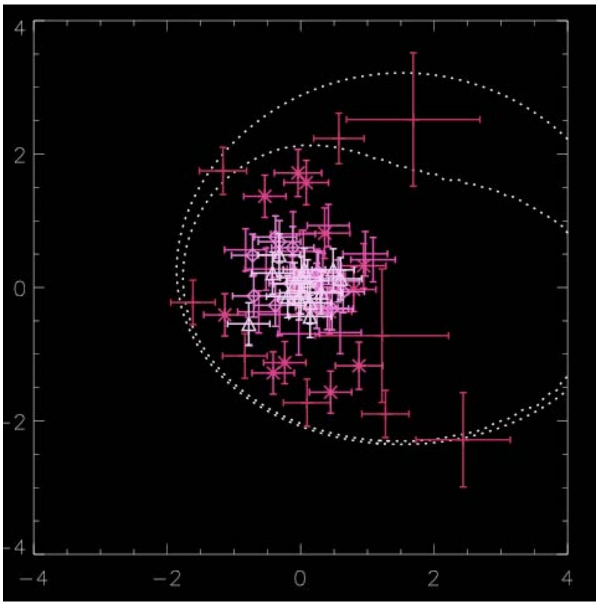

Right: A fully relativistic simulation of the observations as they will be possible with GRAVITY. The hot spot model was assumed. Clearly the motion of the source can be seen in the simulated data.

By means of such simulations our team has shown that GRAVITY will be able to resolve the proper motion of flares. The motions as well as the light propagation are dominated by general relativity, high order images that arise in the strong lensing case of a black hole can become observationally relevant.

S. Gillessen, F. Eisenhauer, T. Paumard, S. Rabien. R.Genzel, N. Hamaus

GRAVITY: the adaptive optics assisted, ultra precision beam combiner for the VLTI

We present the adaptive optics assisted, near-infrared VLTI instrument - GRAVITY - for precision narrow-angle astrometry and interferometric phase referenced imaging of faint objects. With an accuracy of 10 µas, GRAVITY will be able to study motions to within a few times the event horizon size of the Galactic Center massive black hole and potentially test General Relativity in its strong field limit. By virtue of its phase referencing concept GRAVITY will also make possible interferometric imaging for objects as faint as mK = 19, thereby opening up precision interferometry for a wide range of astronomical objects in both Galactic and extragalactic targets. Through its high performance infrared wavefront sensing system, GRAVITY will open up deep interferometric imaging studies of stellar and gas components in dusty, obscured regions, such as obscured active galactic nuclei, dust-embedded star forming regions, and protoplanetary disks. GRAVITY is developed under the leadership of MPE in collaboration with the Observatoire de Paris Meudon, the Max-Planck Institute for Astronomy, and the University of Cologne.

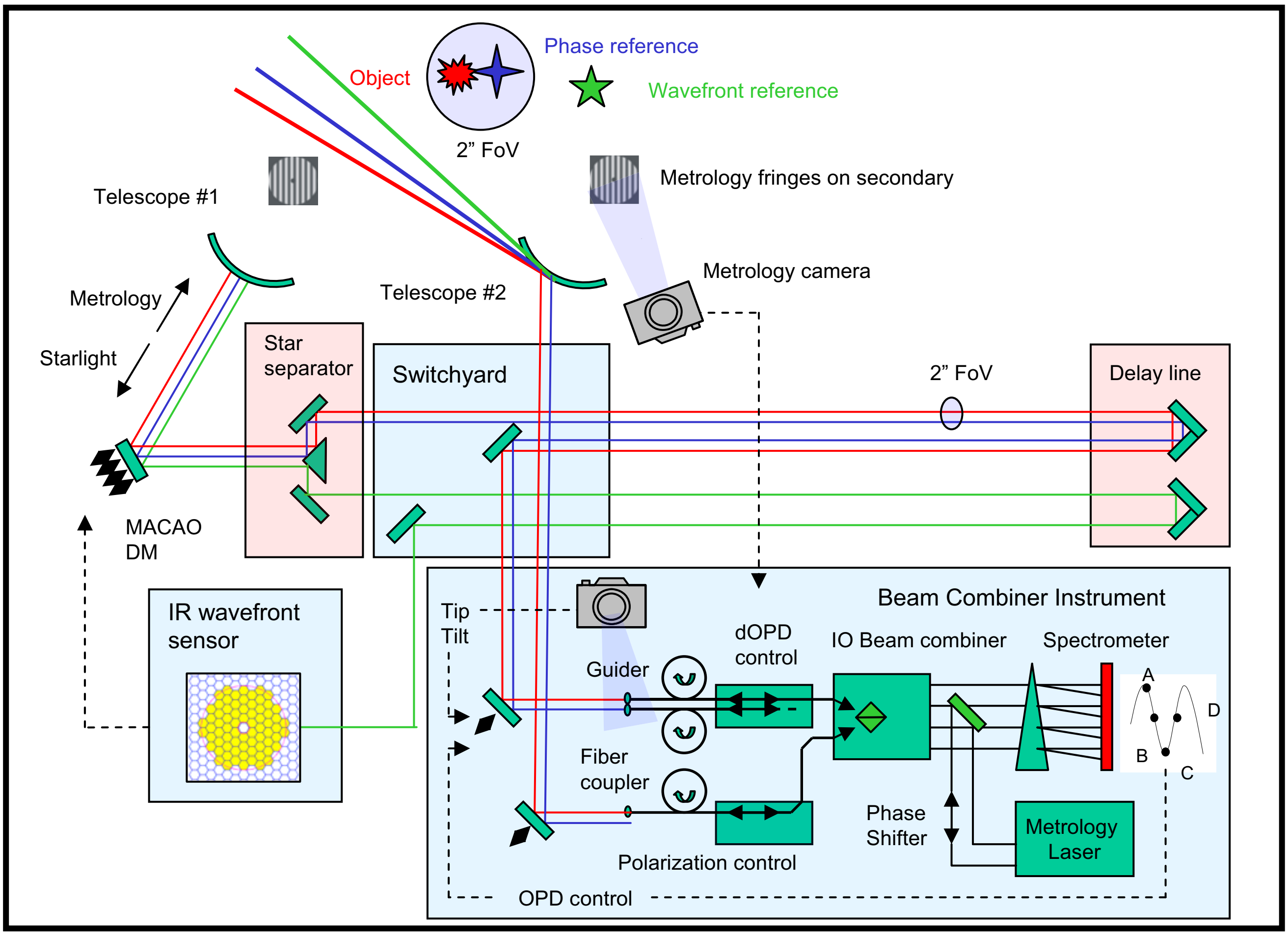

Figure: Overview of the GRAVITY instrument combining the four 8m telescope of the VLTI

References:
• Eisenhauer et al. 2005, AN, 326, 561
• Gillessen et al. 2006, SPIE Proc. Vol. 6268, 33

Rabien, Eisenhauer,Gillessen, Thiel, Graeter, Kellner, Haug, Hofmann et al.

LUCIFER at the Large Binocular Telescope

Lucifer is the new infrared imager and spectrograph at the Large Binocular Telescope becoming available in 2008. Its unique multi-object spectroscopy capabilities enable among others detailed studies of spectroscopic properties of galaxies over a wide range of redshift and classes of statistically significant samples leading to new insights on galaxy formation processes.

The instrument:

LUCIFER is the new near infrared imager and spectrograph for the Large Binocular Telescope. It will support seeing and diffraction limited direct imaging, long-slit and multi object (MOS) spectroscopy. LUCIFER is operating in the 0.9 - 2.5 micron spectral range, covering a field of view of up to 4x4 arcmin. The device is built by a German consortium led by the Landessternwarte in Heidelberg. The IR/Submm group at the MPE contributes the complex MOS-unit that handles the exchange and replacement of long-slit as well as multi-slit slit masks for spectroscopic observations. It is planned to have first-light at the beginning of 2008.

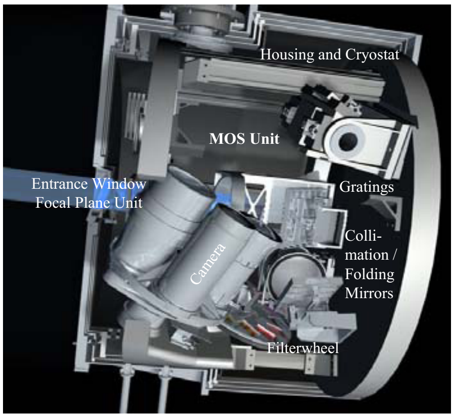

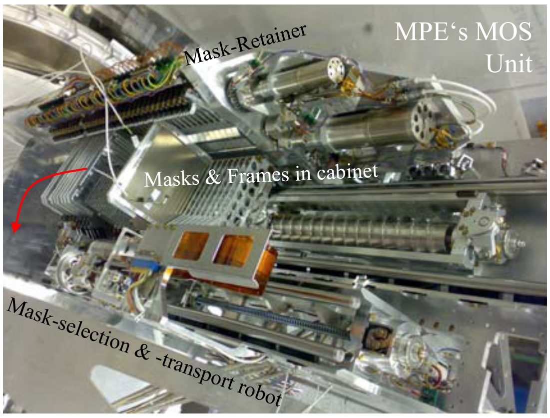

Scheme of the LUCIFER instrument (left) and actual view of the MOS unit (right)

Selected Science Case:

One of the most promising applications of LUCIFER will be in studies of galaxy evolution at high redshift. LUCIFER will allow us to determine key physical properties such as star formation rate, metallicities, stellar populations, velocity dispersions, and virial masses from well understood rest-frame optical spectral diagnostics that are redshifted into the near-IR bands for z ~ 1-4. The multiplexing advantage and field of view in MOS mode will make LUCIFER substantially more efficient than classical long-slit spectrometers, enabling us to study the detailed spectroscopic properties of statistically significant samples, over a range of redshift and galaxy classes and as a function of environment. Such investigations will fill the gap between population studies based on very large samples but comparatively crude photometric information (such as deep/wide photometric surveys) and detailed case studies limited to small numbers of individual galaxies (e.g. from integral field spectroscopy).

References:
• Seifert et al., Proc. SPIE, Vol 4841,962-973 (2003)
• Hofmann et al., Proc. SPIE, Vol 4841,1295-1305 (2003)

Peter Buschkamp, R. Hofmann, F.Eisenhauer, N. M. Förster Schreiber et al.

Preparing for GROND Observations

GROND (Gamma-Ray Burst Optical Near-Infrared Detector) is an imaging detector system for the optical and infrared wavelength range providing the capability of simultaneous observations in seven bands! The instrument was developed at MPE in collaboration with Tautenburg Observatory and will become operant at the ESO/MPI 2.2m telescope on La Silla (Chile) in summer 2007.

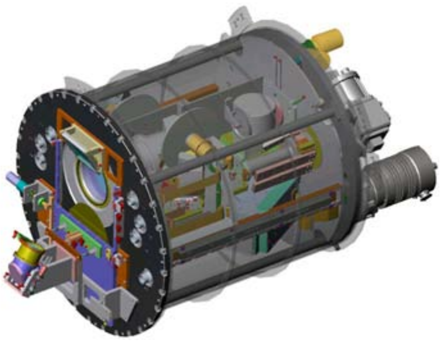

Cylindrical Vacuum Vessel

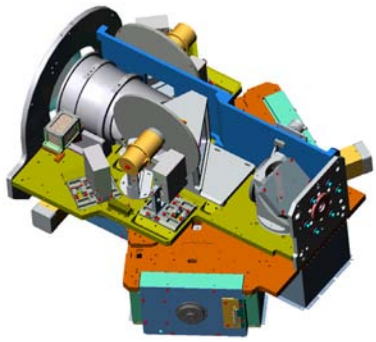

Visual Baseplate

Infrared Baseplate

Optical Pathway

GROND is installed in a cylindrical vacuum vessel with radiation shields and operated at cryogenic temperature which is achieved by using a Closed Cycle Cooler (CCC). All components are mounted on two thermally connected baseplates which are stabilized at 80K. Six dichroics are used to split the incoming beam onto four CCDs and three infrared detectors. 23 lenses made of BaF_2, CaF_2, YA G and Infrasil reduce the focal length by a factor of 2.8 in order to achieve a 10' x 10' field of view. The lenses are mounted in newly designed spring housings and all infrared units are gimbal-mounted and equipped with cryogenic stepper motors to provide focusing at operational temperature. In addition a dither mirror for K_s band observations is implemented.

Scientific Goals

The main scientific goal is the rapid identification of high-redshift ($z > 5$) Gamma-Ray Bursts (GRBs) to allow follow-up high resolution spectroscopy with the Very Large Telescope (VLT) in the same night. The redshift will be estimated by a photometric algorithm using the Lyα break in the afterglow SED.

- determine the epoch of first star formation
- investigating optically dark bursts by observing rapidly in the NIR bands
- determination of the GRB afterglow parameters α, β and p to measure the GRB energy and the density of the GRB environment
- determination of the intrinsic extinction from the **SED** curvature

Observations

- **starting of afterglow observations within 10 min and providing a photometric redshift with ± (0.2 - 0.6) within 30 min**
- g', r', i' and z' with 5.4' x 5.4' FOV and 0.16"/pix
- J, H and K_s with 10.3' x 10.3' FOV and 0.6"/pix
- limiting magnitudes: 23^m in r' for 10 min, 20^m in K_s for 60 min

To ensure efficient observing, the exposure times in the different bands have to be carefully adjusted. Integration times of the detectors are colored gray, readout intervals are green and infrared blocks are marked in red. Dithering is done by the telescope (see brown bars) and also by the K_s band mirror (see blue bars).

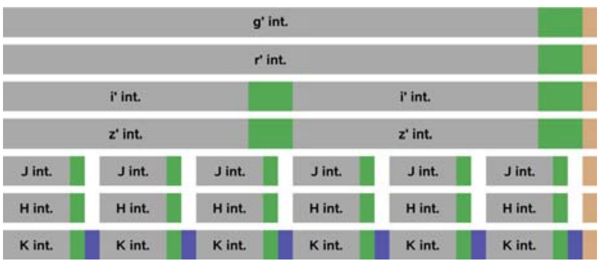

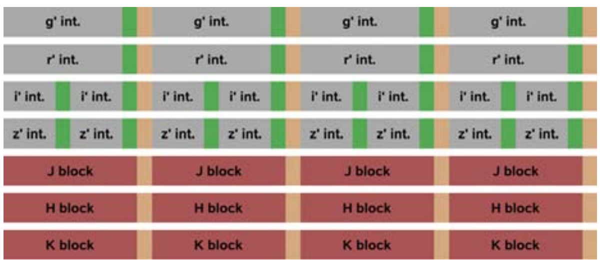

by C. Clemens, J. Greiner, W. Bornemann, M. Deuter, M. Hondsberg, H. Huber, S. Huber, T. Krühler, U. Laux, B. Mican, N. Primak, F. Schrey, G. Szokoly, A. & A. Küpcü Yoldas et al.

OPTIMA-Burst
Prompt GRB Afterglows with High Time Resolution

OPTIMA-Burst is a high time resolution optical photo-polarimeter specifically developed for the study of GRB Afterglows.
It combines a telescope with a quick response time to GRB triggers with a high-speed single-photon counting photo-polarimeter with accurate and absolute tagging of photon arrival-times and full linear polarimetry within adjustable time intervals. Thus the instrument facilitates cross-correllation studies with time resolved observations in other wavelengths, e.g. X-Rays. This allows unique insights into the physics of the ultrarelativistic jets assumed in GRBs and their Afterglows.

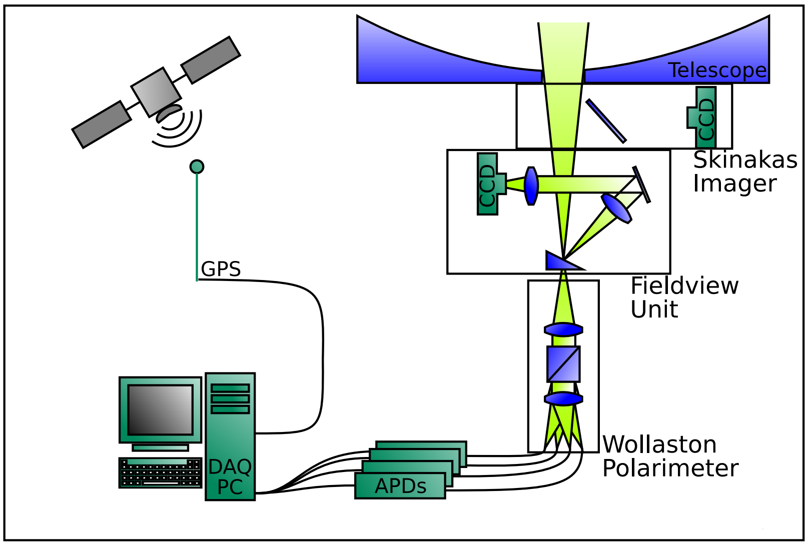

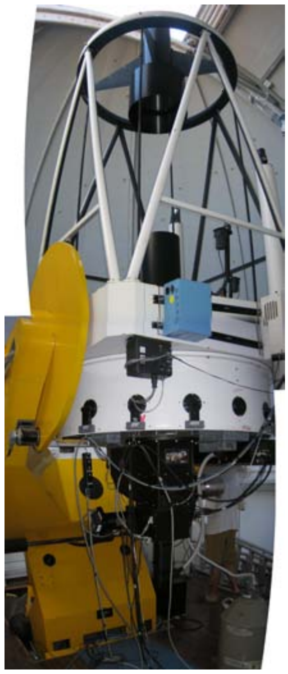

OPTIMA-Burst was deployed for three months in 2006 on the 1.3m Telescope of the Skinakas Observatory (Crete), proving the viability of the observation principle and of the instrument's implementation. Observations of polarized and highly variable sources (e.g. Crab, CVs) allowed the determination of sensitivity. Since no GRB suitable for *prompt*, high time resolved observations from SKO occured during this period, a second long-duration campaign is planned for 2007.

Alltough no observeable GRB was suitable for high time resolution observations, 9 GRBs could in total be observed with OPTIMA's CCD Instrument after delays from around ten minutes to several hours after the burst.

Of these GRBs, GRB060904b is one of the best-sampled early afterglow lightcurves so far ever observed - thanks to, amongst others, OPTIMA-Burst data.

The combined lightcurve shows several interesting features like breaks and re-brightenings. A publication with a detailed analysis of the burst is in preparation by Stefanescu et al.

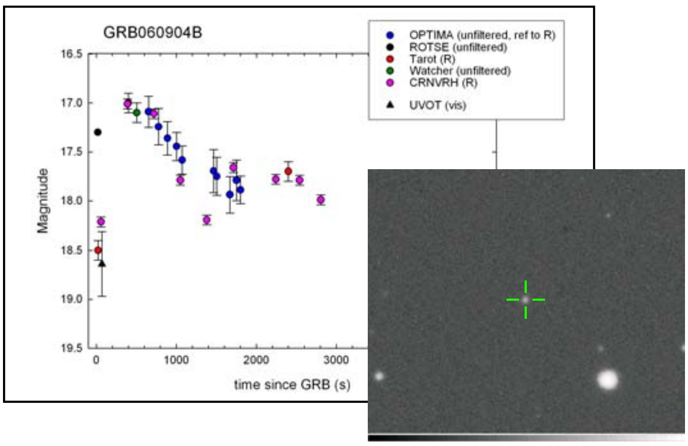

A. Stefanescu et al.

Mirror System and Sensitivity of the eROSITA Telescope

eROSITA: “extended Roentgen Survey with an Imaging Telescope Array”

MPE will provide the X-ray Survey Telescope eROSITA for the resuscitated Russian Spektrum-Roentgen-Gamma Mission to be launched in 2011. The design of the X-ray mirror system is based on that of ABRIXAS: The bundle of 7 mirror modules with the short focal length of 1600 mm makes it still a compact instrument while, however, its sensitivity in terms of effective arae, field-of-view, and angular resolution shall be largely enhanced with respect to ABRIXAS. The instrument's high grasp of more than 800 cm^2deg^2 in the soft spectral range and still 10 cm^2deg^2 at 10 keV combined with a survey duration of 4 years will generate a new rich database of X-ray sources over the whole sky. The scanning strategy is chosen such that the exposure puts emphasis on extragalactic observations: Two regions of the sky – each 30 deg away from a galactic pole – are exposed much deeper thus yielding a deep probe of the extragalactic space.

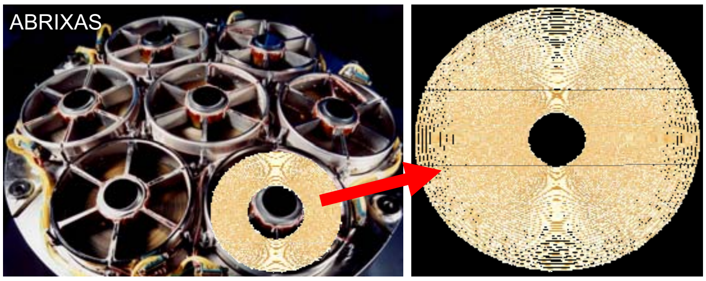

The number of nested mirror shells increases from 27 to 54 with respect to ABRIXAS thus enhancing the effective area in the soft band by a factor of six.
eROSITA is also able to perform pointed observations as the 7 telescope modules are co-aligned.

The original plan based on scientific goals was to perform three surveys:
All-sky Survey (1 year), Extragalactic Survey (2.5 years), Deep Survey (0,5 years).

Problem: How can these surveys performed in an efficient way, i.e. with a minimum loss of observation time, and what are the consequences for the mission planning (scan velocity, orientation towards the Sun, orientation towards the Earth)?

All-Sky Survey:	42000 deg^2 in 1 year	80 % efficiency	→	0.8 years
Extragalactic Survey:	20000 deg^2 in 2.5 years	60 % efficiency	→	1.5 years
Deep Survey:	200 deg^2 0.5 years	20 % efficiency	→	0.1 years
				2.4 years

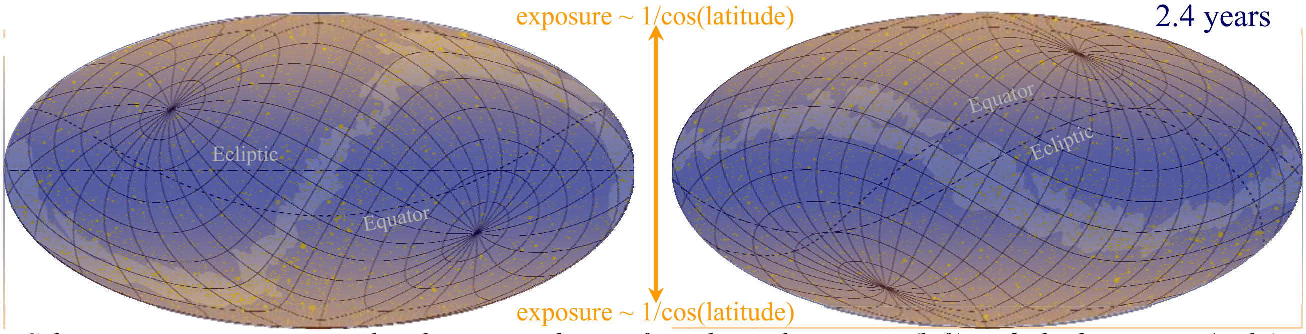

Schematic exposure maps with galactic coordinates for ecliptical scanning (left) and tilted scanning (right)

Solution: To avoid loss of observation time in the Extragalactic Survey and in the Deep Survey the three surveys have to be combined, and a special scan geometry has to be applied: scanning along great circles different from the ecliptical meridians to enhance exposure apart from the galactic plane.

One all-sky survey (with “tilted geometry”):

All-Sky Survey:	42000 deg^2 in 4 years	80 % efficiency	→	3.2 years

References:
• Predehl, P. et al. 2006, “eROSITA”, SPIE proc., V. 6266, pp. 62660P
• Pavlinsky, M. et al. 2006, “Spectrum-RG/eROSITA/Lobster astrophysical mission” SPIE proc., V. 6266, pp. 62660O

Peter Friedrich / eROSITA Team

The eROSITA Science Analysis Software System

Building on experience gained from the ROSAT and XMM-Newton missions, and making extensive use of software packages developed for ROSAT, Abrixas, and XMM-Newton, the eROSITA-*SASS* (Science Analysis Software System) is designed to perform a pipeline processing of the eROSITA data and to provide an interactive software environment for their subsequent in-depth analysis.

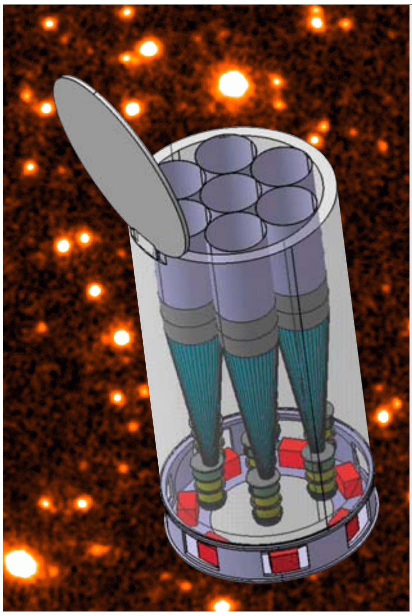

The processing pipeline will ingest and archive science, housekeeping, attitude, and orbit data as provided by the ground station/Russian data centre, create calibrated event lists and related datasets, and accumulate the all-sky survey data in a grid of sky maps. It will detect and characterize both point-like and extended X-ray objects and create a cumulative source catalogue, exposure and sensitivity maps, as well as source specific data products, such as spectra and time-series. An archive of raw data and calibrated data products, to be accessed through a database system, will be kept. Where applicable, SASS software tasks may be run in pipeline mode, under the control of a database system, or interactively, to permit an in-depth scientific analysis of the data. Data formats will be standard-compliant and closely match those of current X-ray astronomy missions, permitting the use of widely-used astronomical data analysis tools. The SASS software development and operation is conducted in close collaboration with the hardware and calibration teams (in-house), as well as with the national and international partners.

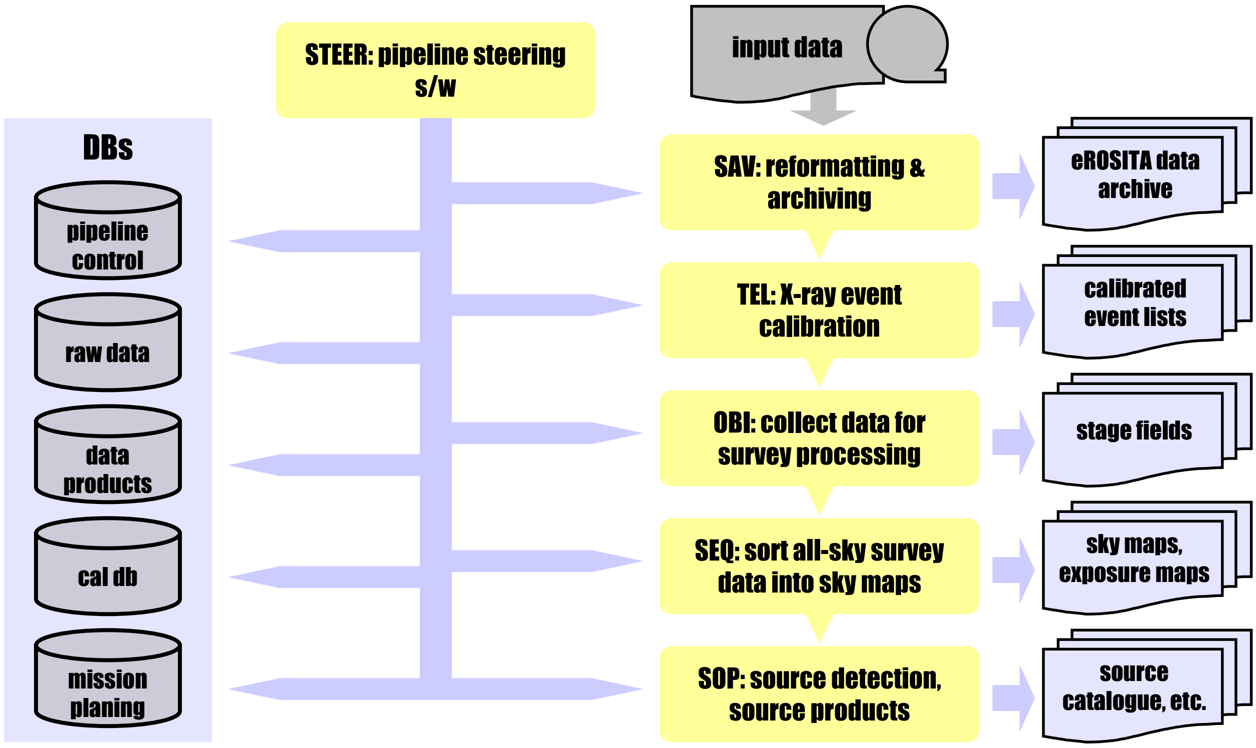

References:

• Predehl et al., eROSITA, Space Telescopes and Instrumentation II: Ultraviolet to Gamma Ray, eds. M.J.L. Turner and G. Hasinger, Proc. of the SPIE, 6266, 62660P (2006)

H. Brunner, G. Lamer (AIP), J. Paul, M. Mühlegger

Simulating eROSITA observations

In parallel with the development of the eROSITA instrument, an X-ray event simulator is being designed within the scope of a PhD thesis. The simulator will be used to “observe” an artificial sky in order to design survey strategies and advanced analysis tools well ahead of the real mission. In particular, the discrimination between pointlike and extended sources will be investigated.

One of the main goals of the eROSITA mission is the study of the large-scale structure of the universe using clusters of galaxies. Therefore they have to be included in the construction of an artificial sky in addition to the X-ray background and point sources. In order to model the cluster component as realistically as possible we plan to use hydro + N-body simulations to form a cluster atlas.

The mock sky will then be folded through the eROSITA telescopes and detectors. These simulated survey fields will be analysed using the eROSITA-SASS software package (see poster by H. Brunner et al.). Cosmological parameters determined from the catalogue of detected clusters (with artificial redshifts) will be compared to the input parameters of the N-body simulations. In this way, the simulation chain will serve as an end-to-end test for the survey and data reduction strategies.

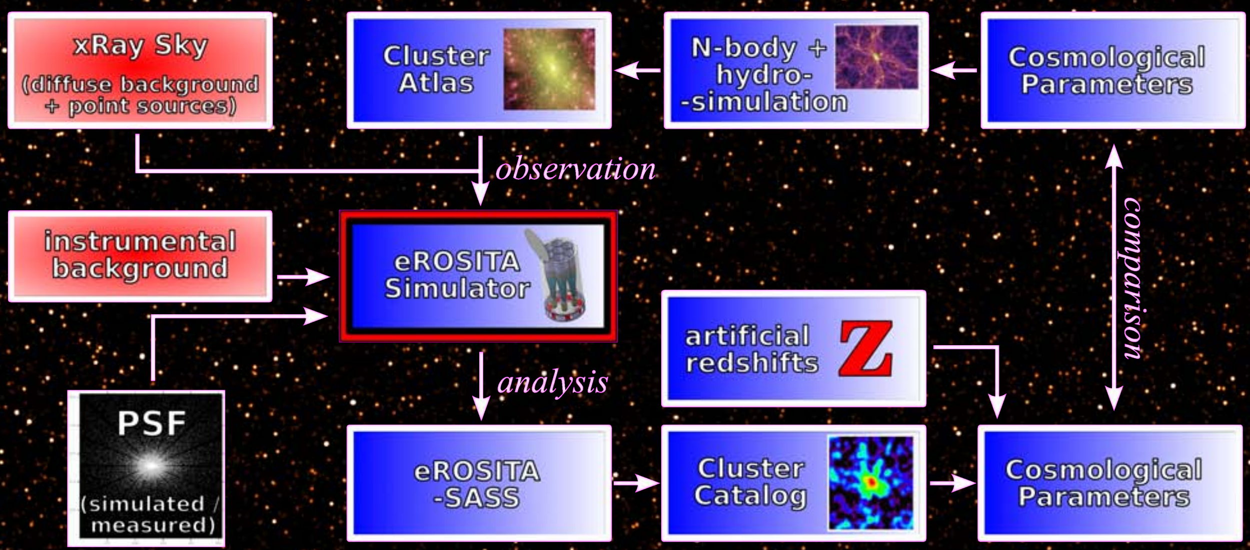

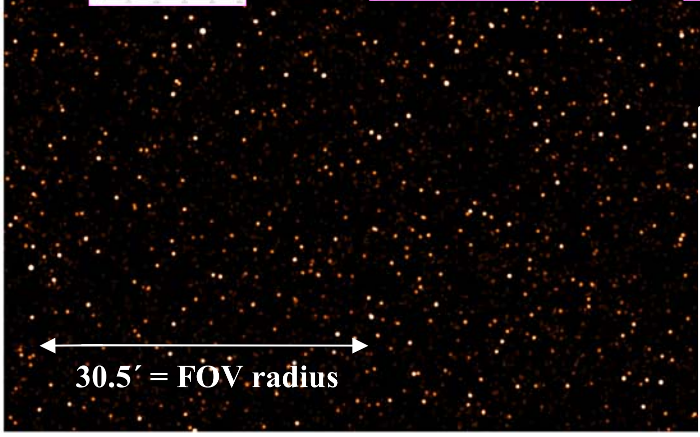

Background picture: simulation of a 2° by 2° survey field, generated by an XMM-SAS simulator program (point sources only).

Exposure time: 2.2 ksec*, corresponding to a field at medium survey latitudes (assuming a survey duration of 4 years). Expected exposure times range from 1.3 ksec at the survey equator to more than 100 ksec close to the survey poles, depending on the scanning pattern. The mean survey PSF was determined by suitably averaging over the FOV.

*) equivalent to ~ 4.5 ksec on XMM EPIC-pn

Reference: Predehl et al., eROSITA, Space Telescopes and Instrumentation II: Ultraviolet to Gamma Ray, eds. M.J.L. Turner and G. Hasinger, Proc. of the SPIE, 6266, 62660P (2006)

Image Credits: - Volker Springel (Millennium Simulation)
- Christopher R. Mullis (XMMU J2235.3-2557)

M. Mühlegger, H. Böhringer, H. Brunner, P. Friedrich

Simbol-X:
A new technology hard X-ray focusing telescope

Simbol-X is a hard X-ray mission, operating in the 0.5 – 80 keV range, proposed as a collaboration between French and Italien space agencies with participation of German Instituts for a launch in 2013. Relying on two spacecraft in formation flying configuration, Simbol-X uses for the first time a ~ 20m focal length X-ray mirror to focus X-rays with energies above 10 keV, resulting in over two orders of magnitude improvement in angular resolution and sensitivity in the hard energy band with respect to non-focusing techniques. The Simbol-X revolutionary instrumentaly capabilities will allow us to elucidate outstanding questions in high energy astrophysics such as those related to black-hole accretion physics and census, and to particle acceleration mechanisms, which are the prime science objectives of the mission. The MPE's involvement in Simbol-X is two fold: the test and calibration of the mirror module and the development, test and calibration of the low-energy pixel detector. The low-energy detector is described in more detail in the contribution of the Semi-Conductor-Laboratory.

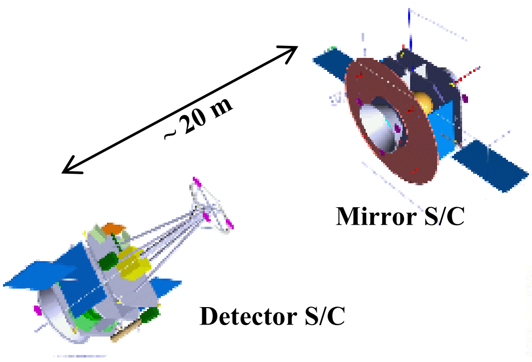

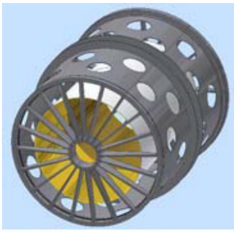

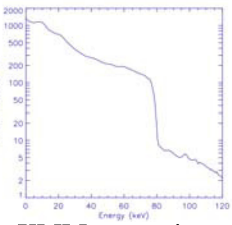

XMM-type mirror system, 100 shells with multilayer

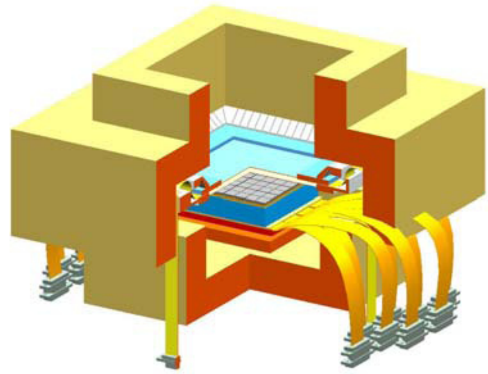

Sandwich-type detectors, 8 x 8 cm² FOV
Top: low-energy macro pixel array (HLL)
Bottom: high-energy Cd(Zn)Te pixellated array (CEA). Active A/C detector to reduce the background.

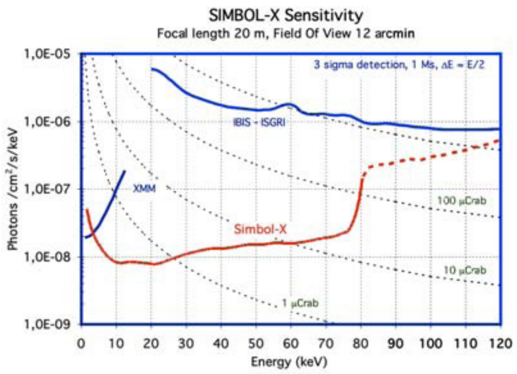

Expected sensitivity

Calculated with a 20 arcsec HEW constant with energy, and a total background level of 2 10-4 cts/cm²/s/keV.
The sensitivity above 80 keV is under investigation. It will depend in particular on the evolution of HEW with energy.

Top level scientific requirements

- **Energy range :** 0.5 – 80 keV [goal 100 keV]
- **Field of view :** 12 arcmin (50 % vignetting, @ 30 keV)
- **Angular resolution :** < 20 arcsec @ 30 keV
- **Attitude reconstruction :** 2 arcsec (radius, 90%)
- **On axis effective area :** > 600 cm2 @ 8 keV, > 100 cm2 @ 70 keV, > 1000 cm2 @ 2 keV
- **Continuum sensitivity :** 10-14 erg/cm2/s/keV [1 Ms, 3σ]
- **Line sensitivity :** 2 10-7 ph/cm2/s @ 68 keV [1 Ms, 3σ]
- **Spectral resolution :** E/ΔE = 40–50 in 6–10 keV range; ΔE < 1.3 keV @ 68 keV [goal 1 keV]
- **Timing accuracy :** 100 μs [goal 50 μs]

Ref.: P. Ferrando et al., Simbol-X: Mission overview; SPIE 6266, p11, 2006

Ulrich G. Briel on behalf of the Simbol-X collaboration

CERN Axion Solar Telescope CAST

With the CERN Axion Solar Telescope (CAST) we search for the elusive particle called axion which was proposed to solve the CP problem of the strong interaction 30 years ago. The X-ray telescope of CAST, developed by our group, is the most sensitive detector system of the experiment which improves the sensitivity beyond the so far best existing limits from astrophysical considerations.

The stellar plasma of stars would be a powerful source for low mass, weakly interacting particles like axions, due to their two photon interaction. As such the Sun can be used to probe the existence of axions, that are a well motivated candidate for the dark matter in our universe. Depending on their mass, axions could contribute to the total energy density of the universe with a fraction of $\Omega_a h^2 \approx 0.3\ (f_a/10^{12}\ \mathrm{GeV})^{7/6}$. Until 2004 the CAST experiment operated for about 12 months, exploring the axion mass range up to 0.02 eV. In the absence of a signal we were able to set an upper limit on the axion to photon coupling of $g_{a\gamma\gamma} < 0.88 \times 10^{-10}\ \mathrm{GeV}^{-1}$ (95 % C.L.).

The CAST helioscope at CERN. From left to right: The He cryogenic system (blue unit), the superconducting magnet providing a 9 T field (blue tube), and the tracking system which allows to follow the Sun for 3 hours per day (yellow structure and the rails on the floor).

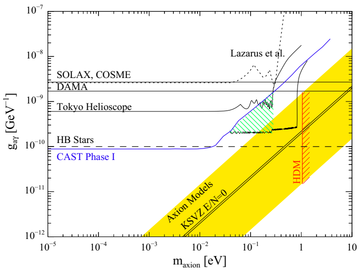

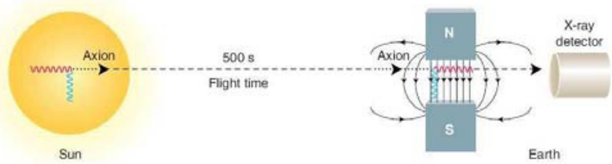

Left: The Axion parameter space, i.e., the axion to photon coupling constant $g_{a\gamma\gamma}$ depending on the axion mass m_a, The upper limit of $g_{a\gamma\gamma} < 0.88 \times 10^{-10}\ \mathrm{GeV}^{-1}$ (95 % C.L.) derived from CAST 2004 data (blue line) is actually the most stringent limit on $g_{a\gamma\gamma}$. The green region marks the parameter range probed during 2006. During 2007 and 2008 we will explore the region with 0.4 eV < m_a < 1.0 eV Right: Schematic view of an axion helioscope illustrating the working principle of the CAST experiment. Axions from the Sun are converted to X-ray photons (Primakoff effect) in a transverse magnetic field, before they reach an X-ray detector.

References:

•R. Peccei and H.R. Quinn, Phys. Rev. Lett 38 (1977) 1440
• P. Sikivie, Phys. Rev. Lett. 51 (1983) 1415
•S. Weinberg, Phys. Rev. Lett. 40 (1978) 223
•F. Wilczek, Phys. Rev. Lett. 40 (1978) 279
•S. Andriamonje, hep-ex/0702006v2 (2007)
•M. Kuster, New J. of Phys. submitted physics/0702188

The MPE CAST Team

Optimal achromatic Fresnel X-ray telescopes

Dispersion corrected X-ray optics combine diffractive Fresnel lenses with divergent refractive components. Compared to sole diffractive ones, the enlarged spectral bandwidth ΔE of achromatic doublets is partially compensated by an extended absorption. Moreover, the non-uniform transmission across the aperture with an effective area A_{eff} affects the PSF. We optimize the throughput $A_{eff} \times \Delta E$ for a given focal spot size of 0.75 mm by varying the ratio $s = N / N_0$.

For medium hard X-rays down to about 4 keV, Lithium in its highest purity provides the best optical performance. The lens may be disengaged from aberrations to a large extent. The Fresnel component could be made from plastics. In its optimized configuration, using s = 5, we expect an angular resolution near 0.02 mas within a field of view (FOV) of up to 400 resolution elements in diameter. A conventional CCD provides an exceptional quantum efficiency and a sufficient spectral selectivity. The overall focal distance of 10^4 km implies the precise formation flight of two spacecraft for the objective and the detector, respectively.

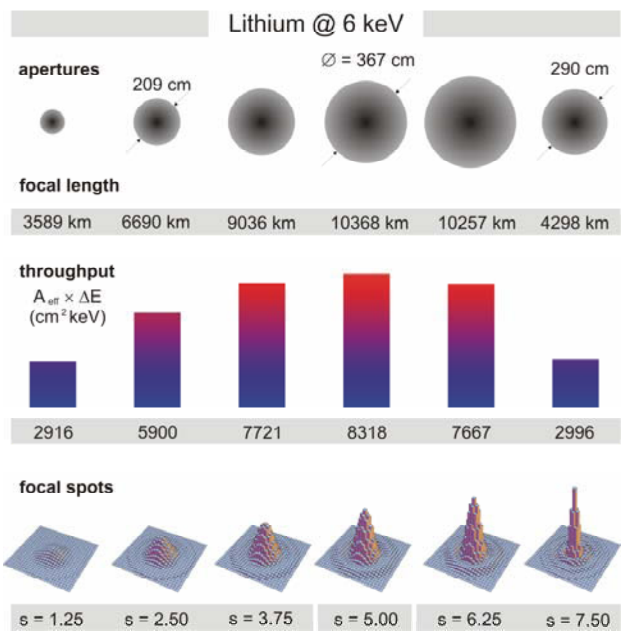

Figure 1. Various apertures made of Li, yielding the same focal spot size of 0.75 mm (HEW). Depending on the ratio $s = N / N_0$ between geometrical and critical zone numbers, the photon throughput will reach its maximum at $s_{opt} = 5$, for an aperture diameter of 367 cm.

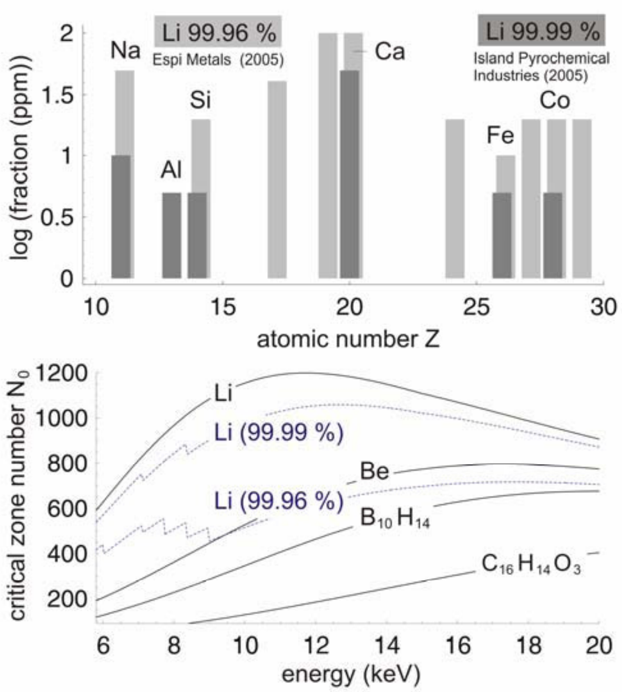

Figure 2. Heavy element contamination on the ppm level for commercially available Li samples (above). Its implications on the optical performance is shown below, where the critical zone number N_0 is plotted for various energies and low-Z materials.

Based on such abilities, we discuss the science case, in particular merging black holes within galaxies. Their dynamical behavior may be investigated with respect to upcoming gravitational wave experiments like LISA as well as, for lots of mergers, their statistical distance distribution.

References:
- G. K. Skinner, "Design and imaging performance of […] Fresnel lenses", *Applied Optics* **43**, 4845 (2004).
- C. Braig and P. Predehl, "Efficient Fresnel X-ray optics made simple", to be published in *Appl. Opt.* (2006).

Christoph Braig, Peter Predehl

The PANTER X-ray Test Facility

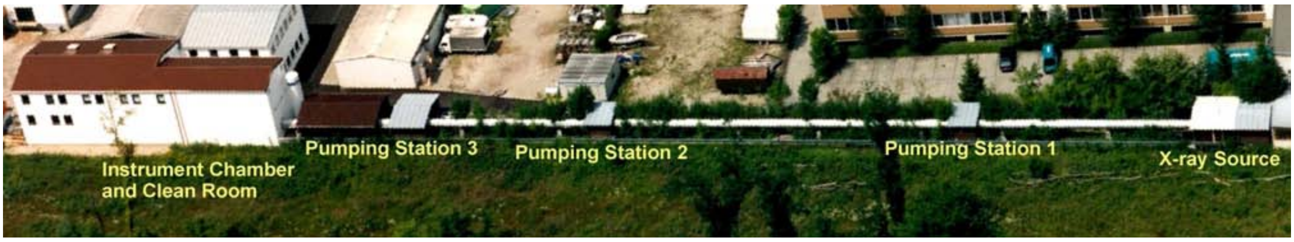

The PANTER facility is located in Neuried in the southwest outskirts of Munich. With its 123 m long vacuum tube (1 m diameter) and the X-ray source system and the main test chamber (3.5 m Ø, 12 m long) it has mostly been used for the characterization of X-ray telescopes as well as tests of detectors, focal plane instruments, reflection gratings, filters, etc. Recent activities include e.g. accompanying and supplementary calibrations and tests for the EPIC-pn camera onboard of XMM-Newton, tests of silicon pore optics devices (HPO, XOU) proposed for the XEUS mission as well as micropore elements made from glass, and tests of multi-layer mirrors for future projects like SIMBOL-X. Recently, the *First Light* of a prototype camera (TRoPIC) for eROSITA has been obtained, which will be extensively used for future mirror calibrations. Additionally, end-to-end tests for CAST instrumentation had been performed.

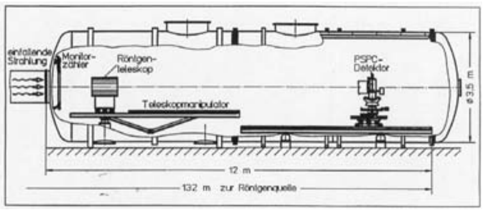

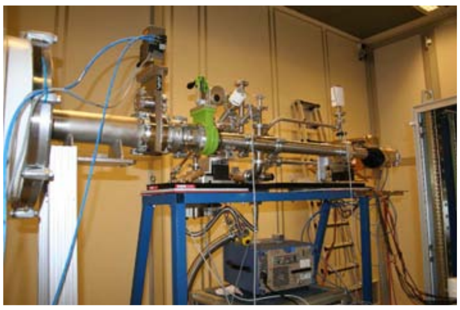

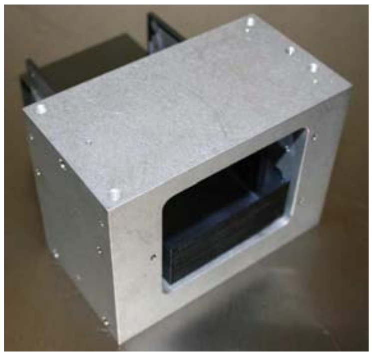

Tandem of silicon pore optics elements (XOU-2) inside interface jig, with the entrance to the "parabolic" part of the Wolter type-I telescope to the right.

In normal configuration instrumentation to be calibrated is installed in the vacuum chamber and measured with the PANTER focal plane instrumentation. In case of end-to-end tests (or devices not suited for vacuum applications) an extension can be flanged to the instrument chamber like for the CAST (CERN Axion Solar Telescope) Micromegas experiment.

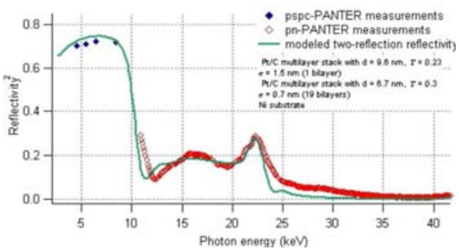

Reflectivity R (parabola) × R (hyperbola) as function of energy (0.3 – 40 keV) for a Pt/C multilayer shell.

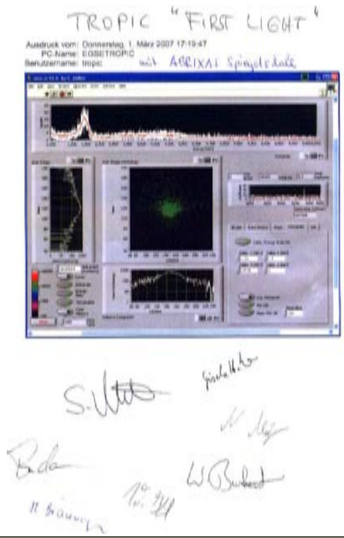

First Light of the TRoPIC camera (prototype for eROSITA) at PANTER, with the new 75 µm × 75 µm pixel framestore CCD developped by the HLL.

The PANTER team

The GLAST Burst Monitor

One of the scientific goals of the Large-Area Telescope (LAT) on GLAST, NASA´s next large γ-ray mission, is the study of GRBs in the energy range from ~20 MeV to ~300 GeV. In order to extend the energy measurement towards lower energies a secondary instrument, the GLAST Burst Monitor (GBM), will measure GRBs from ~10 keV to ~30 MeV and will therefore allow the investigation of the relation between the keV and the MeV-GeV emission from GRBs over more than six energy decades. The γ-ray group of MPE collaborates with a group in Huntsville equally sharing the data rights. It has built the scintillation detectors for the GBM.

The primary roles of the GBM are to measure the low-energy γ-ray emission of GRBs within a large FoV, to localize their position, to communicate this position to the LAT to allow its repointing and to perform time-resolved spectroscopy. These goals can be achieved with an arrangement of 12 thin NaI detectors which are declined to each other to derive the position of GRBs from the measured counting rates. They measure γ-rays from 10 keV to 1 MeV. In order to get an overlap in energy with the LAT for inter-instrument calibration two BGO detectors are mounted on two opposite sides of the GLAST spacecraft which are sensitive to γ-rays from 150 keV to 30 MeV. A picture of the GLAST spaccecraft is shown in

Figure 1. The NaI-detectors of the GBM mounted around the GLAST spacecraft.

Figure 1. A secondary objective of the GBM is to notify external follow-up observers. The GBM detectors have been extensively calibrated at MPE (results see poster by A. von Kienlin). With an effective area between ~100 cm² and ~200 cm² the GBM will detect ~200 bursts in its FoV of ~9 sr. About 60 of those fall into the FoV of LAT thus allowing, if detected, the measurement of burst spectra over an unprecedented energy range of more than 6 decades. An example of such a (simulated) spectrum is shown in Figure 2.

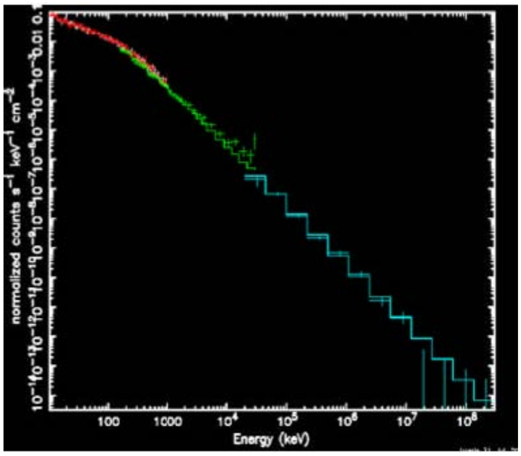

Figure 2. A simulated GBM/LAT GRB spectrum (courtesy Nicola Omodei).

One of the aims of GLAST is the exploration of the delayed high-energy γ-ray emission as it was observed by EGRET from GRB 940217 (Hurley et al. 1994). The origin of these γ-rays is unclear and it is not yet understood how these γ-rays can escape their production site without being absorbed via γ-γ interactions with lower-energy photons. With the measurements of GLAST it is hoped to shed light on this problem.

References:

1 Hurley et al., Nature **372**, 652, 1994

G. Lichti, A. von Kienlin, H. Steinle, R. Diehl, J. Greiner, C. Meegan et al.

Scientific performance of the GBM

The GLAST Burst Monitor (GBM) is the secondary instrument on NASA's next gamma-ray mission GLAST (scheduled for launch in Nov. 2007). It will augment the capabilities of GLAST for the detection of cosmic gamma-ray bursts by extending the energy range (20 MeV to > 300 GeV) of the Large-Area Telescope (LAT) by two BGO-detectors (150 keV to 30 MeV) and 12 NaI(Tl) detectors (10 keV to 1 MeV) to low energies. GBM will also provide rapid on-board GRB locations and time-resolved spectra. The GBM has been built by a collaboration between MPE and MSFC/UAH with an equally share of hardware contributions and data rights.

The scientific performance of the GBM instrument for GRBs is determined with the help of Monte Carlo simulations of the physical detector response, the measured detector properties and background rates scaled appropriately from BATSE measurements. For this the calibration of the energy/channel-relations, the dependences of the energy resolution, the effective areas and the angular responses of the single detectors were performed at MPE with radioactive sources. In addition to this calibrations at low energies (10 – 60 keV) were carried out at the BESSY synchrotron radiation facility in Berlin and at high energies (6 – 18 MeV) at a small Van-de-Graaff accelerator at the Stanford Linear Accelerator Center (SLAC), CA, USA

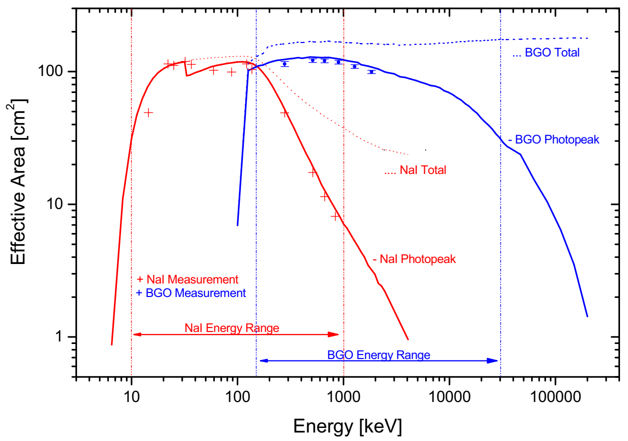

The measured and simulated effective areas of the NaI(Tl)- and BGO-detectors as a function of the photon energy. The energy bands of the two detector types are marked in red (NaI) and blue (BGO).

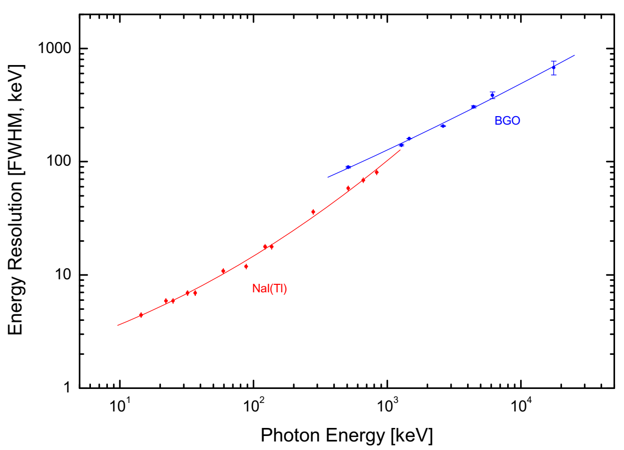

Energy resolution of the EQM NaI(Tl)- and BGO-detector as a function of the photon energy, determined from measurements with radioisotopes.

In the table below the scientific-relevant parameters are summarized and compared with the requirements. It can be seen that all level-1 (NASA top level) requirements are met. With the stated sensitivity, the GBM will detect ~200 bursts/year. About 60 of these bursts will be within the 55° field of view of the LAT. In the year 2006 the GBM was successfully tested, calibrated and integrated onto GLAST.

Parameter	Level-1 requirement	Intra-Project Goal	Expected Performance
Energy range	10 keV – 25 MeV	5 keV – 30 MeV	8 keV – 30 MeV
Energy resolution	<10% (1σ; 0.1 – 1 MeV)	7% (1σ; 0.1 – 1 MeV)	<8% at 0.1 MeV <4.5% at 1 MeV
Effective area	none	NaI: >50 cm² at 6 keV BGO: none	NaI: 48-78 cm² at 14 keV; BGO: >95 cm²
On-board GRB location	none	15° accuracy (1σ radius) within 2 s	<15° in 1.8 s (<8° for SC zenith angle <60°)
On-ground GRB sensitivity	<0.5 photons/(cm² s) (peak flux; 50-300 keV)	0.3 photons/(cm² s) (peak flux; 50-300 keV)	0.47 photons/(cm² s) (peak flux; 50-300 keV)
On-board GRB trigger sensitivity	1 photon/(cm² s) (peak flux; 50-300 keV)	0.75 photons/(cm² s) (peak flux; 50-300 keV)	0.7 photons/(cm² s) (peak flux; 50-300 keV)
Field of view	>8 steradian	10 steradian	9 steradian

References:
- von Kienlin, A., et al. 2004, SPIE 5488, 763
- Lichti G.G., et al. 2004, Baltic Astronomy 13, 311
- Kippen, R.M., et al. 2001, AIP 587, 801
- von Kienlin, A., et al. 2001, ESA SP-459, 529

Andreas von Kienlin, Giselher Lichti, Elisabetta Bissaldi, Helmut Steinle et al.

Understanding the GBM detector calibration: A detailed simulation including the environment

The GLAST Burst Monitor (GBM) is the secondary instrument on NASA's next Gamma-ray mission GLAST. It will enhance the capabilities of GLAST by locating and detecting cosmic gamma-ray bursts at lower energies by the use of 12 NaI detectors (energy range 10 keV to 1 MeV) and 2 BGO-detectors (energy range 150 keV to 30 MeV). GBM was built in a close collaboration between the MPE and the Marshall Space Flight Center (MSFC).
The angular and energy response of each GBM detector has been calibrated using various radioactive sources at different incidence angles relative to the detector in a laboratory environment at the MPE in 2005. To facilitate the understanding of the reconstruction of the detector response, a detailed simulation of the whole laboratory environment and the setup of the calibration source was performed. A modified version of the CERN GEANT 4 simulation software (provided by collaborators at the Losa Alamos National Laboratory) was used.

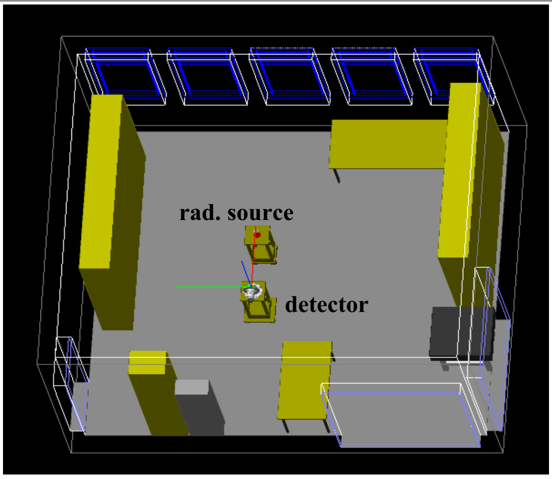

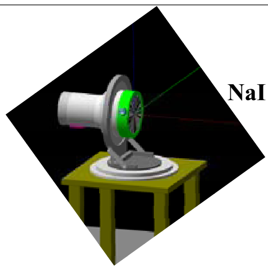

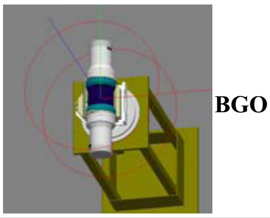

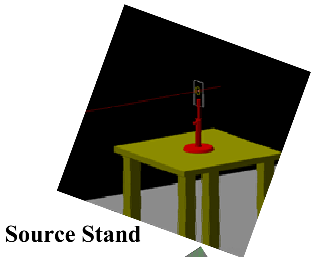

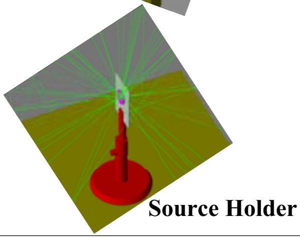

Calibration Setup

The full environment (laboratory) of the calibration setup was modeled. All components (walls, windows, furniture, floor, ceiling etc.) could be activated or deactivated for interactions of the radiation.

The radioactive sources used for the calibration were placed onto a source holder at a fixed position near the middle of the room. This source holder was mounted on a wooden stand raising it about one meter above the laboratory floor. The distance from the detector to the source was 1.16 m.

The detector mounting, that rested also on a wooden stand, could be rotated around three axes to change the angle of the incident radiation.

Detector Models

Complete detailed models of a NaI detector, a BGO detector, and their mounting brackets as they are used on the spacecraft were created.

In addition, the complex holding structure, which enabled a rotation of the detectors around all three axes during the calibration was included in the model.

Radioactive Calibration Sources
(main energies in MeV):
^{109}Cd (0.022), ^{241}Am (0.059),
^{57}Co (0.122, 0.134), ^{203}Hg (0.279),
^{137}Cs (0.662), ^{51}Mn (0.835),
^{22}Na (0.511, 1.275),
^{88}Y (0.898, 1.836)

The radioactive material of the calibration sources was contained in a sphere of about 1 mm diameter in the center of a flat plastic disc. This disc was mounted to the source holder made from PVC.

Scattering of Radiation

A significant part of the radiation emitted isotropically from a source is scattered by various objects in the laboratory, including the air. With increasing energy of the radiation, an increasing fraction of the scattered radiation reaches the detector and contributes to the source background (i.e. background induced by the isotropic radiation of a source present). At 22 keV, only few percent of the detected radiation are scattered photons. Most photons reach the detector directly. But at 1.275 MeV a significant part of the detected radiation is from scattered photons. The table sumarizes this findings.

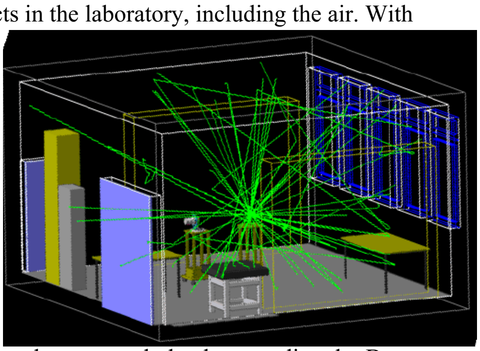

Summary of Results

	NaI			BGO
component	22 keV	122 keV	1.275 MeV	4.43 MeV
direct infall	94.0 %	91.0 %	75.0 %	70.0 %
scattered rad. total	6.0 %	9.0 %	25.0 %	30.0 %
walls	< 0.1 %	0.6 %	12.0 %	13.0 %
source holder	4.6 %	7.5 %	3.0 %	2.0 %
source stand	0.1 %	< 0.1 %	< 0.1 %	< 0.1 %
detector stand	<0.1 %	< 0.1 %	2.0 %	< 0.1 %
floor	< 0.1 %	0.8 %	8.0 %	15.0 %
other furniture	< 0.1 %	< 0.1 %	< 0.1 %	< 0.1 %
air	1.3 %	< 0.1 %	< 0.1 %	< 0.1 %

Simulation runs with 10^6 detected photons each.

Helmut Steinle, Andreas von Kienlin, Elisabetta Bissaldi, Giselher Lichti, Roland Diehl, Jochen Greiner, et al.

PK-3 Plus – Complex Plasma Research on the ISS

The research on complex plasmas is one of the fastest growing fields in plasma physics. Complex plasmas are plasmas containing solid particles typical in the micrometer range. Due to this heavy component gravity plays an important role in the investigation of this special state of so-called "soft matter". A mandatory pillow of this research is based on investigations under microgravity conditions on board of the International Space Station ISS. PK-3 Plus is the new long-term laboratory launched to the ISS end of 2005. It allows detailed investigations of complex plasmas under microgravity conditions. Compared to its pre-cursor PKE-Nefedov, operational 2001-2005, it has an advanced hard- and software. Much better diagnostics and especially a much better homogeneity of the complex plasma allow more detailed investigations, helping to understand the fundamentals of complex plasmas.

Scientific objectives of PK-3 Plus on the ISS:

- homogenuous complex plasmas in
  - fluid phase
  - crystalline phase
- phase transitions (melting and crystallisation)
- critical phenomena and critical point
- electrorheological complex plasmas
- two-phase flow
- linear and non-linear waves
- self-excited instabilities
- growth of particles

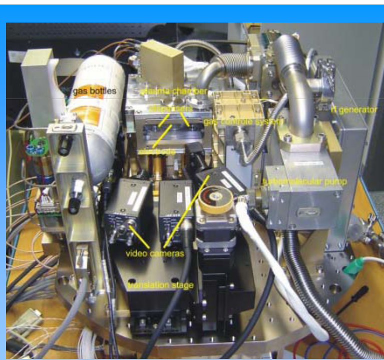

Physical Apparatus of the PK-3 Plus lab, developed at MPE.

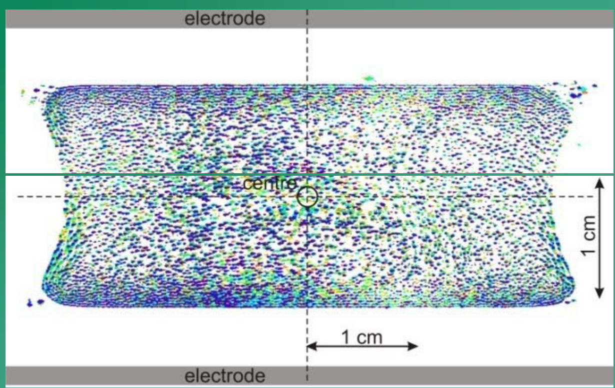

Homogeneous distribution of a complex plasma under µg-conditions.

German ESA Astronaut Thomas Reiter on board of the ISS with the PK-3 Plus laboratory with the Experiment Container including the physical apparatus mounted in the Service Module. (Courtesy of NASA)

Conclusions

In 2006 we performed 4 missions with a total of 12 individual experimental runs, each about 1.5 h µg time. The results show the perfect functioning of the lab and provided us very interesting new insights into the physics of complex plasmas. It is foreseen to operate the Lab on the ISS until 2009, at least.

A. Ivlev, T. Hagl, U. Konopka, G. Morfill, H. Rothermel, M. Rubin-Zuzic, R. Sütterlin, H. Thomas

PK-4: Complex Plasmas in Space – the next Generation

PK-4 is an experiment designed to investigate complex plasmas in a combined dc/rf discharge under microgravity conditions on board the International Space Station following the successful experiments PKE-Nefedov and PK-3 Plus. The dc discharge plasma is produced in a glass tube. In addition an rf discharge can be applied by external rf coils. The set-up is especially suited for studying the liquid phase of complex plasmas. In the laboratory and in parabolic flights such experiments were carried out, the plasma conditions were determined, and the design for the ISS was tested.

Complex plasmas are low-temperature plasmas containing microparticles with a diameter of a few microns. These microparticles are highly negatively charged by collecting several thousand electrons on their surface. Therefore they interact strongly with each other, leading to liquid and even crystal phases. So far, complex plasmas are mostly studied in rf plasma chambers. PK-4 uses a dc or combined dc/rf discharge produced in a glass tube of 30-40 cm length and 3 cm diameter (see Figures). In this way, the microparticles streaming through the glass tube can be observed, allowing in particular to study the fluid phase of complex plasmas, e.g. shear flow or the transition from laminar to turbulent streaming.

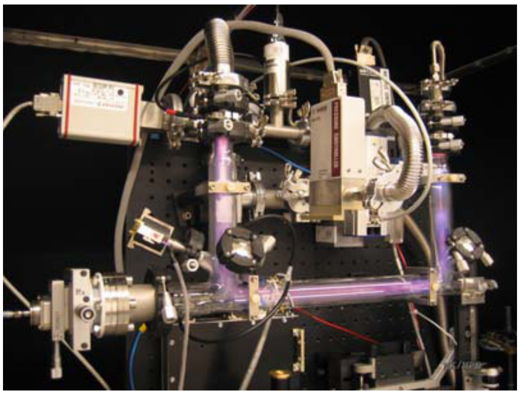

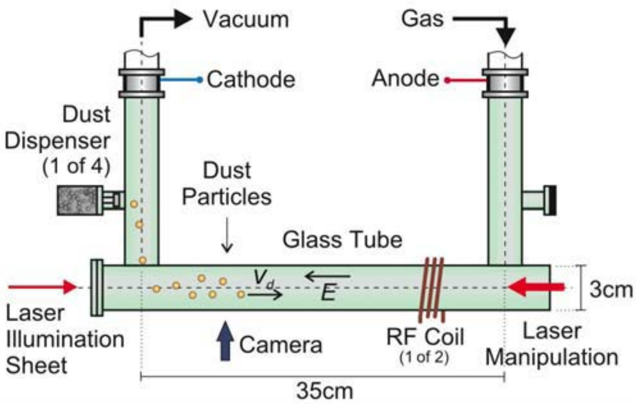

Since 2002 we perform experiments with PK-4 within a laboratory predevelopment phase, supported by DLR, in collaboration between MPE and IHED (Moscow). Three set-ups, two at the MPE for laboratory and parabolic flight experiments and one at IHED, were constructed [1]. So far we investigated dust waves and charging of the microparticles [2], the ion drag force acting on the microparticles [3], microparticle cloud collisions, the simulation of a Laval nozzle, the formation of clusters, and the viscosity of a complex plasma fluid. In addition measurements of the plasma conditions in the PK-4 plasma chamber were performed. These experiments were conducted in the laboratories at MPE and IHED as well as in four ESA parabolic flight campaigns. The final aim of PK-4 is the investigation of a complex dc plasma under microgravity on board the International Space Station following the successful complex rf discharge plasma experiments PKE-Nefedov and PK3-Plus. The preparations of the space experiment PK-4, scheduled for 2009, started with a ESA phase A/B study in the beginning of 2006. Within this phase we perform studies of the PK-4 design and test components and system functions in the laboratory and under microgravity conditions in parabolic flights, which will allow the construction of the flight hardware in a forthcoming phase.

References:
[1] V. Fortov et al., Plasma Phys. Control. Fusion 47 (2005) B537
[2] S.A.Khrapak et al., Phys. Rev. E72 (2005) 016406
[3] V. Yaroshenko et al., Phys. Plasmas 12 (2005) 093503

S. Albrecht, M. Chauduri, C. Deysenroth, M. Fink, T. Hagl, H. Höfner, S. Khrapak, M. Kretschmer, A. Ivlev, S. Mitic, G.E. Morfill, S. Ratynskaia, C. Rau, K. Tarantik, M.H. Thoma, V. Yaroshenko

Technology for Silicon radiation detectors

The MPI Halbleiterlabor (semiconductor laboratory, HLL) is a joint research facility of the Max-Planck institutes for physics and for extraterrestrial physics. In an 800 m² clean room, engineers and technicians produce silicon detectors for the research activities of the Max-Planck institutes - in particular for X-ray astronomy and high-energy physics.

The HLL offers a highly flexible production line which uniquely combines processing of ultra-pure silicon wafers on both sides with the small-scale technology of VLSI electronics.
Our technology is continuously being optimized and extended. These optimizations are aimed towards low noise performance (by minimizing leakage current and integrating electronics on-chip), low-energy response (by ultra-thin entrance windows), and large area devices (by tight process control and extensive inspection-repair strategies). The technology is run on 6“ wafers and offers a minimum feature size of 1,5 μm with an overlay accuracy below 0,5 μm, several insulation and passivation layers and up to 4 conductive layers (2x polysilicon, 2x aluminum).
Routinely produced sensors are: **Fully depleted charge coupled devices** (pnCCDs) with parallel readout as used onboard the X-ray satellite XMM-Newton. Recent productions with framestore technology are foreseen for the mission eROSITA. **Silicon drift detectors** (SDDs) for high-resolution, high-rate spectroscopy at synchrotron light sources and Free Electron Lasers at SLAC and DESY, for X-ray microscopy at BESSY and for the hadron physics experiment SIDDHARTA. These sensors also work in the NASA Mars rovers and find strong interest in industry. In particular, products based on SDDs originally designed and fabricated for scientific experiments have been successfully introduced as X-ray detectors in scanning electron microscopes. **Active pixel devices** with **DEPFET** amplifiers are developed for XEUS and linear collider vertex detectors like ILC. High position resolution, thinned material and fast readout are key items for this next detector generation. Active pixel detectors combined with SDD structures led to scalable pixel sizes up to 1mm² as needed for the BepiColombo and SimbolX missions.

Top line: The cleanroom showing wet chemistry (left) and wafer inspection areas (right). Middle line: The dicing, mounting and bonding room. Bottom line: Samples of DEPFET sensor for XEUS (left) and pnCCDs for eROSITA(right).

eROSITA pnCCD camera

We develop for the eROSITA X-ray space telescope the pnCCD cameras for spectroscopy and imaging of X-ray photons. The detector concept is based on that of the XMM-Newton pnCCD which performs excellent measurements since launch of the satellite in 1999 till today. The improvements, we had implemented in the eROSITA pnCCD and its analog signal processor, showed in the tests substantial performance enhancements.

The German eROSITA (extended Roentgen Survey with an Imaging Telescope Array) telescope has the main scientific goal to test cosmological models and to perform an all-sky survey in the energy band from 0.3 keV to 10 keV [1]. It will be launched into a low earth orbit on the Russian Spectrum-Roentgen-Gamma satellite in 2011. eROSITA comprises seven identical mirror systems with seven X-ray CCD cameras in the foci. The key part of the focal plane camera is the frame store pnCCD which is designed and produced in the MPI semiconductor laboratory for the eROSITA project [2].

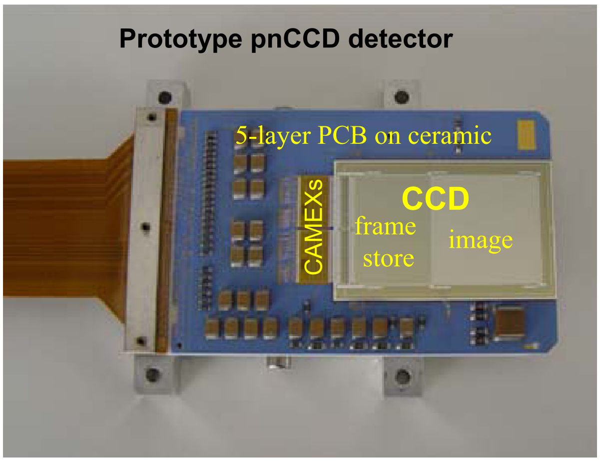

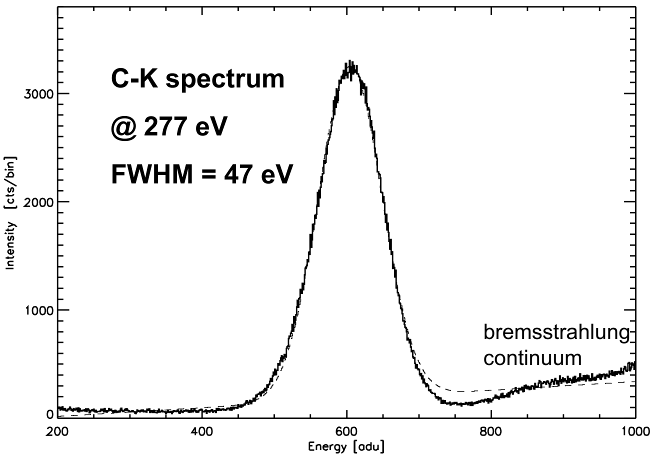

Prototypes of the pnCCD detector were tested for a proof of concept and an evaluation of the performance of the eROSITA flight cameras. As result of an improved CCD design and fabrication technology in combination with a redesigned CAMEX analog signal processor, the detector shows significant improvements compared to the previously developed XMM-Newton pnCCD detector, as shown in the table. The main three objectives for camera development are presently:

- Extensive prototype detector testing
- Production of flight pnCCDs and CAMEX
- Prototyping of flight camera with the necessary modifications in mechanical, thermal and electric design.

pnCCD	**eROSITA**	**XMM-Newton**
Total # pixels	1,032,192	153,600
Pixel size	75 x 75 μm²	150 x 150 μm²
Read noise	2 el. rms	5 el. rms
CTI	2×10^{-5}	50×10^{-5}
FWHM@5.9keV	all: 138 eV	singles: 155 eV
Out of time	0.4 %	6 %
Sens. depth	450 μm	300 μm
Operation mode	frame store	fullframe

References:

[1] P. Predehl, G. Hasinger, H. Böhringer, et al., Proc. SPIE, 6266, 2006.

[2] N. Meidinger, R. Andritschke, O. Hälker, et al., Nucl. Instr. & Meth., A568, 2006.

N. Meidinger on behalf of the MPI semiconductor laboratory and the eROSITA team

Extracting pnCCD Characteristics

The pnCCDs for X-ray spectroscopy and imaging produced in the MPI Semiconductor Lab need to be characterized in order to study the effects of technological and design improvements. The characteristics of pnCCDs (in particular their spectroscopic performance) are evaluated by our CCD analysis software package. Finally the best devices will be selected for applications such as eROSITA.

Key features of the analysis software:
- Processing of raw CCD frames
- Calculation and application of corrections (e.g. offset and common-mode subtraction, gain correction)
- Event filtering (extracting photon lists)
- Analysis of split events (i.e. evaluation of interactions generating charges distributed over one or more pixels)
- Extraction of the key parameters, in particular noise and energy resolution

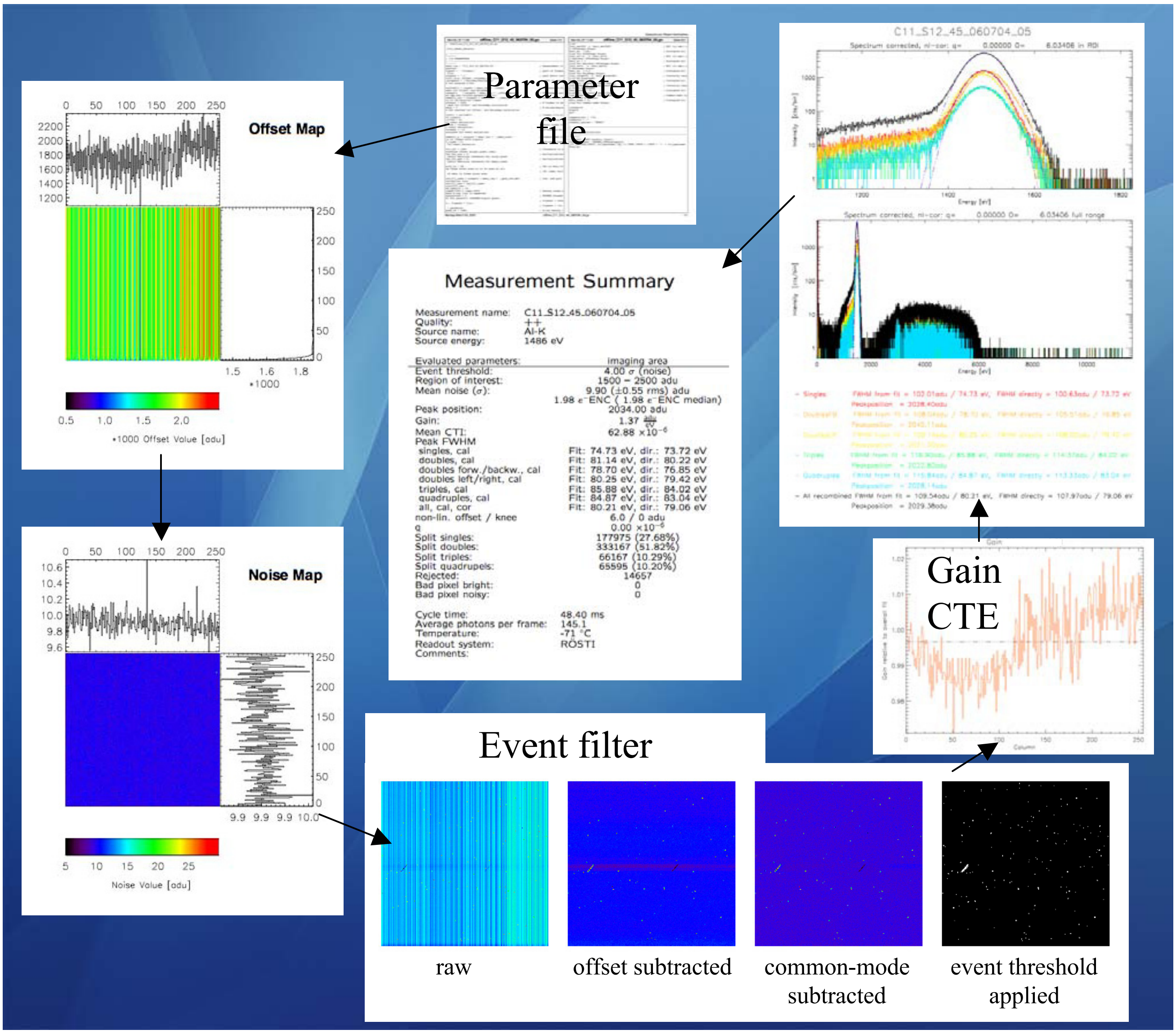

R. Andritschke, G. Hartner, N. Meidinger, P. Holl

DEPFET based focal plane arrays for X-ray imaging experiments

Developed at the MPI semiconductor laboratory, the combined detector-amplifier structure DEPFET (DEpleted P-channel FET) is a promising new building block for future x-ray imaging detector devices. Driven by the success of the first prototyping production of DEPFET-based devices, focal plane instrumentation for a large variety of experiments has been proposed, which consists of an array of DEPFET structures.

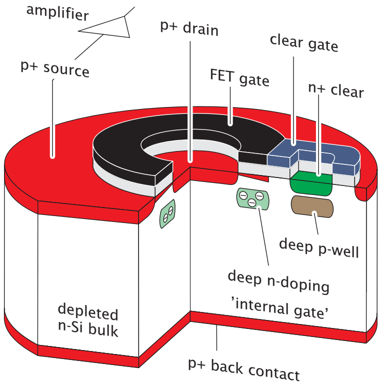

***Figure 1:** Cross-cut through a DEPFET structure.*

Based on the principle of sideways depletion, the DEPFET device uses an internally generated potential minimum for electrons located directly underneath the channel of a conventional MOSFET to locally integrate charge carriers generated within the silicon bulk. The presence of charges within this so-called *internal gate* modifies the channel conductivity, which can be detected with suitable front-end electronics. A cross-cut for a circular DEPFET structure can be seen in figure 1. The sensitive area of a DEPFET device can be adapted to a wide range of requirements, from ~30 x 30 µm^2 up to sizes in the cm^2 range by adding driftring structures (see figure 3, poster on Macropixel devices). Larger focal plane arrays based on DEPFETs are built by arranging an array of DEPFET cells of the requested size and specifications onto a common silicon bulk (see figure 2). DEPFET FPAs are fully depleted detector devices with 100 % fill factor and excellent QE given by the entrance window.

They exhibit excellent signal to noise ratios due to their low input capacitance. No charge transfer is needed, as all charge is stored and amplified in-situ. This also increases radiation hardness, as no deterioration of CTE can occur. The devices are area efficient, as no frame store area is needed. Their fast readout capability provides for low pileup probability. Flexible interconnections provide for optional readout sparsification or fast, repetitive readout of certain ROIs, e.g. when observing bright sources. In addition, they have a low power consumption, as pixels are only required to be turned on during readout.

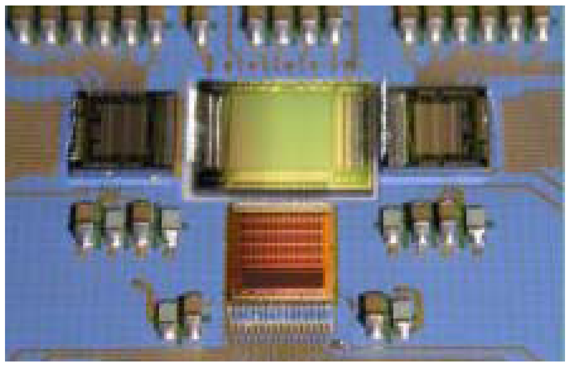

***Figure 2:** Photo of a fully assembled XEUS prototype hybrid with 64 x 64 pixels of 75 x 75 mm2 size, with its control and readout electronics.*

DEPFET based focal plane detectors are currently being investigated for:

- The **XEUS wide field imager**: A 1024 x 1024 pixel array with 75 x 75 µm^2 pixel size.
- The focal plane detectors for **SIMBOL-X**: A 128 x 128 pixel array with 625 x 625 µm^2 pixel size.
- The focal plane sensors for the **MIXS** instruments on **BepiColombo**: 64 x 64 pixel arrays with 300 x 300 µm^2 pixel size.

The devices for SIMBOL-X and Bepi-Colombo are matrices of Macropixels, as shown in figure 3.

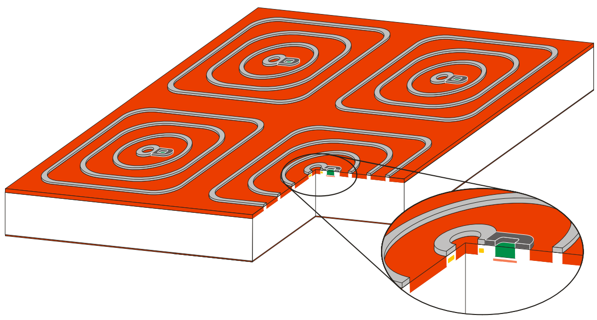

***Figure 3:** Sketch of a focal plane assembly based on a Macropixel (DEPFET combined with driftring structure) array as proposed for BepiColombo and SIMBOL-X.*

References:

- *J. Treis et al.*: Study of noise and spectroscopic performance of DEPMOSFET matrix prototypes for XEUS, *NIM A 568, 191-200, 2006*
- *P. Lechner et al.:* The wide field imager for the european X-ray observatory, *Conference record of the IEEE NSS, 2006*

J. Treis, DEPFET Group, MPI Halbleiterlabor

DePMOSFET Macropixel

The DePFET is a combined amplifier-detector structure, which can simultaneously collect, store and amplify charge signals from a silicon detector bulk. DePFET macropixels merge the innovative DePFET concept with the approved silicon drift chamber technology. By adapting the size of the surrounding drift chamber, one can build arbitrary scalable pixel sensors for x-ray imaging optimized with respect to pixel size, energy resolution and power consumption.

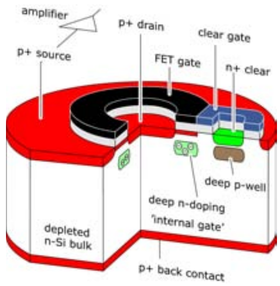

Fig. 1: Cross section of a circular DePFET pixel cell. Charges collected in the „internal gate“ modulate the transistor current.

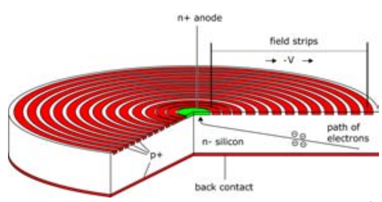

Fig. 2: Cross section of a SDD. Electrons generated in the sensitive bulk are driven upwards to the front surface while drifting to the center of the detector.

The DePFET Principle

The DePMOSFET is a p-channel MOSFET integrated upon a fully depleted high-resistivity silicon bulk (Fig. 1). A potential minimum is created by the help of an additional deep-n implantation directly below the transistor channel. Electrons released in the silicon bulk will drift to this so-called „internal gate“ and stay there, modulating the transistor current by inducing additional charge carriers in the channel. Thus the transistor current is a function of the charge stored in the internal gate. The charge can be removed by applying a positive voltage pulse to an adjacent n+-doped „clear“-contact. The charge information can be retrieved by comparing the transistor current values before and after the clear pulse. [1]

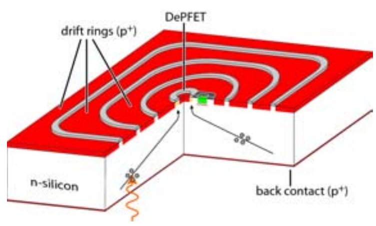

Fig. 3: Schematic view of a Macropixel cell with three drift rings. In the centre you can see the DePFET which serves as readout element

The Silicon Drift Detector (SDD)

SDDs use sidewards depletion to form a large sensitive area with a low readout capacitance independent of the detector size. A potential, formed by suitably biased drift rings, drives the signal electrons created within the detector volume towards the internal gate in the center (Fig. 2). SDDs show low noise because of the low readout capacity and high peak to background ratio because radiation enters the detector through a thin homogeneous backside window

The DePFET Macropixel

The Macropixel detector concept combines the DePFET principle with the SDD, i.e. it uses the DePFET as the readout element in the center of the SDD [2]. As both, DePFET and SDD, work upon a sidewards depleted bulk the combination is easy to perform (Fig. 3). This way one can design arbitrarly scalable pixels with the possiblility to store charge until readout. The macropixels are suited for X-ray optics where the spatial resolution is only in the area of sqare millimetres but high energy resolution is required. Additionaly one reduces the overall pixel count and thus decreases energy consumption and readout time.

References:
- [1] J. Treis et al. First results of DePFET based Active Pixel Sensor prototyes for the XEUS Wide Field Imager, SPIE 5501 89 2004
- [2] C. Zhang et al. Development of DePFET Macropixel detectors, Nuclear Instruments and Methods in Physics Research A 568 (2006) 207-216

DEPFET Group - Thomas Lauf, MPE, Halbleiterlabor - thl@hll.mpg.de

Hard X-Ray Cameras

As all back-illuminated detectors Silicon Drift Detectors (SDDs) exhibit excellent properties in the optical bandwidth. If coupled to scintillators they can measure the amount of the incident light and, if pixelated, the spatial intensity distribution. The low noise amplification allows for an energy resolution solely limited by the photon statistics of the light generation and the collection processes in the scintillator.

The low noise amplification and the high quantum efficiency in the optical bandwidth make silicon drift detectors suitable for the light detection of scintillators like CsI(Tl) or LaBr3 (see Fig. 1). The segmentation of the SDDs in subunits of tens of mm^2 allows for a precise reconstruction of the light centroid of the incident X-rays. Thus the space point of the position of the interaction within the scintillating crystal can be measured (see Fig. 2). This technique was used for the proof of the principle of a hard X-ray camera to be used in astrophysics as well as in medical applications. In the energy range up to 100 keV - as planed for Simbol-X or XEUS - a 3 mm thick scintillator would be sufficient. Compton Cameras are used to detect higher energies. Therefore a thicker scintillator crystal is needed (some cm for energies in the range of MeV). A design for an Anger camera system is shown in Fig. 3.

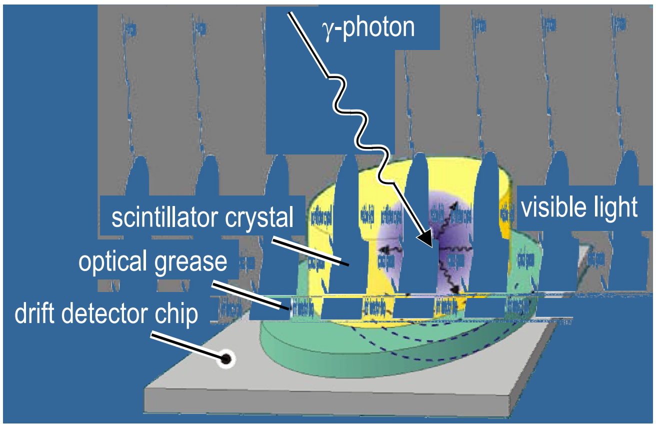

Fig. 1: A scintillator is coupled to a light sensitive silicon drift detector with the help of optical grease. The SDD is subdivided into individual cells (not visible), each equipped with an on-chip amplifier.

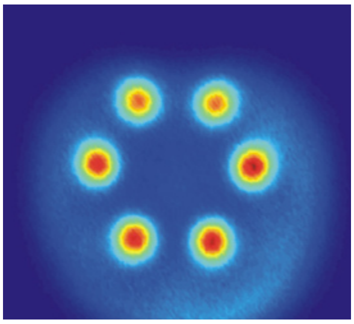

Fig. 2: A pinhole grid with 6 holes (hole diameter: 300 μm) arranged in a circle with 3 mm diameter was illuminated with X-rays of 122 keV of energy. The measured light distribution of all cells (in this case: 19) was used to find the centroid of the scintillation light. As can be appreciated in the figure, this was done with unprecedented success. The position of the holes was measured with a spatial resolution of better than 170 μm (FWHM).

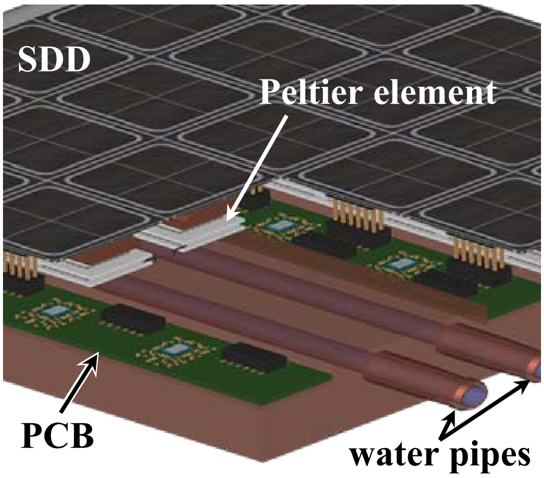

Fig. 3: Anger camera system as designed and proposed by C. Fiorini, Politecnico di Milano. The picture shows the quad SDD units, the Peltier elements below coupled to water pipes and the signal processors on the on the green PCBs. The scintillator which has to be coupled on top of the SDD is not shown. The system is designed to achieve a position resolution of better than 1 mm.

References:
- C. Fiorini, A. Gola, M. Zanchi, A. Longoni, H. Soltau, L. Strüder, NIM A 571, 126 – 129, 2006
- C. Fiorini, A. Gola, M. Zanchi, A. Longoni, P. Lechner, H. Soltau, L. Strüder, IEEE TNS, Vol. 53 No. 4, Part 2, 2392 – 2397, Aug. 2006

L. Strüder and G. Schächner

How to distinguish **100** optical photons from **101**?

- Performance studies of an ultra low noise DEPFET detector -

In this work we demonstrate theoretically and experimentally the capability to reduce the readout noise of an optical and X-ray photon detector based on the semiconductor DEPFET device below a level of only **0.2e⁻** ENC (equivalent noise charge). With such ultra low readout noise values it is possible to detect single photoelectrons produced after an optical photon interaction with silicon in terms of a real linear amplifier. The readout method used is called "Repetitive Non Destructive Readout" (**RNDR**). By transferring the collected charge from one readout node (DEPFET 1) to the other (DEPFET 2) and vice versa the same charge can be measured non-destructively and arbitrarily often.

Single optical photon detection with high quantum efficiency and, even more fascinating, the possibility to distinguish between different numbers of photoelectrons e.g. 100 from 101 has been confirmed in measurements.

Realisation and operation

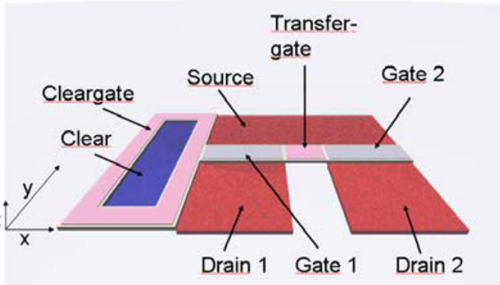

Our RNDR devices were realised by a combination of *two* DEPFET-detectors and a transfergate between them. The signal charge is collected and stored under gate 1 and gate 2 in the so-called internal gates (n-doped regions) and can drift from one DEPFET to the other by applying a positive voltage to the transfergate. The determination of the collected signal charge is done by measuring the Source-Drain current with full and empty internal gate. The difference of these two measurements is proportional to the amount of transferred charge. Such a measurement can be done with a precision of about 3 e^- ENC. Because the charge is not lost, but stored in the other DEPFET after the measurement, the same charge can be measured the same way arbitrarily often. Taking the average value of a large number *n* of these measurements, the noise is reduced by $1/\sqrt{n}$. An additional n-contact clears the pixel from time to time (Clear). The main advantage of such a detector is to greatly reduce the influence of the 1/f noise to the readout noise.

Performance

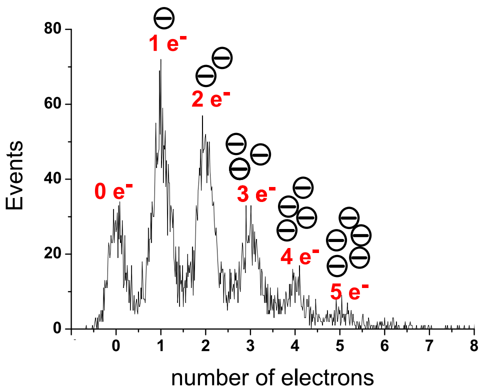

The figure to the left shows a measurement, where the detector was illuminated before readout by a very weak optical laser source (672 nm). Afterwards the collected charge has been measured 300 times, resulting in a noise of (3.1e^-ENC)/sqrt(300) = 0.18e^-ENC. The spectrum shows firstly a clear separation of the peaks which belong to different numbers of collected photoelectrons and secondly the poisson nature of the photon source. By further increase of the laser intensity it is also possible to distinguish between e.g. 100 electrons and 101.

Applications

The most obvious application is single optical photon counting, but also an ultra low noise x-ray detector for e.g. extremely red-shifed astronomical objects can be realised. Already under production are RNDR-Matrices and small CCDs with RNDR-devices as readout-nodes, which combines the established CCD properties with a ultra low noise readout.

References:

• Stefan Wölfel et al, "Sub-electron noise measurements on repetitive non-destructive readout devices", Nucl. Instr. and Meth. A 566 (2006) 536-539
• James Janesick et al, "New Advancements in Charge-Coupled Device Technology - Subelectron Noise and 4096x4096 Pixel CCDs", Astronom. Society of Pacif. Conf., Series No. 6, 1989

DEPFET Group - Stefan Wölfel, MPE, Halbleiterlabor, steppke@hll.mpg.de

Close up view of a pnCCD pixel

X-ray pnCCDs have been used with great success as the detector for the EPIC-pn camera on the XMM-Newton mission and are selected as the detectors for the coming eROSITA X-ray satellite mission. pnCCDs are used to detect X-ray photons in the energy range of 0.1keV to 10keV. A photon absorbed in the silicon bulk of the detector creates a cloud of electron-hole pairs which are separated in a drift field. The signal electron cloud expands during its drift to the pixel structure on the front side and can spread over up to four neighboring pixels . We have measured and simulated the exact signal charge distribution depending on the incidence position of an X-ray photon. The results can be used to improve the position resolution of pnCCDs to the order of 1µm or to study the charge collection process already in the design phase of a new device.

The idea of the measurement method is to scan a pixel and to measure the pulse heights of the pixel and its neighbors for each position. With the mesh experiment originally invented by H. Tsunemi, this is done in a single measurement. A hole grid in front of the CCD defines a large number of different X-ray photon incidence positions on the pixel structure, see figure 1. White regions in fig. 1. indicate high average signal amplitudes, i.e. when a photon hits the middle of a pixel and all signal electrons are collected in this pixel.
Data from the pixels below each hole are used to reconstruct the performance of a single `virtual´ pixel. This is possible due to the homogeneity of the pixel structure of a pnCCD.

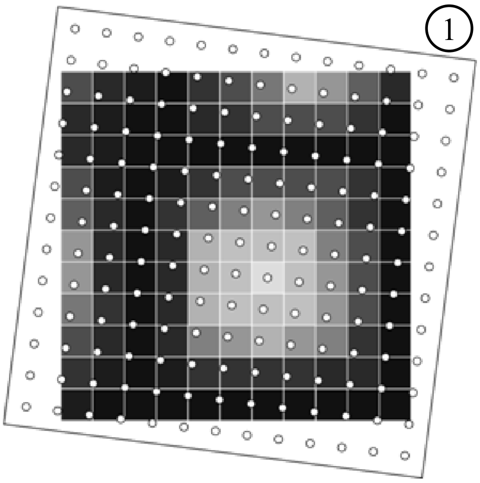

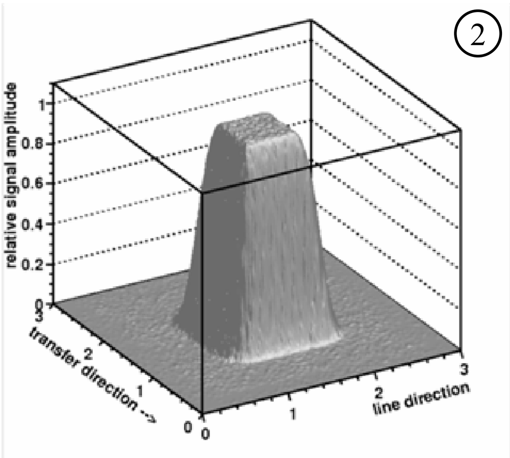

An analysis result of prime importance is the `**c**harge **c**ollection **f**unction´ (CCF) of a pixel. It shows how much signal charge is collected in a pixel for each photon incidence position, see figure 2. An X-ray photon incident close to the border or corner of a pixel creates a split event. The signals of the pixels are defined by the pulse height to position correlation of the CCF. With the pixel coordinates and their pulse height information, the incidence position of the X-ray photon can be reconstructed with an accuracy to the order of 1µm.

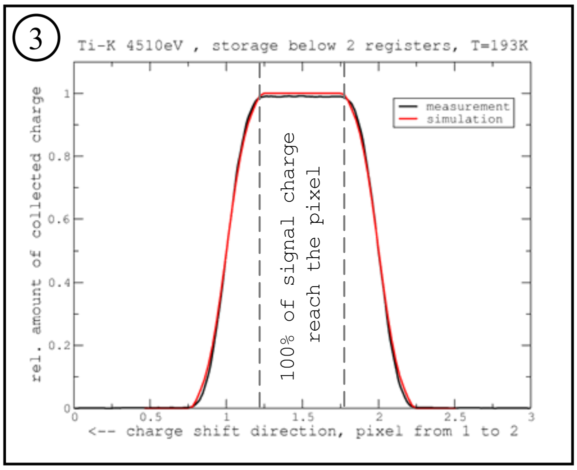

Another use of the measured charge collection function is to check and improve the accuracy of numerical device simulations. Figure 3. shows a plot of both the measured and simulated CCF of a pnCCD with 75µm pixels. It shows that in a central region with a width of one half pixel, the signal electrons created by an X-ray photon are completely collected in the pixel.

References:
- H. Tsunemi et al., Jpn. J. Appl. Phys. **36**, p. 2906, 1997
- N. Kimmel et al., Nucl. Instr. and Meth. A **569**, pp. 134-140, 2006

eRosita/pnCCD-Group, MPE, Halbleiterlabor - Nils Kimmel (nik@hll.mpg.de)

Sub-pixel spatial resolution of EPIC-pn CCD camera

Since the charge cloud induced by an X-ray photon has a finite size, we can get better position accuracy for X-ray events than CCD pixel size using signals of adjacent pixels. The sub-pixel resolution is important for eROSITA calibration and future measurements. Using focusing images of eROSITA test shell, step scan measurements inside the CCD pixel were performed. The results offer the opportunity to reconstruct the original location point of the X-ray photon with sub-pixel level.

EPIC-pn CCD and PSPC have been used as focal plane detectors in PANTER facility. Tests and calibration of X-ray optics for eROSITA have been going on in PANTER. The proposed angular resolution of eROSITA is 15" HEW (Half Energy Width), that is comparable to the pixel size of pn-CCD (150 μm corresponds to 19" at 1600 mm focal length). It also should be noted that central core of the focal image is much sharper than HEW. Therefore sub-pixel resolution is necessary to characterize full imaging capability, in particular the central core.

Experiment at PANTER facility
- EPIC pn-CCD: 150 μm pixel size
- Using focusing image of eROSITA test shell
- Step scan measurement
  - CCD is shifted in steps of 30 μm (1/5 of pixel size).
  - 5 (horizontal) x 5 (vertical) steps
  - in total 25 points, uniformly sampled

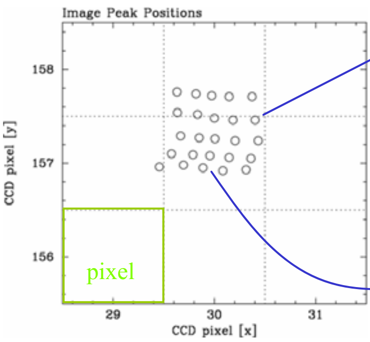

***Fig. 1**: Peak positions of focusing images. 30 μm shifts can be seen as expected. 25 points evenly cover one pixel.*

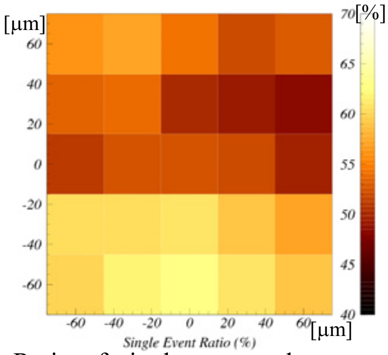

***Fig. 2**: Ratio of single pixel events obtained from each step. Aspect corresponds to Fig. 1. The pixel boundary is on the second line from the top and on the first line from the right.*

Ratio of single events shows remarkable variation in vertical direction compared with that in horizontal direction. Two possible reasons: CCD behavior is differ in two directions, the focusing image is elongated in horizontal direction.

By adding 25 images, that sample one pixel uniformly, we can obtain the averaged branching ratio as follows, single pixel events 58 %, doubles 34 %, triples 5 %, quadruples 2 %.

From this ratio, size of the region where incident X-rays result in each grade can be roughly estimated (Fig. 3).

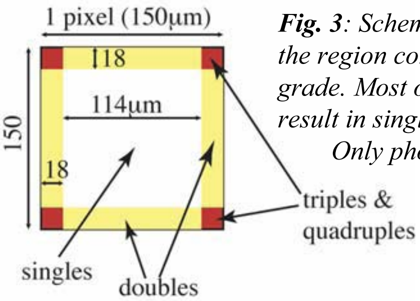

***Fig. 3**: Schematic illustration of the region contributed to each grade. Most of incident photons result in single pixel event. Only photons located in the small area can create electrons in adjacent pixels.*

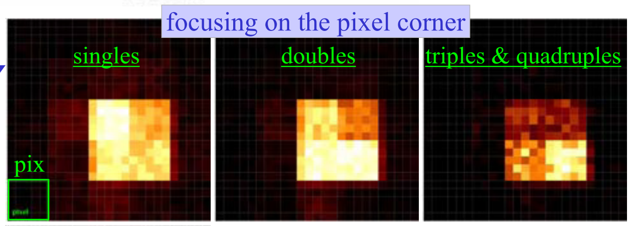

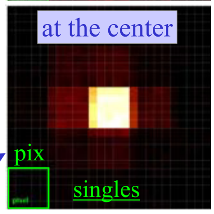

***Fig. 4 Upper**: Peak of focusing image hits pixel corner. Images of various grades; singles (left), doubles (middle), triples & quadruples (right). **Lower**: Peak hits pixel center. Image of single pixel event. Each image represents 5x5 pixels of the CCD.*

Great difference is evidently seen in the two cases. On the occasion of calibrating experiments, we have to avoid such pixel effects.

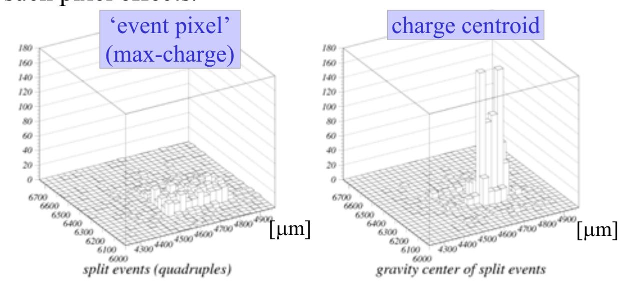

***Fig. 5**: Application of 'charge centroid method' to the quadruple events. X-ray position is randomly determined in the pixel with the largest signal in the event (left). The 'charge centroid method' is to employ the center of gravity of the event (right).*

Further experiments and careful consideration are necessary to restore images down to sub-pixel level. The implications of this technique are important for future missions as well as eROSITA calibration.

References: •H. Tsunemi et al., NIM A 477 (2002) 155-160 •E. Miyata et al., NIM A 513 (2003) 322-326

K. Misaki, M.J. Freyberg, P. Friedrich, The PANTER team

Development of integrated analog signal processors for future X-ray missions

Future missions demand larger detectors and higher frame rates, both raising the amount of analog data that has to be processed per second. To deliver these speed improvements without scarifying energy resolution new circuit concepts in new technologies have to be utilized. Our readout concept makes use of full column parallel readout to avoid multiplexing of weak detector signals therefore using more readout time for amplification and noise filtering. Our integrated readout amplifiers are already used for SOHO and XMM. Currently we are developing new versions for eROSITA, BepiColombo, Simbol-X and XEUS.

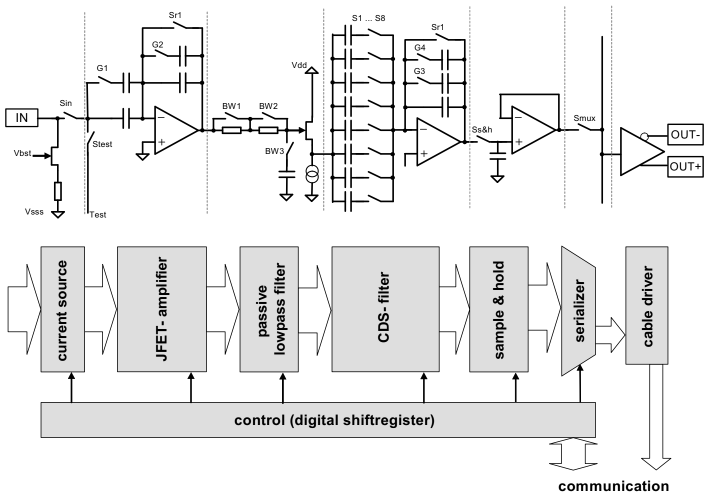

The CAMEX readout ASIC amplifies the weak signals from the detector. After signal amplification the signal if filtered, first by a passive low pass, second by a multi correlated double sampling (MCDS) stage. This filtering improves the signal to noise ratio. The measured signals are then serialized and sent to an ADC for further software based analysis.

For faster signal readout we are developing a trapezoidal filter which will be the optimum for white noise dominated applications, i.e. projects requiring high frame rates.

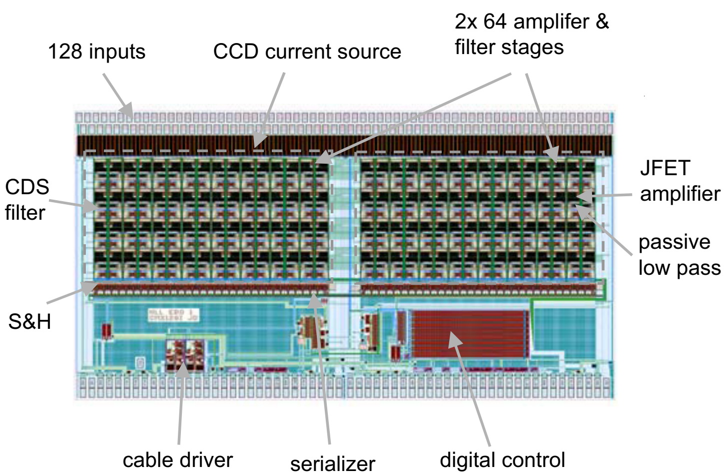

To handle the complexity of multi-ASIC systems a sophisticated on-chip digital logic section was developed. This enables to optimize signal gain and noise filtering properties for a specific application by easy digital programming

The Layout is showing a 128 channel CAMEX readout ASIC for pnCCDs. readout ASIC with 128 channels. This multichannel integrated readout amplifier ASICs is manufactured in the proven 0.8µ JFET-CMOS process from IMS Duisburg.

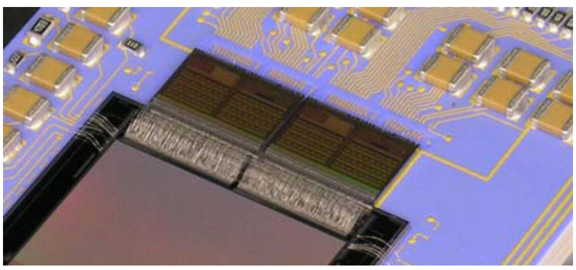

The ASICs are designed to fit the specific requirements of the detector. Input stage and pitch has to be tailored - shown here is a CAMEX variant for pnCCDs with 75µm pitch.

For detectors with more than 128 readout channels its possible to place the ASICs next to each other, without leaving an insensitive gap in the detector readout.

Sven Herrmann - Matteo Porro – MPI Halbleiterlabor

The center for free electron laser studies CFEL

The Max-Planck Gesellschaft has initiated a project linked to the new generation of X-ray sources, i.e. the free electron lasers with photon energies up to 25 keV, planned at DESY in Hamburg and at SLAC in Stanford. In the frame of CFEL the development of new synchrotron focal plane arrays plays a major role. The MPI-HLL, as a part of CFEL, has proposed to install pnCCDs for the experiment at the FLASH and LCLS light sources The more advanced Linear Silicon Drift Detector (LSDD) arrays for high speed imaging – up to 5 million images per second – are foreseen for the XFEL facility at DESY in 2014.

The European X-ray Free-Electron Laser Facility is a new international scientific infrastructure to be built in the north west of Hamburg [1]. The purpose of the Facility is to generate extremely brilliant (peak brilliance ~ 10^{33} photons/s/mm^2/mrad^2/0.1%BW), ultra-short (~ 100 fs) pulses of spatially coherent X-rays with wavelengths down to 0.1 nm, and to exploit them for revolutionary scientific experiments in a variety of disciplines spanning physics, chemistry, materials science and biology. The European XFEL will use super conducting LINAC technology, which allows for a high repetition rate. It will produce up to 30000 pulses per second with a minimum framing time of 200 ns. In order to fully exploit the high repetition rate enabled by the super-conducting technology of the LINAC, innovative pixellated 2D X-ray detector systems with single photon resolution and sampling times down to 200ns must be designed and developed. The frame readout speed between 1 and 5 MHz and the temporally associated amount of data are the main challenge in the development of such a system.

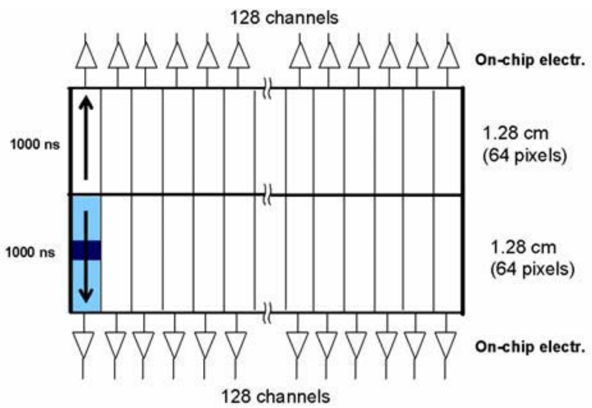

Fig.1 Schematic view of one LSDD detector subunit, composed of 256 channels with a pixel size of 200µm. The charges collected in the detector volume are drifted by a suitable electric field to 256 individual read-out anodes equipped with an on-chip amplifying electronics (e.g. DePMOS). The position of interaction in the direction perpendicular to the drift field is given by the column-wise geometrical segmentation, while in the direction of the drift field it is given by the drift time.

References:

[1] http://www.xfel.net

[2] M. Porro et al., "Spectroscopic performance of the DePMOS detector/amplifier device with respect to different filtering techniques and operating conditions**"**, IEEE Transactions on Nuclear Science, Volume 53, Issue 1, Part 2, Feb. 2006

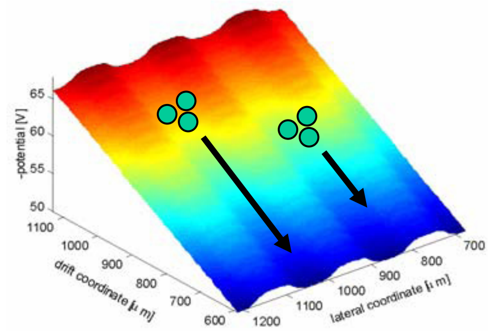

Fig.2 Diagram of the electron potential in a plane parallel to the LSDD detector surface. Signal electrons are collected in the nearest drift channel perpendicular to the detector surface and then drift parallel to the surface to the respective anode. During the drift process the charges are confined in one individual column.

The Semiconductor Laboratory has submitted a proposal for the realization of a detector system based on a fully depleted high-speed X-ray Linear Silicon Drift Detector (LSDD). Thanks to its charge transport scheme and its intrinsic amplification, given by amplifying DePMOS [2] readout anodes integrated on the detector chip, LSDD is able to provide high speed, high dynamic range and low noise at the same time. The final detector system will be composed of 1k x 1k pixels.

The Linac Coherent Light Source (LCLS) at SLAC will start operation 4 years ahead of the XFEL in Hamburg with similar X-ray parameters but reduced integral flux. Scientist of the MPG intend to join experiments at an early stage. CFEL has offered to implement a 1k x1k pnCCD detector operating at 120 Hz as a focal plane instrument for X-rays from 0.1 keV to 15 keV.

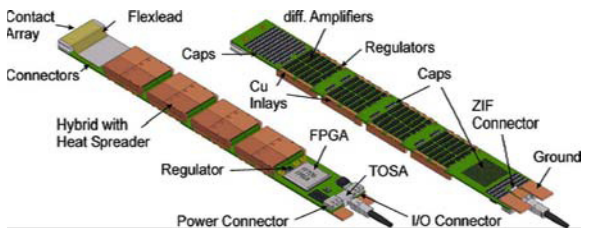

Fig. 3. Sketch of the proposed readout module for the LSDD. One of these modules is orthogonally connected to a detector subunit of the size of 25mm x 25 mm. It should provide analog amplification, analog to digital signal conversion, data storage and data transmission, fulfilling severe requirements in terms of speed, area occupancy and power consumption. The module should be able to handle a peak data rate coming from the detector of 500 Gb/s.

M. Porro - R. Hartmann - S. Herrmann - E. Lama Vaquero - L. Strüder - A. Wassatsch

Theory in the German Astrophysical VO

We show results of efforts done within the German Astrophysical Virtual Observatory (GAVO). GAVO has paid special attention to the introduction of theory data (simulations) into the Virtual Observatory (VO). The main emphasis of GAVO in this context was to investigate the use of relational database technology in the analysis of results of large scale structure simulations, as well as in their online publication. We also show prototypes of so called Virtual Telescopes, online services to "observe" simulation results so as to produce results that can directly be compared to corresponding observations.

The Millennium Database

We have used a relational database to store the detailed assembly histories of sub-haloes resolved by the *Millennium* simulation [1], and of all the galaxies that form within these structures for two independent models of the galaxy formation physics. We have created web applications (see Fig. 1) that allow users to query these databases remotely using the standard Structured Query Language (SQL). This allows easy access to all properties of the galaxies and halos, as well as to the spatial and temporal relations between them and their environment. Information is output in table format compatible with standard Virtual Observatory tools and protocols.

Time evolution in the Millennium database is embodied in the storage of merger trees of both dark matter halos and galaxies. To store such hierarchical data structures in a relational database we invented a new method that allows fast retrieval of the history (and future) of arbitrary nodes in the tree, illustrated in Fig.1. Also spatial searches require special indexing techniques, for which we have investigated various space filling curves, but also a simple "zone" approach, similar to that proposed for the SDSS SkyServer database in [2] For more details see the documentation on the website [3] and the announcement in [4].

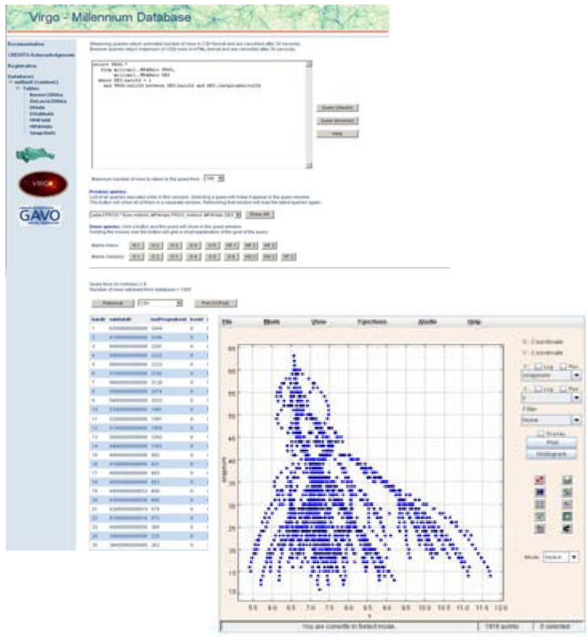

Fig 1: GAVO web interface for querying the Millennium databases. Results can be obtained in a variety of formats and can be visualised online using the VO-India's VOPlot facility.

Virtual Telescopes

Here we show examples of existing web applications that illustrate the concept of the *virtual telescope.* By modeling the relevant aspects of the real observational configuration, including sources, possible absorbing/emitting/lensing foregrounds as well as the instrumental characteristics, virtual telescopes produce mock images that can be directly compared to real observations, possibly using tools developed for real observations.

As such, virtual telescopes form an important tool by which the virtual observatory aims to bridge the gap between observers and theorists. The examples in Fig.2 as well as others are available on the GAVO web site (http://www.g-vo.org) for online execution.

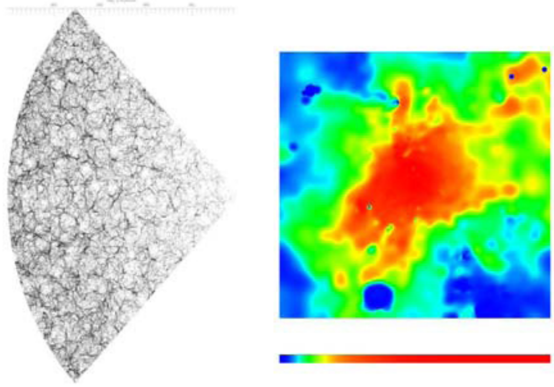

Fig 2: Two examples of results of a virtual telescope, one creating mock catalogues through a cosmological simulation, the other creating images of hydro simulations of galaxy clusters

References and further links

[1] *Springel V. et al. 2005 Nature 435, 629*

[2] *http://research.microsoft.com/research/pubs/view.aspx?tr_id=736*

[3] *http://www.g-vo.org/Millennium*

[4] *Lemson & the Virgo Consortium, astro-ph/0108019*

Acknowledgements *The Millennium database was built in close cooperation with the MPA. GAVO is funded by the German Federal Ministry for Education and Research.*

Gerard Lemson and Wolfgang Voges, GAVO,

Max-Planck-Institut für extraterrestrische Physik, Garching, Germany

Finding Galaxy Clusters with Grid Computing

Reliable identification of clusters of galaxies, which can be analyzed to deduce cosmological parameters, requires the combination of optical and x-ray surveys.[1] The extensive data storage and computational power needed are best obtained by using grid computing technology, which MPE is developing within the framework of the German Astronomy Community Grid.[2] The software and hardware solutions delivered will be applicable to many problems in modern astronomy.

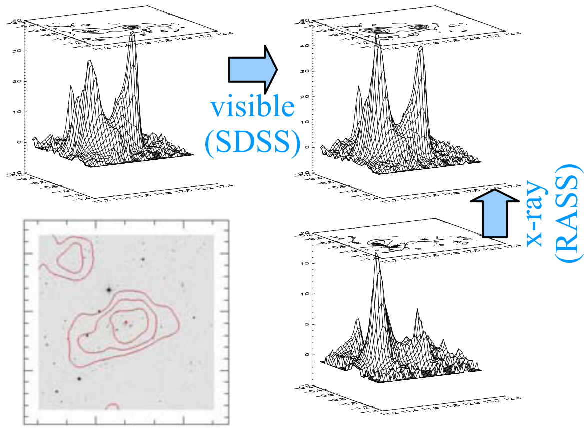

A cluster is a localized region with many galaxies and x-ray-emitting gas. But a filament seen end-on also has many galaxies, and AGNs emit x-rays but are not associated with clusters. Only by combining both types of observations can clusters be reliably identified. The algorithm developed at MPE first calculates a likelihood map from galaxy positions and magnitudes, then another map from x-ray photons, and finally multiplies the two together. This requires access to large astronomical catalogs and, for the large sky coverage needed for statistical analysis, long run times, so grid computing is attractive.

Grid computing allows users to easily share heterogeneous computational resources across administrative domains – computing power, data storage, or even equipment like robotic telescopes. A key concept is authentication of the user by a certificate created using public key cryptography. Another central idea is logical identification of resources, so that the user does not have to know exactly where his data and program are stored or where his calculations are carried out. In most cases of interest, the job can be parallelized and run on many hosts simultaneously.

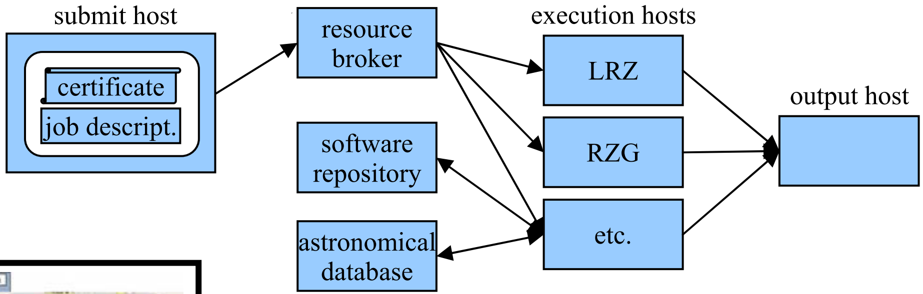

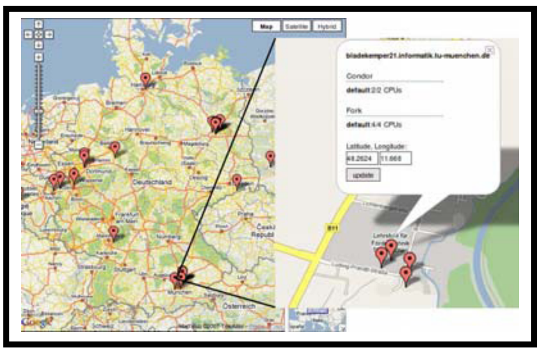

Grid computing becomes more practical and accepted when it is supported by additional technology such as workflow engines, data streams, and monitoring and steering. The map on the left shows an application that dynamically displays the geographic location and current status of resources in the German Astronomy Community Grid.

References:
1. Detection of X-ray clusters of galaxies by matching RASS photons and SDSS galaxies within GAVO, P. Schuecker, H. Böhringer, and W. Voges, *Astronomy&Astrophysics* **420**, 61–74 (2004).
2. http://www.gac-grid.de/

Arthur Carlson, Wolfgang Voges, Peter Schuecker, Hans Böhringer

Know-How Transfer

Information Based Analysis of Structural Image Content

Searching in data bases for images without using verbal descriptors or manual tagging of the stored images is desired in many applications. The aim of "query by image content" is to search in data bases for images by providing only a template or a set of image samples that have desired properties in common. Some elements of such a future search engine, including steps of advanced image processing, feature extraction and hierarchical image retrieval are presented.

The methodological approach is demonstrated with a set of images representing 111 so called Brodatz structures, widely used for testing image analysis techniques (Fig. 1a). In a first step the intensity values of the images are rescaled with respect to their structural information content. Next, several characteristics of the textures, concerning e.g. the intensity distribution and structural properties are quantified. The results, including the exploitation of scaling properties of the textures, are embedded in a feature space. Based on this multidimensional representation several similarity measures between supplied image(s) and images of a library are estimated and compared. Finally, a hierarchical cluster analysis is performed to yield a set of rank ordered reference images.

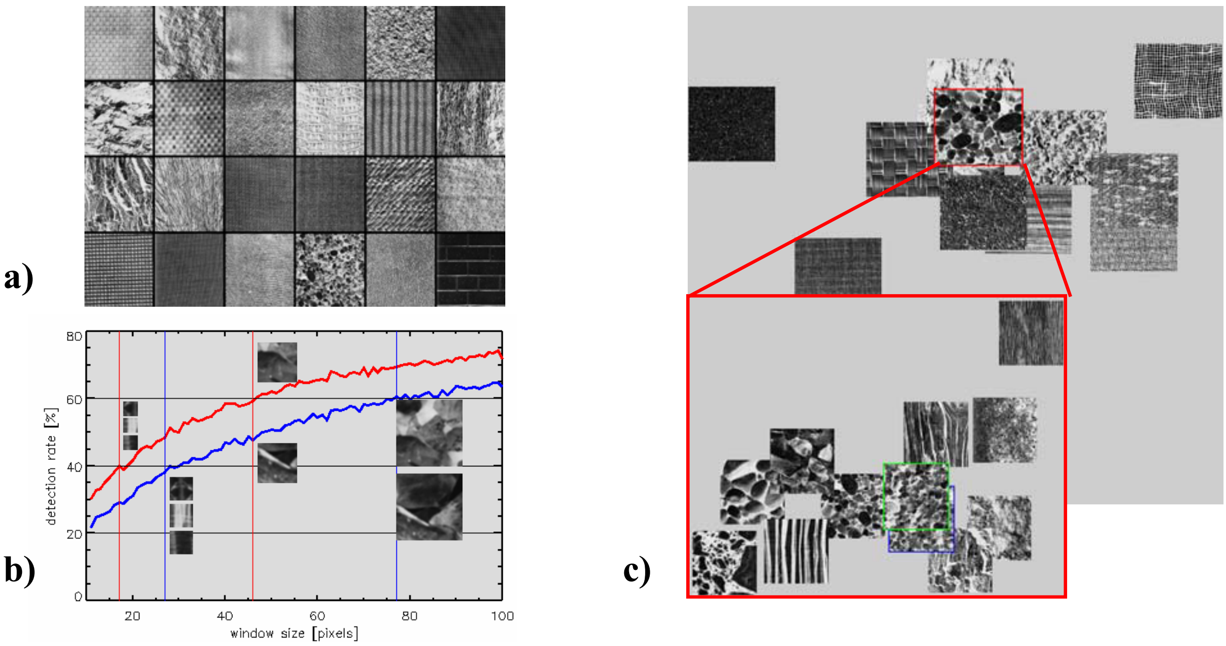

Figure 1: a) "Brodatz structures" (subset) used for testing. b) Comparison of the detection rate of texture probes using different similarity measures (blue = linear, red = information based distance measure) as a function of the size of the probe. The inserts indicate the necessary size of the probe to achieve a detection rate of 40% (red vertical line) and 60% (blue line) on average for the different measures. c) Example of a hierarchical image retrieval: The elements within the red rectangle form a subcluster and contain the provided texture sample (marked by the green frame).

To assess the reliability of the measures and extracted features, texture detection rates are investigated between disjoint probes of the same set of textures (Fig. 1b). The Kullback-Leibler entropy – used as similarity measure - yields the best detection rate in these tests. The information based data rescaling improves the detection rate by an additional amount in combination with texture measures. Fig. 1c shows a result of a hierarchical image retrieval: each texture in the upper part of Fig. 1c represents a subcluster of similar textures in terms of the choosen similarity measure. The true distances of the cluster representatives are approximated in a two-dimensional projection. One of the subclusters, containing the provided texture example, is shown in detail. The hierarchical retrieval can be tuned iteratively by introducing information based weights and by providing additional texture probes.

W. Bunk – T. Aschenbrenner – R. Pompl – F. Jamitzky

Characterization of microwave plasma torch for decontamination

An atmospheric low-gas temperature plasma torch using microwave has been developed and applied to sterilization of bacteria. To produce discharges, Ar gas of 2.2 slm is used and microwave power of 95 W is applied to the electrodes in the torch. At a position of 17 mm away from the torch, the gas temperature is 28 degrees, sufficiently cool so that the plasma doesn't harm living organisms. When an *Escherichia coli* culture is placed at this position for 2 minutes, the bacteria are almost completely killed in a 40 mm diameter circle. Tests with other cultures have also shown the bactericidal effect. We consider that this technique could be used for different medical application, in particular wound healing and, have started a clinical study for the therapy of chronic foot and leg ulcers.

The plasma torch consists of 6 stainless steel electrodes placed inside an aluminum cylinder. In this study, only Ar gas (purity 99.998%) is used in order to minimize the production of toxic gases. 2.2 slm is applied from the base of the electrodes through a Teflon shower plate which regulates gas flow around the electrodes. Microwave power of 2.45 GHz is applied to the electrodes through coaxial cables via a 2 stub tuner. The input power is 95 W. 6 small plasmas are produced between each of the electrode's tips and the inner surface of the cylinder.

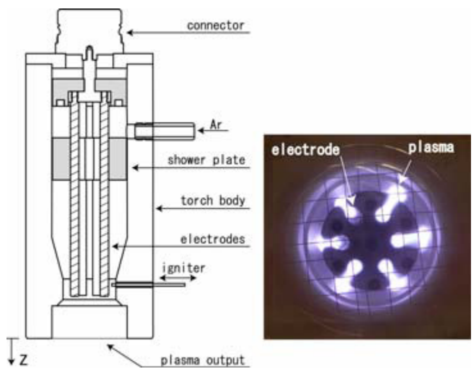

The figure shows the z-profiles (z: distance from the torch) of the measured temperature, NO_2 density at the torch axis and the floating potential of a grid electrode. In the vicinity of the torch, the gas temperature is relatively high. However, just after the opening of the torch (z = 2 mm) until z = 13 mm, the gas temperature has decreased drastically. At z = 13 mm, the temperature is 40 degrees, low enough so that the plasma does not harm human skin. From the measurement of the NO_2 density profile, at z = 8 mm there is a maximum. This indicates that the plasma flow from the torch faces the ambient air around the position. In order to determine how the plasma is distributed below the torch, the floating potential of the grid is measured. The potential also decreases as z increases, almost in the same way as the gas temperature.

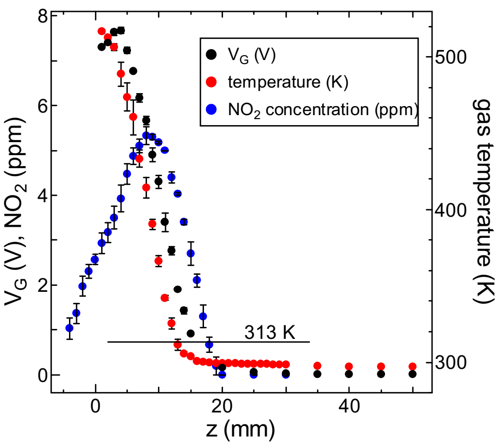

We observed the plasma exposure effect on bacteria. For example, when an *E.coli* culture is placed 17 mm away from the output of the torch for 2 minutes, a sterilizing effect on the bacteria can be observed as shown in the figure. In a circle of 40 mm diameter, a bactericidal effect has been observed. The boundary of the inhibition zone is a little fuzzy and the area is slightly larger than the opening of the torch. The surface temperature of the agar plate increased 5.7 degrees and reached 28 degrees during the treatment.

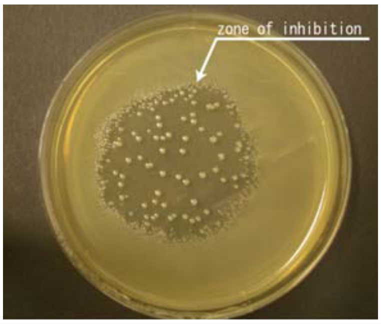

*Krankenhaus München Schwabing, **ADTEC Plasma Technology Co. Ltd.

T. Shimizu, B. Steffes, R. Pompl, F. Jamitzky, W. Bunk, K. Ramrath, B. Peters*, W. Stolz*, H.-U. Schmidt*, T. Urayama**, S. Fujii**, G. Morfill*

Analysing Time Series using Symbolic Dynamics

We introduce a methodology to characterize synchronization phenomena in time series based on a variant of symbolic dynamics (SD). In SD instead of representing trajectories by infinite sequences of numbers one watches the alternation of symbols. In this context, synchronization is identified by typical symbol patterns which frequently appear during symbol evolution. By applying our method to a prototype non-linear coupled system, we are able to describe different types of synchronization and other details of the coupled dynamics.

Synchronization is a process where two (or many) systems adjust a given property of their motion to a common behavior due to a coupling or forcing. Consider a sequence *x=(4,7,9,10,6,11,3)*. We define symbols which reflect the order of all possible subsequences. For instance, for subsequences of length *p=2*, only two symbols *A=(0,1)* and *B=(0,1)* are possible. Then, the symbolic representation of the sequence becomes $R_{p=2}(x) = (A,A,A,B,A,B)$ Figure 1 shows the symbolic representation of two time series (red symbols) for *p=4*. Given two symbols S_1 and S_2 there always exists a symbol *T* called transcription such that $T[S_1]= S_2$. Green symbols in Fig. 1 show the transcriptions between the symbolic representations of the time series. For *p>2* the set of symbols *G* can be divided into non-overlapping classes C_i ($G=\Sigma C_i$) satisfying a power property, namely if *S* ™ C_N then $S^N=I$, where *I* is the identity. Figure 2 shows the transcription matrix for *p=3,* where the two possible "power classes", i.e. $S^2=I$ (red symbols) and $S^3=I$ (black symbols) are shown. In order to characterize synchronization, we evaluate the

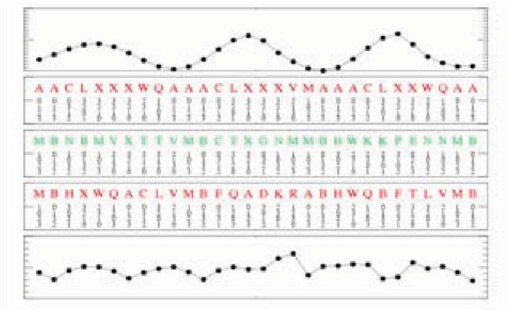

Figure 1

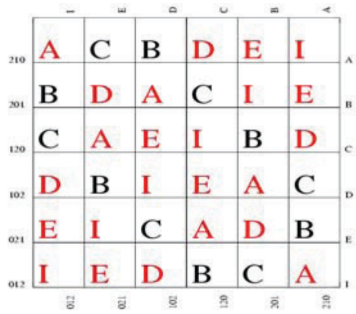

Figure 2

Shannon entropy of the probability distribution of transcriptions *Π(T)*, i.e. $E^N(p) = -\sum_i \Pi(T_i)\log\Pi(T_i)$, where *i* runs over the transcriptions in power class *N*. We apply the method to a bi-directionally coupled Roessler-Roessler system[1]. Figure 3 shows *E* for the "power 3 class" versus the coupling parameter *k* between the Roessler subsystems. Vertical full lines from left to right indicate transitions to phase-, generalized-, and lag-synchronization, respectively. Vertical dashed lines indicate periodic windows. The surrounding plots are delay coordinates plots for *p=7* and different *k* where the power classes of the occurring transcriptions are displayed in different colors. Colors from deep blue to yellow indicate increasing powers. Figure 3 shows that using information measures for the power classes allows us to reveal the complex synchronization dynamics of this system.

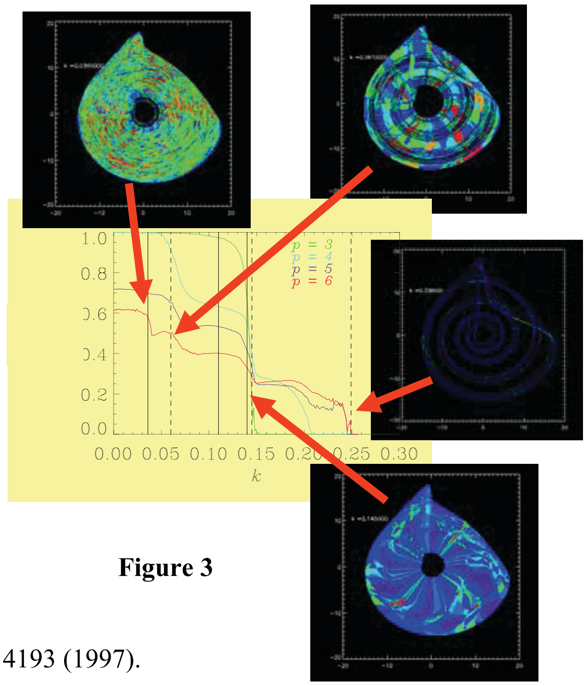

Figure 3

References:

• M. Rosenblum, A. Pikovsky, and J. Kurths, *Phys. Rev. Lett.* **78**, 4193 (1997).

Roberto Monetti and Wolfram Bunk

Chaotic Motions of the AFM

An atomic force microscope can be viewed as an impact oscillator. These systems are a special class of continuous time dynamical systems which undergo intermittent impact collisions and have dynamical trajectories in state space which are piecewise continuous, however, with discontinuities in the velocities resulting from the collisions of the tip with the surface.

Even if the system is linear in the absence of impacts, such as a freely oscillating AFM cantilever, the overall dynamics of the AFM exhibits a rich variety of behavior because of the non-linearity introduced by the impacts of the tip. In this work methods from dynamical systems theory have been used in order to investigate the phenomena resulting from the non-linearities induced by the interaction of the tip with the sample surface like hysteresis and sub-harmonics of the trajectories.

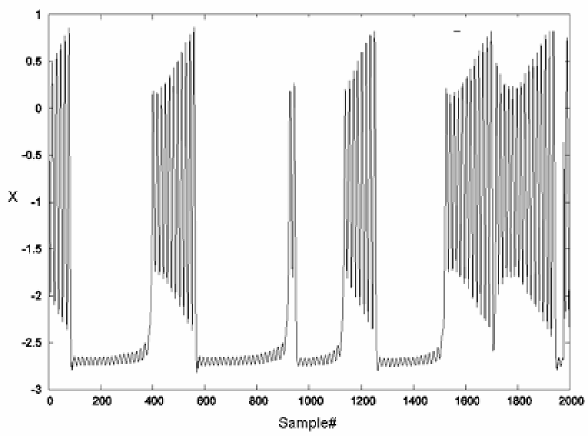

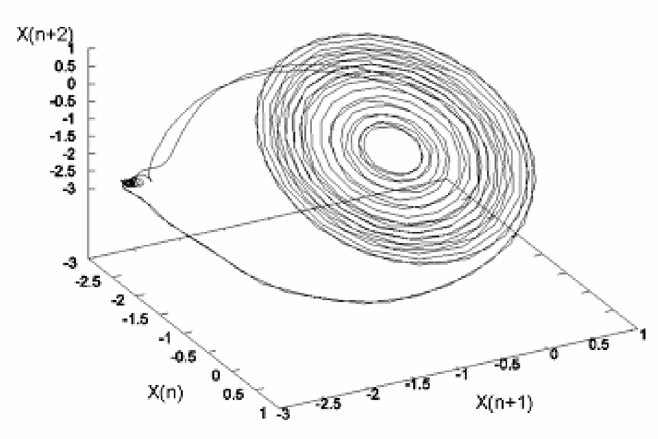

Figures: Upper left panel: Time series of the deflection signal of the cantilever during the snap-off phase showing clear signs of intermittency. Upper right: Delay coordinate embedding of the deflection signal showing two attractors. Lower right: Power spectrum of the deflection signal showing a peek at the driving frequency and a scaling of f^{-1} corresponding to On-Off intermittency or type III. The inset shows the experimental setup.

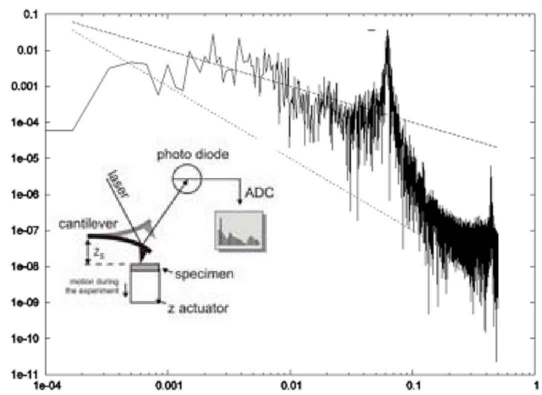

We report about a new chaotic mode of the AFM that has not been observed so far. During the retraction of the tip from the surface the deflection signal shows strong indications of intermittent behavior. The intermittency has been characterized to be either of Type III or on-off intermittency. Furthermore, understanding the dynamics of the system could help improve the overall system performance by being able to control the AFM in some desired dynamical regime or by preventing the AFM from going into some undesirable regime which would eventually result in system failure.

References:

• F. Jamitzky , M. Stark ,W. Bunk ,W. M. Heckl and R. W. Stark, Chaos in dynamic atomic force microscopy, Nanotechnology 17 (2006) p. 213 – p. 220

• F. Jamitzky and R. W. Stark, Intermittency in dynamic atomic force microscopy, NOLTA Proceedings 2006

F. Jamitzky, W. Bunk, W. M. Heckl and R. W. Stark

Efficiency and Medical Compatibility of Low-Temperature Plasma Sterilization

Low-temperature plasmas are an attractive tool for many medical applications. The objective of our project is to utilise the benefits of this technique to the healing of chronic foot and leg ulcers. We developed a device that operates under atmospheric conditions. This contribution investigates the efficiency of plasma treatment on a wide range of bacteria that are relevant to wound healing. Also the medical compatibility of plasma treatment is analysed ex-vivo using human blood and skin tissue.

The bactericidal effect of low-temperature plasmas is used in sterilizing surfaces of e.g. medical instruments. Their properties, like contact-free treatment and penetration of small cavities, make this technique highly attractive for medical in-vivo applications. In the project "plasma medicine" the suitability of this technique in the treatment of chronic foot and leg ulcers is investigated in cooperation with the Ludwig-Maximilians-Universität/Krankenhaus München Schwabing and ADTEC Plasma Technology Co., Ltd. (Japan). Bacterial colonization of the wounds leads to a prolonged healing process which is further complicated by germs that are resistant to many antibiotics. Our approach is the reduction of the bacteria load on the wounds by application of low-temperature plasma at atmospheric pressure. To this purpose a new plasma device (a microwave plasma torch) has been developed by our group.

Before low-temperature plasmas are applied in-vivo, its bactericidal efficiency and medical compatibility have to be verified. The first has been accomplished by treating bacteria strains relevant to wound healing. A clear sterilizing effect after two minutes of treatment could be observed in all tested samples including antibiotic-resistant bacteria. However, the size of the sterilized area depends on the bacteria type (see Fig. 1). In order to investigate the medical compatibility of plasma treatment, comprehensive ex-vivo tests of human blood, skin and cell samples have been conducted. In one of these tests, we treated human skin, which had to be taken routinely during regular surgery. The treatment was performed minutes after the surgery. The results did not show any deterioration, when the treatment time was kept within reasonable limits (see Fig. 2). In another experiment 5 ml of human blood was treated with the plasma device for one and two minutes respectively. The subsequent blood count did not show changes with respect to the untreated sample.

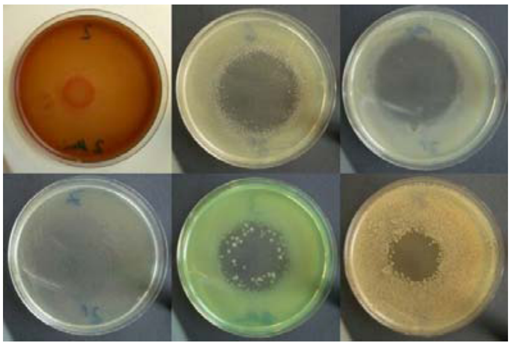

Fig 1: *Examples of bacterial cultures on agar plates after 2 minutes of plasma treatment. The transparent areas correspond to the sterilized region.*

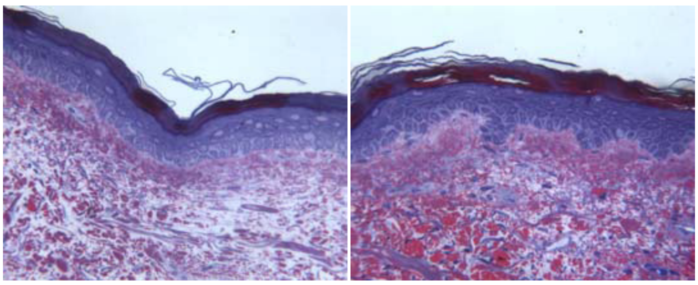

Fig 2: *Histological images of skin samples, treated ex-vivo. After 2 minutes no changes could be observed (right image) with respect to the untreated control sample (left image).*

The results of these tests enabled a clinical study that started end of 2005 and will last until mid of 2007. First analysis of the available results confirms a reduction of the bacteria load on the wound. Also, no unwanted side-effects have been observed and the patients did not report painful sensations during or after the treatment.

* Hospital Munich Schwabing, Munich, Germany   + ADTEC Plasma Technology Co. Ltd., Hiroshima, Japan

R. Pompl – T. Shimizu – H.U. Schmidt – W. Bunk – F. Jamitzky – B. Steffes – K. Ramrath* - W. Stolz* - T. Urayama+ – S. Fujii+ – G. Morfill*

Characterising bone structure for the diagnosis of osteoporosis

Osteoporosis is a metabolic bone disorder considered by the World Health Organisation (WHO) as one of the ten most important diseases worldwide. Bone mineral density (BMD) is the standard clinical parameter used for the diagnosis of this disease. BMD is a global measure of the mineral content of the bone and completely disregards the bone trabecular micro-architecture. The scaling index method (SIM) is introduced in this context as a novel approach to quantify structural differences in the bone trabecular network of healthy persons and patients with osteoporosis.

The information about the bone structure was obtained from the 3D high-resolution magnetic resonance (HRMR) images of distal radii (*Fig.1a*), which can be regarded as a 4D point distribution, where the fourth dimension corresponds to the grey level of the point (voxel). For each point of the image the weighted cumulative point distribution using a Gaussian shaping function was calculated and structural decomposition of the image according to its structural elements was obtained [1]. The probability distribution of the scaling indices $P(\alpha)$ (Fig.2) for osteoporotic patients is shifted to the higher values in comparison with healthy ones, because the structural deterioration of bone tissue leads to less trabecular structure present in the distal radius. From the spectrum of scaling indices $P(\alpha)$ a 3D nonlinear structure texture measure m^d was extracted using a filtering procedure with two sliding windows of variable width (*Fig.2*). We pointed our attention to the region of scaling indices $\alpha \in [2,3]$, which corresponds to the transition from trabecular (*Fig.1b*) to marrow bone (*Fig.1c*) micro architecture.

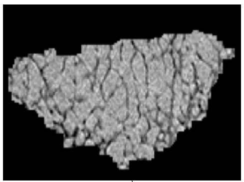

a)

*Fig.1.*Distal radii:
a) Segmented region of the HRMR
b) $\alpha \in [0; 2.5]$
c) $\alpha \in [2.5; 4]$

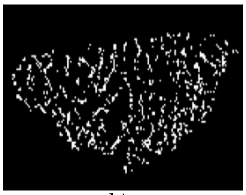

b)

c)

The SIM-derived texture measures m^d, BMD and 2D morphometric parameters were analysed by means of a receiver operating characteristic method (ROC), with regard to the spine fracture status. We obtained a higher value of the area under the curve (AUC) for m^d (AUC=0.85 in vivo [2] and AUC=0.89 in vitro) compared with BMD and trabecular separation Tb.Sp. (*Tab.1*), which means a superior diagnostic performance for differentiating patients with and without osteoporotic spine fractures. Statistical validation of our results using bootstrap and jackknife techniques showed significantly better results for m^d than for BMD and 2D morphometric parameters (*Tab.1*), i.e. m^d performed in both resampling methods with the lowest standard deviations and therefore highest consistency among all parameters. From the presented results one may conclude that the local 3D scaling index method can be used for the prediction of fracture risk, caused by osteoporotic changes in trabecular bone microstructure.

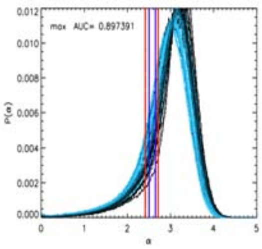

Fig.2. Spectrum of scaling indices α of healthy (blue) and osteoporotic (black) patients. Two sliding windows (red and dark blue) for the best value of AUC

AUC	max	bootstrap	jackknife
m^d	0.85	0.865±0.054	0.843±0.01
BMD	0.71	0.712±0.085	0.706±0.014
Tb.Sp	0.59	0.683±0.09	0.676±0.015

Tab.1. Maximum and mean values of the AUC

References:

- 1. Boehm HF, Raeth C, Monetti R, Mueller D, Newitt D,Majumdar S,Rummeny E, Morfill G, Link T, Invest Radiol 38(5): 269-280 (2003)
- 2. D.Mueller, T.M.Link, R.Monetti, J.Bauer, H.Boehm, V.Seifert-Klauss, E.J.Rummeny, G.E.Motfill, C.Raeth, *Osteoporos Int(2006)*17:1483-1493

I.N.Sidorenko, R.A.Monetti, D.Mueller, E.Rummeny, T.M.Link, J.Bauer, C.Raeth

Quantitative Description of Synchronization in Electrical Brain Activity *

A number of different synchronization measures is tested for their suitability to discriminate between electrical brain activity in interictal phases (between attacks) in an epileptic child and regular brain activity of an age-matched control group.

The electroencephalogram (EEG) of epileptic patients in acute phases is characterized by epileptiform features such as spikes and waves. However in periods between the attacks the EEG often appears inconspicuous and lacks such obvious signatures. It is supposed that even in this interictal periods electrical brain activity differs from that of healthy subjects regarding synchronization behavior. Multichannel EEG recordings (21 leads) allow for studying spatial-related synchronization effects. A new method for the quantitative assessment of spatio-temporal structuring of brain activity is presented. This approach combines several correlation measures that are sensitive to linear and/or non-linear relations in multichannel scalp EEG with an hierarchical cluster algorithm. In time domain synchronization is characterized by Pearson´s coefficient, Spearmans rank-order correlation coefficient and mutual information. In the frequency domain the applied quantities are Kullback-Leibler (KL) distance on the Fourier spectra or measures, which quantify the relations of instantaneous phases based on the Hilbert transformation. Beside a quantitative description of the overall degree of synchronization the spatial relations are investigated by means of the cluster characteristics. This methods are employed in a case study of a child with frontal lobe epilepsy and tested against an age-matched control group. The chosen information measures not only demonstrate their suitability in the characterization of the ictal and interictal phases, but they also reflect the recovery during successful medication (see Fig.1). The suitability of the different measures to discriminate the two groups is expressed by a contrast parameter (see Fig.2). Fig. 3 displays the locally resolved contrast parameter for the KL-distance. The synchronization of brain dynamics recorded by pairs of electrodes is color-coded according to their discriminatory power between the two groups.

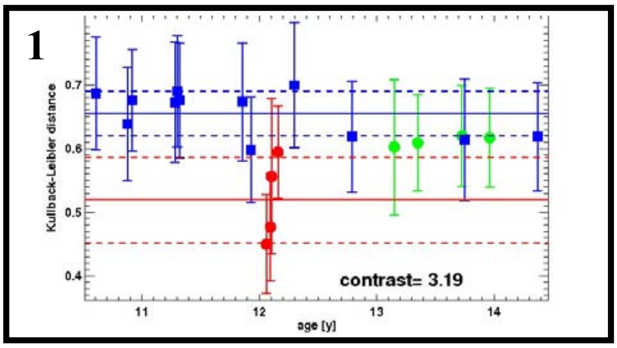

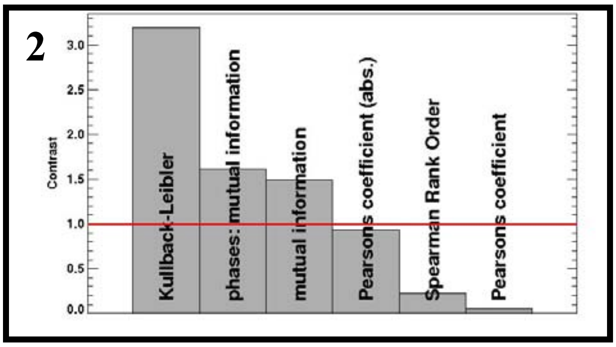

Fig.1: *Mean KL-distance and standard deviation of the different EEG recordings (red: epileptic child acute phase, green: epileptic child non-acute phase, blue: control group). Medication results in a synchronization of the brain towards the characteristics of the control group.*

Fig.2: *Comparison of the contrast values for the different measures. High contrast reflects an enhanced sensitivity of the corresponding quantity to the different electrical brain synchronization in the epileptic patient compared to the control group.*

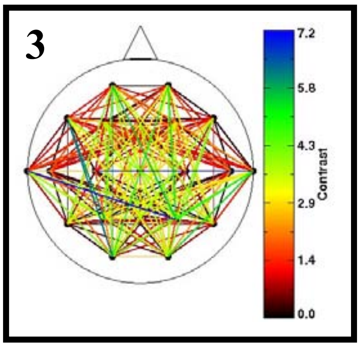

Fig.3: *Color-coding of the contrast for every pair of electrodes based on the KL-distance.*

* Collaboration with S. Springer, Heckscher Klinik für Kinder- u. Jugendpsychiatrie, München

Th. Aschenbrenner, W. Bunk, S. Springer, R. Pompl*